UNIVERSITY OF SOUTHAMPTON

The dynamic analysis and control of cracked rotating beams

by

Ahmed YASHAR

A thesis submitted in partial fulfillment for the degree of Doctor of Philosophy

in the

Faculty of Engineering and the Environment

Institute of Sound and Vibration Research

July 2018

UNIVERSITY OF SOUTHAMPTON

ABSTRACT

FACULTY OF ENGINEERING AND THE ENVIRONMENT
INSTITUTE OF SOUND AND VIBRATION RESEARCH

Doctor of Philosophy

by Ahmed YASHAR

This thesis covers the dynamic modelling of un-cracked and cracked rotating beams. Accordingly, a new model of a rotating cracked beam is developed using the finite element and the Rayleigh-Ritz method to characterise and analyse its dynamic behaviour. The effect of various parameters are investigated, such as rotational speed, hub ratio and slenderness ratio. In addition, the critical speed, buckling speed and veering phenomena are identified. The numerical results produced are shown to be in good agreement with models based on finite element representations.

In addition to the theoretical investigations, experimental validation is presented. A test rig was designed and manufactured with a changeable rotating hub mount for different test requirements. Moreover, the rig was conceived to incorporate capabilities such as applying variable rotational speed using a variable frequency driver and provide vertical base excitation input to the centre of rotation of the hub. The tests were performed using random excitation at the root of the rotating cantilever beam to excite the flapwise modes of the beam. The responses were then measured optically using a high-speed camera, and the images were post-processed using a digital image correlation (DIC) method. This non-invasive optical method was used to extract the temporal deflection of the beam. The frequency response functions are then obtained from the measured responses. The estimated modal frequencies were compared with numerical simulations to validate the Rayleigh-Ritz and FE numerical models at various rotational speeds. Furthermore, an experimental crack detection was implemented and the results showed a good match to the introduced actual crack location and depth. The crack detection approach on the rotating cracked beam uses the fundamental and second natural frequencies.

For vibration control of the rotating beam, a real-time velocity feedback control was applied using a remote single optical high-speed camera. An electromagnetic actuator was designed and mounted on the rotating hub to apply a feedback force on the rotating beam. The results for vibration control of the rotating beam show significant active damping and reduction in the amplitude of the first resonance over a wide range of rotational speeds.

Contents

List of Figures

List of Tables

UNIVERSITY OF Southampton

Research Thesis: Declaration of Authorship

Print name:	Ahmed Muhammed Ibrahim YASHAR

Title of thesis:	The dynamic analysis and control of cracked rotating beams

I declare that this thesis and the work presented in it is my own and has been generated by me as the result of my own original research.

I confirm that:

1. This work was done wholly or mainly while in candidature for a research degree at this University;
2. Where any part of this thesis has previously been submitted for a degree or any other qualification at this University or any other institution, this has been clearly stated;
3. Where I have consulted the published work of others, this is always clearly attributed;
4. Where I have quoted from the work of others, the source is always given. With the exception of such quotations, this thesis is entirely my own work;
5. I have acknowledged all main sources of help;
6. Where the thesis is based on work done by myself jointly with others, I have made clear exactly what was done by others and what I have contributed myself;
7. Either none of this work has been published before submission, or parts of this work have been published as:

    - Yashar, A., Ghandchi-Tehrani, M. and Ferguson, N. (2016). Dynamic behaviour of a rotating cracked beam. Journal of Physics: Conference Series, 744, p.012057.
    - Yashar, A., Ferguson, N. and Tehrani, M. (2017). Measurement of rotating beam vibration using optical (DIC) techniques. Procedia Engineering, 199, pp.477-482.
    - Yashar, A., Ferguson, N. and Ghandchi-Tehrani, M. (2018). Simplified modelling and analysis of a rotating Euler-Bernoulli beam with a single cracked edge. Journal of Sound and Vibration, 420, pp.346-356.

Signature:		Date:	

Acknowledgements

Firstly, I would like to express my sincere gratitude to my supervisors Dr Maryam Ghandchi Tehrani and Dr Neil Ferguson for the continuous support of my Ph.D. study and related research, for their patience, motivation, and immense knowledge. Their guidance helped me in all the time of research and writing of this thesis. I could not have imagined having a better advisor and mentor for my Ph.D. study.

My sincere thanks also goes to the Mistry of Higher Education and Scientific Research in Iraq for providing a full Ph.D. scholarship.

Last but not the least; I would like to thank my family: my parents and my wife for supporting me spiritually throughout writing this thesis and my life in general.

. . .

Nomenclature

a	Crack depth
b	Beam width
$c_i j$	Element flexibility
d	The displacement vector for flapwise motion
$\bar{d}$	An arbitrary vector
f	The transverse lateral distributed force
f_e	Frequency measured from the experimental test
f_s	Frequency estimated from the simulation
g	Element gyroscopic term
h	Beam height
i	Current
l	Element length
n	The number of shape functions
r	Hub radius
s	stretch
s	Laplace variable
w	The transverse displacement
x	Location along the beam
$\bar{w}, \bar{v}, \bar{s}$	Arbitrary weight for weight functions

A	Cross sectional area
B_m	Flux density
C	Flexibility constant
C_D	Crack depth
C_L	Crack location
E	Young's modulus of elasticity
F	A correction factor
F_m	Electromagnetic actuator force
G(s)	Transfer function of the plant
$\mathbf{G}$	The gyroscopic matrix
H(s)	Transfer function of the controller

I	The second moment of area
J	The strain energy
$\mathbf{K}$	The stiffness matrix
L	Beam length
L_m	Electric conductor coil length
$\mathcal{L}$	Lagrangian functional
$\mathbf{M}$	The mass matrix
N	The shape functions
O	Centre of rotation
P, P_1	The longitudinal (axial) force
P_2	The shear force
P_3	The bending moment
$R_{w,v,s}$	The admissible function
$\mathbf{S}$	The rotational motion-induced stiffness
$\mathcal{S}$	The action integral
T	The transformer matrix
V	The Velocity vector
W	The lateral amplitude (flapwise)
$\mathcal{W}$	The work done
$Y_{w,v,s}$	The shape function
X, Y, Z	Coordinate system fixed on the beam

α	The slenderness ratio
β	The Ritz coefficients
γ	The angular speed ratio
δ	The hub ratio
ε	Strain
θ	Slope in flapwise bending
κ	The stress intensity factor (SIF)
μ	The longitudinal deflection
ξ	Crack depth ratio
ρ	Mass density
σ	Stress
ϕ	The rotational deflection
ϖ	The frequency ratio
ϖ	An arbitrary weight function
ω	The natural frequency
ψ	Slope in chordwise bending
Θ	Slope
Π	The elastic energy available

Ω	Rotational speed (rpm)

Subscripts

e	Element
w, v, s	subscript representing flapwise, chordwise

Abbreviations

AFG	The Axially functionally graded
CLR	Crack location ratio
DIC	The Digital Image Correlation
DIP	The Digital Image Processing
FEM	The Finite Element Method
KE	The Finite Element Method
PE	The potential energy

Chapter 1

Introduction

Throughout modern history, turbomachinery remains a highly relevant mechanism in rotating structures, such as wind turbines, helicopter blades and gas turbines. These devices are essential in daily life supporting cities with power generation or use in transportation, such as helicopters and aeroplanes. Typically, turbomachines comprise a number of high speed rotating blades, nominally identical and dynamically balanced. The operation of such machines can give rise to safety and durability issues. For example, in the helicopter case flying a massive engine with sharp blades above buildings could seriously endanger peoples lives. To overcome these problems, the possible failure of these devices must be considered and carefully eliminated or minimised to avoid human and material losses. For these reasons, health monitoring and vibration control of rotating systems are constantly being developed and the pace of the growth in the research in this area increases with improvements in computing capacity as well as instrumentation and data acquisition from installed systems.

One of the most critical areas in health monitoring of a rotating structure is crack detection, which is a cause for catastrophe and sudden collapse in turbomachinery applications. It is essential to understand how the crack occurs, to prevent or deal with it using detection techniques. In addition to the manufacture or operational error, cracks can occur due to environmental reasons such as erosion and corrosion or due to the fatigue. Erosion occurs because of the physical impact of small solid particles such as sand Castorrini et al. (2016), also according to Han et al. (2018) the leading edge of the blade is more subjected to this type of damage. Corrosion takes place because of a chemical reaction between moisture and metal blades Davis (2000) and this kind of damage can occur anywhere in the helicopter body. According to the type of metal, both erosion and corrosion can cause cracks on the blade surface. Besides, there are non-environmental causes of cracks, such as accidents or fatigue. Accidents can be caused by misusing the device mentioned above or by the fatigue of a material produced by frequently applied loads on the blades from opposing directions Chen et al. (2013). In addition, the blades can be subjected to variable forces in both direction and amplitude. As a result, each

Figure 1.1: Applications of rotating beams. Wind turbine REpower 5M in the North Sea off the coast of Belgium Hillewaert (2008). A General Electric J85-GE-17A turbojet engine (1970) Acharya (2008). Bell 206 Jetranger helicopter Field (2006).

taking off and landing decreases the lifespan of a helicopter blade and increases the crack probability.

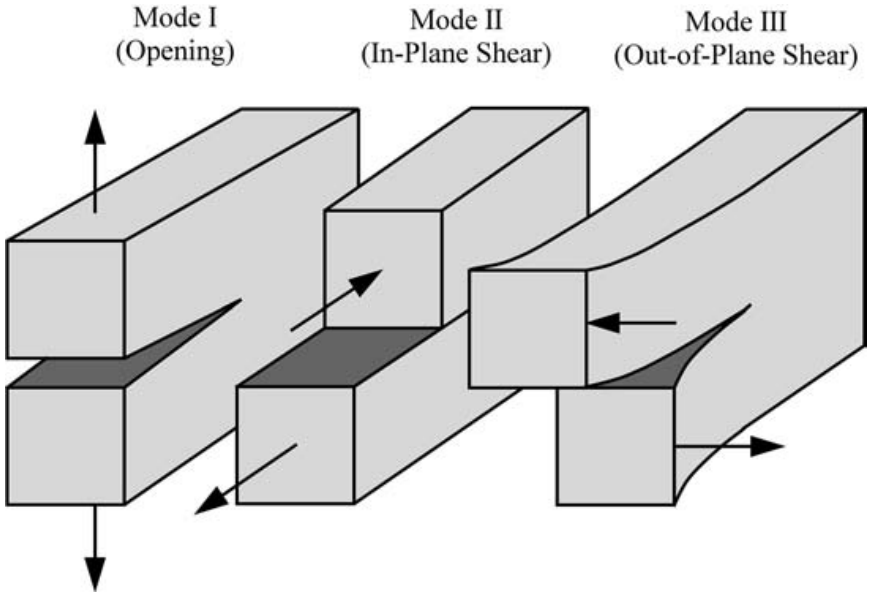

Figure 1.2: Crack modes. (Anderson, 2005)

The characteristic and behaviour of typical cracks can be very different but typically are characterised according to three main factors, which are type, location and the depth of the crack. Crack types are either opening, sliding and tearing Anderson (2005) as

shown in Figure 1.2. These types give different behaviour depending on the direction of the crack relative to the direction of any applied force. In addition to these modes, there are two different variables that change the effect of the crack, firstly, the location of the crack according to the attached structure or fixed points, for example, in the wind turbine the centre of rotation. When the crack is near the root, the effect increases because of the moment principle. When the distance from the tip of the blade to the crack is longer, the effect of the crack becomes greater. The second variable is the depth of the crack Liu and Jiang (2014). The deeper cracks impact more than the shallow ones.

In accordance with this information, crack detection is a complicated procedure because there are different types, sizes, directions and orientations of the cracks. This is why there are numerous methods to detect blade cracks, each approach designed to inspect specific types of these defects. One of the earliest methods is x-ray pictures, which inspects damages and cracks, though cracks smaller than half an inch were impossible to detect with this method G. P. Engels and Thomas (1993). The second method is Magnetic Flux Preventive (MFP); this method is perfect to examine even tiny faults (in all the types of cracks) on the surface of a metallic blade. However, magnetic flux does not work on non-magnetic blades such as titanium and aluminium G. P. Engels and Thomas (1993). The third method is Cockpit Blade Inspection Method (CBIM) Centro de Publicaciones (2006); the process involves pressurising the inner hollow of the rotor blades with nitrogen. When a crack is present, the pressure is lost and this indicates on the cockpit display. This method is used in Sikorsky S-61 Series helicopters Figure 1.3. The first two methods (X-Ray Pictures and Magnetic Flux Preventive) can be applied in special laboratories that have the necessary equipment. The third method (Blade Inspection Method) has the advantage of a real-time indicator that can detect hairline fractures while the helicopter is on a mission.

Furthermore, according to Marks et al. (2017) the structural health monitoring (SHM) techniques typically applied for helicopters and wind turbines can detect defects long before they have influenced the performance of the system. Moreover, acoustic emission (AE) considers one of the powerful mechanisms for detecting the source of energy release from the structure, such as due to fatigue crack initiation, growth or corrosion. The advantage of this technique is in passive monitoring, which does not require external excitation to detect and identify damage. However, the disadvantage of this technique is that other acoustic signals exist, such as vibration or due to noise from the gearbox, which can be incorrectly interpreted as a defect (Baxter et al. (2007)). Moreover, the health and usage monitoring system (HUMS) has received considerable attention recently for increasing the mission safety and the equipment reliability in addition to reducing the maintenance costs. However, this system is based on monitoring the gearbox and the usage of the helicopter (Pawar and Ganguli (2007)). As a result, detection of cracks is of very great importance especially their location and orientation, since the

symptoms can be different for each case. Most of these techniques are based on an in-depth analysis of the signal from different locations of the vehicle. The signal processing is based on analysing this data for comparison against a pattern of the signals recorded for the healthy state of the structure. Then, the changes in these patterns are studied constantly and remotely with consideration of the structure's age. For example, Dervilis et al. (2014) used damage diagnosis of a wind turbine based on pattern recognition.

Figure 1.3: Sikorsky S-61L Chen (2012)

This thesis presents a new approach to investigate and analyse the vibrational behaviour of rotating cantilever beams with and without cracks, which can be representative for example of helicopter blades or wind turbines blades, using optical measurements. The numerical results of the developed models will be illustrated and compared with the results reproduced from previously published work.

A model of uniform cross-section cantilever beam will be considered and the free and forced vibration characteristics will be calculated. In addition, the effect of the angular rotational speed will be considered, by comparing the natural frequencies with respect to the rotational speed.

Subsequently, a numerical model of the crack will be introduced into the rotating system and the same analysis will be performed on the cracked system. The outcome of this will be compared with the theoretical results obtained from FEM and the Rayleigh-Ritz method, to validate the models developed and to compare the method with a wide range of published literature on the vibration of rotating beams, crack modelling and analysis of rotating cracked beams and blades.

The design of an experimental test rig will be presented for comparison to the theoretical predictions. In addition to the open crack, a bilinear or breathing crack will be modelled for time-domain simulations using FEM. The experimental results will be acquired using

a high-speed camera and three types of recently developed digital image processing methods.

Finally, two applications will be presented based on the model developed in the last part of this thesis, which is to do with crack identification and active vibration control of the rotating beam. The crack location and depth detection will be based on the experimental measurement and theoretical updated model. Regarding vibration control, a simulation model in addition to the experimental test will be performed using velocity feedback. The latter based on non-contacting optical measurements and electromagnetic force application.

1.1 The aims and objectives of this research

In general, the aims of this research are; **firstly**, to determine via modelling the dynamic behaviour of cracked and un-cracked rotating beams. **Secondly**, to identify the crack, if it exists, from changes in the free and forced vibration characteristics. **Thirdly**, to apply a suitable non-invasive method to measure the natural frequencies of the rotating beam using optical measurements instead of using typical accelerometer sensors. **Finally**, the project aims to apply active control methods to reduce or minimise the vibration of the rotating beam.

The first objective covers the characterisation and analysis. This will require the development of a new approach, using both the Finite Element Method and the Rayleigh-Ritz method using method of variational energy principles for rotating cracked beams, considering the additional flexibility and centrifugal stiffening due to the crack and rotation, respectively. Moreover, the gyroscopic effect will be included to simulate most of the actual applied loads to structure.

For crack identification, the model of a crack is introduced to the rotating beam model. The model should accurately represent the effect of different crack location, depth and orientation. In addition, calculation of the second and third modes are required besides the fundamental mode to identify the crack. These results will be compared with the un-cracked beam and the difference will lead to a potential identification methodology for the crack, its depth and its location.

Typical vibration instrumentation such as accelerometers have disadvantages for rotating systems, mainly due to the wiring and the extra mass. Therefore optical measurement techniques will be applied to provide accurate and non-intrusive measurements for validation of the model, the crack identification and also active control.

Active vibration control of a rotating beam will be considered. Using optical measurement the velocity feedback control method will be implemented on the non-rotating and rotating beam. Generally, rotating beams can be controlled passively by limiting the

rotational speed range, adding mass/damping and changing the profile design. Alternatively, active control can be used by employing sensors and actuators to control the vibration by providing control forces in order to reduce undesirable vibrations or add damping, etc.

1.2 The structure of the thesis

This thesis is organized into eight chapters. The scope of each chapter is provided as follows.

Chapter 2 presents the literature survey, which reviews the relevant methods that are currently used for modelling a rotating beam, either cracked or uncracked. In addition, the relevant optical measurement methods are presented including a brief description of the relevant digital image processing techniques such as digital image correlation. Furthermore, experimental work covering vibration measurement and crack detection are mentioned.

Chapter 3 covers the main methods for modelling a rotating beam, firstly by a simple force equilibrium method and then using Hamilton's principle. In addition, various numerical methods to solve the resulting partial differential equations are shown in detail, using either the finite element or Rayleigh-Ritz method. Then, the modelling of a rotating cracked beam element is developed with a massless spring connecting the two segments of the beam and incorporating this within the FE model. Likewise, the crack is also introduced into the Rayleigh-Ritz approach, as a reduction in the potential energy of the system due to the additional flexibility of the crack.

In chapter 4 the results of simulations using the main two numerical modelling approaches are shown, focusing on various aspects such as comparing the two approximate methods. Moreover, the effects of different parameters such as rotational speed, hub radius and slenderness ratio on the natural frequency speed curves are illustrated. The explanation of how they affect the results are described. Moreover, the effect of an open crack and a bilinear crack are illustrated.

Chapter 5 presents an overview of the experimental design, which is subsequently manufactured with specific dimensions, and a mechanism to measure the vibration of the flapwise and chordwise vibrations of the rotating beam with and without crack. Furthermore, the results are obtained for different beam dimensions using high speed cameras in different configurations. Three different image processing methods namely digital image correlation (DIC), marker detection and colour blob detection are evaluated and contrasted. Moreover, the natural frequency results are then compared with the simulation results.

Chapter 6 applies an optical measurement method and image processing to detect and identify the location and depth of a crack in a rotating beam. The method developed is based on experimentally measuring the two lowest natural frequencies of the rotating beam at different rotational speeds and generating natural frequency versus rotational speed curves. Then, comparing these curves with the corresponding ones obtained from a numerical two-dimensional parametric study, the parameters of which are the crack location and depth, an updated Rayleigh-Ritz model is used to identify the optimum fit for identification of the crack properties.

Chapter 7 applies active vibration control on a rotating beam. The active control strategy is velocity feedback. Firstly, a simulation model is developed and tested to reduce the amplitude of the vibration during the rotation of the beam. Then, a novel experimental test is performed using a high speed camera, as a sensor, and an electromagnetic actuator after modifying the earlier test rig for this application. Active control is applied at different rotational speeds and behaviour of the open and close-loop system is analysed to obtain the gain margin and the phase margin of the system for stability analysis.

In chapter 8, the overall conclusions and suggestions for future work are provided.

1.3 The contributions to date

This thesis includes numerical and experimental contributions to the field of the vibration modelling and control of rotating beams with and without cracks.

- The numerical contribution starts with models of a rotating cantilever beam using a Rayleigh-Ritz method, with a special trial function to reduce the numerical errors. In addition, a new rotating open and bilinear cracked finite element is developed, using an energy method and the principle of fracture mechanics. Furthermore, the gyroscopic coupling effect, which couples the stretch and bending motion of the chordwise vibration, is considered in this new rotating cracked beam model. Moreover, a novel model of a cracked cantilever beam is developed by subtracting the effect of the crack from the total potential energy of the intact rotating cantilever beam utilizing the Rayleigh-Ritz method.
- The experimental contribution to date is the design and manufacturing of a test rig with a multi functional rotating hub. The rig has the ability to test a beam up to a controllable speed of 24000 rpm and apply an excitation through the rotating shaft to the base of the rotating cantilever beam. Furthermore, the flapwise vibration

can be measured using an optical high speed camera. In addition, the rig possesses the ability to perform an active vibration test using an electromagnetic actuator.

- The experiment uses recently available optical measurements for the non-invasive or remote measurement of the vibration, comprising three different types of digital image processing. The experimental and simulation results were compared to verify the results.
- Active vibration control of rotating beam based on real time, remote optical measurement and velocity feedback.

This study has a potential impact and application in the development of a health monitoring and vibration control system for rotating structures, such as wind turbines or helicopter blades.

Chapter 2

Literature review

Rotating beams play a significant role in the design of various engineering applications such as gas turbine blades, helicopter propellers and wind turbines. Cracks are the most common defects in these structures that might lead to increased vibration, which can eventually destroy the structure. Investigations are often made regarding the vibrational behaviour of a cracked rotating blade, which includes crack identification and detection methods so that consecutive damage could be prevented or reduced.

This chapter will concentrate on studies, which investigate the area of rotating cracked beams. Three main aspects that deal with modelling a rotating beam structure with and without cracks will be discussed in the first three sections, which include modelling of rotating beams, modelling of cracks and modelling of rotating cracked beams.

In addition, the digital image correlation is used to measure the vibration without contact with the vibrating object. The method can determine the vibration of the rotating structure. Furthermore, several experimental results and procedures will be explained in the final section.

2.1 Vibration of rotating homogeneous cantilever beams

The main two well-known beam theories are Timoshenko and Euler-Bernoulli. The main assumptions are based on small displacement of linear vibration. These assumptions can be listed in three main points for the Timoshenko beam theory;

- The material in the plane, which is perpendicular to the longitudinal axis before deformation, will remain in the plane during deformation.
- The displacement along the unloaded direction is zero (plane strain assumption).

- Along any cross-section the displacement in the loaded direction is the same, which means there is no stretch in the thickness of the beam.

Regarding Euler-Bernoulli beam, the additional assumption is that the shear deformations are negligible if the beam is long and thin so that the aspect ratio (length to thickness) is greater than 10 Inman and Tech (2006). Intact rotating beams are generally simplified as being a one dimensional Euler-Bernoulli or Timoshenko beam subjected to centrifugal forces.The stretching causes additional stiffness to the bending stiffness of the structure, with certain consequences in the variation of the natural frequencies and the mode shapes. Numerous published studies have looked into the effect of the rotational speed on the natural vibration of rotating cantilever beams, which will be briefly presented below.

Various studies deal with modelling and developing mathematical expressions to describe vibration of rotating beams. Rubinstein and Stadter (1972) studied the vibration of rotating simply supported-free uniform beams and found that the natural frequencies of bending vibration tended to increase above those for the non-rotating beams due to the centrifugal effect. Bhat (1986) applied the Rayleigh Ritz method for modelling a cantilever rotating beam (fixed-free) with a tip mass, using beam characteristic orthogonal polynomials to evaluate the natural frequencies of the flexural modes. However, both studies only considered the lateral vibration of cantilever beams, which is in the flapwise motion.

Subsequently, a significant improvement in describing the vibration of rotating beams were proposed by Yoo and Shin (1998), where a new set of coordinates was introduced based on stretching and bending deformation using energy methods. Cai et al. (2004), Chung and Yoo (2002) and Yang et al. (2004) expressed the linear partial differential equations for the flapwise, chordwise and stretch motions of a rotating beam, which consist of a non-cartesian variable to describe the elastic (stretch) deformation as shown in Figure 2.1, and two Cartesian variables (chord-wise and flap-wise deformations). All of the displacements in the three directions are linear and Chung and Yoo (2002) used a finite element method, derived from Hamiltonian's principle, which was also used by Kim et al. (2013), to investigate the free vibration characteristics of rotating beams for the axial, chordwise and flapwise motion. The new coordinates introduce the coupling effect between the chordwise and the longitudinal vibration, which significantly changes the vibration behaviour by veering between chordwise bending and longitudinal stretched modes. In contrast, Zhao and Wu (2017) indicate that the Coriolis term does not significantly affect the chordwise bending frequency of a rotating beam without crack. Advanced investigations subsequently have been developed to study rotating beams with specific profile and shapes. Rao and Gupta (2001) included the effects of twist, offset, speed of rotation and taper ratios on the natural frequencies and mode shapes of a rotating twisted and tapered beam using a finite element method. However, an

important contribution is the application of the dynamic stiffness method (DSM) by Banerjee et al. (2006), which extended the analysis to a wider context at the same time as providing accurate results using the Frobenius method. The method formulated the dynamic stiffness matrix for the dynamic analysis of rotating tapered beams. The dynamic stiffness method has all the features of the finite element method, nevertheless the DSM allows an exact vibration analysis of structures to be possible.

Simultaneously, another group of research has worked on optimizing beam profile shape or dimensions to adjust the natural frequencies, which could increase the working life of the blades or the rotating structures. Yoo et al. (2006) introduced an optimisation method for rotating cantilever beams to satisfy certain modal characteristics, resulting in the beam profiles as shown in Figure 2.2. The shape optimization was performed to increase the fundamental frequency of the beam. Ozdemir and Kaya (2006) investigated the vibration characteristics of rotating tapered cantilevers following both Euler-Bernoulli and Timoshenko beam theory from a differential transformation method (DTM). This investigation led to finding an inverse relationship between the taper ratio and non-dimensional natural frequency, as shown in Figure 2.3, where the taper ratio is $1 - \frac{A_f}{A_b}$ with A_f and A_b being the free end area and the area of the cantilever base, respectively. In practice, for example, wind turbines or helicopter blades are not uniform beams and they are considered to have a taper ratio. Again, their study was also limited to flapwise direction motion. However, Mazanoglu and Guler (2017) proposed a flapwise and chordwise flexural vibration analysis for centrifugally stiffened for the axial direction tapered beam. The axially functionally graded (AFG) model was simulated using the Rayleigh-Ritz method and compared with solid FE model built in FE simulation software. The model simulated different boundary conditions. The Rayleigh-Ritz method also can be adapted for composite material using a different structural theory. An example is the Classical Laminated Plate Theory Chai (1994), where the free vibration of beams on different support conditions were studied. Another reported study used a first-order shear deformation theory (FSDT) Oliveri and Milazzo (2018). Here in these two theories the change in mass density and the elasticity of the material were necessary in order to formulate the problem for its solution using the Rayleigh-Ritz method.

In addition to modelling and optimisation, the frequency and time domain responses were investigated to study the behaviour of the rotating cantilever beam under various operating conditions. Chung and Yoo (2002) studied the time response of rotating beams during start-up, steady speed and decreasing speed. With two different patterns of running machine (smooth running and non-smooth running), as shown in Figure 2.4, the results led the investigators to conclude that working under a smooth running condition causes a large reduction in the vibration of the rotating beam. Obviously, from all of these different research results, which include modelling, optimising and analysis, the conclusions are consistent in that increasing the rotational speed leads to an increase in the natural frequencies of vibration for rotating cantilever beams.

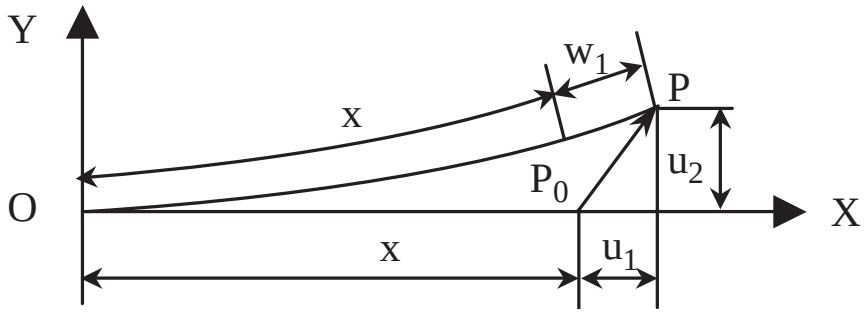

Figure 2.1: Description of the deformation of a rotating beam.
u_1, u_2, w_1 represent the deformation in the X direction, Y direction and non-Cartesian stretch direction. (Cai et al., 2004)

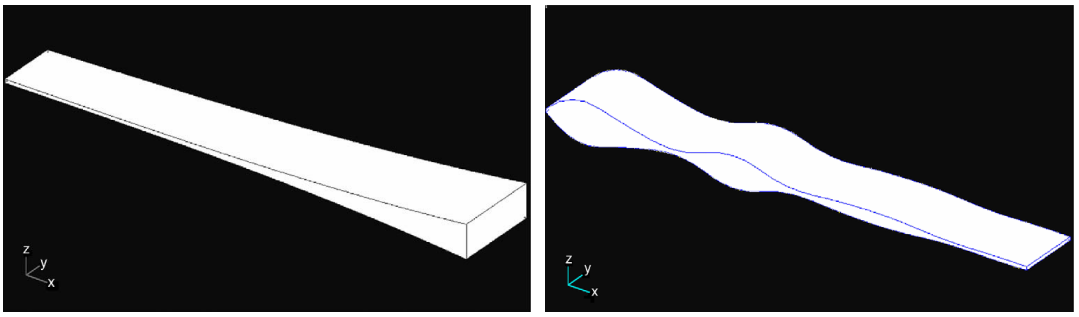

(a) Beam shape that minimises the first natural frequency.

(b) Beam shape that maximises the first natural frequency

Figure 2.2: The optimisation research of rotating cantilever beams (Yoo et al., 2006).

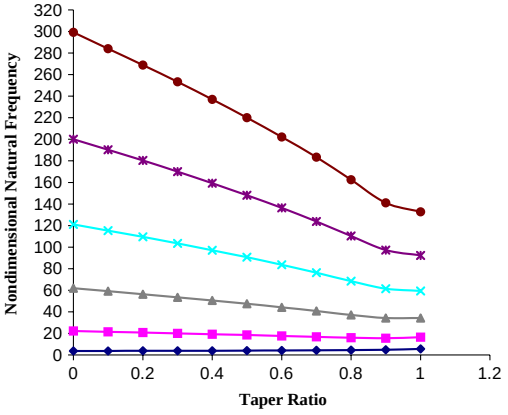

Figure 2.3: The inverse relationship between the taper ratio and the six lowest non-dimensional natural frequencies. Hub ratio= 0 (Ozdemir and Kaya, 2006). The taper ratio is the function of the change of the beam area at the tip compared to the base area.

@

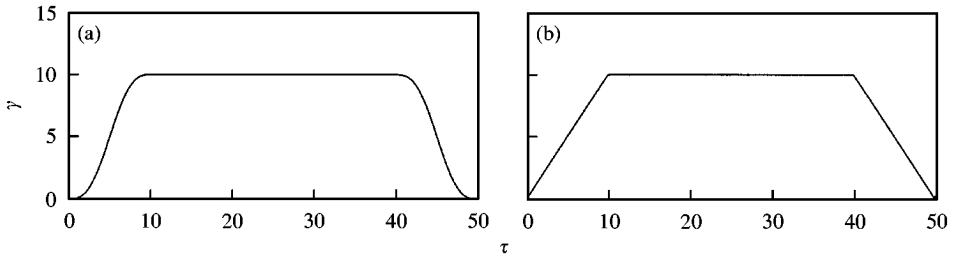

Figure 2.4: Profiles of the dimensionless rotating speed γ for the dimensionless time τ: (a) the smooth profile and (b) the non-smooth profile (Chung and Yoo, 2002). The forms lead to reduced vibration during operation of speed up and slowing down of the rotational speed.

2.2 Crack modelling

A decrease in the natural frequencies occurs in cracked beams because of the additional flexibility that is brought forth due to the presence of cracks. Countless researchers have looked into the modelling of cracks. In general, these models are based on crack modes, which are three in type namely opening, sliding and tearing as shown in Figure 1.2 (Anderson, 2005). These modes depend on the location and orientation of the crack according to the forces, which are applied to the structure.

The analysis of the local flexibility of the cracked area in the structural element has been computed by relating the flexibility to the crack stress intensity factor (SIF), which shows the stress intensity near to the tip of a crack that occurs due to remote loads or residual stresses. According to this principle, a method was developed for the calculation of the SIF based on local bending stiffness Schijve (2004), which is the inverse of the local flexibility of a cracked beam that can be determined theoretically. The stress intensity factor can be obtained from (2.1),

$$K = \sigma\sqrt{\pi a}F \tag{2.1}$$

where σ, F and a represent the applied stress, correction factor from the geometry change and crack length, respectively. This concept was applied subsequently by numerous researchers. Anifantis and Dimarogonas (1984) extended the Paris equation principle, which is used to determine the deflection of a cracked member, to calculate the deflection of cracked elements in the buckling of a cracked beam. A similar approach was used by Gounaris and Dimarogonas (1988) to develop a single cracked element consistent matrix for an Euler-Bernoulli beam; the ability of this research was limited in finding the crack size when the location of the crack is known by measuring the amplitude of vibration . Qian et al. (1990) developed a finite element model of a cracked cantilever beam with an edge-crack, by deriving an element stiffness matrix of a beam with a crack from an integration of the stress intensity factors, which shows a very good agreement with the experimental results. However, this work was restricted to in-plane vibration, which did

not include the tearing mode of vibration. Another publication by Chondros et al. (1998) studied a continuous cracked beam vibration theory for the lateral vibration of cracked Euler-Bernoulli beams with single/double edge open cracks. They also compared the results of a double edge for the crack with experimental results. Multi cracked beams can also be modelled using their technique. Various applications used different cross sectional area or structural design that needs a number of stress intensity factors. Zheng and Kessissoglou (2004) determined the natural frequencies and mode shapes of cracked rectangular and circular cross sectional beams using the finite element method based on fracture mechanics principles. An overall additional flexibility matrix was added to the flexibility matrix of the corresponding intact beam element to obtain the total flexibility matrix of the cracked beam.

Regarding structural design, Ibrahim et al. (2013) investigated the effects of crack depth and crack location on the in-plane free vibration of cracked frame structures numerically using the Finite Element Method. The results of this research show clear relationships between the crack location and crack depth versus natural frequencies and concluded that an inverse relationship existed between the crack depth ratio and the natural frequencies. Moreover, the closer the crack is to the fixed end of the beam, the larger is the crack effect on the natural frequencies. Similar effects were studied by Panigrahi and Parhi (2009) and the results were compared with solid models built using FE software, as shown in Figure 2.5.

Further investigations were discovered where determining the crack depth using open crack models lead to an underestimation of the actual depth of the crack, which could be a reason to ignore the seriousness of the crack. Therefore, the breathing or closing crack was studied to mitigate this issue. The breathing or closing crack was studied by Vigneshwaran and Behera (2014) using Castigiliano's theorem and strain energy release rate (SERR) to calculate the influence coefficients, which were later used to find the stiffness of the cracked beam. To simplify the non-linearity of a closing crack the breathing crack beam can be modelled as a piecewise linear system (bilinear breathing crack). Chondros et al. (2001) followed this simple bilinear beam approach with only two states, either fully open or fully closed, as shown in Figure 2.6. It was also assumed that the undeformed state of the beam is a transition period from the open state to closed state. Simulation of a bilinear crack was represented as a time variable stiffness crack Ruotolo et al. (1996), where the properties of a crack are changing with time. In addition, the time variation was represented as a square-wave function. The equation of motion becomes,

$$M\ddot{u} + D\dot{u} + (K - \delta K f(t))u = R \tag{2.2}$$

where M, D and K represent mass matrix, damping matrix, stiffness matrix and $f(t)$ is represented by a square wave as shown in Figure 2.7. The upper and lower side of the wave represent opening and closing movement of the crack. Actual or physical crack face contact were studied by Chati et al. (1997). This approach is more realistic from

the physical means than the time variable stiffness. The study of either the fully open and fully closed crack state was defined depending on the slope of the left and right hand side of the crack. Furthermore, SDOF and two DOF models of a bilinear crack were identified to determine the first two lower bilinear frequencies as given in Equations 2.3 and 2.4 and shown in Figures 2.8 and 2.9.

$$\Omega_0 = \frac{2\omega_1\omega_2}{\omega_1 + \omega_2} \quad \longrightarrow SDOF \tag{2.3}$$

$$\Omega_1 = \frac{2\omega_{11}\omega_{21}}{\omega_{11} + \omega_{21}} \quad \Omega_2 = \frac{2\omega_{12}\omega_{22}}{\omega_{12} + \omega_{22}} \quad \longrightarrow \quad 2DOF \tag{2.4}$$

where Ω_0, Ω_1 and Ω_2 represent the fundamental bilinear frequency of SDOF system, the first lower bilinear frequency of the two DOF system and the second lowest bilinear frequency of two DOF lumped mass system respectively. ω_1 and ω_2 are the fundamental natural frequencies for a SDOF system with a single and double spring respectively. Finally, ω_{11}, ω_{12}, ω_{21} and ω_{22} are the fundamental and second natural frequency for the first mass and the fundamental and second natural frequency for the second mass respectively Chati et al. (1997). This model was built to understand the essential nonlinear dynamics of the cracked beam.

According to these studies, cracks can be modelled by the following two steps, firstly by using the stress intensity factors, which are based on the principles of fracture mechanics and secondly by applying the Paris equation to calculate the deflection of the cracked elements. Using these steps, the equation of motion for cracked beams can be formulated.

The cracks are divided into three types: opening, sliding and tearing as shown in Figure 1.2(Anderson, 2005). These types are dependent on the load direction. However, the most important factors, which reduce the natural frequencies, are the crack depth and its location.

Cracks can be modelled based on:

1. The boundary relationships between crack sides (l:left and r:right). Considering
   (a) Continuity of vertical displacement, $v_l = v_r$
   (b) Discontinuity of the slope or cross section relation, $\grave{v}_l = \grave{v}_r +$ fracture term, where $\grave{}=$ partial derivative with respect to x, where x is the length along the beam.
   (c) Equilibrium of vertical bending moment, $M_l = M_r$
   (d) Equilibrium of shear force. $S_l = S_r$

   The continuity refers to equal values on both sides of the crack. Regarding discontinuity, this is where stress intensity factors will be added to the equation's

right-hand side to become equal with the left side as in point (b) (Karaagac et al., 2009; Ibrahim et al., 2013).

2. An additional local flexibility by considering the crack as a massless spring. Here the flexibility of the beam will be calculated first, then the extra flexibility that is generated by the crack will be added to the beam's flexibility. (Qian et al., 1990; Vigneshwaran and Behera, 2014)

3. The elasto-plastic crack, being similar to the previous two methods, with the only difference is to consider the plastic zone in the calculation. (Krawczuk et al., 2000)

4. Bilinear crack or breathing crack, which is variable with time. A bilinear-type breathing crack is either fully open or fully closed as illustrated. The response develops as a function of time as shown in Figure 2.6. (Chondros et al., 2001)

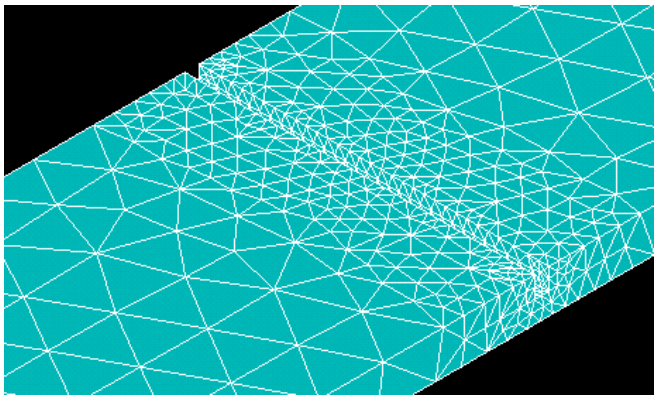

Figure 2.5: Cracked beam meshed with solid element. (Panigrahi and Parhi, 2009)

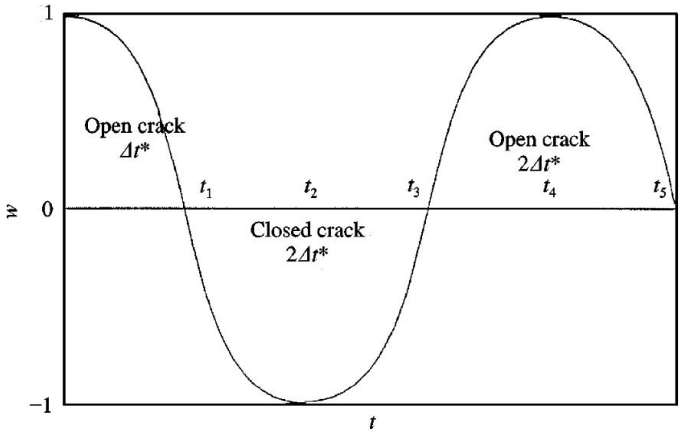

Figure 2.6: Lateral motion of a simply supported beam with a breathing crack at the mid-span initially bent in its first mode, where t, w refer to time and vibration amplitude, respectively. Chondros et al. (2001)

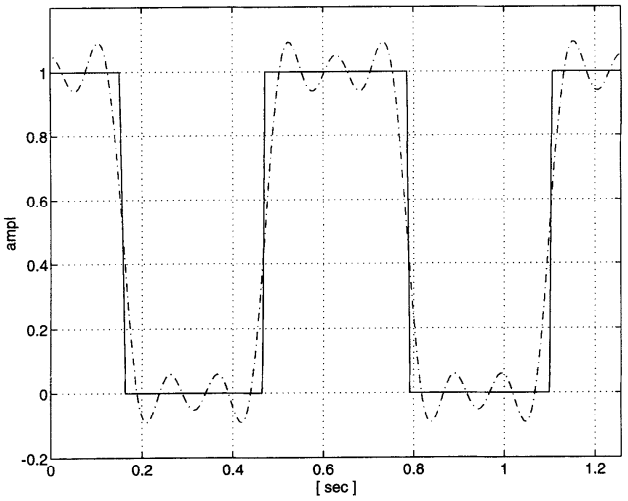

Figure 2.7: The dotted line represents an approximation to the square wave (Ruotolo et al., 1996)

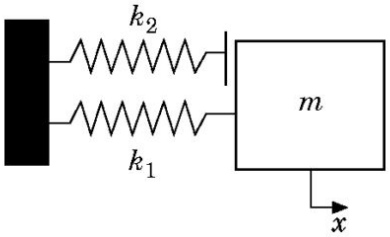

Figure 2.8: The SDOF bilinear system Chati et al. (1997)

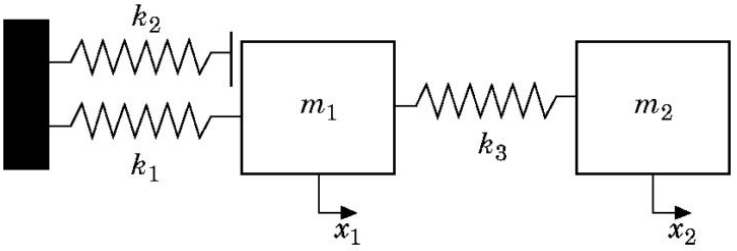

Figure 2.9: The two DOF bilinear system Chati et al. (1997).

2.3 Vibration of rotating cracked cantilever beams

The probability that cracks occur becomes much higher in dynamic structures, especially when the structures are rotating objects because of physical impacts or friction with other objects or cyclic loading. Therefore the investigations into cracked blades or rotating beams were carried out from as early as the 1970s, yet some failure cases were reported during the 1950s Bachschmid et al. (2010).

Most researchers built their models based on the local flexibility, correlated to the crack geometry. Chen and Shen (1997) and Lien-Wen and Chiung-Lu (1988) investigated the

vibration and stability of thick rotating blades with a single crack by considering the transverse shear deformation effect and the rotary inertia effect. Numerous research has been concentrated on rotating cracked shafts Papadopoulos and Dimarogonas (1987); Sekhar and Prabhu (1998); Silani et al. (2013) deal with axial and lateral coupling vibration of cracked rotating shaft, health monitoring in rotors and detecting cracks in rotating shafts, respectively.

Kim and Kim (2003) numerically simulated a rotating cantilever beam with a breathing crack. The local flexibility matrix was determined by a mechanical fracture approach. This study mentioned the importance of modelling breathing cracks, since for an open cracked beam the outcome revealed a frequency reduction and underestimated the crack depth due to neglecting the influence of opening and closing of the crack. However, most research carried out before Chung and Yoo (2002) have modelled rotating beams without considering the effect of the gyroscopic coupling between the longitudinal and chordwise vibrations.

Furthermore, statistical methods have been used to identify cracked rotating beams. Banerjee and Pohit (2014) studied the crack detection (location and size) on a rotating cantilever beam based on fractal dimension (FD), which is a statistic of a geometrical ratio, as shown in Figure 2.10. The main focus of their study was to extract damage from measuring the fractal dimension between two successive points on the mode shape, as shown in Figure 2.10(c) for a rotating cracked beam.

Silani et al. (2013) studied vibration analysis of rotating systems having cracks by modifying the integration limits of the flexibility matrix of the crack, which provides more accurate results. The research provided a dynamic response of a rotor with an open and closed crack using the frequency/time domain approach and it is considered as a basis for producing an on-line monitoring system. However, modelling needs to be modified so it fits on rotating blades or beams.

According to the authors, not much investigation has been made into the area of rotating cracked beams, "from the literature review, it is evident not much work has been carried out on cracked rotating beams."(Banerjee and Pohit, 2014). In addition, "compared with enormous research on vibration analysis of intact rotating beams, less attention has been focused on the vibration characteristics of cracked rotating beams." (Cheng et al., 2011). From the previous two papers, that were published in 2011 and 2014, it is evident that a lot of research might still be applicable in this area and still needs to be developed.

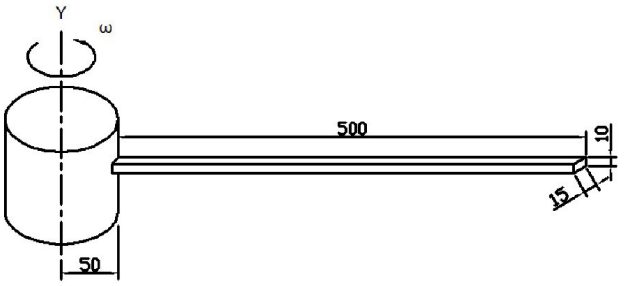

(a) Beam dimensions.

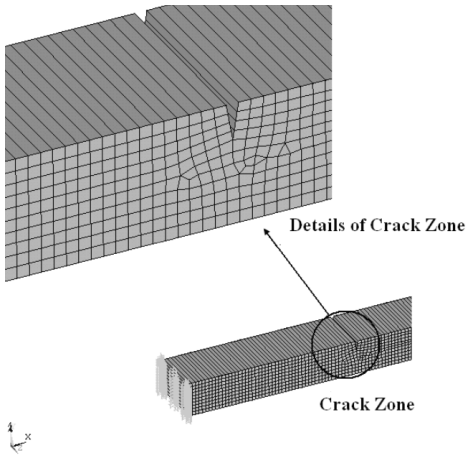

(b) Finite element modelling of the cracked beam

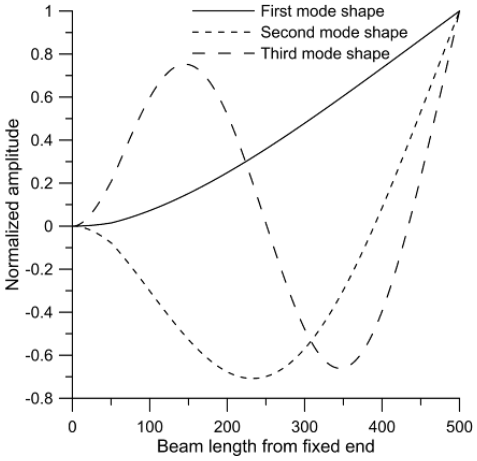

(c) The first three mode shapes of cracked beams for rotational speed 100 rad/sec

Figure 2.10: Modelling and results of a rotating cracked cantilever beam (Banerjee and Pohit, 2014)

2.4 Digital image correlation method

Digital Image Correlation (DIC) is a full-field image analysis method, non-intrusive, based on grey value digital images, which is easy to implement. Powerful optical metrology can thus determine the outline and measure the deformations of an object under load in two or three dimensions.

The elementary principle of DIC is the tracking (or matching) of the same spots (or pixels) between the two pictures taken before and after deformation. In order to calculate the displacements of point P, a square reference subset of $(2M + 1) \times (2M + 1)$ pixels centred at point P (x_0, y_0) from the reference image is selected and used to track its corresponding location in the deformed image, where M refer to the minimum numbers of pixels for each point or spot is a number varying from different software and also depends on the test specimen size. A square subset, rather than an individual pixel, is selected for matching since the subset comprising a wider variation in grey values

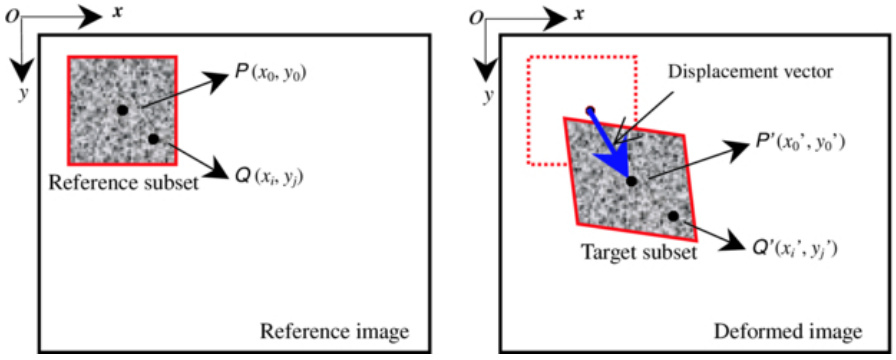

Figure 2.11: Basic principle of subset-based DIC method: tracking the same pixel point in the reference and deformed image determine its displacement vector Pan et al. (2009).

distinguishes itself from other subsets, and can, therefore, be more uniquely recognised in the distorted image as shown in Figure 2.11.

One of the most important advantages of this method is its ability to measure the vibration without attaching sensors to the system, especially in the high-speed rotating system where attaching extra sensors such as accelerometer are not viable due to connecting the wiring. Even for wireless sensors, the mass of sensors could be considerable and affect the vibration of the system.

Due to the rapid increase in the image recording speed and quality, recently the digital image correlation methods have become accessible and applicable in numerous vibration analysis. For example, Hagara et al. (2015) performed experimental modal analysis of the vibration of plates using high-speed digital image correlation. The block diagram for a test setup is shown in Figure 2.12, where an impact hammer is used to excite the object and two high-speed cameras feed a stereo image to the data acquisition system. Cameras are set to 2000s frame per second (sample per second) to measure response approximately between 0 and 1000 Hz. It is worth mentioning that a stereo camera system is usually employed to measure 3D displacement. This system has the capability to detect out of plane displacement. Nevertheless, a single camera system can be applied to assess the lateral oscillation of the beam as in Romaszko et al. (2015), where the camera is set up perpendicular to the plane of motion. Furthermore, Molina-Viedma et al. (2018) used a combination of digital image correlation and a motion magnification algorithm. This was performed in order to provide numerical information in the magnified videos and perform DIC mode shape characterisation at high frequencies, through increasing the amplitude of the displacements. Furthermore, the phase change in the different scale magnified video frames were used to extract the motion of the structure. Utilizing an edge detection approach, this method allows a full field motion study to be carried out without special coating of the structure with point or other markers Yang et al. (2017). However, due to the multi post-processing stages this method limited to the optical vibration measurement and not suitable for real-time control applications.

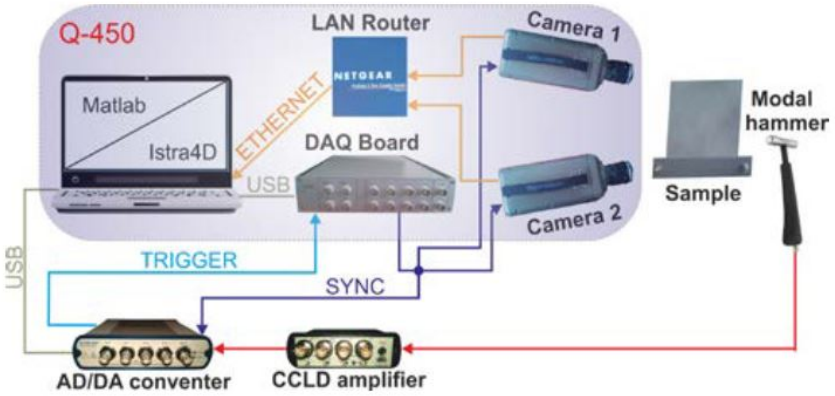

Figure 2.12: Block scheme for correlation system Q-450 Dantec Dynamics used for the purposes of experimental modal analysis Hagara et al. (2015).

2.5 Experimental work on crack detection

Experimental studies have been performed by numerous researchers to validate the numerical results. Selected works are listed below, which would give an idea about specimen selection and test setup. Cantilever non-rotating beams are usually chosen as specimens in examining the effects of cracks. Excitation methods vary between hammer impact and using electrodynamic shakers, which are typically attached to the base of the cantilever beam. Roving accelerometer or hammer positions are used in a procedure to estimate the mode shapes. Chondros et al. (2001) studied a breathing crack and assumed two states for the cracked beam (fully open crack and fully closed crack). The experimental model was built as a prismatic beam made of aluminium. A sharp notch was placed at the mid-span with a perpendicular orientation to the longitudinal axis and the longest length of the cross section, i.e. the height of the beam. One end of the beam was fixed to the shaker table, and the other end was set free. Thirty specimens were set up with crack depths ranging from 5 to 60% of the beam thickness. A similar test was performed with simply supported beams. The analysis based on the effect of crack depth on the natural frequency are shown in Figure 2.13.

Vakil Baghmisheh et al. (2012) carried out six beam experiments with different crack positions and depths. The crack was created using a 0.5mm thickness saw. The dimension of the beam was 820mm length, 20mm width and 10mm thickness, made of aluminium with density 2700 kg.m^{-3} . The beam was fixed free. Hammer testing was performed by hitting at 90mm distance from the fixed end and the dynamic response was measured by an accelerometer placed at 650mm from the fixed end. The results were obtained using a FFT analyser. Figure 2.14 shows the experimental results of the frequency response with and without crack.

Nahvi and Jabbari (2005) studied crack detection using experimental modal data and an FE model. The cracked beam modelled was 290mm length, 22.5×13mm cross-section,

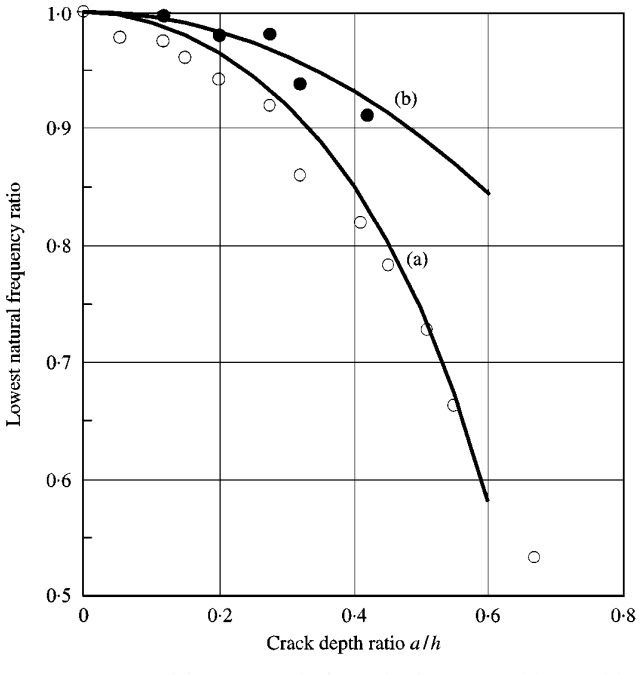

Figure 2.13: Natural frequency versus crack depth ratio $\frac{a}{h}$ where a = crack depth, h = cross section hight
(a) continous crack model,
(b) breathing crack,
(white circle) experimental result of open crack,
(black circle) experimental result of breathing crack.
(Chondros et al., 2001)

2800 kg.m^{-3} density, 0.3 Poisson's ratio, 175 GPa Young's modulus. An impact hammer test was performed using a 8202 B&K hammer and an accelerometer (PCB Triaxial ICP). Nahvi and Jabbari (2005) used the first two natural frequencies to identify the crack in the beam. To obtain the best results the beam was excited at various points along the length, as shown in Figure 2.15. The test was repeated eight times.

The previous three research attempts repeatedly implemented a classic method using force excitation and acquisition of the accelerometer data. Nevertheless, recently researchers tend to use visual methods, since it is non-intrusive. To be exact, there is no additional mass due to attaching an accelerometer. Moreover, there is no necessity to use a roving hammer or accelerometer, owing to full-field imaging. Even more, the environment of the test could avoid connecting the test specimen to the analyser by wires such as moving parts, for example blades or the propeller of turbines. The digital image correlation was used in research as mentioned previously in section 2.4 by Romaszko et al. (2015); Hagara et al. (2015).

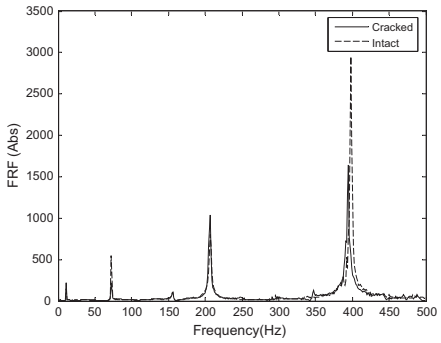

Figure 2.14: Frequency response of a cantlever beam with and without crack. (Vakil Baghmisheh et al., 2012)

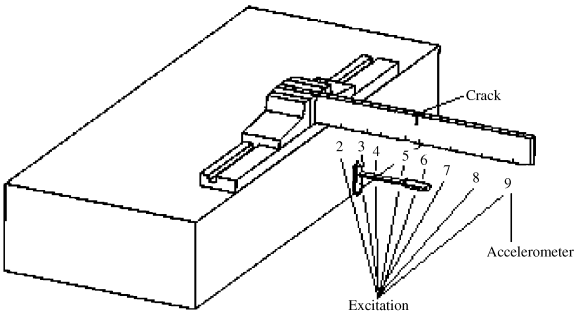

Figure 2.15: Diagram representation of the beam, attachment points of excitation and accelerometer. (Nahvi and Jabbari, 2005)

Conclusion

An overview of the dynamic behaviour of a rotating cantilever beam with and without crack provides a picture of the studies that focused on two main aspects that will contribute to developing a new model of a rotating cracked cantilever beam. These aspects are the modelling of a rotating beam and modelling of a cracked beam.

Each topic is well established, however in the case of studying rotating cracked beams there is a lack of publications and many gaps are observed, such as considering the gyroscopic effect, which was introduced to the rotating intact beam after 2002. Regarding the effect of cracks, open and breathing cracks are modelled and studied carefully in non-rotating structures. In rotating structures, most research which deals with cracked rotating structures discount the effect of stretch vibration and thus the coupling of modes in the chordwise vibration. Nevertheless, investigation into rotating cracked beams still needs to be extended as mentioned in Section 2.3.

Therefore, an aim of the research is to investigate the vibrational behaviour and control of rotating beams with and without cracks. The primary contribution of this study thus far is on introducing a crack modelled using fractional mechanics principles to the rotating beam possessing three-dimensional described vibration (including flapwise, chordwise and stretched vibration). Also, the gyroscopic effect is considered which couples the chordwise and stretch modes together. In addition to the crack, introducing a new method of measuring will be applied using a digital image correlation method, which is a non-invasive and remote measuring method. This study has a potential future application in remote and non-invasive real-time health monitoring of rotating structures, such as wind turbines or even in high speed rotating helicopter blades especially with the vast improvement in camera sensors and computational speed. The next chapter covers the original developments in modelling the intact and cracked rotating beam pursued and developed in this study.

Chapter 3

Modelling of a rotating beam with and without crack

3.1 Introduction

This chapter will provide an introduction to the modelling of a rotating cracked cantilever beam. In general, beams have three main types of vibration which are extensional, torsional and bending. Similarly, rotating cantilever beams can possess these three main types of vibration. However, the focus of this thesis is on the bending and stretch modes. As shown in Figure 3.1, the first type of motion is the flapwise motion, which is a lateral bending motion perpendicular to the plane of rotation, i.e. out of the plane of rotation. The second type of motion is the chordwise vibration, which is also bending motion conversely it is parallel to the plane of rotation. While the third type of motion is called a stretch, which occurs radial along the longitudinal axis of the beam. The rotational motion applies a radially centrifugal force on the beam. This additional force tends to stretch the beam in the axial direction and increase the beam natural frequencies.

In the first part of this chapter three different modelling approaches are developed for a rotating beam. The equation of flapwise vibration of the rotating cantilever beam is used first, employing a simple force equilibrium equation. This method is simple and straightforward to use to formulate a model, but the representation of the motion is limited to the flapwise vibration. Therefore, a more general description of the three-dimensional motion of the flapwise and chordwise vibration of the rotating beam will be derived using Lagrange's equations as in Chung and Yoo (2002).

The equations of motion for the rotating beam will be solved numerically using a finite element method (FEM). Regarding FEM, two types of rotating beam elements will be generated. The first one is an element with two degrees of freedom at each node used for the flapwise motion and the second model is one having three degrees of freedom at

the nodes used for the chordwise vibration. This difference is related to the coupling of chordwise and stretch motion and is independent of the flapwise motion. These elements will be explained in detail in section 3.2.1.

Subsequently, a new three dimensional model of a rotating beam is developed utilizing a variational method (Rayleigh-Ritz). The model proposed is based on a combination of the shape functions for the static deflection of a tip loaded cantilever beam. Later, the corresponding stiffness and mass matrices are obtained.

Next, the additional local flexibility that is generated by an open crack will be included in the mathematical dynamic formulation by applying fracture mechanics' principles. The open crack is modelled as a massless spring, which creates a relationship between the strain energy and the applied force on the structure as discussed by Dimarogonas (1996); Zheng and Kessissoglou (2004).

Finally, the additional flexibility in the proposed model that is generated from the crack is introduced to the system by subtracting the effect of the crack from the total potential energy of the system when using Rayleigh Ritz method. This is instead of the typical crack modelling, which considers two intact segments in the left and right of the crack and the total potential energy of the system are obtained by summation the energy of the intact parts and the massless spring.

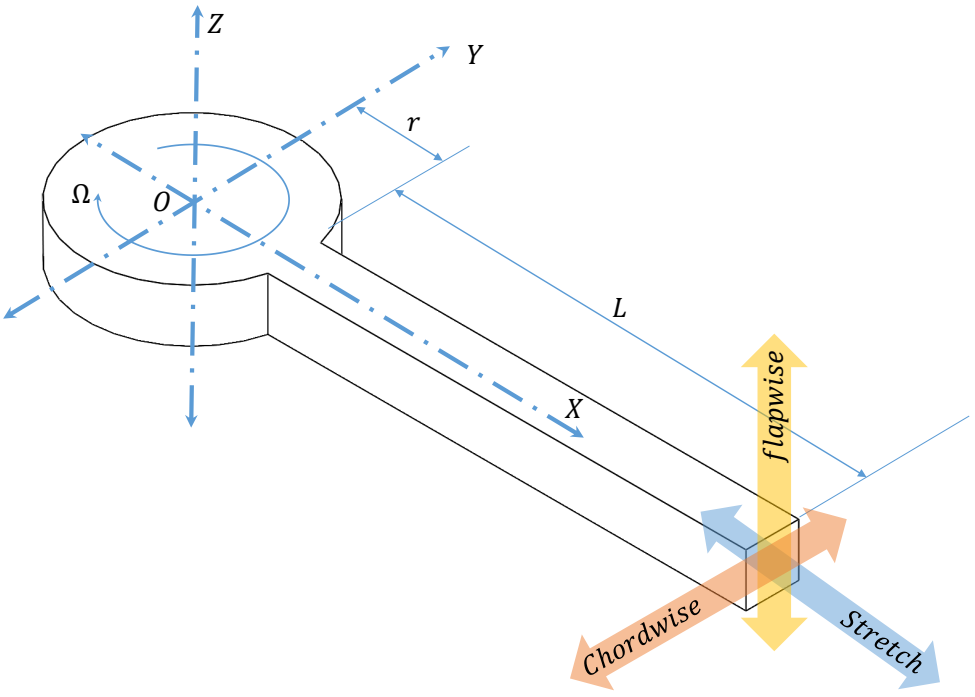

Figure 3.1: Rotating cantilever beam configuration.

3.2 Modelling of a rotating uncracked cantilever beam

A rotating beam is considered as a homogeneous Euler-Bernoulli, uniform and isotropic cantilever beam of a length L, with a cross sectional area A, Young's modulus of elasticity E and mass density ρ. It is attached to a rigid hub with radius r about an axis through point O as shown in Figure 3.1. The cantilever beam and the rigid hub are rotating about the vertical axis z with angular velocity Ω. The cantilever beam's length is along the x axis. The chordwise vibration occurs in the xy plane, parallel to the plane of rotation, and flapwise vibration in the xz plane, perpendicular to the plane of rotation. This coordinate system (xyz) rotates with the hub. According to many researchers (Kim et al., 2013; Lima, 2012; Cheng et al., 2011), rotating cantilever beams can possess two main types of vibration. The first one is the flapwise motion, which is perpendicular to the plane of rotation and the second one is in the chordwise direction, which is parallel to the plane of rotation, as shown in Figure 3.1.

The equation of motion for the lateral flapwise vibration of the beam subjected to an axial force can be written as;(Rao, 2007)

$$\rho A\frac{\partial^2 w}{\partial t^2}+\frac{\partial^2}{\partial x^2}\left(EI\frac{\partial^2 w}{\partial x^2}\right)-\frac{\partial}{\partial x}\left(P\frac{\partial w}{\partial x}\right)=f(x,t) \tag{3.1}$$

where ρ, A, E, I, w, P and f represent the mass density, cross sectional area, modulus of elasticity, second moment of area, transverse displacement, longitudinal axial force and transverse lateral distributed force, respectively. For free vibration and uniform cross section, Equation 3.1 can be rewritten as

$$\rho A\frac{\partial^2 w}{\partial t^2}+EI\frac{\partial^4 w}{\partial x^4}-\frac{\partial}{\partial x}\left(P\frac{\partial w}{\partial x}\right)=0 \tag{3.2}$$

For a rotating beam, the axial force P is due to and equal to the centrifugal force in Figure 3.2 and can be obtained from,

$$P(x)=\int_x^L \rho A\Omega^2(x+r)dx=\rho A\Omega^2\{r(L-x)-\frac{1}{2}(L^2-x^2)\} \tag{3.3}$$

The equation of motion for the transverse vibration of the rotating beam can be obtained by substituting Equation 3.3 into Equation 3.2;

$$\rho A\frac{\partial^2 w}{\partial t^2}+EI\frac{\partial^4 w}{\partial x^4}-\rho A\Omega^2\frac{\partial}{\partial x}\left\{[r(L-x)-\frac{1}{2}(L^2-x^2)]\frac{\partial w}{\partial x}\right\}=0 \tag{3.4}$$

For the free vibration of the rotating beam, a harmonic solution of the following form is assumed.

$$w(x,t)=W(x)\cos(\omega t-\phi) \tag{3.5}$$

where W, ω, ϕ are the amplitude, angular frequency and the phase of the vibration. Substituting the solution, Equation 3.5, into Equation 3.4 yields,

$$-\rho AW\omega^2 + EI\frac{d^4W}{dx^4} - \frac{1}{2}\rho A\Omega^2\frac{d}{dx}\left\{[r(L-x) - \frac{1}{2}(L^2-x^2)]\frac{dW}{dx}\right\} = 0 \tag{3.6}$$

and the boundary conditions assumed are

$$\begin{aligned} W(x) = \frac{dW(x)}{dx} = 0 \quad , \quad x = 0 \\ \frac{d^2W(x)}{dx^2} = \frac{d^3W(x)}{dx^3} = 0 \quad , \quad x = L \end{aligned} \tag{3.7}$$

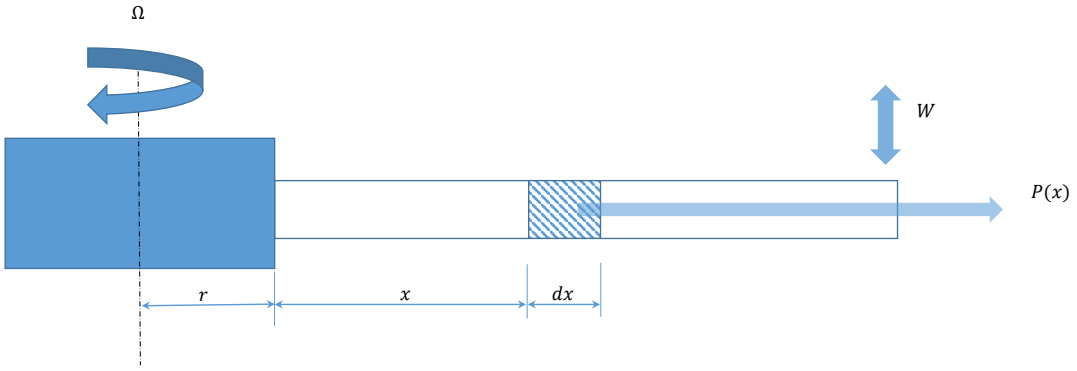

Figure 3.2: Lateral vibration of the beam subjected to an axial force $P(x)$

The exact solution of Equation 3.6 is difficult to obtain analytically due to the inclusion of centrifugal force and the term $\frac{d}{dx}(x^2\frac{dw}{dx})$. Nevertheless, an approximate method using a numerical method such as the finite element method or the Rayleigh-Ritz method can be used to solve this equation, as will be explained in detail in the next two sections.

3.2.1 An energy method using Chung and Yoo (2002)'s approach

Obtaining the equation of motion for the rotating cantilever beam using the continuous system is already known. However, the result of this method is particular for the flapwise vibration. In order to calculate both the flapwise and chordwise vibration, it is necessary to use a general method that enables one to describe the system in three dimensions. Most recent research (Chung and Yoo, 2002; Kim et al., 2013; Lima, 2012) follows an energy method, which is firstly an evaluation of the displacement and the velocity of the deflection. Then, calculation of both the Lagrangian functional and work done on the system is used to derive the equations of motion, as explained later by applying an extended Hamilton principle (Chung and Yoo, 2002). Finally, the equations of motion can be solved by one of the numerical approximations.

The extended Hamilton's principle, which is based on the kinetic energy, potential energy and the work done on the system, will be used to derive the differential equations of motion. This principle can be expressed mathematically as

$$\mathcal{S} = \int_{t_i}^{t_f} (\mathcal{L} + \mathcal{W}) dt = 0 \tag{3.8}$$

where $\mathcal{S}$ is defined as the action integral (Thomsen, 2003), t_i, t_f represent the initial and final time, respectively. $\mathcal{L}$ is known as Lagrangian functional or the Lagrangian density function, and $\mathcal{W}$ represents the work done on the system by non-conservative forces. The Lagrangian functional $\mathcal{L}$ is related to both kinetic KE and potential energy PE and is given by the following equation,

$$\mathcal{L} = KE - PE \tag{3.9}$$

Replacing Equation 3.9 into Equation 3.8 and also taking into account that the variational and integration operators are interchangeable, Hamiltons principle can also be stated as

$$\int_{t_i}^{t_f} (\delta KE - \delta PE + \delta \mathcal{W}) dt = 0 \tag{3.10}$$

To estimate the kinetic energy of a mechanical system, the velocity field of the system needs to be evaluated first, which requires a description of the velocity at any specific point through a set of generalised coordinates. Let V_Q represents the velocity vector of any specific point Q in a mechanical system, the kinetic energy can then be expressed as follows

$$KE = \frac{1}{2} \int_0^L \rho A \quad V_Q^T \quad V_Q \quad dx \tag{3.11}$$

where ρ and A are the material density and the cross-section area. The superscript ^{T} denotes the transpose. It can easily be evaluated knowing the strain and stress fields of the system. With ε as the strain field and σ as the stress field, the potential energy is then estimated as,

$$PE = \frac{1}{2} \int_0^L \int_A \varepsilon^T \sigma dx \tag{3.12}$$

The strain field is derived from the displacement field via the Green's tensor, while the stress field is evaluated using the strains and the widely known elastic constants from the generalized Hooke's law.

According to Kim et al. (2013), the displacement of point Q to Q', as shown in Figure 3.3, can be expressed in terms of the component displacements u_x, u_y and u_z where they correspond to the axial, chordwise and flapwise deformations, respectively. There is a geometrical relation between the length of the beam before and after the deformation as given in Hh (1995) by

$$x + s = \int_0^{x+u_x} \left[1 + \left(\frac{\partial u_y}{\partial \eta}\right)^2 + \left(\frac{\partial u_z}{\partial \eta}\right)^2\right]^{\frac{1}{2}} d\eta \tag{3.13}$$

where s represents the change in beam's length (stretch) and η is a dummy variable. The velocity of the point Q in Figure 3.4, can also be found from,

$$\mathbf{V}_Q = (\dot{u} - \Omega u_y)\mathbf{i} + [\dot{v} + \Omega(r + x + u_x)]\mathbf{j} + \dot{w}\mathbf{k} \tag{3.14}$$

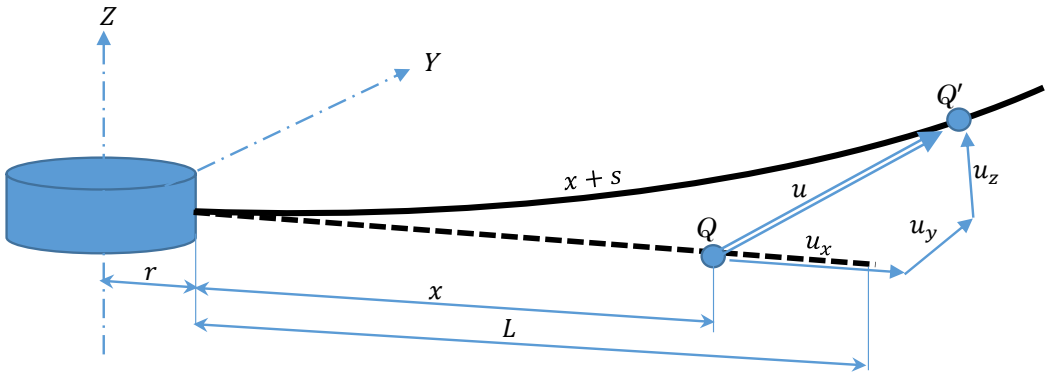

Figure 3.3: Configuration of a rotating cantilever beam.

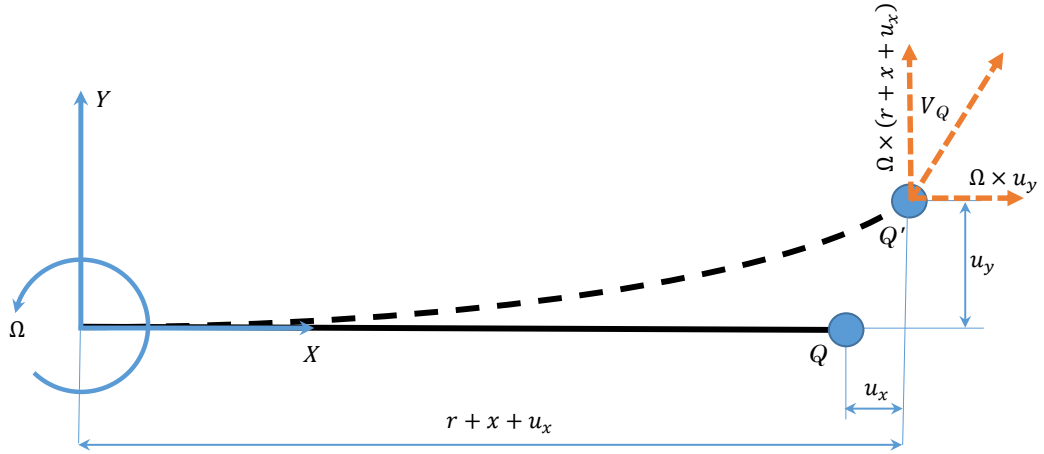

Figure 3.4: Top view of the system, showing the relation between the angular and linear velocity.

Following the result by Kim et al Kim et al. (2013), leads to a set of nonlinear partial differential equations. After simplifying the differential equations and linearisation by

neglecting higher order terms in the displacements, the following linear partial differential equations can be obtained,

$$\rho A\left(\frac{\partial^2 s}{\partial t^2}-2\Omega\frac{\partial v}{\partial t}-\Omega^2 s-\dot{\Omega}v\right)-EA\frac{\partial^2 s}{\partial x^2}=\rho A\Omega^2(a+x) \tag{3.15}$$

$$\rho A\left(\frac{\partial^2 v}{\partial t^2}-2\Omega\frac{\partial s}{\partial t}-\Omega^2 v-\dot{\Omega}s\right)+EI_z\frac{\partial^4 v}{\partial x^4}-\rho A\Omega^2\frac{\partial}{\partial x}\left(r(L-x)+\frac{1}{2}(L^2-x^2)]\frac{\partial v}{\partial x}\right)=p_v \tag{3.16}$$

$$\rho A\frac{\partial^2 w}{\partial t^2}+EI_y\frac{\partial^4 w}{\partial x^4}-\rho A\Omega^2\frac{\partial}{\partial x}\left([r(L-x)+\frac{1}{2}(L^2-x^2)]\frac{\partial w}{\partial x}\right)=p_w \tag{3.17}$$

where p_v and p_w are the applied forces per unit length along the beam in the y and z directions and I_y, I_z are the second moment of area about the y and z directions. It is interesting that Equation 3.15 and Equation 3.16 are coupled together, while Equation 3.17 is independent of the other two. The boundary conditions from Equation 3.7 are given by

$$\begin{aligned} s=v=w=\frac{\partial v}{\partial x}=\frac{\partial w}{\partial x}=0 \quad , \quad x=0, \\ \frac{\partial s}{\partial x}=\frac{\partial^2 v}{\partial x^2}=\frac{\partial^2 v}{\partial x^2}=\frac{\partial^3 v}{\partial x^3}=\frac{\partial^3 w}{\partial x^3}=0 \quad , \quad x=L. \end{aligned} \tag{3.18}$$

A solution which satisfies the governing equation of motion together with the boundary conditions at every point over the domain is known as a strong form of solution. Conversely, a weak form of solution satisfies the conditions in an integral sense.

Following this step, the weak forms need to be obtained from the strong forms that are given by the partial differential equations and the corresponding boundary conditions. To derive the weak forms for the equation of motions for the Euler-Bernoulli beam, Eqs.(3.15)-(3.17) are multiplied by the weighting functions $\bar{s}$, $\bar{v}$ and $\bar{w}$ respectively, summed and integrated over the length L as follows.

For the chordwise

$$\begin{aligned} \rho A\int_0^L\left[\bar{s}\left(\frac{\partial^2 s}{\partial t^2}-2\Omega\frac{\partial v}{\partial t}-\Omega^2 s-\dot{\Omega}v\right)+\bar{v}\left(\frac{\partial^2 v}{\partial t^2}-2\Omega\frac{\partial s}{\partial t}-\Omega^2 v-\dot{\Omega}s\right)\right]dx \\ +\int_0^L\left(EA\frac{\partial\bar{s}}{\partial x}\frac{\partial s}{\partial x}+EI\frac{\partial^2\bar{v}}{\partial x^2}\frac{\partial^2 v}{\partial x^2}\right)dx \\ +\rho A\Omega^2\int_0^L\left[r(L-x)+\frac{1}{2}(L^2-x^2)\right]\frac{\partial\bar{v}}{\partial x}\frac{\partial v}{\partial x}dx \\ =\int_0^L\{\rho A\Omega^2(r+x)\bar{s}+[p_v-\rho A\bar{\Omega}(r+x)]\bar{v}\}dx \end{aligned} \tag{3.19}$$

and for the flapwise

$$\rho A \int_0^L \bar{w} \frac{\partial^2 w}{\partial t^2} dx + EI_y \int_0^L \frac{\partial^2 \bar{w}}{\partial x^2} \frac{\partial^2 w}{\partial x^2} dx + \rho A \Omega^2 \int_0^L \left[r(L-x) + \frac{1}{2}(L^2 - x^2) \right] \frac{\partial \bar{w}}{\partial x} \frac{\partial w}{\partial x} dx = \int_0^L \bar{w} p_w dx \quad (3.20)$$

The displacements and weighting functions are now approximated by the shape functions as

$$\begin{aligned} \bar{s} &= (\bar{d}_e^{sv})^T N_s; s = N_s^T d_e^{sv} \\ \bar{v} &= (\bar{d}_e^{sv})^T N_v; v = N_v^T d_e^{sv} \\ \bar{w} &= (\bar{d}_e^{w})^T N_w; w = N_w^T d_e^{w} \end{aligned} \quad (3.21)$$

$$d_e^{sv} = \{s_e, v_e, \theta_e, s_{e+1}, v_{e+1}, \theta_{e+1}\}^T \quad (3.22)$$

$$d_e^{w} = \{w_e, \psi_e, w_{e+1}, \psi_{e+1}\}^T \quad (3.23)$$

where d_e^{sv} and d_e^{w} are the element displacement vector for the chordwise and flapwise motion, respectively. $\bar{d}_e^{sv}$ and $\bar{d}_e^{w}$ are arbitrary vectors with the same dimensions of d_e^{sv} and d_e^{w} correspondingly. Finally N_s,N_v and N_w represent the trial shape functions.

Introducing these approximate solutions (3.21) in the weak equations given by Equation 3.19 and Equation 3.20, the integrations produce equations which can also be written in a matrix form. This yields the discretized equations for the chordwise and flapwise motion as,

$$\sum_{e=1}^{N} (\bar{d}_e^{sv})^T \{ m_e^{sv} \ddot{d}_e^{sv} + 2\Omega g_e^{sv} \dot{d}_e^{sv} + [k_e^{sv} + \Omega^2 (s_e^{sv} - m_e^{sv}) + \dot{\Omega} g_e^{sv}] d_e^{sv} \} = \sum_{e=1}^{N} (\bar{d}_e^{sv})^T f_e^{sv} \quad (3.24)$$

$$\sum_{e=1}^{N} (\bar{d}_e^{w})^T [m_e^{w} \ddot{d}_e^{w} + (k_e^{w} + \Omega^2 s_e^{w}) d_e^{w}] = \sum_{e=1}^{N} (\bar{d}_e^{w})^T f_e^{w} \quad (3.25)$$

where m_e^{sv}, g_e^{sv}, k_e^{sv} and s_e^{sv} are the element mass, the element gyroscopic, the element stiffness and the element motion-induced stiffness matrices for the chordwise motion. Meanwhile, m_e^{w}, k_e^{w} and s_e^{w} are same factors for flapwise motion. f_e^{sv} and f_e^{w} are the element load vectors for the chordwise and flapwise motions.

The weak form requires the conversion of the continuous system to the discrete elements, which can have degrees of freedom and can be solved by a finite element method or by given shape functions using the Rayleigh-Ritz method. However, the next step is to represent the system dynamics by a system of matrices and convert the weak form to the equations of motion based on the mass and stiffness matrices.

Modelling of the beam element is widely known and mentioned in numerous textbooks (Rao, 2005; Jochems et al., 2002). One of the significant tasks in producing the element matrix is the element's degrees of freedom at each node. Therefore, the beam elements can be split into two cases. The first type of beam elements have two degrees of freedom at each node, and they are the lateral displacement and slope. This type of beam element is more suitable for flapwise vibration, which comprises vertical movement of the cantilever beam above and under the plane of rotation. The second type of beam element has three degrees of freedom according to the shape function for the element, the movement left and right in the ZX plane; in addition, it has axial movement i.e. longitudinal deformation. These two types of elements share the property that both of them have two nodes. These two types of elements will be discussed in detail in the next two sections.

Solving the system of differential equations using the finite element methods requires discretization of the beam into n numbers of two-noded elements as shown in Figure 4.1, where the numbers above and below of the beam in Figure 4.1 refer to the number of the elements and nodes respectively, while s, v and w represent three DOFs of each node of the element and they refer to the stretch, chordwise and flapwise direction of deflection. The finite element shape function for both the flapwise and the chordwise deformation can be expressed as a cubic polynomial as they are the consequence of the bending moment and shear force. Whereas the stretch deformation can be expressed as a linear polynomial as a result of an assumed longitudinal force only.

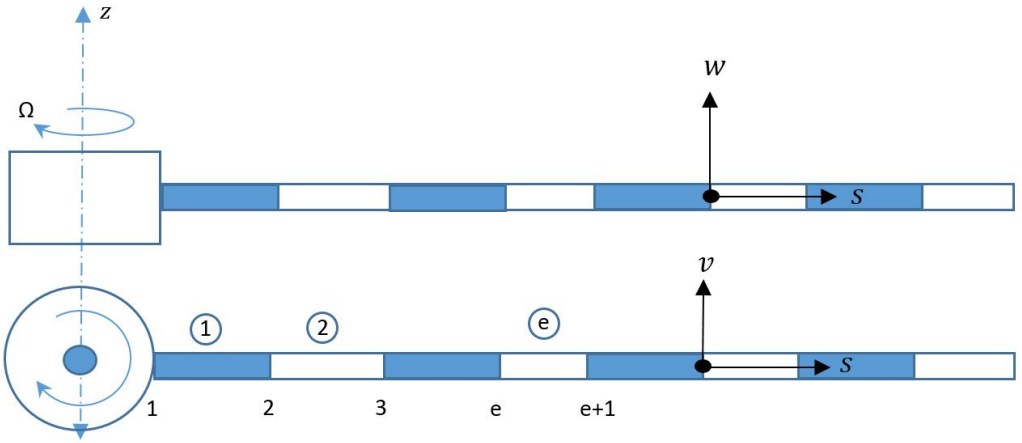

Figure 3.5: Configuration of the elements in the finite element method.

According to the previous qualitative description the finite element shape functions assumed are

$$\begin{aligned} s &= a_1 + a_2 x \\ v &= a_3 + a_4 x + a_5 x^2 + a_6 x^3 \\ w &= a_7 + a_8 x + a_9 x^2 + a_{10} x^3 \end{aligned} \tag{3.26}$$

where a_i are the constant coefficients related to the deformation and slope at each node. These deformations are s_e for stretch, v_e for chordwise and w_e for flapwise also θ_e and ψ_e represents slopes in chordwise and flapwise, respectively as shown in Figure 3.6. Note that the subscript e refers to the element.

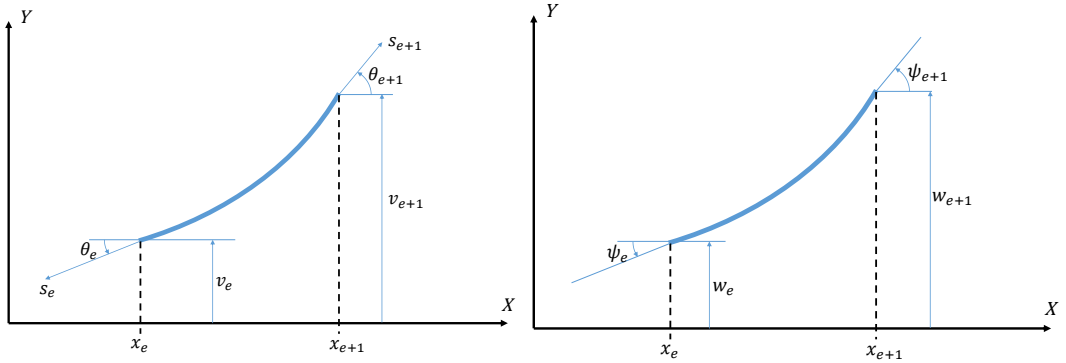

(a) The chordwise motion.

(b) The flapwise motion.

Figure 3.6: Finite element for the chordwise (three degrees of freedom for each node) and flapwise motions (two degrees of freedom for each node).

$$N_s = \{(x_{e+1} - x)/h_e, 0, 0, (x - x_e)/h_e, 0, 0\}^T . \tag{3.27}$$

$$\begin{aligned} N_v = \{&0, (x - x_{(e+1)})^2(2x - 3x_e + x_{(e+1)})/h_e^3, (x - x_e)(x - x_{(e+1)})^2/h_e^2, \\ &0, -(x - x_e)^2(2x + x_e - 3x_{(e+1)})/h_e^3, (x - x_e)^2(x - x_{(e+1)})/h_e^2\}^T. \end{aligned} \tag{3.28}$$

$$\begin{aligned} N_w = \{&(x - x_{(e+1)})^2(2x - 3x_e + x_{(e+1)})/h_e^3, (x - x_e)(x - x_{(e+1)})^2/h_e^2, \\ &- (x - x_e)^2(2x + x_e - 3x_{(e+1)})/h_e^3, (x - x_e)^2(x - x_{(e+1)})/h_e^2\}^T. \end{aligned} \tag{3.29}$$

where h_e represents the element size $h_e = x_{(e+1)} - x_e$.

In order to determine an approximate solution for equations (3.15)-(3.17), the weak forms given by equations (3.19)-(3.20) are discretized using the two-noded beam elements

defined above. After discretizing the domain $[0, L]$ into sub domains $[x_e, x_{e+1}], e = 1, 2, \ldots, N$, as shown in Figure 4.1, and then building the finite element global matrices using for the chordwise,

$$m_e^{sv} = \rho A \int_{x_e}^{x_{e+1}} (N_s N_s^T + N_v N_v^T) dx, \tag{3.30}$$

$$g_e^{sv} = \rho A \int_{x_e}^{x_{e+1}} (N_v N_s^T + N_s N_v^T) dx, \tag{3.31}$$

$$k_e^{sv} = \int_{x_e}^{x_{e+1}} \left(EA \frac{dN_s}{dx} \frac{dN_s^T}{dx} + EI_z \frac{d^2 N_v}{dx^2} \frac{d^2 N_v^T}{dx^2} \right) dx, \tag{3.32}$$

$$s_e^{sv} = \rho A \int_{x_e}^{x_{e+1}} \left[r(L - x) + \frac{1}{2}(L^2 - x^2) \right] \frac{dN_v}{dx} \frac{dN_v^T}{dx} dx, \tag{3.33}$$

$$f_e^{sv} = \int_{x_e}^{x_{e+1}} \{ \rho A \Omega^2 (r + x) N_s + [p_v - \rho A \dot{\Omega} (r + x)] N_v \} dx, \tag{3.34}$$

and for the flapwise

$$m_e^{w} = \rho A \int_{x_e}^{x_{e+1}} N_w N_w^T dx, \tag{3.35}$$

$$k_e^{w} = EI_y \int_{x_e}^{x_{e+1}} \frac{d^2 N_w}{dx^2} \frac{d^2 N_w^T}{dx^2} dx, \tag{3.36}$$

$$s_e^{w} = \rho A \int_{x_e}^{x_{e+1}} \left[r(L - x) + \frac{1}{2}(L^2 - x^2) \right] \frac{dN_w}{dx} \frac{dN_w^T}{dx} dx, \tag{3.37}$$

$$f_e^{w} = p_w \int_{x_e}^{x_{e+1}} N_w dx, \tag{3.38}$$

where m_e^{sv}, g_e^{sv}, k_e^{sv} and s_e^{sv} are the element mass, the element gyroscopic term, the element stiffness and the element motion-induced stiffness matrices for the chordwise motion. Meanwhile, m_e^{w}, k_e^{w} and s_e^{w} are the same parameters for the flapwise motion. f_e^{sv} and f_e^{w} are the element load vectors for the chordwise and flapwise motions.
Introduction of equations (3.26)-(3.35) into equations (3.19)-(3.20) yields the discretized equations. The discretized equation for the chordwise is therefore,

$$\mathbf{M}_{sv} \ddot{d}_{sv} + 2\Omega \mathbf{G}_{sv} \dot{d}_{sv} + [\mathbf{K}_{sv} + \Omega^2 (\mathbf{S}_{sv} - \mathbf{M}_{cv}) + \dot{\Omega} \mathbf{G}_{sv}] d_{sv} = \mathbf{f}_{sv} \tag{3.39}$$

and for the flapwise it is

$$\mathbf{M}_w \ddot{d}_w + (\mathbf{K}_w + \Omega^2 \mathbf{S}_w) d_w = \mathbf{f}_w \tag{3.40}$$

3.2.2 Variational method (Rayleigh Ritz method) for chordwise and flapwise vibration

The Rayleigh-Ritz method is based on the idea that a closer estimate to the lowest eigen function can be obtained by superposing a number of admissible trial functions, which are typically a set of polynomial equations that satisfy the boundary conditions of the beam. If the assumed functions are suitably chosen, this method provides an approximate value for the fundamental frequencies and corresponding mode shapes. An arbitrary number of functions can be used, and the number of frequencies that can be obtained is equal to the number of trial functions used. A large series of admissible trial functions, although involving more computational work, generally leads to more accurate results.

N represents the admissible functions and the subscript letter w refers to the the flapwise direction. The admissible function R_w is assumed as a vector, which is a result of the constant Ritz coefficients that satisfy the boundary conditions $\beta_{w1,w2,w3,...,wn}$ and the shape functions $Y_{w1,w2,w3,...,wn}$ of the static deformation shapes of a non-rotating uncracked cantilever beam that is subjected to a concentrated load on the free end. n represent the number of shape functions used. The admissible and shape functions can be expressed as Equation 3.41 and Equation 3.42 respectively.

$$R_w(x) = [\beta_{w1}\ \beta_{w2}\ \beta_{w3}\ ..\ \beta_{wn}] \begin{bmatrix} Y_{w1}(x) \\ Y_{w2}(x) \\ Y_{w3}(x) \\ : \\ Y_{wn}(x) \end{bmatrix} \tag{3.41}$$

$$Y_{wn}(x) = \left(\frac{x}{L}\right)^{(n-1)} \left(\frac{-Lx^2}{2} + \frac{x^3}{6}\right) \tag{3.42}$$

Introducing the approximate solutions given by equation 3.21 and substituting into the weak equations given by equation 3.19 and 3.20, the equations of motion can also be written in a matrix form, yielding the discretised equations for the flapwise motion as

$$(\bar{d_w})^T[\mathbf{M}_w\ddot{d}_w + (\mathbf{K}_w + \Omega^2\mathbf{S}_w)d_w] = (\bar{d_w})^T\mathbf{f}_w \tag{3.43}$$

where $\mathbf{M}_w$, $\mathbf{K}_w$ and $\mathbf{S}_w$ are the mass, stiffness and motion-induced stiffness matrices for the flapwise motion. $\mathbf{f}_w$ is the load vector for the flapwise motion. The subscript letters w denote the flapwise direction and the matrix terms are

$$\mathbf{M}_w = \rho A \int_0^L R_w R_w^T dx, \tag{3.44}$$

$$\mathbf{K}_w = EI_y \int_0^L \frac{d^2 R_w}{dx^2} \frac{d^2 R_w^T}{dx^2} dx, \tag{3.45}$$

$$\mathbf{S}_w = \rho A \int_0^L \left[r(L-x) + \frac{1}{2}(L^2 - x^2) \right] \frac{dR_w}{dx} \frac{dR_w^T}{dx} dx, \tag{3.46}$$

$$\mathbf{f}_w = p_w \int_0^L R_w dx, \tag{3.47}$$

According to Chung and Yoo Chung and Yoo (2002), the chordwise vibration is coupled with the longitudinal or extensional vibration due to a gyroscopic effect and they are both uncoupled with the flapwise vibration. Furthermore, the chordwise vibration can be written as Chung and Yoo (2002),

$$(\bar{d_{sv}})^T \{\mathbf{M}_{sv} \ddot{d}_{sv} + 2\Omega \mathbf{G}_{sv} \dot{d}_{sv} + [\mathbf{K}_{sv} + \Omega^2 (\mathbf{S}_{sv} - \mathbf{M}_{sv}) + \dot{\Omega} \mathbf{G}_{sv}] d_{sv}\} = (\bar{d_{sv}})^T \mathbf{f}_{sv} \tag{3.48}$$

where subscript letters s and v represent stretch and chordwise directions respectively. $\mathbf{M}_{sv}$, $\mathbf{K}_{sv}$, $\mathbf{G}_{sv}$, $\mathbf{S}_{sv}$ and $\mathbf{f}_{sv}$ are the corresponding mass, stiffness, gyroscopic, rotational stiffness and external force matrices.

$$\mathbf{M}_{sv} = \rho A \int_0^L (R_s R_s^T + R_v R_v^T) dx, \tag{3.49}$$

$$\mathbf{G}_{sv} = \rho A \int_0^L (R_v R_s^T + R_s R_v^T) dx, \tag{3.50}$$

$$\mathbf{K}_{sv} = \int_0^L \left(EA \frac{dR_s}{dx} \frac{dR_s^T}{dx} + EI_z \frac{d^2 R_v}{dx^2} \frac{d^2 R_v^T}{dx^2} \right) dx, \tag{3.51}$$

$$\mathbf{S}_{sv} = \rho A \int_0^L \left[r(L-x) + \frac{1}{2}(L^2 - x^2) \right] \frac{dR_v}{dx} \frac{dR_v^T}{dx} dx, \tag{3.52}$$

$$\mathbf{f}_{sv} = \int_0^L \{\rho A \Omega^2 (r+x) R_s + [p_v - \rho A \dot{\Omega}(r+x)] R_v\} dx, \tag{3.53}$$

where the static deflection function for the chordwise bending and longitudinal vibration can be expressed similar to the flapwise admissible Equation 3.41 and shape functions equation Equation 3.42 and the chordwise bending admissible and shape functions equations become Equation 3.54 and Equation 3.55 respectively. The chordwise longitudinal admissible and shape functions become Equation 3.56 and Equation 3.57 respectively.

$$R_v(x) = [\beta_{v1}\ \beta_{v2}\ \beta_{v3}\ ..\ \beta_{vn}] \begin{bmatrix} Y_{v1}(x) \\ Y_{v2}(x) \\ Y_{v3}(x) \\ \vdots \\ Y_{vn}(x) \end{bmatrix} \tag{3.54}$$

$$Y_{vn}(x) = \left(\frac{x}{L}\right)^{n-1}\left(\frac{-Lx^2}{2} + \frac{x^3}{6}\right) \tag{3.55}$$

$$R_s(x) = [\beta_{s1}\ \beta_{s2}\ \beta_{s3}\ ..\ \beta_{sn}]\begin{bmatrix} Y_{s1}(x) \\ Y_{s2}(x) \\ Y_{s3}(x) \\ \vdots \\ Y_{sn}(x) \end{bmatrix} \tag{3.56}$$

$$Y_{sn}(x) = \left(\frac{x}{L}\right)^{n-1}\left(\frac{x}{L}\right) \tag{3.57}$$

3.3 Crack modelling

3.3.1 Crack modelling using the Finite Element Method

According to fracture mechanics theory, an open crack in a structure can be considered as a source of additional local flexibility because of the increase in the strain energy in the area surrounding the crack tip. The idea of substituting massless springs instead of a crack is to create the relationship between the strain energy and the applied loads as shown in Figure 3.7. The flexibility coefficients are stated in terms of stress intensity factors (SIF).

Applying Castigliono's theorem, the linear elastic deflections are determined based on the partial derivatives of the energy (Silani et al., 2013; Zheng and Kessissoglou, 2004). In Figure 3.8, the generalized loading conditions is shown for a beam with a rectangular cross section and an open edge surface crack. The beam is loaded statically with an axial force, P_1, shear forces, P_2 and P_3, bending moments, P_4 and P_5, and torsional torque, P_6. However, determining the additional flexibility can be achieved using Hooke's law, which introduces the stiffness that relates the force acting and the resulting deflection displacement. The flexibility can also be calculated from this law using equation (3.58).

$$c_{ij} = \frac{\partial \delta_i}{\partial P_j}, (i, j = 1, 2, 3). \tag{3.58}$$

In this equation c_{ij}, δ_i, Π_c and P_i represent the additional flexibility, the displacement, the additional strain energy and the effective loads respectively, and can be obtained from Castiglione's second theorem.

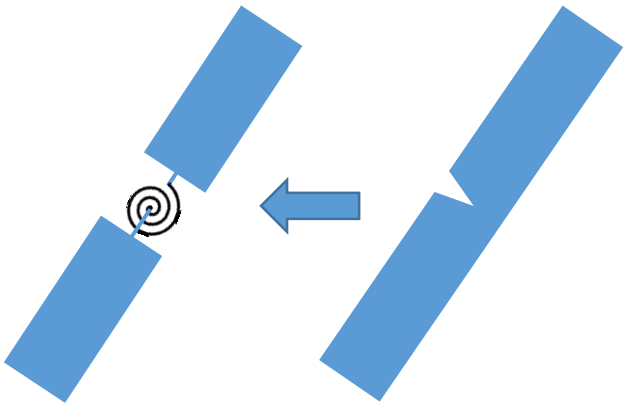

Figure 3.7: Modelling the crack as a massless torsional spring.

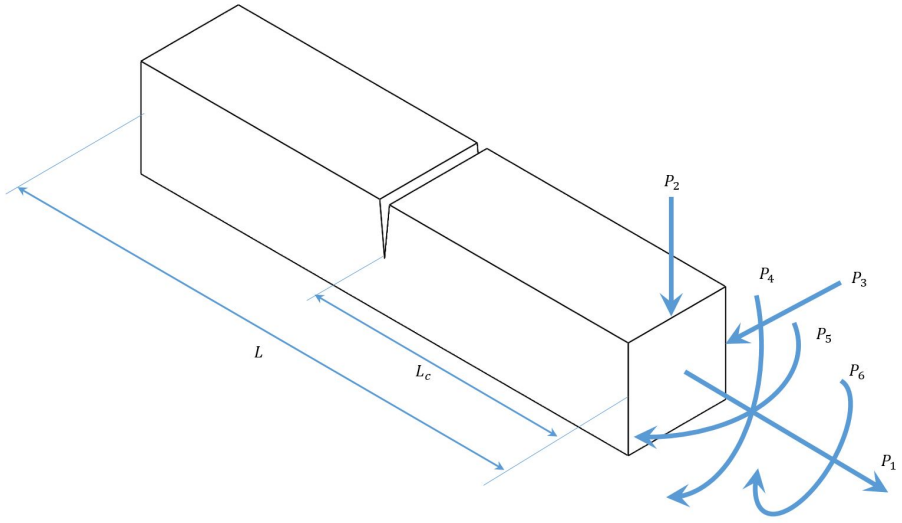

Figure 3.8: Beam with an open crack under generalized loading condition.

$$\delta_i = \frac{\partial \Pi_c}{\partial P_i} \tag{3.59}$$

$$\Pi_c = \int_{A_c} J dA \tag{3.60}$$

where A_c is the effective crack area and J is the strain energy release rate function expressed as (Tada et al., 2000a).

$$J = \frac{1}{E'}\left[\left(\sum_{i=1}^{n}\kappa_{Ii}\right)^2 + \left(\sum_{i=1}^{n}\kappa_{IIi}\right)^2 + \left(\sum_{i=1}^{n}\kappa_{IIIi}\right)^2\right] \tag{3.61}$$

For plane stress problem (Zheng and Kessissoglou (2004)) $E' = E$ and for the plane strain problem $E' = E/(1-\mu^2)$, κs are the stress intensity factors (SIF) due to forces.

I, II, III represent the modes of the crack namely opening, sliding and tearing respectively, and $i = 1, 2, 3, ..., n$ related to the applied loads on the beam $P_1, P_2, P_3, ..., P_n$. In this study, the in-plane vibration beam model is developed. The applied forces are shown in Figure 3.9. Rearranging Equation 3.61 to match the case of the in-plane vibration Ibrahim et al. (2013), yields

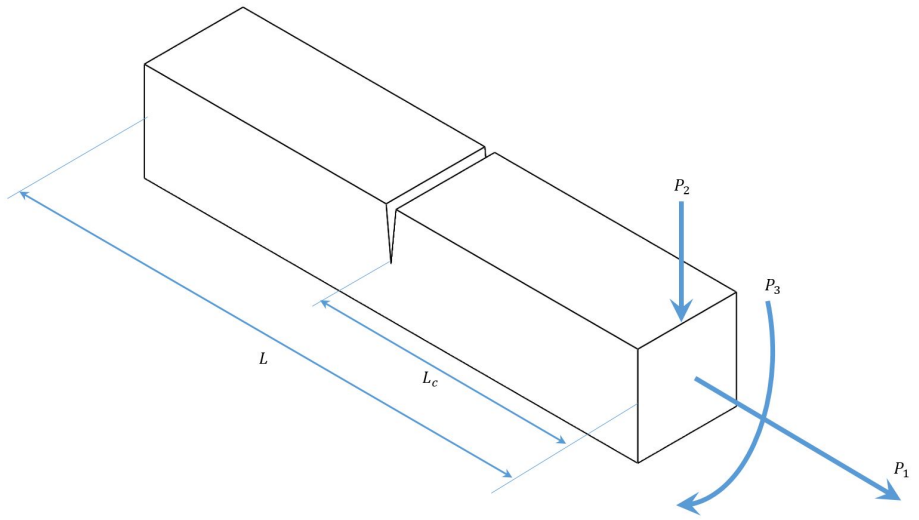

Figure 3.9: Beam with an open crack under in-plane loads condition

$$J = \frac{1}{E'}\left[(\kappa_{I1} + \kappa_{I2} + \kappa_{I3})^2 + (\kappa_{II2})^2\right]. \tag{3.62}$$

where according to Ozturk et al. (2016) the SIF for each force and mode becomes

$$\kappa_{I1} = \frac{P_1}{bh}\sqrt{\pi\xi}F_1 \tag{3.63}$$

$$\kappa_{I2} = \frac{3P_2L_c}{bh^2}\sqrt{\pi\xi}F_I \tag{3.64}$$

$$\kappa_{I3} = \frac{6P_3}{bh^2}\sqrt{\pi\xi}F_I \tag{3.65}$$

$$\kappa_{II2} = \frac{P_2}{bh}\sqrt{\pi\xi}F_{II} \tag{3.66}$$

where ξ is the crack depth, F_i is the correction factors of the SIF. Notice that a is the final crack depth, whereas ξ is the depth within the process of going from zero crack depth to final depth a, which is the maximum crack depth.

$$F_1 = \sqrt{\frac{2}{\pi\xi}\tan\frac{\pi\xi}{2}}\frac{0.752 + 2.02\xi + 0.37\left[1 - \sin\left(\frac{\pi\xi}{2}\right)\right]^3}{\sqrt{\cos\left(\frac{\pi\xi}{2}\right)}} \tag{3.67}$$

$$F_I = \sqrt{\frac{2}{\pi\xi}\tan\frac{\pi\xi}{2}}\frac{0.923 + 0.199\left[1 - \sin\left(\frac{\pi\xi}{2}\right)\right]^4}{\sqrt{\cos\left(\frac{\pi\xi}{2}\right)}} \tag{3.68}$$

$$F_{II} = (3\xi - 2\xi^2)\frac{1.122 - 0.561\xi + 0.085\xi^2 + 0.18\xi^3}{\sqrt{1-\xi}} \tag{3.69}$$

Substituting Equations 3.59 to 3.67 into Equation 3.58, yields,

$$c_{ij} = \frac{\partial^2}{E'\partial P_i \partial P_j}\int_o^a \left[\frac{P_1}{bh}\sqrt{\pi\xi}F_1 + \frac{3P_2L_c}{bh^2}\sqrt{\pi\xi}F_I + \frac{6P_3}{bh^2}\sqrt{\pi\xi}F_I\right]^2 + \left[\frac{P_2}{bh}\sqrt{\pi\xi}F_{II}\right]^2 d\xi \tag{3.70}$$

where c_{ij} is the additional flexibility that results from the existence of a crack.

One considers the additional local flexibility due to the existence of the crack by updating the global stiffness matrix of the uncracked rotating beam. The updated stiffness matrix is calculated by replacing the corresponding terms in the uncracked beam stiffness element where the crack is introduced. The stiffness of the cracked element is obtained by adding the local flexibility c_{ij} due to the crack to the flexibility of the intact beam element. This is then used to find the local stiffness of the cracked element and substituted into the original stiffness matrix.

$$\sum_{e=1}^{N}(\bar{d}_e^{sv})^T\{m_e^{sv}\ddot{d}_e^{sv} + 2\Omega g_e^{sv}\dot{d}_e^{sv} + [kc_e^{sv} + \Omega^2(s_e^{sv} - m_e^{sv}) + \dot{\Omega}g_e^{sv}]d_e^{sv}\} = \sum_{e=1}^{N}(\bar{d}_e^{sv})^T f_e^{sv} \tag{3.71}$$

$$\sum_{e=1}^{N}(\bar{d}_e^{w})^T[m_e^{w}\ddot{d}_e^{w} + (kc_e^{w} + \Omega^2 s_e^{w})d_e^{w}] = \sum_{e=1}^{N}(\bar{d}_e^{w})^T f_e^{w} \tag{3.72}$$

where kc represent the stiffness of a cracked beam.

As a result, in this chapter all the main equations of motion are derived. Firstly, the equation of motion for the flapwise vibration are developed from the continuous system approach (force equilibrium) as in Equation 3.6. Secondly, the equations of motion for both the flapwise and chordwise are derived using an energy method, which is a general method for this situation and it is based on the Hamiltonian principle as in Equation 3.15 to Equation 3.17. Moreover, new equations of motion for the cracked rotating beam are

developed by modelling a linear open crack using fracture mechanic principles. The additional flexibility, which is generated by the crack, is calculated using the strain energy release rate as in Equation 3.61, then Castigliono's theorem Equation 3.60. The final formulae for the cracked rotating beam are Equation 3.71 for the chordwise and Equation 3.72 for flapwise.

In this section, the crack element will be developed from fracture mechanics, which is explained in section 3.3. The flexibility can be calculated by substituting (3.59) into (3.58).

$$c_{ij} = \frac{\partial^2 \Pi}{\partial P_i \partial P_j} \tag{3.73}$$

where c_{ij}, Π and $P_{i,j}$ are the flexibility, the displacement and the effective loads, respectively. The displacement Π_c and Π_i for the cracked and intact element respectively are equal to

$$\Pi_c = \frac{b}{E} \int_0^a (\kappa_{I1} + \kappa_{I2} + \kappa_{I3})^2 + (\kappa_{II2})^2 da \tag{3.74}$$

$$\Pi_i = \frac{P_3^2 L}{2EI} + \frac{P_3 P_2 L^2}{2EI} + \frac{P_2^2 L^3}{6EI} + \frac{P_1^2 L}{2EA} \tag{3.75}$$

The total flexibility coefficient for crack element is

$$c_{ij} = c_{ij}^i + c_{ij}^c \tag{3.76}$$

The element stiffness matrix of the crack element can be found from the equation,

$$k_c = T^T \, c^{-1} \, T \tag{3.77}$$

where T represents the transformation matrix, which is obtained from the equilibrium condition see Figure 3.10.

$$[P_{1l} \, P_{2l} \, P_{3l} \, P_{1r} \, P_{2r} \, P_{3r}]^T = T \, [P_{1r} \, P_{2r} \, P_{3r}]^T \tag{3.78}$$

For flapwise vibration the transformation matrix is equal to

$$T = \begin{bmatrix} -1 & -l & 1 & 0 \\ 0 & -1 & 0 & 1 \end{bmatrix}^T, \tag{3.79}$$

for chordwise vibration the transformation matrix is equal to

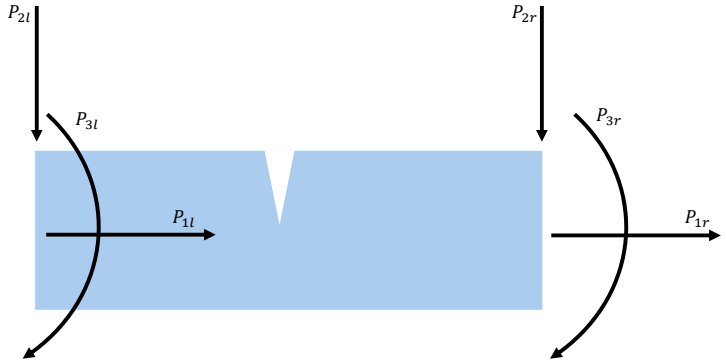

Figure 3.10: Applied force on the chordwise cracked element. Subscripts r, l refer to the right and left hand ends of the element.

$$T = \begin{bmatrix} -1 & 0 & 0 & 1 & 0 & 0 \\ 0 & -1 & l & 0 & 1 & 0 \\ 0 & 0 & -1 & 0 & 0 & 1 \end{bmatrix}^T \tag{3.80}$$

where l represents the element length.

3.3.2 Introduction of a crack in the Rayleigh-Ritz model

Regarding fracture mechanics theory, an open crack in a structure can be considered as a source of additional local flexibility because of the increase in the strain energy in the area surrounding the crack tip. The idea of substituting massless springs instead of a crack is to create the relation between the strain energy and the applied loads as shown in Figure (3.11).

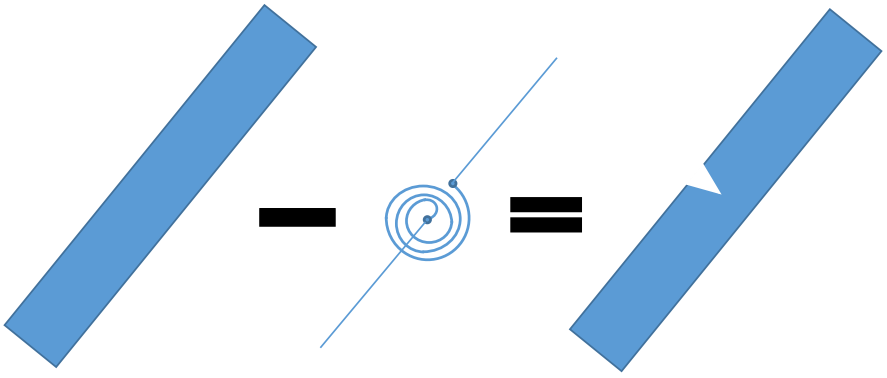

Figure 3.11: Modelling the crack using a massless torsional spring. The potential energy of the rotational massless spring is subtracted from the total potential energy of the intact beam using the rotations on the faces of the opening crack.

The typical method of modelling a cracked beam is based on dividing the beam into two segments and building a relationship between two sides using the compatibility conditions. The transverse displacement, bending moment and shear force are equal through the cracked edge. Nevertheless, the presence of the crack introduces a discontinuity or change in the slope of the beam, which is proportional to the bending moment that is transmitted through the cracked section. For the axial vibration, it is assumed that the tensile force is the same through the cracked segments. However, the axial displacement is proportional to the transmitted force through the crack, and it is proportional to the tensile force. The bending and axial discontinuity can be expressed as presented in Fernández-Sáez et al. (1999) and Ibrahim et al. (2013).

$$\Theta_2 = \Theta_1 + \Delta\Theta, \qquad \Delta\Theta = C_{v,w} P_3 \tag{3.81}$$

$$s_2 = s_1 + \Delta s, \qquad \Delta s = C_s P_1 \tag{3.82}$$

where $\Delta\Theta$, C, P_3 represent slope discontinuity, flexibility constant and the bending moment transmitted through the crack section. Δs and P_1 represent the discontinuity of axial displacement and tensile force respectively. The flexibility constant is dependent on the geometrical dimension of the cross section and can be derived from the stress intensity factor κ_c (SIF).

$$\kappa_c = \sigma\sqrt{\pi a} F\left(\frac{a}{h}\right) \tag{3.83}$$

here σ, a, h and F are the stress according to the bending moment or tensile force, crack depth, beam thickness and correction factor respectively. F depends on the crack's mode and force configurations. The stress σ and the correction factor F for the bending moment and opening mode can be obtained from Zheng and Kessissoglou (2004); Eroglu and Tufekci (2016). $P1$, $P2$ and $P3$ refer to the longitudinal load, shear load and bending moment respectively (see Figure 3.9). The subscripts I and II are for the opening and sliding modes of crack.

$$\sigma_{P_3} = \frac{6P_3}{bh^2} \tag{3.84}$$

$$F_{IP_3} = \sqrt{\frac{2}{\pi\xi}\tan\frac{\pi\xi}{2}}\,\frac{0.923 + 0.199\left[1 - \sin\left(\frac{\pi\xi}{2}\right)\right]^4}{\sqrt{\cos\left(\frac{\pi\xi}{2}\right)}} \tag{3.85}$$

The effect of the sliding mode is neglected in this study due to its very small effect relative to the opening bending moment mode. For shorter and thicker beam this sliding mode becomes more considerable defect. The stress and error function in Equation 3.86 to

Equation 3.88 are for the sliding mode.

$$\sigma_{IP_2} = \frac{3P_2}{bh^2} \tag{3.86}$$

$$\sigma_{IIP_2} = \frac{3P_2}{bh} \tag{3.87}$$

$$F_{IIP_2} = (3\xi - 2\xi^2)\frac{1.122 - 0.561\xi + 0.085\xi^2 + 0.18\xi^3}{\sqrt{1-\xi}} \tag{3.88}$$

where b represents the beam width and the crack depth to thickness ratio $\xi = (a/h)$, while for the tensile and opening mode, are

$$\sigma_{P_1} = \frac{P_1}{bh} \tag{3.89}$$

$$F_{IP_1} = \sqrt{\frac{2}{\pi\xi}\tan\frac{\pi\xi}{2}}\frac{0.752 + 2.02\xi + 0.37\left[1 - \sin\left(\frac{\pi\xi}{2}\right)\right]^3}{\sqrt{\cos\left(\frac{\pi\xi}{2}\right)}} \tag{3.90}$$

These error functions, reported by Tada et al. (2000b), are accurate to better than 0.5% for any crack depth ratio ξ. The total strain energy of the elastic deformation of the crack is given by,

$$PE_{total} = \int_{A_c} J\, dA_c \tag{3.91}$$

where J is the elastic energy available per unit increase in the crack surface area. The width of the crack is fixed i.e. $dA_c = b\, da$ and the integration is applied along the depth of the crack which is a.

$$J = \frac{\kappa_c^2}{E} \tag{3.92}$$

Substituting equations 3.83-3.92 into equation 3.91, yields

$$PE_{P_3} = \left(\frac{3\pi P_3^2 h}{EI}\right)\int_0^a \left(\frac{a}{h^2}\right) F_{IP_3}^2\, da \tag{3.93}$$

$$PE_{P_1} = \frac{\pi P_1^2 h}{EA}\int_0^a \left(\frac{a}{h^2}\right) F_{IP_1}^2\, da \tag{3.94}$$

where PE_{P_3} is the strain energy due to the bending and PE_{P_1} is the tensile strain energy due to tension. Utilizing Castigliano's theorem (Chondros and Dimarogonas (1998)), the change in the rotation angle $\Delta\Theta$ and the change in the stretch length Δs corresponding to the applied moment and longitudinal force can be expressed as,

$$\Delta\Theta = \frac{\partial PE_{P_3}}{\partial P_3} \tag{3.95}$$

$$\Delta s = \frac{\partial PE_{P_1}}{\partial P_1} \tag{3.96}$$

Finally, the additional flexibility in flapwise C_w, chordwise C_v and stretch C_s directions due to the presence of the opening crack can be expressed as

$$C_v = C_w = \frac{\Delta\Theta}{P_3} \tag{3.97}$$

$$C_s = \frac{\Delta s}{P_1} \tag{3.98}$$

According to this approach, an admissible function of the non-rotating intact beam satisfies the boundary conditions and it is used directly without any modification. The potential energy of the system is modified to include the effect of the extra flexibility due to the existence of the crack.

The potential energy of the non rotating intact beam can be expressed as,

$$PE_{P_3-intact-nonrotate} = \frac{EI}{2}\int_0^L \frac{d^2R_{v,w}}{dx^2}\frac{d^2R^T_{v,w}}{dx^2}\,dx \tag{3.99}$$

$$PE_{P_1-intact-nonrotate} = \frac{EA}{2}\int_0^L R_s\,R^T_s\,dx \tag{3.100}$$

The additional potential energy due to the centrifugal effect on the intact beam can be written as,

$$PE_{centrifugal} = \frac{1}{2}\Omega^2\rho A\int_0^L (r(L-x) + \frac{1}{2}(L^2-x^2)\frac{dR_{v,w}}{dx}\frac{dR^T_{v,w}}{dx}\,dx \tag{3.101}$$

Finally, the presence of additional flexibility due to the crack can be represented by a massless rotational spring and the corresponding potential energy in the spring has two components, which can be expressed as (Afshari and Inman (2012)),

$$PE_{P_3-crack} = \frac{1}{2}(\Delta\Theta)P_3 = \frac{1}{2}EIC_{v,w}\left(\frac{d^2R_{v,w}}{dx^2}\frac{d^2R^T_{v,w}}{dx^2}\right) \tag{3.102}$$

$$PE_{P_2-crack} = \frac{1}{2}(\Delta s)P_1 = \frac{1}{2}EAC_s(R_s\,R^T_s) \tag{3.103}$$

The kinetic energy of the system KE is equal to the kinetic energy of the beam itself, i.e.

$$KE_{flapwise} = \frac{1}{2}\rho A\int_0^L R_w\,R^T_w dx \tag{3.104}$$

$$KE_{chordwise} = \frac{1}{2}\rho A\int_0^L (R_s\,R^T_s + R_v\,R^T_v)dx \tag{3.105}$$

The Rayleigh-Ritz method can now be employed after determining the kinetic and potential energies of the system.

When applying the mode shapes of the uncracked beam as the admissible functions for the Rayleigh-Ritz approximation, the maximum strain energy needs to be altered to account for the reduction of the energy as a result of the presence of the crack. This energy reduction is proportional to the amount of additional flexibility due to the rotational spring. As a result, the total potential energy of the cracked rotating beam is equal to the summation of the potential energy of the uncracked beam and the additional potential energy due to the centrifugal force with subtraction of the potential energy of the massless rotating spring representing the crack.

$$PE_{total} = PE_{intact-nonrotate} + PE_{centrifugal} - PE_{crack} \tag{3.106}$$

Substituting equations 3.99-3.100, 3.101 and 3.102-3.103 into equation 3.106 provides the total strain energy of the system for the flapwise vibration and the equations 3.104-3.105 gives the kinetic energy. These two energies were subsequently used to calculate the flapwise and chordwise natural frequency of the rotating cracked cantilever beam.

3.4 Summary of the modelling approaches

In this chapter, a rotating cracked beam was modelled using force equilibrium for the flapwise motion. Using this model the equations of motion were derived by applying Hamilton's principle for both the flapwise and chordwise vibration. Then, the residual weight function is applied to convert the equations of motion to a weak form. The discretised system can then be solved using two approximate methods, which are the finite element and the Rayleigh Ritz methods.

The finite elements chosen are based on two different types of beam elements; the first type have two degrees of freedom at each node, which are the lateral displacement and slope. The second element type have three degrees of freedom at each node, which are the longitudinal and lateral displacements and the slope. In the Rayleigh Ritz method, the entire beam is selected as a one domain and the static deflection of a tip loaded cantilever beam is selected as shape functions terms for the admissible functions for the bending mode and axial deformation for the stretch mode.

Regarding the crack modelling, in the finite element model the crack is presented as a connection between the two segments comprising beam elements. The assumption of this connection is built upon continuity in the shear force, bending moment and the lateral deformation of the two cracked edges. The formulation given have follows from analysis previously presented from static analysis. However, the effect of the crack appears in the discontinuities of the slope. On the other hand, the crack is introduced into the intact beam by applying the Rayleigh Ritz method. The additional flexibility due to the crack is subtracted from the total potential energy of the intact rotating beam. The

most significant advantage of this approach is that the beam shape functions due to the crack are unchanged and correspond to a series of functions based on the deformation of tip loaded intact cantilever beam.

The numerical solution for these model will be presented in detail in the following chapter, including the comparison between the two approaches, which are the FE model and the Rayleigh Ritz implementation. Their relative accuracy, computational effect and limitations will be presented and discussed.

Chapter 4

Numerical results

In this chapter numerical results will be presented using both the finite element models and the Rayleigh-Ritz method, which were developed and derived in the previous chapter. The numerical simulations will start with defining the dimensions of the beam. Then the results for uncracked non-rotating and rotating beams will be shown. Next, the results for an open cracked rotating beam will be presented. Finally, the simulations of a bilinear cracked beam will be given and discussed with conclusions. Various parameter studies will be undertaken and explained. For the convenience of the discussion and for the sake of comparison with results in the literature, the following dimensionless parameters will be introduced.

$$\delta = \frac{r}{L}, \qquad \alpha = \sqrt{\frac{AL^2}{I_z}}, \qquad \gamma = \frac{\Omega}{\omega_{n_1}}, \qquad \varpi = \frac{\omega}{\omega_{n_1}}, \tag{4.1}$$

where δ, α, γ, ϖ and ω_{n_1} represent the hub ratio, the slenderness ratio, the angular speed ratio, the frequency ratio and the fundamental natural frequency of an identical but non-rotating cantilever beam, respectively.

4.1 Simulation model properties

The dimensions and properties of material were selected to simplify the analysis, as given in Figure 4.1 and Table 4.1, where the value of α is set to 70 to compare with the previously published study by Chung and Yoo (2002). This value of α is based on the dimensionless relationship between the cross section and the length of the beam. The beam cross section was chosen to be square, and the beam length long enough so that the beam would satisfy EulerBernoulli beam theory. In addition, changing the value of α for a fixed length of the beam means a change in the thickness of the beam when having the rectangular cross section. For example, multiplying α by 2 for the fixed length of

the beam means reducing the height of the beam to half. In contrast, dividing the α by 2 means increasing the height of the beam to the double for the same beam length.

Whilst the main focus of this chapter is a presentation of the results of the newly developed models, at the end of the chapter there is some coverage of a simple model for a breathing crack for completeness.

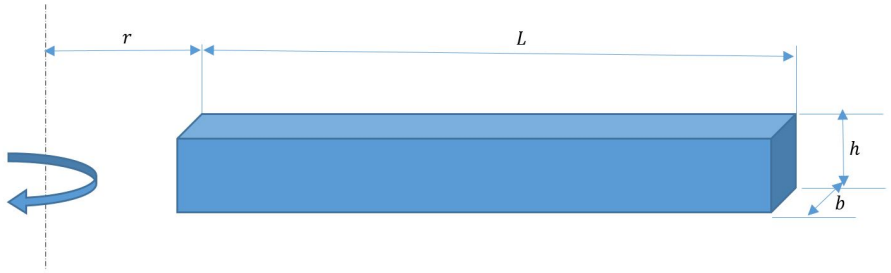

Figure 4.1: Configuration of a rotating cantilever beam.

property	quantitiy
beam length(L)	0.5m
height(h)	0.0247m
width(b)	0.0247m
density(ρ)	2770 kg.m^{-3}
elasticity(E)	7.1$\times$10^{10} Pa
poison ratio(v)	0.33

Table 4.1: Model properties of the square section beam

4.2 Beam without crack

The numerical results for a rotating intact cantilever beam are examined first. Table 4.2 reproduces results from Chung and Yoo (2002), where one can see how the first four natural frequencies for a stationary beam are converging with increased number of elements in the FEM model. Similar convergence can be observed using the Rayleigh-Ritz method when increasing the number of shape functions, as given in Table 4.3. Notice that, the number of frequencies is equal to the number of trial functions in the Rayleigh-Ritz method. For example, in Table 4.3 when the number of trial functions is equal to 1 only the fundamental natural frequency is calculated. Also, for the number of elements greater than 10 in the FEM model and the number of functions greater than 3 in the Rayleigh-Ritz method, the results for the fundamental natural frequency are in good agreement. The time is included for a MATLAB calculation for relative comparison only. In addition, for the stationary non-rotating square section cantilever beam the first seven flapwise frequencies are equal to the first nine chordwise frequencies, except

for the fourth and eighth, since for a stationary beam the chordwise bending and axial vibration is uncoupled, as shown in Table 4.4.

No. of elements	**1st**	**2nd**	**3rd**	**4th**	**Time(sec)**
5	1	6.270	17.610	34.789	0.2145
10	1	6.267	17.552	34.419	0.4277
20	1	6.267	17.548	34.388	0.6343
40	1	6.267	17.547	34.386	0.8337
60	1	6.267	17.547	34.386	1.0508
80	1	6.267	17.547	34.386	1.2996
100	1	6.267	17.547	34.386	1.4671
Exact	1	6.267	17.547	34.386	

Table 4.2: Convergence of the dimensionless natural frequencies for the non-rotating intact cantilever beam using FEM

No. of trial functions	**1st**	**2nd**	**3rd**	**4th**	**Time(sec)**
2	1	7.629	0	0	0.0659
3	1	6.315	26.985	0	0.0767
4	1	6.292	18.077	66.200	0.0876
5	1	6.269	17.908	36.754	0.0929
6	1	6.267	17.571	36.233	0.1035
7	1	6.267	17.550	34.515	0.1085
8	1	6.267	17.547	34.427	0.1230
9	1	6.267	17.547	34.388	0.1428
Exact	1	6.267	17.547	34.386	

Table 4.3: Convergence of the dimensionless natural frequencies ϖ for the non-rotating intact cantilever beam using the Rayleigh-Ritz method

No. Frequency	**Chordwise**	**Flapwise**
1st	1	1
2nd	6.267	6.267
3rd	17.547	17.547
4th	31.328	-
5th	34.386	34.387
6th	56.858	56.860
7th	86.005	86.004
8th	95.245	-
9th	122.855	122.837

Table 4.4: Dimensionless natural frequencies ϖ of the non-rotating intact square section cantilever beam using the Rayleigh-Ritz method

Regarding the mode shapes, the comparison between this work and that by Chung and Yoo (2002) also shows an excellent agreement for various rotational speeds. The comparison is done by applying the Modal Assurance Criterion (MAC), which is a

statistical indicator of the correlation in the mode shapes. The general formula for the MAC, as given in Pastor et al. (2012)

$$MAC(r,q) = \frac{|\{Q_A\}_r^T \{Q_X\}_q|^2}{(\{Q_A\}_r^T \{Q_A\}_r)(\{Q_X\}_q^T)\{Q_X\}_q} \tag{4.2}$$

where $\{Q_X\}_q$ and $\{Q_A\}_r$ represent the respective eigenvectors coming from the FEM in Chung and Yoo (2002) method and corresponding point position of this work (Rayleigh Ritz), respectively, and the superscript T refers to the transpose of the the vector matrix. When the MAC is 1, there is a perfect agreement and a MAC of 0, means there is no correlation between the two results.

In the MAC plot, given in Figure 4.2, the abscissa axis represents the mode shapes calculated by the Rayleigh-Ritz Method, and the ordinate axis represents the mode shapes calculated by the FE model. The red squares show the matching modes. When the cantilever beam is non-rotating, the MAC for the chordwise vibration is shown in Figure 4.3. The 4th and 8th modes represent the longitudinal vibration likewise when the beam is rotating $\gamma = \frac{\Omega}{\omega_1} = 7.11$ the 4th and 7th similar effect can be observed at $\gamma = 14.22$ and $\gamma = 28.44$.

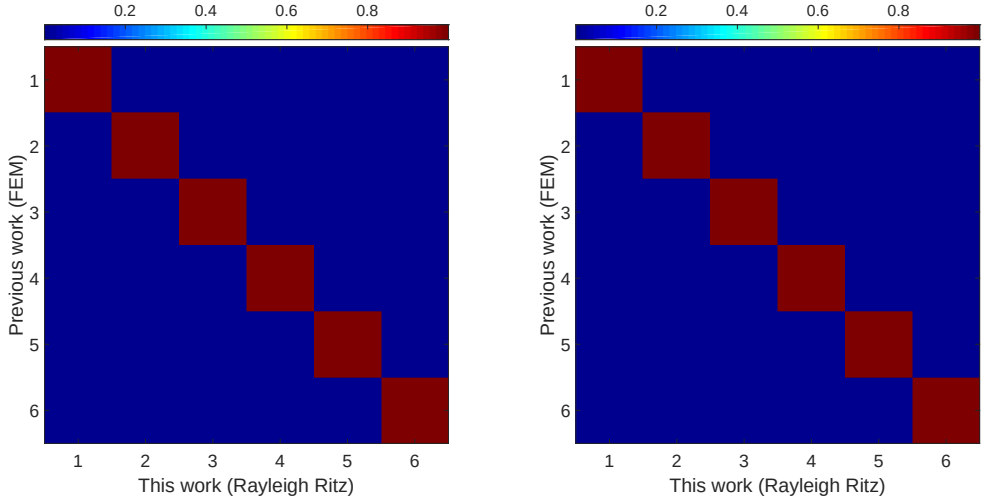

(a) MAC in flapwise vibration at γ=0

(b) MAC in flapwise vibration at γ=7.11

(c) MAC in flapwise vibration at γ=14.22

(d) MAC in flapwise vibration at γ=28.44

Figure 4.2: The MAC plots for the flapwise vibration at non-rotating $\gamma = 0$ and for rotating speeds ratio $\gamma = 7.11, 14.22$ and 28.44 ($\gamma = \frac{\Omega}{\omega_{n1}}$)

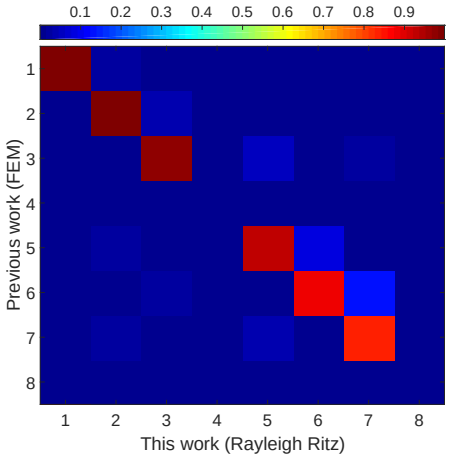

(a) MAC for the chordwise vibration at γ=0

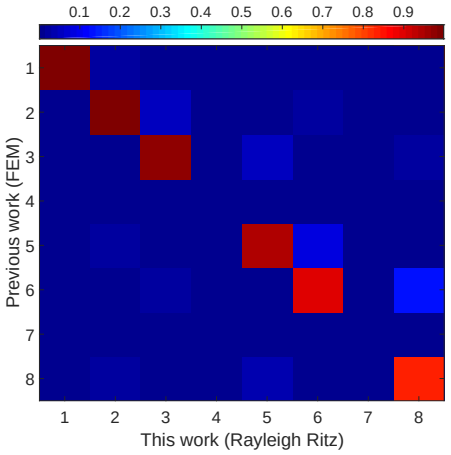

(b) MAC in chordwise vibration at γ=7.11

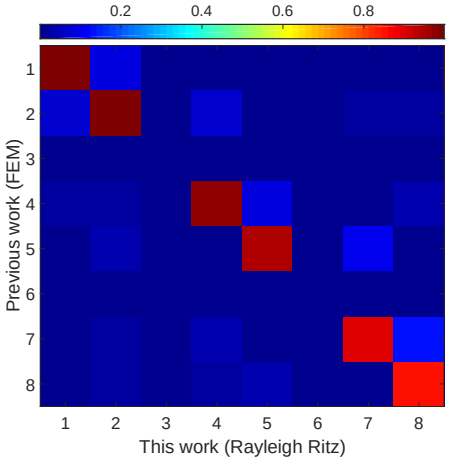

(c) MAC in chordwise vibration at γ=14.22

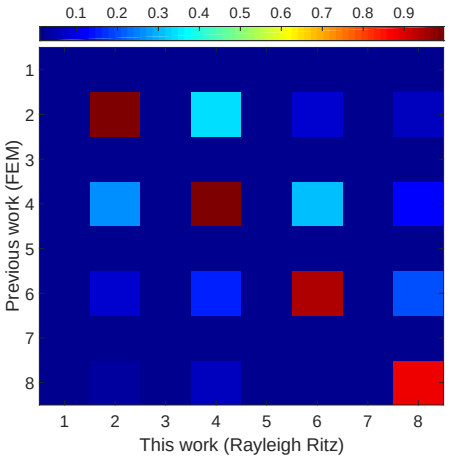

(d) MAC in chordwise vibration at γ=28.44

Figure 4.3: The MAC plots for the chordwise vibration at non-rotating $\gamma = 0$ and for rotating speeds $\gamma = \frac{\Omega}{\omega_{n1}} = 7.11, 14.22$ and 28.44

4.2.1 Flapwise vibration of a rotating cantilever beam

Flapwise vibration is described in chapter 3 as the vibration that appears in a plane perpendicular to the plane of rotation. Nevertheless, this vibration is affected by numerous parameters, such as the rotational speed, hub ratio and beam slenderness. All of these factors produce variations in the natural frequency of the rotating cantilever beam.

Table 4.5 shows a comparison between the results obtained by the Rayleigh-Ritz method with results reproduced from Chung and Yoo (2002), and the solid finite element model assembled using the commercial FE software ANSYS. Substantial agreement in the final results is achieved and the accuracy of Rayleigh-Ritz method is validated. The maximum percentage error between the finite element (Chung and Yoo, 2002) and present work (Rayleigh-Ritz method) is equal to 0.006% at zero speed for the flapwise vibration. This error value becomes less for γ within the range of 0 - 2.844 non-dimensional rotational speed.

As shown in Figure 4.4, increasing the rotational speed leads to an increase in the dimensionless natural frequency, due to the tension that is generated from centrifugal forces. Note that the natural frequencies for the flapwise vibration monotonically increase with rotating speed.

In additional to the rotational speed, there is another parameter, which significantly affects the natural frequencies of the rotating cantilever beam, which is the hub ratio. The increase in the hub ratio for a fixed length cantilever leads to an increase in the natural frequencies due to a proportional relationship between the stiffness and the centrifugal force as shown in Figure 4.5.

Finally, from Table 4.6, one can see the slenderness ratio α has a negligible effect on the dimensionless natural frequency of the flapwise vibration, where the results are divided by the fundamental natural frequency of the non-rotating beam with the same slenderness dimensions.

	frequency $\bar{\omega}$			
γ	**Chung and Yoo 2002**	**ANSYS**	**RRM**	**Error %**
0	1.000	1.001	1.000	0.006
0.284	1.047	1.048	1.047	0.000
0.569	1.177	1.177	1.177	0.000
0.853	1.364	1.364	1.364	0.002
1.138	1.588	1.588	1.588	0.000
1.422	1.834	1.833	1.834	0.000
1.706	2.093	2.091	2.093	0.001
1.991	2.360	2.357	2.360	0.000
2.275	2.633	2.629	2.633	0.000
2.560	2.908	2.903	2.908	0.001
2.844	3.186	3.180	3.186	0.000

Table 4.5: Comparison between different methods for the fundamental natural frequency of the flapwise vibration (Chung and Yoo (2002), FE using ANSYS and Rayleigh-Ritz model)

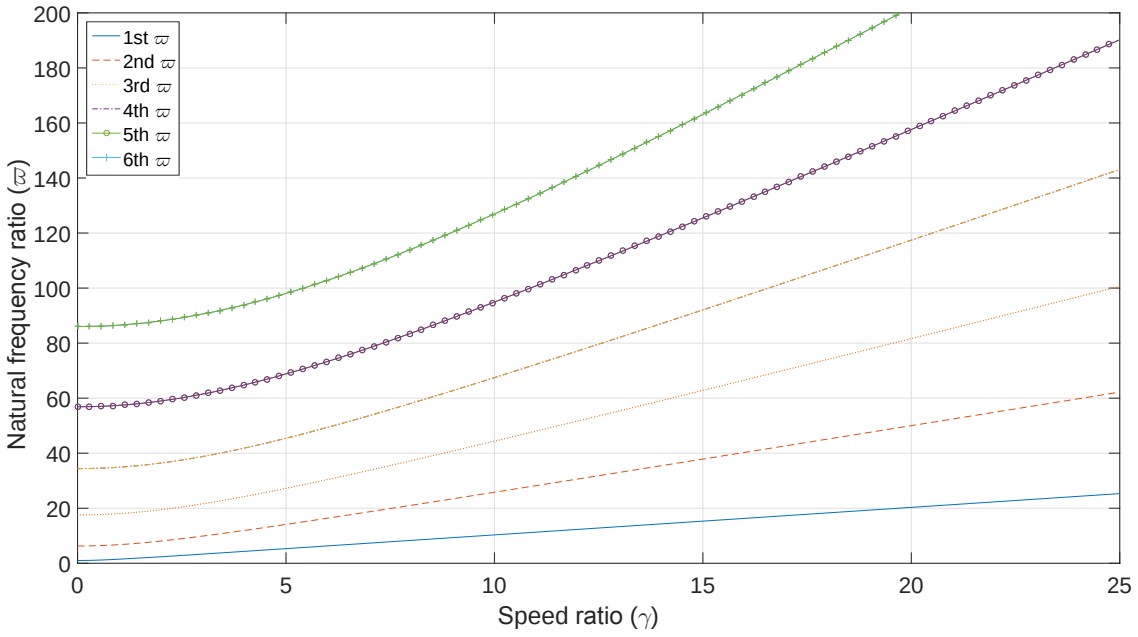

Figure 4.4: First five natural frequencies of flapwise vibration of a rotating cantilever beam

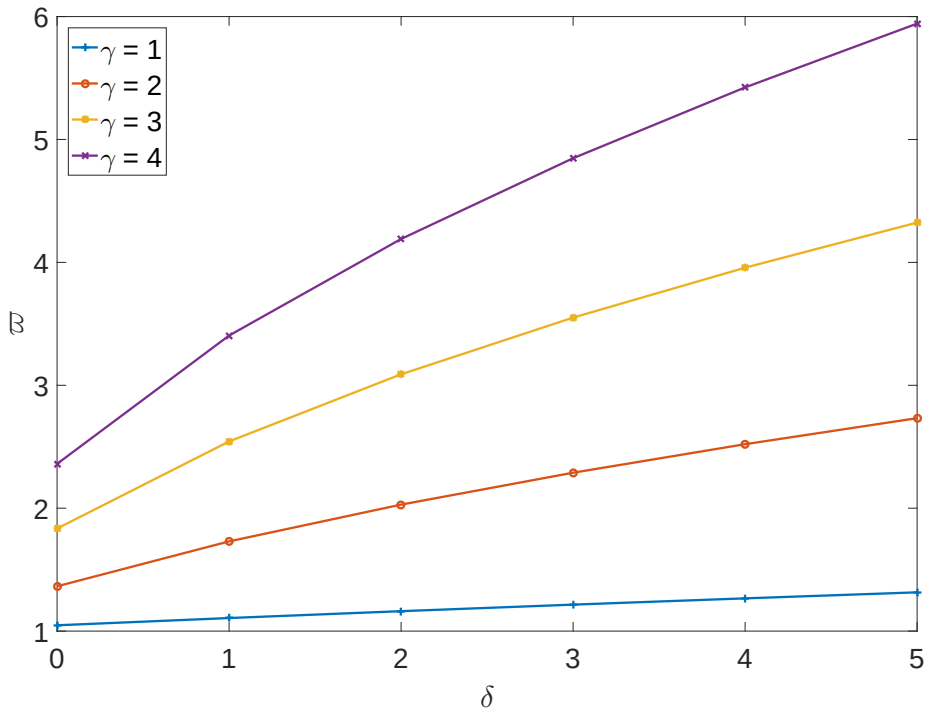

Figure 4.5: The effect of the hub ratio (δ)on the dimensionless fundamental natural frequency (ϖ) for three rotational speeds (γ).

γ	$\alpha = 17.5$	$\alpha = 35$	$\alpha = 70$	$\alpha = 140$	$\alpha = 280.5$
0	1.000	1.000	1.000	1.000	1.000
2.844	3.186	3.186	3.186	3.186	3.186
5.688	6.006	6.006	6.006	6.006	6.006
8.532	8.844	8.844	8.844	8.844	8.843
11.38	11.685	11.684	11.685	11.684	11.685
22.753	23.065	23.063	23.065	23.063	23.065
25.597	25.916	25.914	25.916	25.914	25.916
28.441	28.763	28.766	28.763	28.766	28.763

Table 4.6: The effect of the slenderness ratio on the flapwise vibration for various non-denominational rotational speeds γ.

4.2.2 Chordwise vibration of a rotating cantilever beam

Chordwise vibration, described in chapter 3, is the vibration that takes place in a plane parallel to the plane of rotation. However, this vibration and the corresponding natural frequency is affected by numerous factors, for instance, the rotational speed of the beam, the hub ratio and the slenderness ratio. Furthermore, there are several different critical behaviours of the rotating cantilever beam such as veering phenomena, critical speed and buckling speed.

Table 4.7 illustrates a very good agreement in the fundamental dimensionless natural frequency for the chordwise vibration calculated by this study, the work by Chung and Yoo (2002) and an FEM model using ANSYS, for $\alpha = 70$ and various values of hub ratio δ and speed ratio γ. The maximum percentage error between this work and the previous one Chung and Yoo (2002), is equal to 1.264 at $\delta = 1$ and $\gamma = 0.569$.

Regarding the rotational speed, as in flapwise vibration, the natural frequencies are changing with the changes in the angular velocity. Seemingly in Figure 4.6(a), the existence of the gyroscopic coupling influences the bending and stretching modes created by a rotational motion, which results in the veering phenomena in the natural frequency versus speed plot. The veering phenomena occurs when the natural frequency of two different modes become closer to each other. In chordwise vibration, the veering phenomena arises due to coupling of bending and stretching modes. For example, when roughly $\gamma = 7.5$ the 3rd and 4th natural frequencies veer together for a slenderness ratio of $\alpha = 70$ while the 5th and 6th natural frequencies veer at about γ for slenderness ratio of $\alpha = 17.5$ (see Figure 4.6).

Figure 4.7, shows in detail the veering points for the lower natural frequencies. The circles V1, V2 and V3 indicate the veering phenomena. The 3rd, 5th and 6th dimensionless natural frequencies correspond to the modes that are veering from being primarily bending vibration to longitudinal vibration in V1 and V3, as illustrated in Figure 4.7(b) to Figure 4.7(j). For example the 3rd frequency is veering from the third mode shape of bending vibration as in Figure 4.7(b) to the first mode of stretch vibration as in Figure 4.7(c). However, the 4th and the 6th are veering from longitudinal vibration to bending vibration at V1 and V2. For instance, the 4th dimensionless natural frequency is veering from the first mode of longitudinal vibration as in Figure 4.7(d) to the 3rd dimensionless natural frequency of the bending mode as in Figure 4.7(e).

Another noticeable fact is the existence of potential instability, when the fundamental natural frequency of the chordwise vibration reduces to zero. This speed can be defined as the critical speed or buckling speed as discussed in Lima (2012); Chung and Yoo (2002).

Considering the slenderness of the beam, Figure 4.6(b) shows how the values of the slenderness ratio affects the rotating beam. Increasing the slenderness leads to an increased

chance of veering at low frequencies, since the beam becomes thinner and more able to bend than to stretch. While decreasing the slenderness ratio means a thicker cross section and the probability of veering at low frequencies is reduced.

Finally, the most significant feature is the resonance issue and the matching between the rotational speed and the fundamental natural frequency of the chordwise vibration. The rotational speed γ and chordwise dimensionless fundamental natural frequency ϖ become equal when γ is approximately equal to 1.1 in Figure 4.8(a). This problem is not apparent in the flapwise vibration when inspecting Figure 4.8(b). An additional factor that plays a part in increasing the natural frequency is the hub ratio δ, which enhances the radius of the hub, leading to an increase in the natural frequencies as shown in Figure 4.9. One can also see that increasing the hub ratio eliminates the critical speed issue, as illustrated in Figure 4.9 where the figure shows the relationship between the rotational speed and dimensionless fundamental frequencies. Each of these coloured curves represent the fundamental frequency for a different hub ratio. When the hub is removed, i.e. the hub ratio is equal to $\delta = 0$, the intersection occurs with the $\Omega = \gamma$ line which represents the dimensionless natural frequency being equal to the rotational speed, occurs again at around $\gamma = 1.1$.

δ	γ	**ANSYS**	**Chung and Yoo 2002**	**RRM**	**Error %**
0	0.569	1.028	1.029	1.029	0
	2.844	1.422	1.413	1.413	0
	14.219	2.264	2.088	2.088	0.008
1	0.569	1.248	1.235	1.250	1.264
	2.844	3.744	3.711	3.711	0
	14.219	13.157	11.745	11.740	0.043
5	0.569	1.883	1.889	1.889	0
	2.844	7.819	7.754	7.754	0.006
	14.219	37.885	21.101	21.086	0.068

Table 4.7: Comparison between different prediction methods for the chordwise fundamental natural frequencies. δ, γ represent the hub ratio ($\frac{r}{L}$) and the rotational speed ratio $\frac{\Omega}{\omega_{n_1}}$ respectively. RRM=Rayleigh Ritz Method

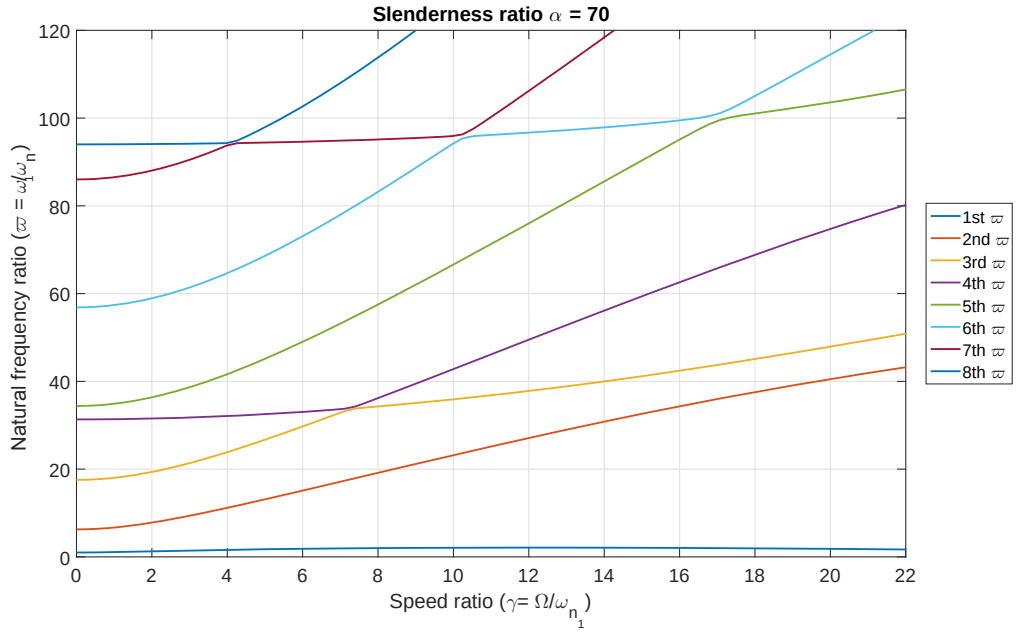

(a) Chordwise vibration of a rotating cantilever beam at $\alpha = 70$

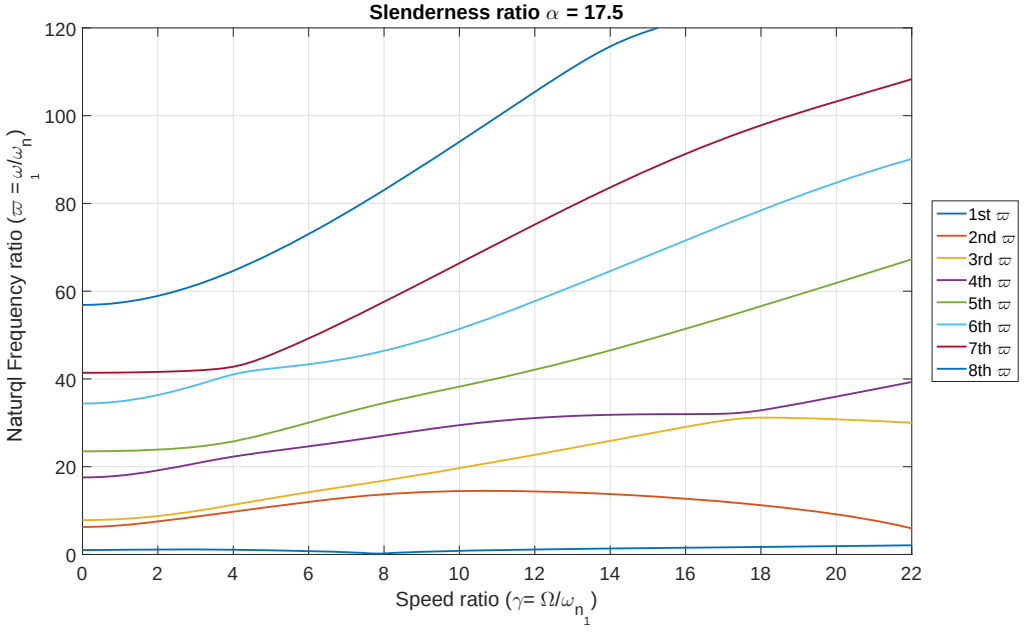

(b) Chordwise vibration of a rotating cantilever beam at $\alpha = 17.5$

Figure 4.6: Chordwise vibration of a rotating cantilever beam showing the effect of rotational speed for different values of the slenderness ratio.

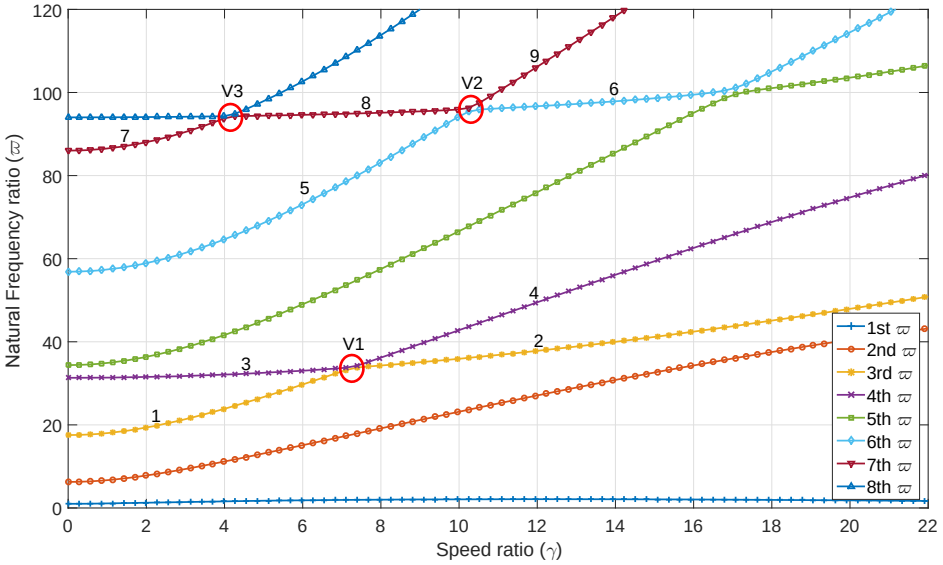

(a) Dimensionless natural frequencies versus rotation speed. The red circle indicate to the veering modes. 3rd, 5th and 6th are veering from bending vibration to longitudinal vibration at points V1 and V3 while the 4th and 6th modes are veering from being longitudinal modes to bending modes at points V1 and V2.

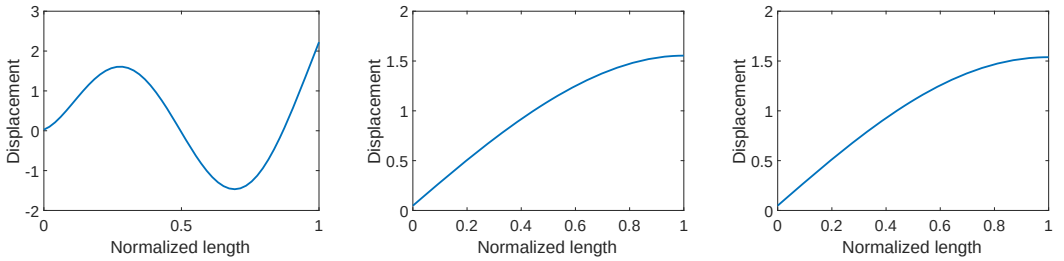

(b) Mode shape at point 1 γ=2 (c) Mode shape at point 2 γ=8 (d) Mode shape at point 3 γ=2

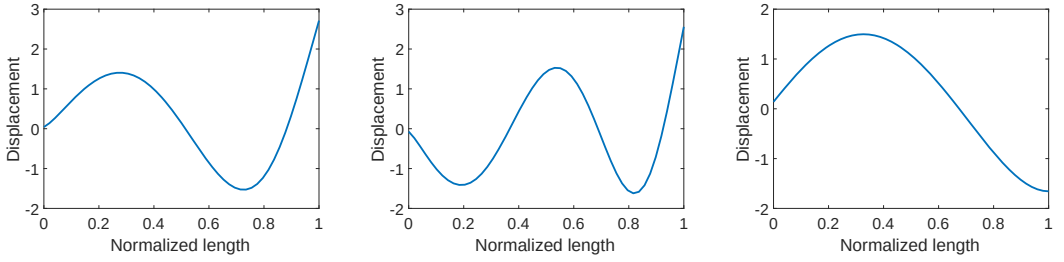

(e) Mode shape at point 4 γ=8 (f) Mode shape at point 5 γ=10 (g) Mode shape at point 6 γ=16

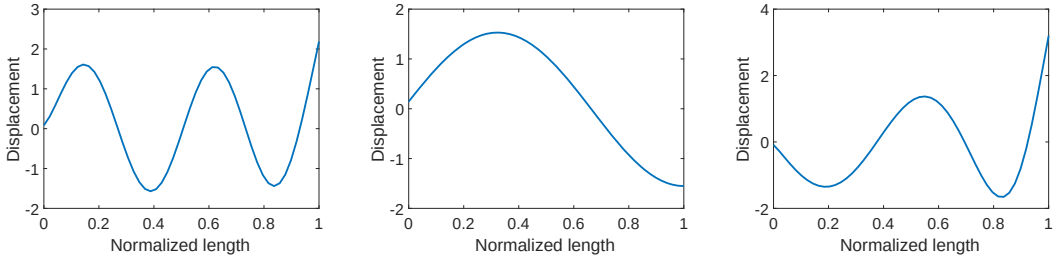

(h) Mode shape at point 7 γ=4 (i) Mode shape at point 8 γ=10 (j) Mode shape at point 9 γ=16

Figure 4.7: Mode shapes before and after veering. x-axis and y-axis represent the position along the length of the beam and the chordwise displacement, respectively. Figures (b), (e), (f), (h) and (j) show the mode shapes of bending vibration while Figures (c), (d), (g) and (i) show the mode shaped of longitudinal vibration.

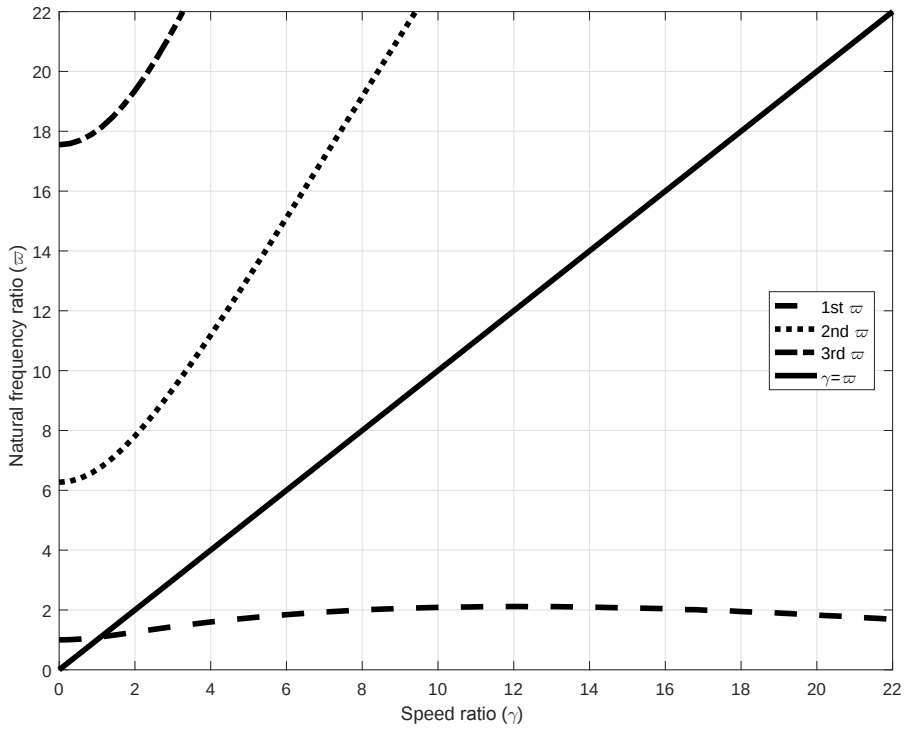

(a) Rotating speed and chordwise natural frequency at $\delta = 0$

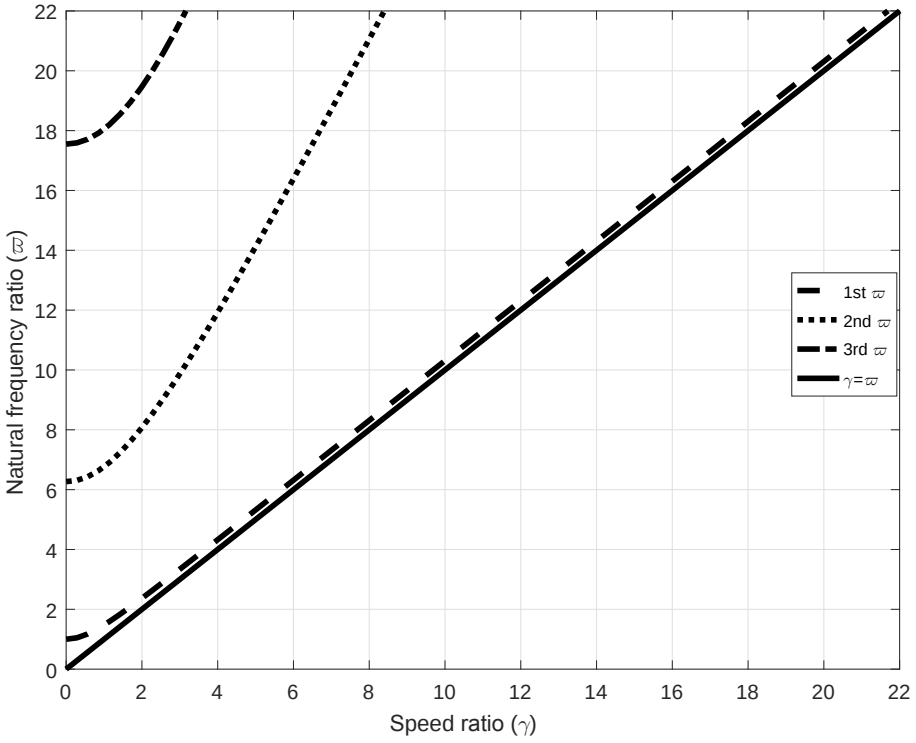

(b) Rotating speed and flapwise natural frequency at $\delta = 0$

Figure 4.8: Natural frequency versus rotating speed at hub ratio $\delta = 0$ showing the critical speed for the chordwise vibration (a), which is not the case in flapwise vibration (b).

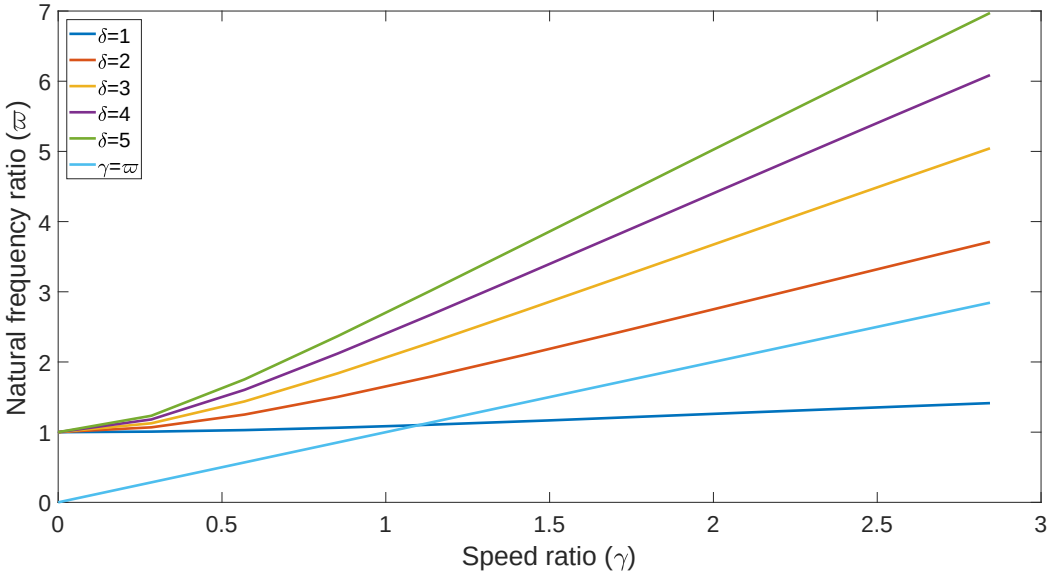

Figure 4.9: The effect of the hub ratio (δ) on the dimensionless chordwise fundamental natural frequency (ϖ) for different rotational speed ratio (γ)

4.2.3 Time and frequency domain analysis

Subsequently, the time domain response of the base harmonically excited for a rotating intact cantilever beam has been calculated for flapwise and chordwise vibration, as shown in Figures 4.10 and 4.11, respectively. It can be seen in the first initial part of the time domain response that the beam undergoes a transient response, whilst the second part shows the beam has reached steady state response. In addition, the direct frequency response was calculated and is shown in Figure 4.12 for flapwise vibration and Figure 4.13 for chordwise vibration. These simulation results were calculated for a rectangular cross section beam with specifications $L = 300\text{mm}$, $b = 15\text{mm}$, $h = 2\text{mm}$, $\rho = 2770\ \text{kg/m}^3$, $E = 7.1 \times 10^{10}\text{Pa}$ and applying Rayleigh damping for the first two lower frequencies, assuming $\zeta = 0.01$ as a damping ratio. Figure 4.14 shows the results of the frequency response calculated from a transfer function with harmonic input and from the time domain by using 'ode45' function in MATLAB with step sine input. The symbols (*) refer to the step sine response in the time domain using the amplitude of the steady state results for each excited frequency.

Figures 4.15 and 4.16 show the effect of the rotational speed on the lowest three natural frequencies of the flapwise and chordwise mode of the cantilever beam respectively. Increasing the rotational speed leads to an increase in the natural frequency of the rotating cantilever beam, due to the centrifugal force, which increases the stiffness of the beam (as was shown in the second term of the equation (3.40)). However, this increase in the chordwise natural frequency is less than shown previously due to the cross sectional profile (2mm width and 15mm hight for the chordwise versus 15mm width and 2mm height in flapwise) and the gyroscopic effect of the chordwise motion.

The response amplitude increases or decreases, for the particular excitation frequency, depending upon the closeness or remoteness of the excitation frequency from the resonance frequencies. For example, Figure 4.17 shows the time domain response for the free end of a rotating intact cantilever beam, when the base excitation frequency is 10Hz. Increasing the rotational speed from 0 rpm to 1000 rpm helps to reduce the vibration amplitude. This is because the increase in the natural frequency increases the separation between the excitation frequency and the resonance.

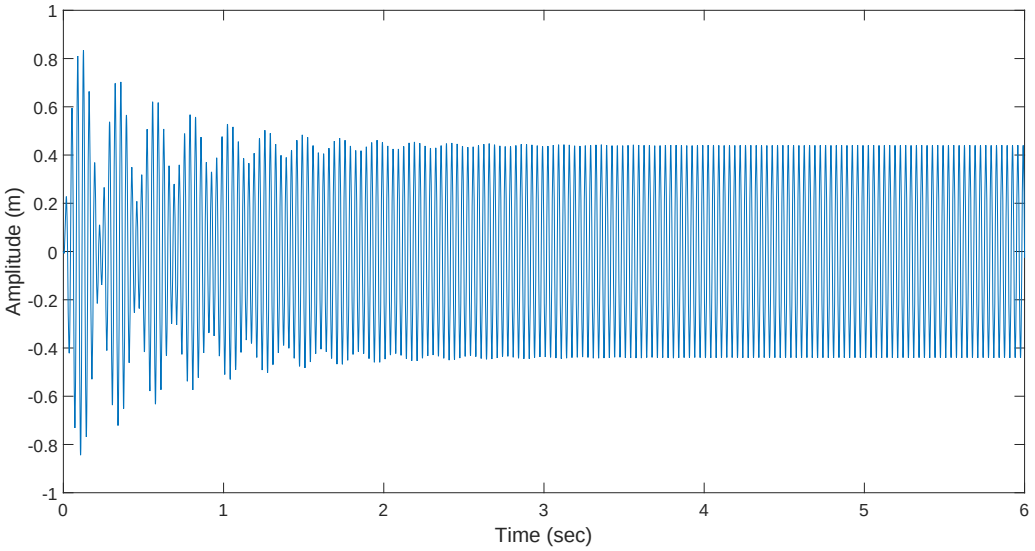

Figure 4.10: Time domain response of the free end of a flapwise vibration beam for a 30Hz flapwise base excitation and 1000 rpm rotating speed.

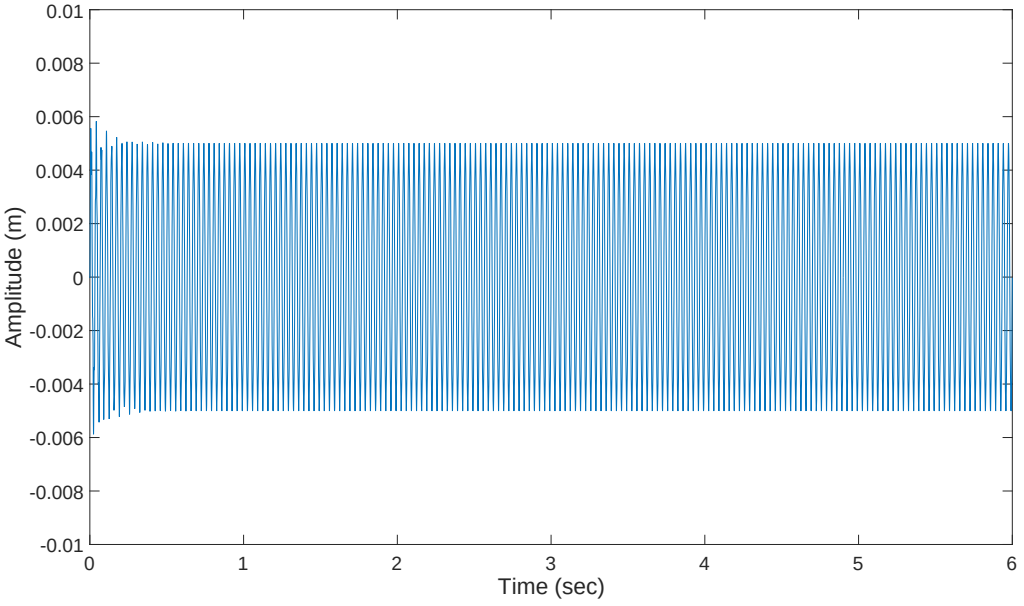

Figure 4.11: Time domain response of the free end of a chordwise vibration beam for a 30Hz chordwise base excitation and 1000 rpm rotating speed.

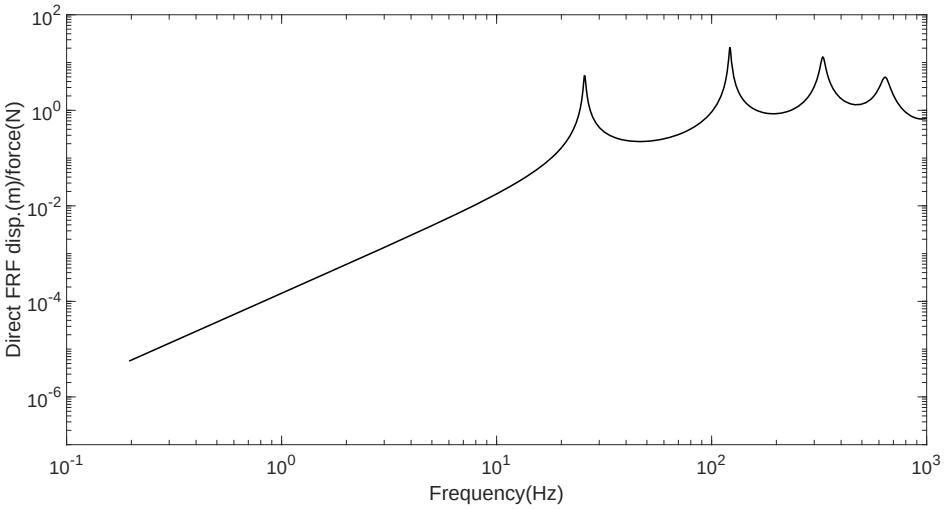

Figure 4.12: Frequency response for the flapwise vibration of the free end of the rotating cantlever beam at 1000 rpm.

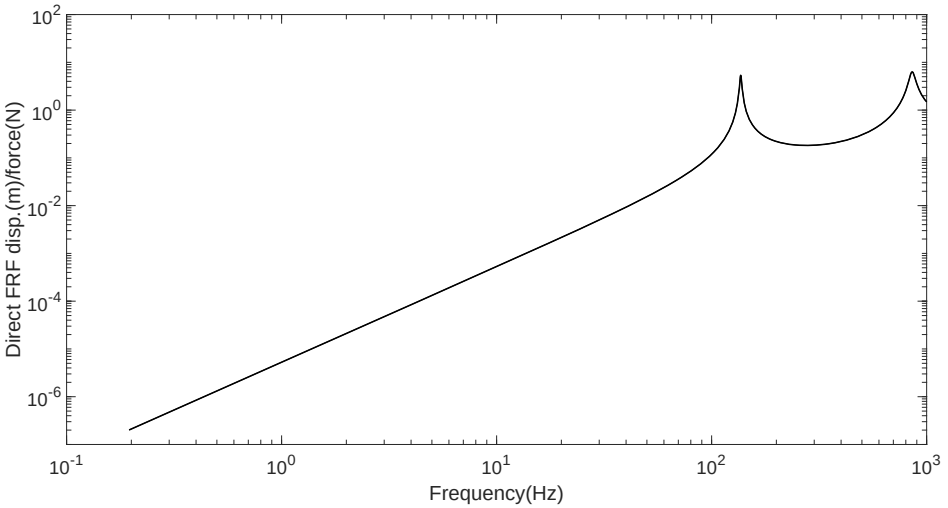

Figure 4.13: Frequency response for the chordwise vibration of the free end of the rotating cantilever beam at 1000 rpm.

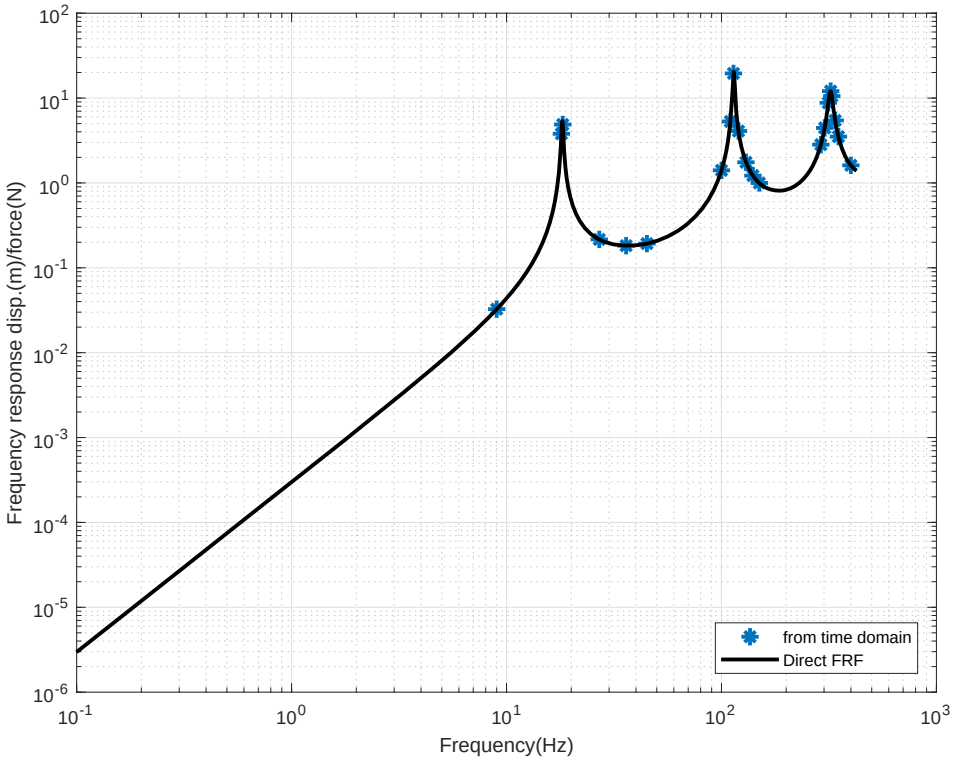

Figure 4.14: Frequency response of the free end of the uncracked rotating cantilever beam. The black solid line represents the direct FRF, where the blue stars represent the amplitude of the steady state response calculated from the time domain response.

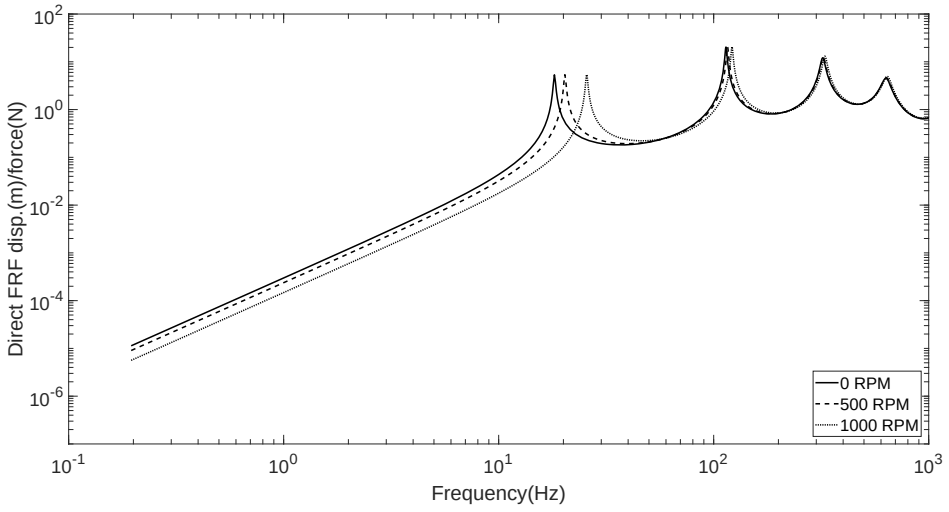

Figure 4.15: Frequency response for the flapwise of the free end of a base excited uncracked cantilever beam for different rotational speeds. Increased rotational speed leads to an increase in the resonance frequencies.

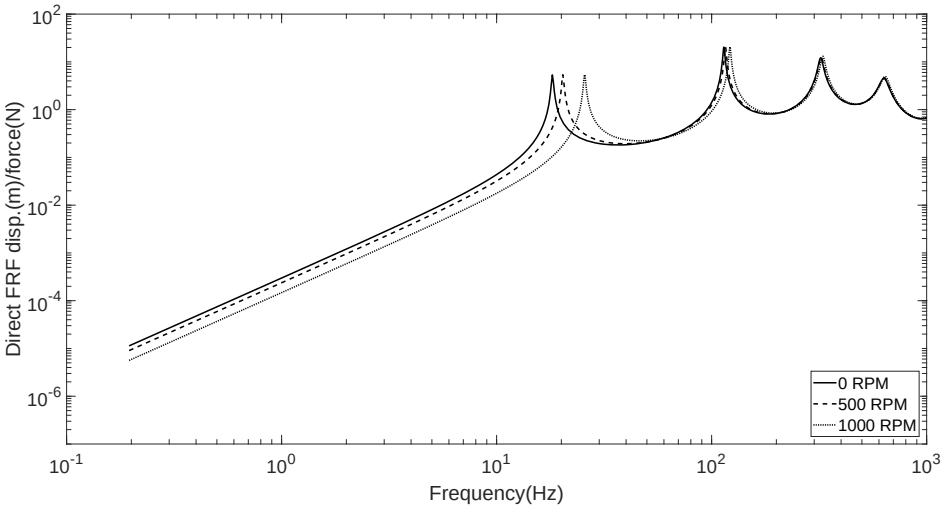

Figure 4.16: Frequency response for the chordwise of the free end of a base excited uncracked cantilever beam for different rotational speeds. Increased rotational speed leads to an increase in the resonance frequencies

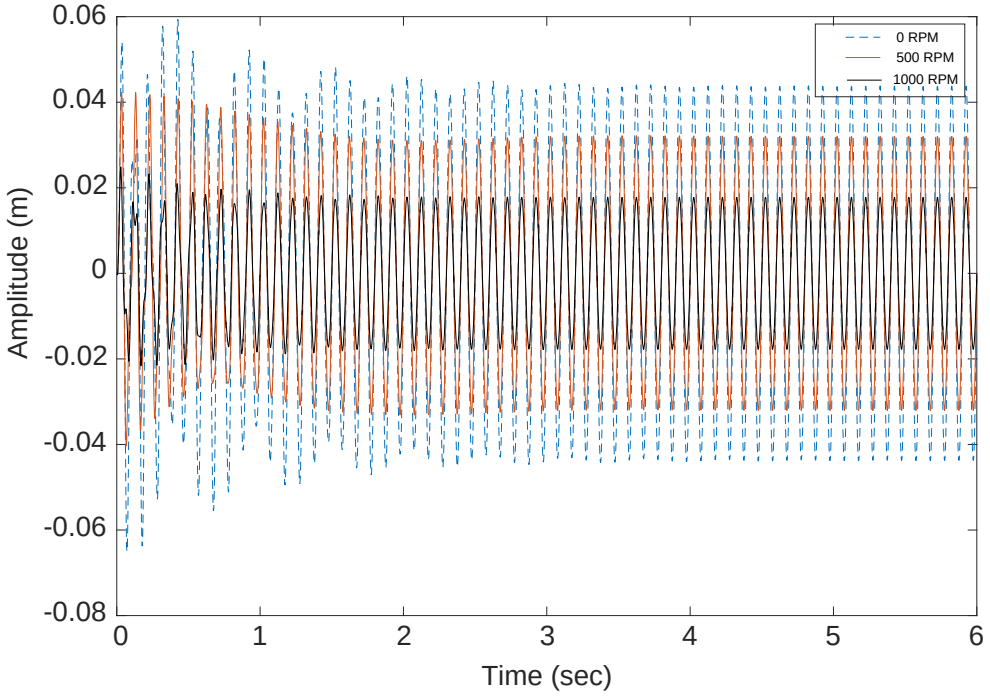

(a) Time domain response of a rotating uncracked cantilever beam at non-rotating, 500 and 1000 rpm respectively, when excited by a base excitation at 10Hz.

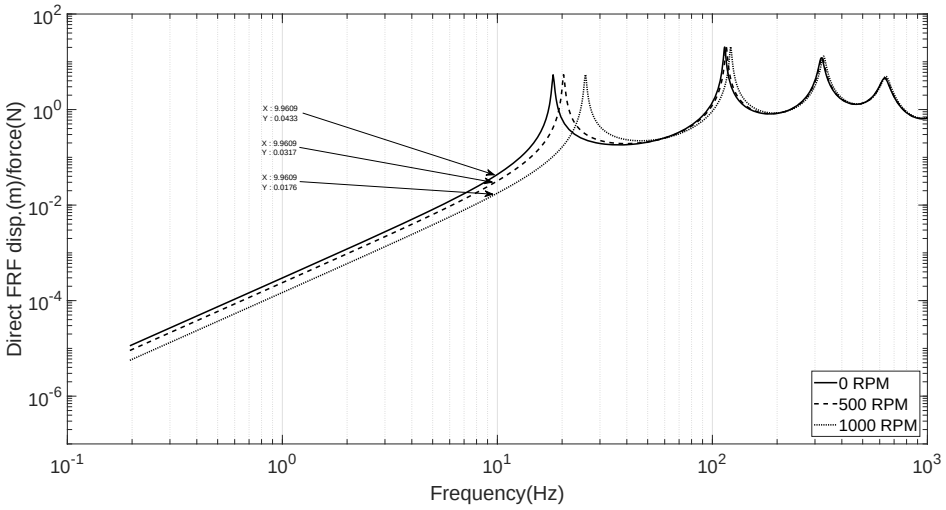

(b) Frequency response of the free end of a base excited uncracked cantilever beam for different rotational speeds. Increase in rotational speed leads to an increase in the natural frequencies. In addition, the increase in the speed caused a reduction in the response amplitude for the 10Hz base exitation, due to a shift in the resonance frequency.

Figure 4.17: Time and frequency domain for the flapwise rotating beam with base excitation.

4.3 Beam with a crack using the finite element method

A finite element model of a cracked beam was simulated using the formulation given in equations (3.71) and (3.72). The cracked beam model utilizes a cantilever beam with a crack on a single edge. In order to compare the results, a solid finite element model was assembled in a commercial FE code ANSYS. The model is presented in Figure 4.18. In Figure 4.19 the numerical simulations are shown for the beam with a crack at its midpoint for two different crack depths. The two set of results for the natural frequencies are in excellent agreement.

There are numerous factors that affect the natural frequencies related to cracks, for example, the depth of the crack, its location and the orientation of the crack according to the direction of the loads (see Ibrahim et al. (2013)). Figure 4.19 shows that when the crack depth is equal to half the beam thickness, i.e. $a = h/2$, the dimensionless natural frequencies for a crack at the root of the beam drops to 0.78, while for a crack depth less than $a = h/3$ the frequency ratio is about 0.91. A deeper crack leads to a greater reduction in the frequency than a shallow one because of the additional flexibility, as expected.

Examining the effect of the crack location, it appears that when the crack is close to the root of the beam, i.e. close to the end, which is attached to the hub, the effect of the crack becomes more significant and conversely this effect reduces when the crack is closer to the free end. This results from the bending moment being greatest at the fixed end. In addition, the crack effect vanishes or is negligible at some frequencies when it is located at a node of the higher order modes. This becomes evident in the results for the second and higher modes. Table 4.8 shows the agreement between the present work and an ANSYS FE model using solid elements. The maximum percentage error is 0.33% for the fundamental natural frequency at $\gamma = 0$ and 0.66% for the second natural frequency for the non-rotating beam.

Considering the influence of the two main parameters, the crack location and the rotational speed in one graph Figure 4.20, where one can observe a clear picture of how the crack reduces the natural frequency. In addition, it can give a pre-estimation of the possible crack location. To assist the identification of the crack location the results are shown using the same two parameters in a 3D plot of the second relative natural frequency as shown in Figure 4.21.

Utilizing the fundamental natural frequency chart in Figure 4.20 side by side with the second natural frequency in Figure 4.21, a better estimation of the crack location can be provided when the crack occurs in the second half of the beam, where the fundamental frequency has a low sensitivity to the crack location. Figures 4.22 and 4.23 clearly show the sensitivity of the two lowest natural frequencies of a rotating beam with respect to the crack location for a fixed rotational speed.

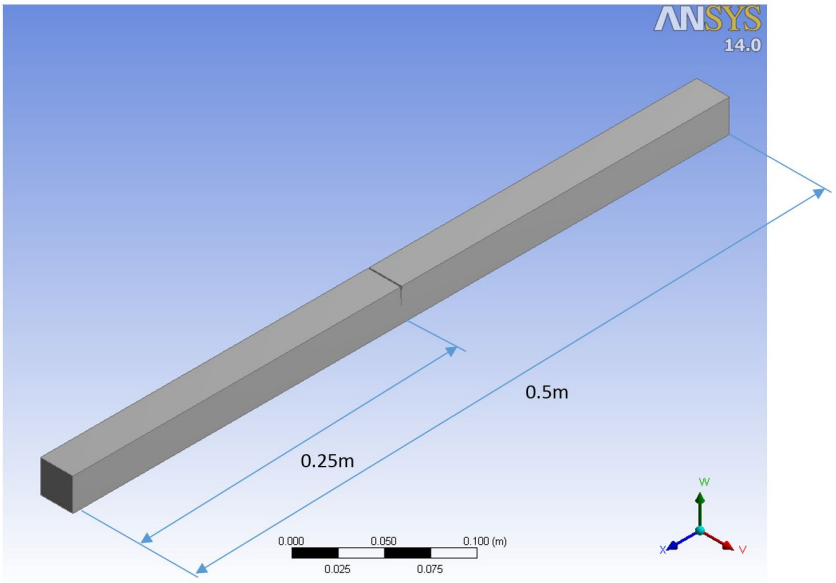

Figure 4.18: A FE model of a cracked beam

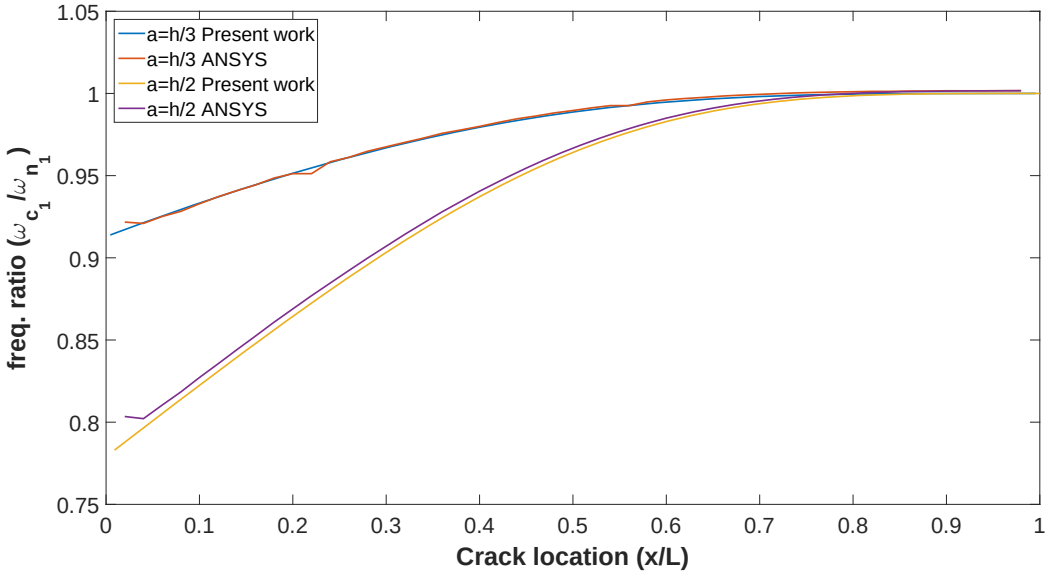

Figure 4.19: Comparison between the present FE work and an ANSYS FE model (solid elements) for the fundamental frequency ratio of the cracked non-rotating cantilever beam

	1st ϖ			**2nd ϖ**		
γ	**present work**	**ANSYS**	**Error %**	**present work**	**ANSYS**	**Error %**
0.000	0.966	0.969	0.335	5.476	5.512	0.661
0.284	1.016	1.019	0.269	5.526	5.561	0.629
0.569	1.153	1.154	0.136	5.675	5.706	0.542
0.853	1.348	1.350	0.160	5.914	5.937	0.395
1.138	1.579	1.580	0.049	6.232	6.249	0.257
1.422	1.830	1.829	0.023	6.619	6.626	0.113
1.706	2.092	2.091	0.070	7.061	7.060	0.026
1.991	2.362	2.359	0.105	7.549	7.538	0.150
2.275	2.636	2.632	0.134	8.073	8.052	0.262
2.560	2.913	2.908	0.163	8.626	8.595	0.360
2.844	3.191	3.185	0.189	9.202	9.161	0.445

Table 4.8: Comparison between the present work and an ANSYS FE model for a single edge cracked rotating beam. The dimensions of the beam are 0.5m, 0.0247m and 0.0247m for the length, height and base, respectively. The crack is located at the middle of the beam with depth equal to 0.5 of the height of the beam.

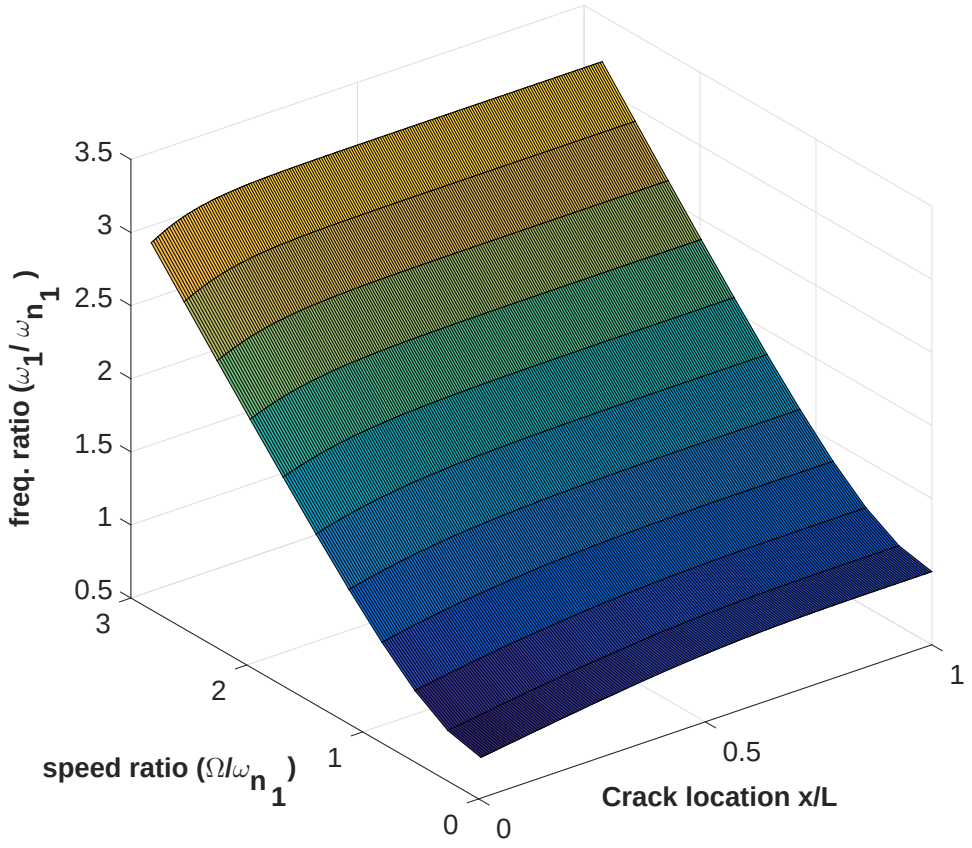

Figure 4.20: The first natural frequency ratio as a function of the crack location and rotational speed. The crack depth a is half of the beam thickness i.e. $a = h/2$

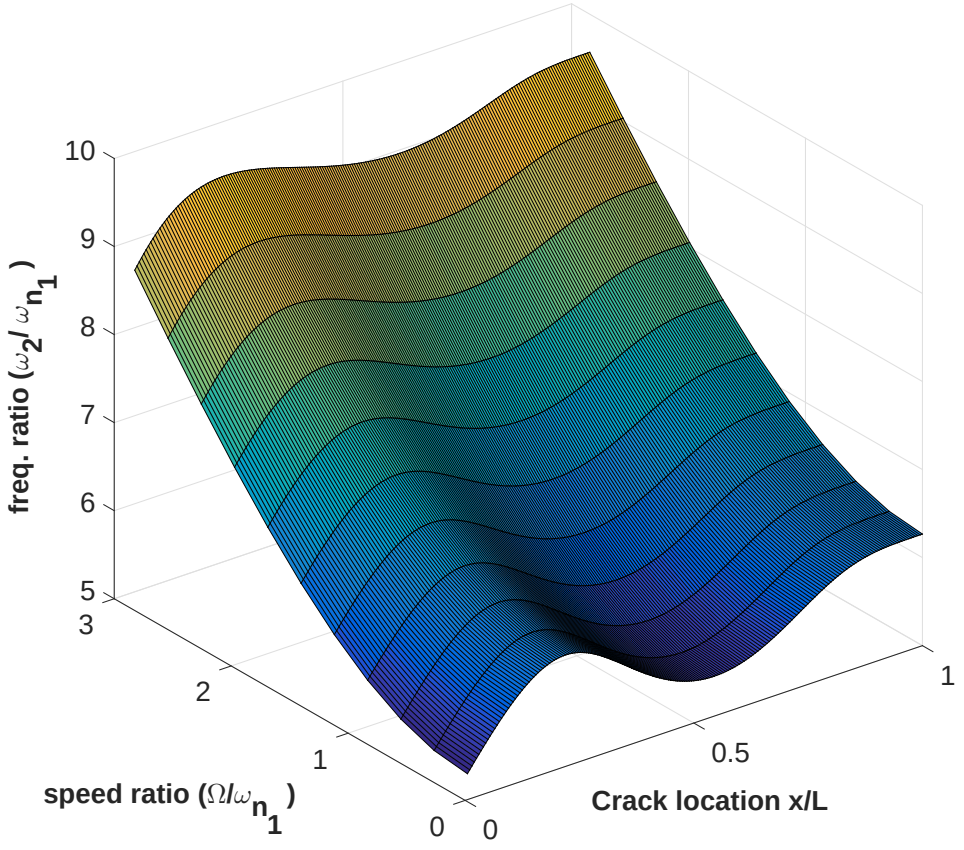

Figure 4.21: The second natural frequency ratio as a function of the crack location and rotational speed. The crack depth a is half of the beam thickness $a = h/2$

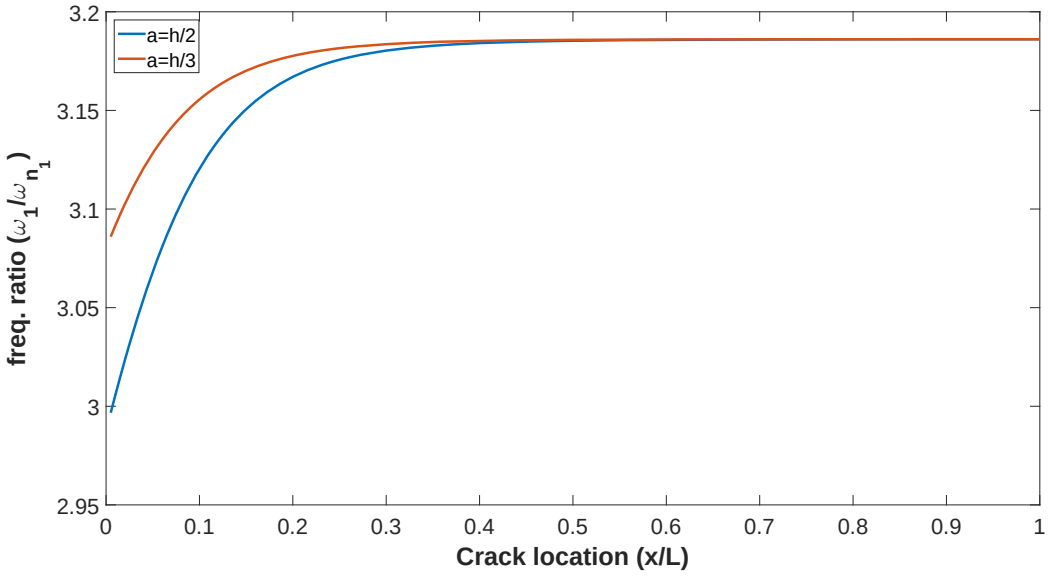

Figure 4.22: The effect of the crack's depth and location on the first natural frequency ratio. The dimensionless speed $\gamma = \Omega/\omega_{n_1} = 2.844$ for the two crack depths.(red line: $a = \frac{h}{3}$), (blue line: $a = \frac{h}{2}$).

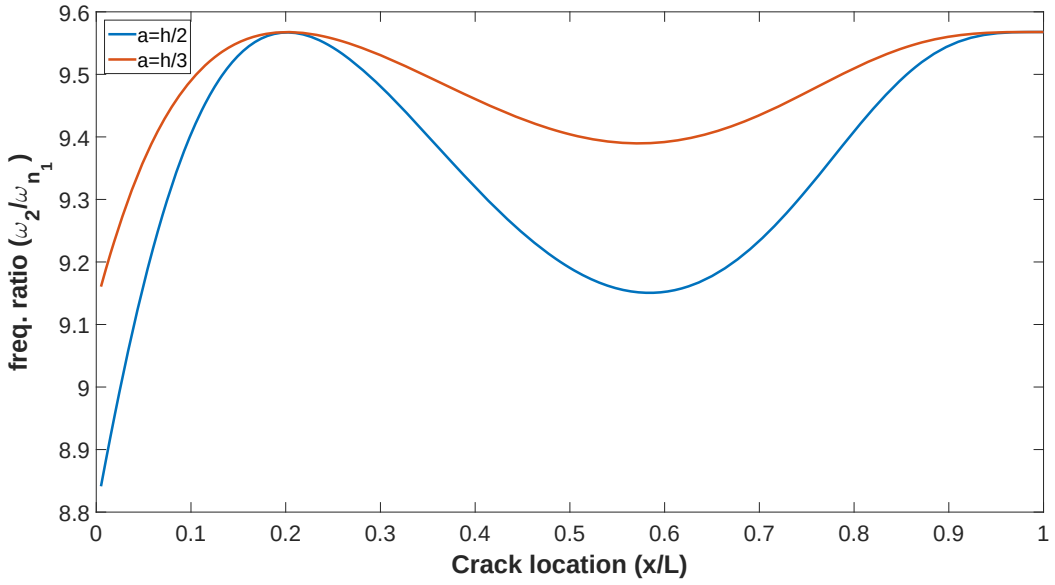

Figure 4.23: The effect of the crack's depth and location on the second natural frequency ratio. The dimensionless speed $\gamma = \Omega/\omega_{n_1} = 2.844$ for the two crack depths.(red line: $a = \frac{h}{3}$), (blue line: $a = \frac{h}{2}$).

4.4 Beam with an open crack modelled using the Rayleigh Ritz method

The numerical results for the newly developed simple model are compared with the previously illustrated FE model in section 4.3. The results are also compared with a solid 3D element model assembled and solved using ANSYS. The solid model was built using a mesh of hexahedral solid elements (3073 nodes and 1453 elements) with a fine sized mesh around the crack tip as shown in Figure 4.24. The frequency ratio for the natural frequencies of the rotating cracked beam for different fixed rotational speeds against the fundamental frequency of the uncracked beam are shown in Figure 4.25. The natural frequencies all increase as the rotational speed increases. The estimated values using the Rayleigh-Ritz method show good agreement with the values from the one dimensional FE model with a maximum error less than 0.5% in the third mode.

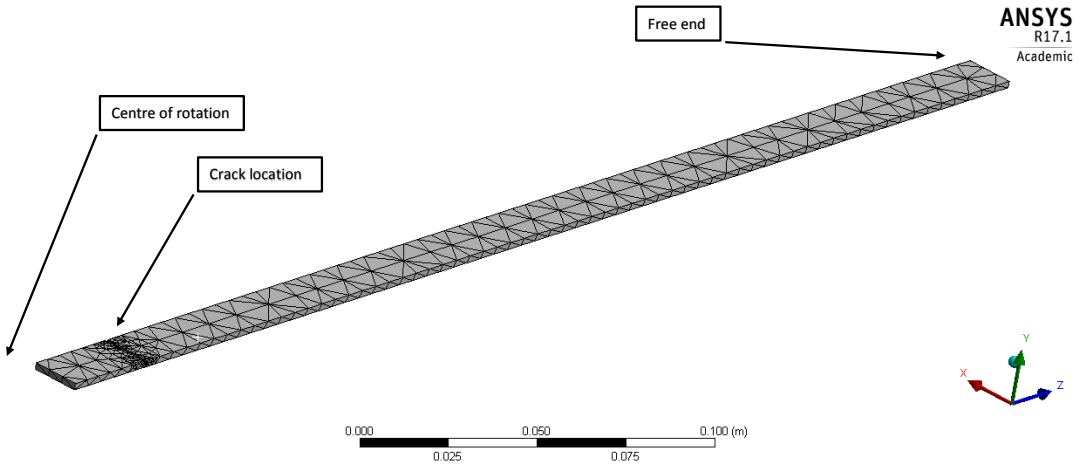

Figure 4.24: Rotating cracked cantilever beam modelled using 3D hexahedral FE elements in ANSYS.

Figure 5.7 shows the effect of the crack location on the natural frequencies of the rotating beam. The closer the crack is to the hub supporting the cantilever beam, the greater the reduction in the natural frequencies. Moreover, when the crack is located at a modal node, its effect becomes less evident, as shown for the second and third modes in Figure 5.7. The maximum error occurs in the first mode when the crack is located at the root (fixed end) of the rotating beam.

In addition to the natural frequency comparison, the mode shapes of the cracked rotating blades were evaluated and compared with the corresponding modes using the finite element model. Figures 4.27 show the Modal Assurance Criterion (MAC) between the results of the present work and the one dimensional FE model. The diagonal white squares indicate the good agreement between the mode shapes using the two approaches.

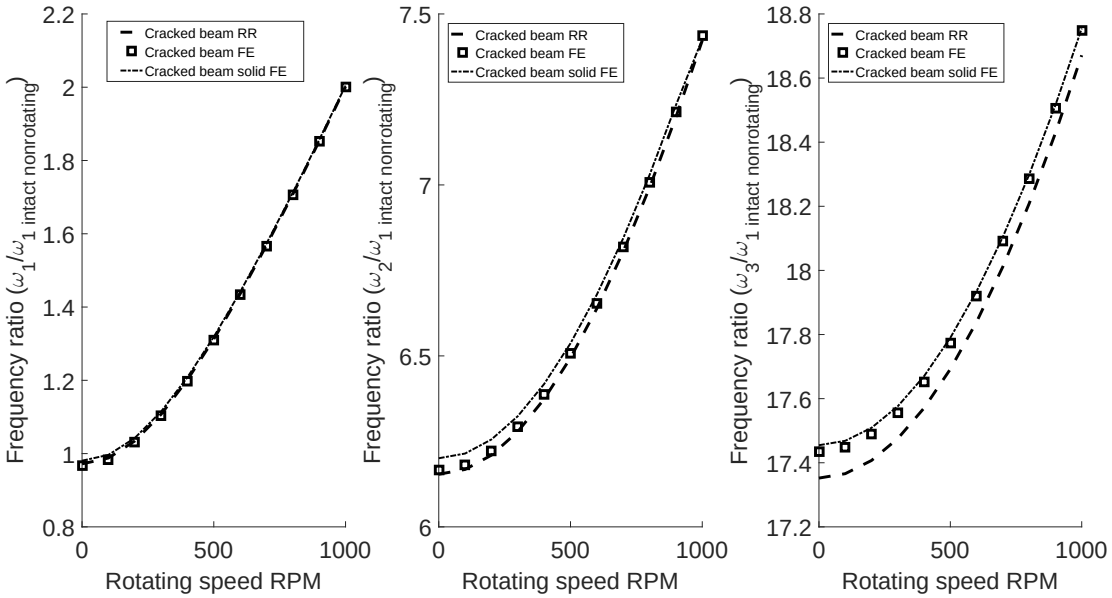

Figure 4.25: Lowest three flapwise natural frequencies of a rotating cracked beam versus the rotational speed. Crack location ratio is 0.075 of the beam length, crack depth ratio is 0.5 of the beam thickness. The maximum error is about 0.5% in the third mode.

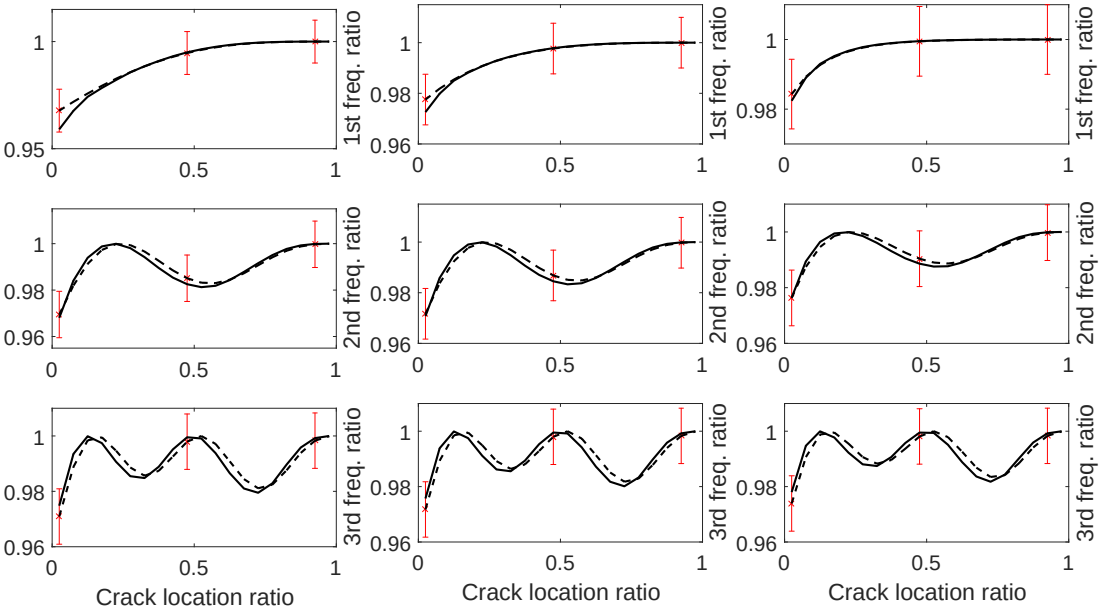

Figure 4.26: Frequency versus crack location as a ratio of crack position divided by beam length for the lowest three flapwise frequencies of a rotating cracked beam, for three different rotational speeds ((a) non-rotating, (b) for 500 rpm and (c) for 1000 rpm) and crack depth ratio ξ is 0.5. Solid and dashed lines refer to the proposed method and FEM results, respectively. The error bars are 1% difference.

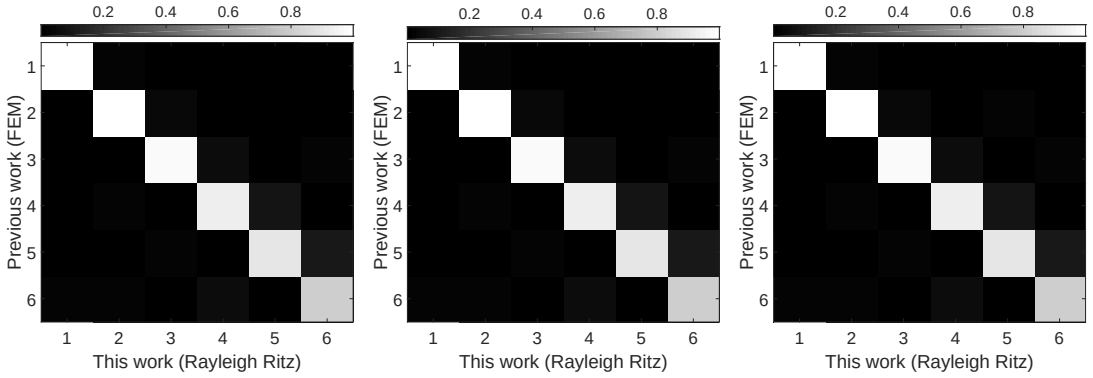

(a) (b) (c)

Figure 4.27: MAC diagrams for the lowest six modes from FE and the Rayleigh Ritz method the flapwise vibration of the rotating cracked beam. The crack location ratio is 0.075 and the crack depth ratio is 0.5 and rotational speeds (a) non-rotating, (b) 500 rpm and (c) 1000 rpm.

Regarding chordwise vibration, similar comparison was made for the lowest three natural frequencies with a model built using one-dimensional beam finite elements Yashar et al. (2016) and a solid finite element model using ANSYS. The frequency ratio between the natural frequency of the rotating cracked beam for different fixed rotational speeds against the fundamental frequency of the uncracked beam are shown in Figure 4.28. The estimated values using the Rayleigh-Ritz method show good agreement with the values obtained from one dimensional FE models having a maximum error of less than 0.77% in the third mode.

Furthermore, the crack location versus the natural frequency was compared in the chordwise vibration with the FE model and shows good agreement with a maximum error less than 1% for the at first natural frequency when the crack is close to the root of the cantilever beam. Likewise, the mode shapes of the chordwise vibration cracked rotating beams were evaluated and compared with the corresponding modes produced from the finite element model. Figure 4.30 shows the Modal Assurance Criterion (MAC) between the results of the proposed method and the FE model. The diagonal white squares indicate the good agreement for the mode shape matching between the two approaches.

Figure 4.31 shows the flapwise and chordwise natural frequency ratios versus rotational speed for the same cross sectional dimensions and identical crack location and depth. The chordwise vibration shows less sensitivity to the rotational speed than the flapwise vibration, due to the gyroscopic coupling effect in the chordwise vibration.

The coupling between bending and longitudinal displacements in the chordwise plane leads to a veering phenomena in the natural frequency versus rotational speed graph as can be seen in Figure 4.32. In the third lowest natural frequency, the bending chordwise mode natural frequency veers to become a stretch mode at the speed of 5900 rpm. The fourth is veering from bending to stretch at a rotational speed of 3800 rpm, then veering

from stretch to bending again at a speed 5900 rpm. A similar phenomena appears in the fifth to seventh natural frequencies at the rotational speeds of 2800, 2050 and 1450 rpm respectively.

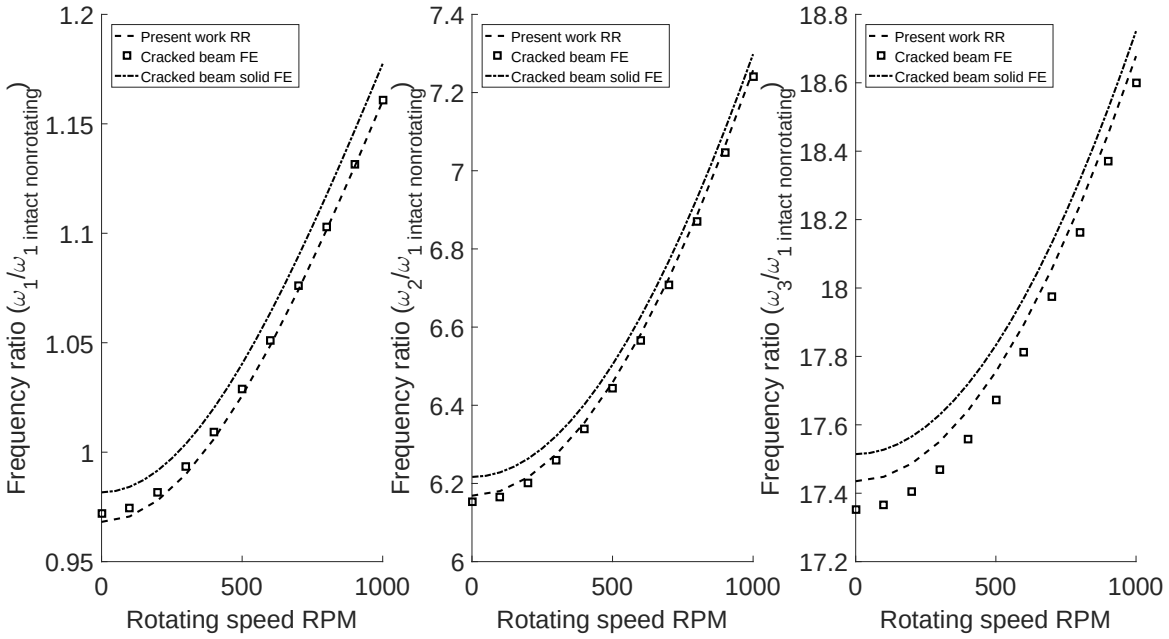

Figure 4.28: Lowest three chordwise natural frequencies of a rotating cracked beam versus the rotational speed. The crack location ratio is 0.075 of the beam length, the crack depth ratio is 0.5 of the beam thickness. The maximum error is about 0.77% in the third mode.

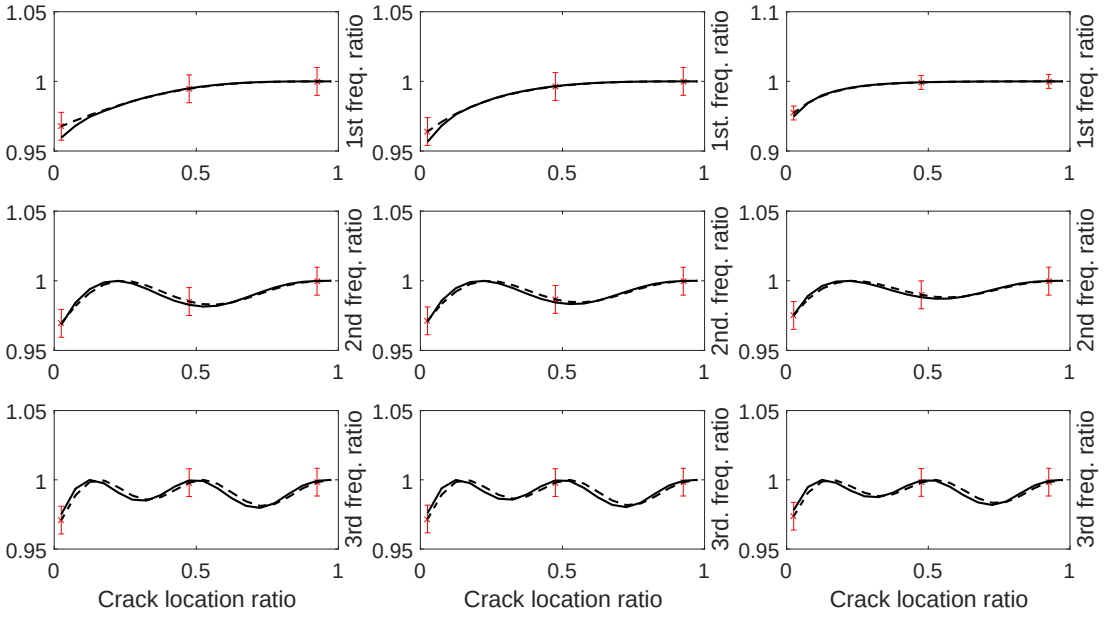

Figure 4.29: Natural frequency versus crack location for the lowest three chordwise natural frequencies of a rotating cracked beam at three different rotational speeds ((a) non-rotating, (b) for 500 rpm and (c) for 1000 rpm) and crack depth ratio ξ is 0.5. Solid and dashed lines refer to the proposed method and FEM respectively. The error bars are of 1% difference.

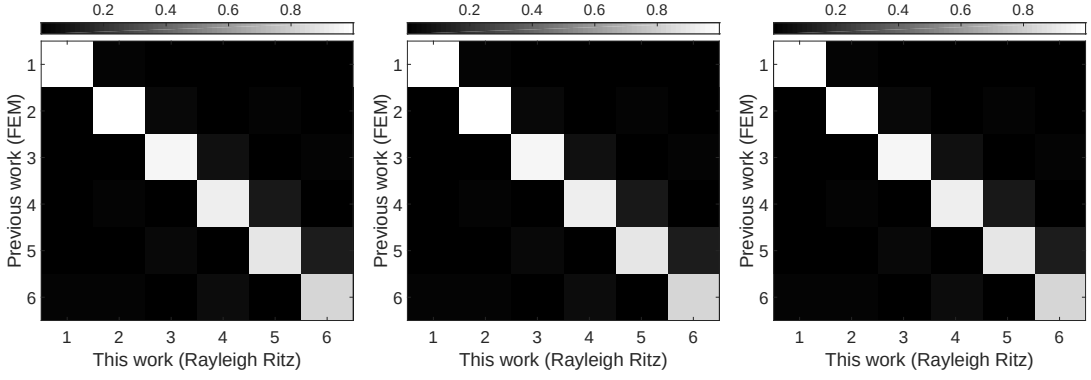

Figure 4.30: MAC diagrams for the lowest six modes of the chordwise vibration of the rotating cracked beam. The crack location ratio is 0.075 and the crack ratio is 0.5 and rotational speeds (a) non-rotating, (b) 500 rpm and (c) 1000 rpm.

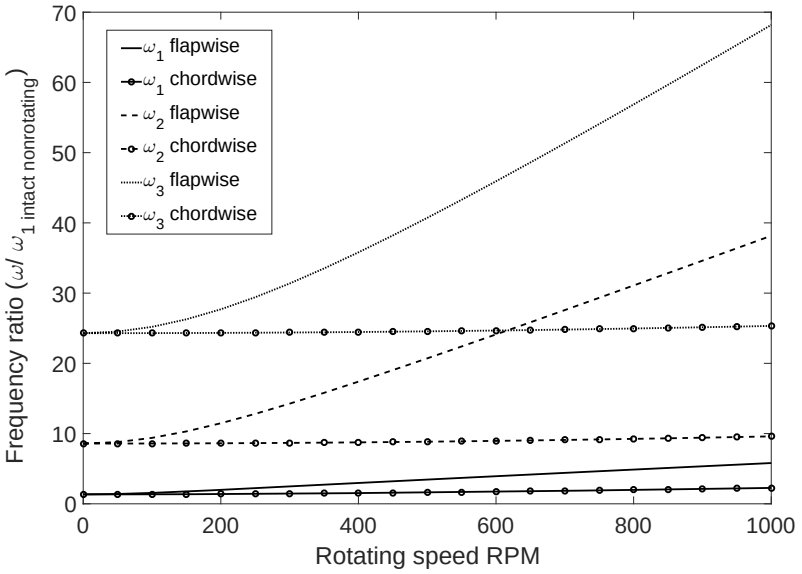

Figure 4.31: Lowest three flapwise and chordwise natural frequencies of a rotating cracked beam versus the rotational speed of the same cross sectional dimension. The crack location ratio is 0.075 and the crack depth ratio is 0.5

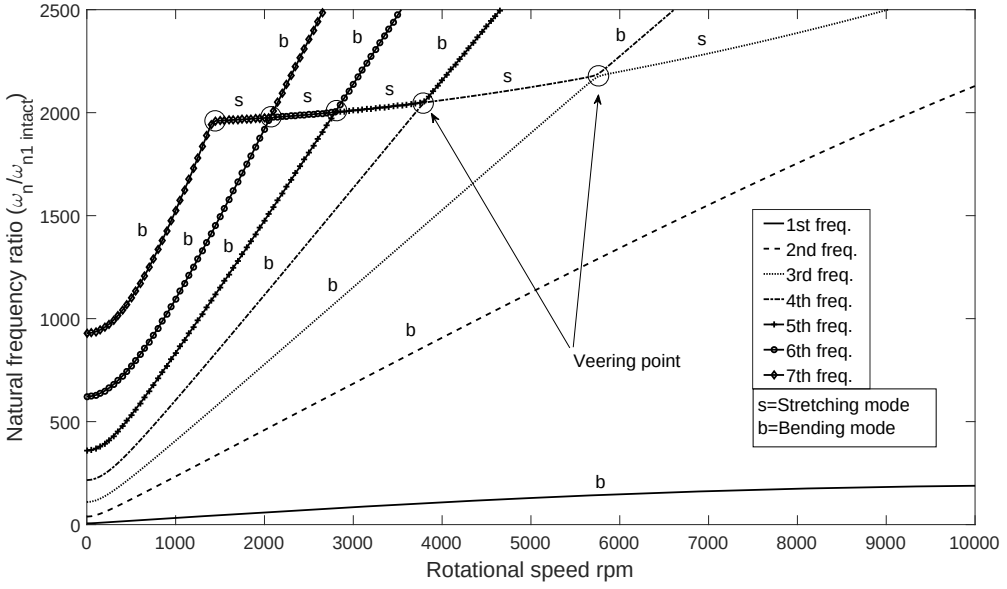

Figure 4.32: The veering of the bending and stretching natural frequencies at high rotational speed in the chordwise plane for the rotating cracked beam. The seven lowest natural frequencies are shown, where s represents stretching and b represents bending modes. The crack location ratio is 0.075 of the beam length and the depth ratio is 0.5 of the beam thickness.

4.5 Beam with a breathing crack (Bilinear crack)- an alternative formulation

A breathing crack is also often described as being a fatigue, closing crack or bilinear crack Vigneshwaran and Behera (2014); Yan et al. (2013); Andreaus et al. (2007); Chatterjee (2010); Friswell and Penny (1992). It is a type of crack, which changes its stiffness according to the load applied to the structure. For example, when the crack is under a tensile load, it is fully open and the beam has minimum bending stiffness, conversely when the crack is subjected to a compression load, it is fully closed and the beam behaves as an intact system. The behaviour in the fundamental mode of a beam with a breathing crack can be representing as a SDOF system as illustrated in Figure 4.33 below.

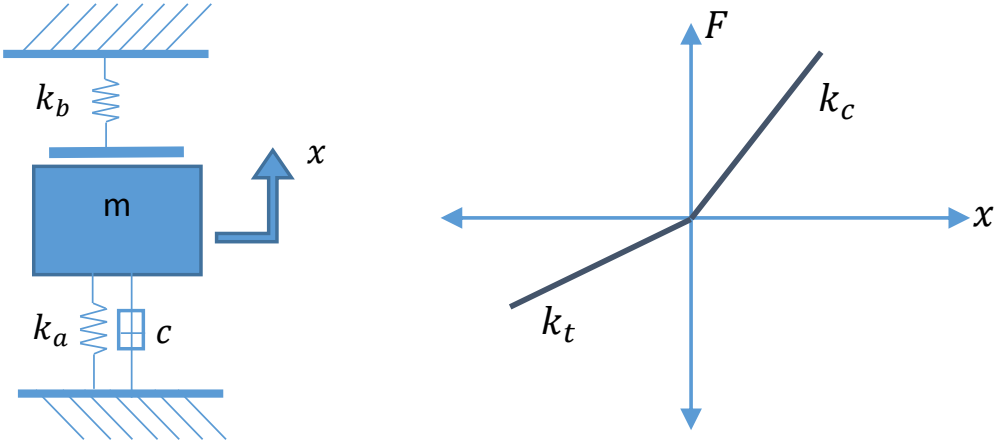

Figure 4.33: SDOF bilinear system, where $k_c = k_a + k_b, k_t = k_a$.

When the displacement is positive, i.e. $x \geqslant 0$, the equivalent stiffness of the system is equal to the total stiffness $k_c = k_a + k_b$. In contrast, the stiffness of the system is equal to $k_t = k_a$ which represents the stiffness of the system,

$$m\ddot{x} + c\dot{x} + k_t x = 0, x \geqslant 0 \tag{4.3}$$

$$m\ddot{x} + c\dot{x} + k_a x = 0, x < 0 \tag{4.4}$$

According to this definition, the frequency of the free vibration of the mass and hence beam is changing during one half cycle of oscillation between ω_1 and ω_2, where $\omega_1 = \sqrt{\frac{k_t}{m}}$ and $\omega_2 = \sqrt{\frac{k_a}{m}}$. The bilinear frequency of the system can be calculated by finding the time of one complete cycle of the period of oscillation, which is the combination of the upper half cycle and lower half cycle as shown in Figures 4.34 and 4.35 below.

$$t_1 = \frac{2\pi}{\omega_1}, t_2 = \frac{2\pi}{\omega_2}, \tag{4.5}$$

$$\omega_{bilinear} = \frac{2\pi}{t_{bilinear}} \tag{4.6}$$

$$= \frac{2\omega_1\omega_2}{\omega_1 + \omega_2} \tag{4.7}$$

$\omega_{bilinear}$ represents the bilinear frequency of the system Yan et al. (2013); Douka and Hadjileontiadis (2005)

Regarding the response in the frequency domain, a significant difference between the opening and the closing stiffness leads to multiple harmonic frequencies, which can be used in detecting bilinear cracks. For example, a frequency response for a SDOF system should have one peak, which represents the resonance of the system. However, when the bilinear effect occurs, harmonic frequencies will appear in the frequency domain in addition to the main resonance frequency of the system, as can be seen in Figure 4.36.

Due to the non-linear effect, the procedure to extract the step frequency response in Figure 4.36 was based on applying a sine displacement excitation on the base and evaluating the displacement response. Then, the amplitude of the main response frequency is obtained by using a single term Fourier series fit of the time domain after removing the transient duration. These steps are repeated at the different excitation frequencies starting from 0.005 Hz to 1 Hz. Also, the response is obtained at different excitation amplitudes corresponding 0.01, 1, 50 and 100 mm.

This type of bilinear pattern, known as a homogeneous system, where the response amplitude is proportional to the amplitude of the input excitation. For example, Figure 4.36 shows the response of a nonlinear system for the various input amplitudes and the ratio between the output and the input is remained fixed.

The same principle for representing the cracked rotating cantilever beam with a bilinear crack, that behaves as either fully opened or as fully closed during vibration according to the direction of motion of the beam was investigated and shown in Figure 4.37, (see Bovsunovsky and Surace (2015)).

Figure 4.39 shows the base excitation FRF comparison of a rotating intact cantilever beam with a linear open crack and breathing crack. The bilinear curve lays in between the frequency behaviour of the open crack and the intact beam frequency curves. The first resonance frequency for the intact beam, with open crack and beam with bilinear crack are approximately 25.66Hz, 25.23Hz and 25.5, respectively. Obviously, the bilinear frequency for the first resonance follows equation (4.7). However, this result does not reveal the harmonic frequencies of the bilinear crack due to the small effect of the crack. A significant bilinear crack most likely causes several harmonic frequencies, as can be

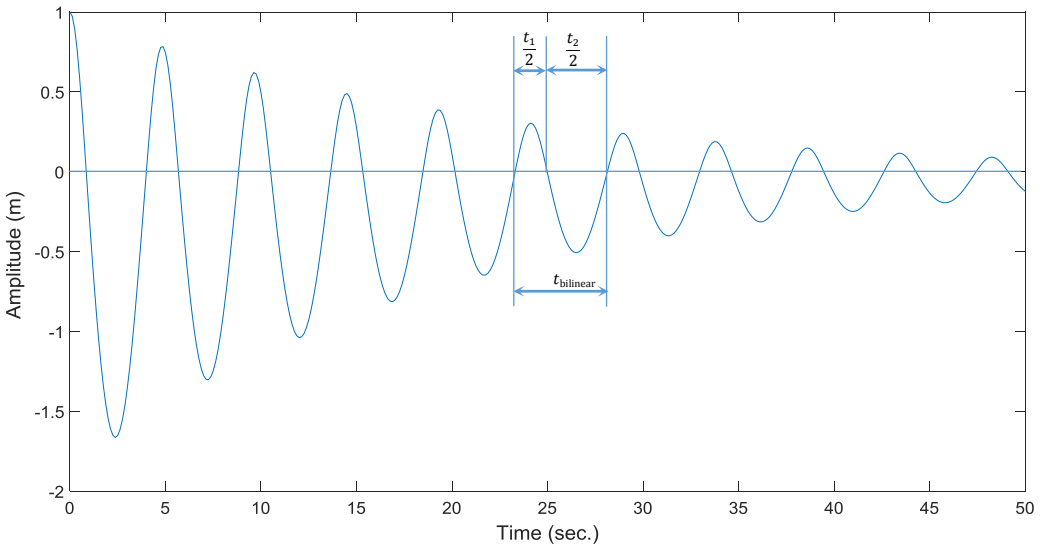

Figure 4.34: SDOF bilinear system under free vibration.

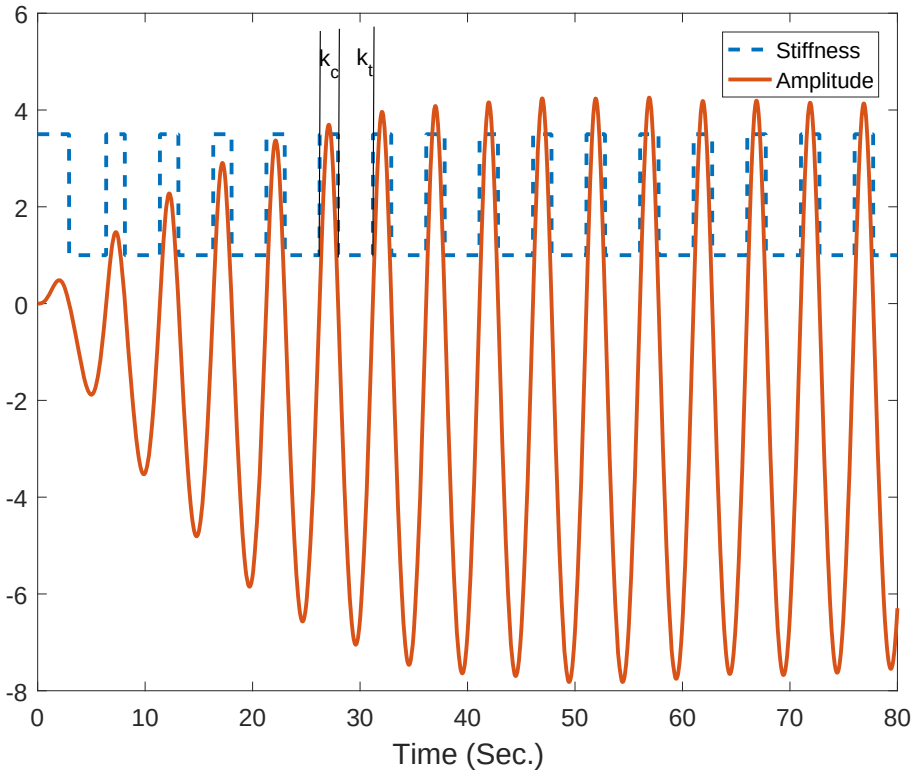

Figure 4.35: Blue and orange lines represent the stiffness and amplitude of a bilinear SDOF system respectively.

seen in Figure 4.39. The first resonance occurs at about 39.5Hz, which leads to a harmonic at 79Hz which is twice the fundamental frequency.

Comparison of the time domain response of the free end of a rotating cantilever beam for an intact, open cracked and bilinear cracked is shown in Figure 4.40. Obviously, the

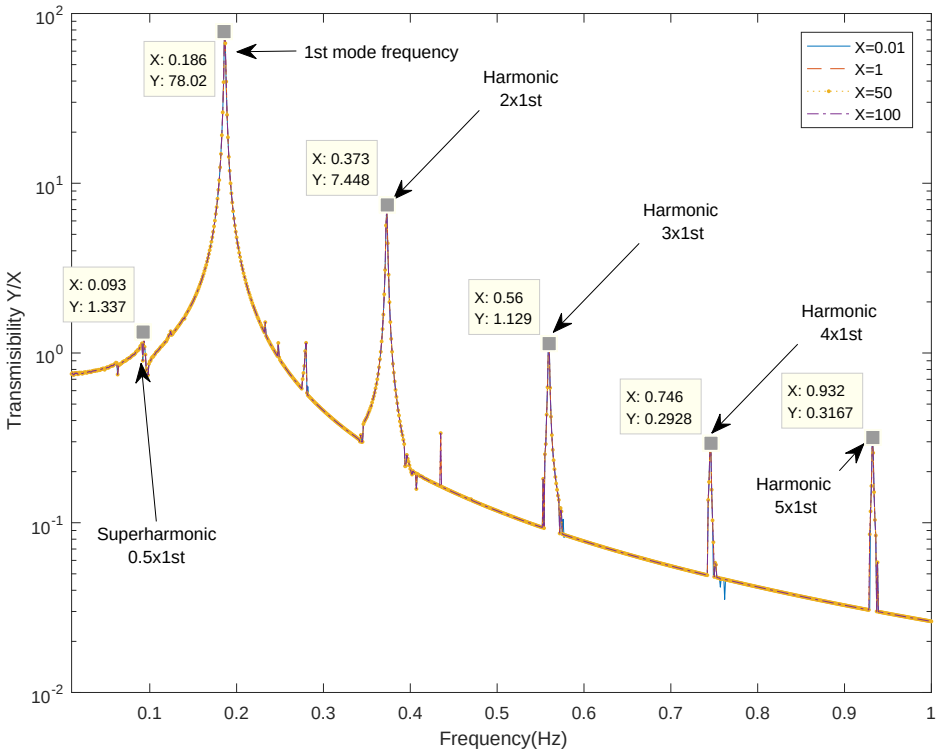

Figure 4.36: SDOF bilinear system frequency response function for base excitation. This system vibrates with several harmonics generated from the bilinear stiffness. However, the output amplitude is directly related to the input amplitude. The amplitude of the frequency response remains unaltered for various input amplitudes. This figure is the simulation of simple mass spring system response to the base excitation where X represents the displacement of the the base and Y is the displacement of the mass. This result is obtained from the time domain. The mass, stiffness of open crack, stiffness close crack and damping are 1 Kg, 1 N/m, 2 N/m and 0.01 N.s/m, respectively.

bilinear crack shows unsymmetrical displacement around the static equilibrium position.

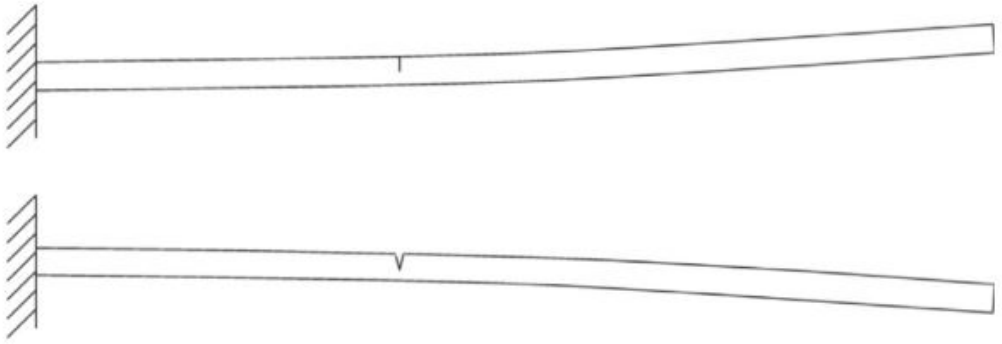

Figure 4.37: A Cantilever beam with breathing crack. According to the direction of motion, the state of the crack switches between fully opened of fully closed. Bovsunovsky and Surace (2015)

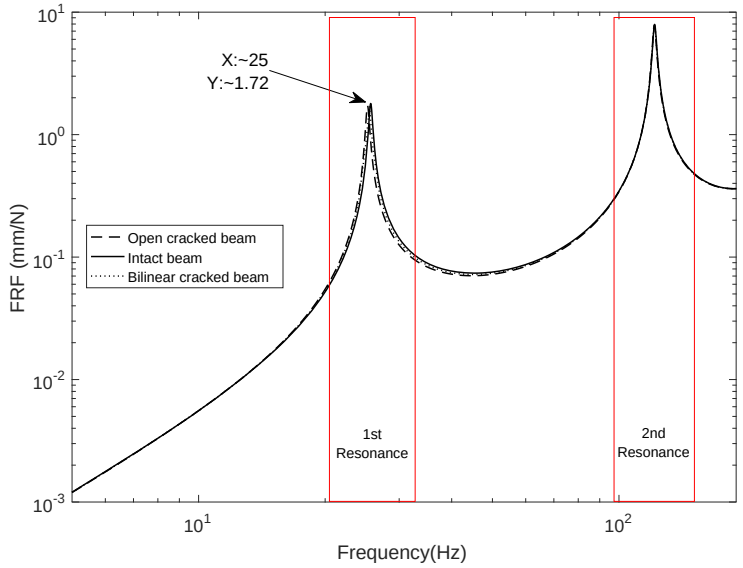

Figure 4.38: Comparison of the FRF for three types of rotating cantilever beam. The first curve is for an intact beam, the second curve for a beam with an open crack and the third for a beam with breathing crack. The bilinear crack FRF is obtained from time domain simulation of the forced base vibration. All three FRFs are determined for the rotating cantilever with a free end. The beam dimensions are 300mm, 15mm and 2mm for the length, width and thickness, respectively. and the rotational speed is 1000 rpm. The crack is located at 0.25 of the beam length from the root and the depth is in 0.55 of the beam thickness.

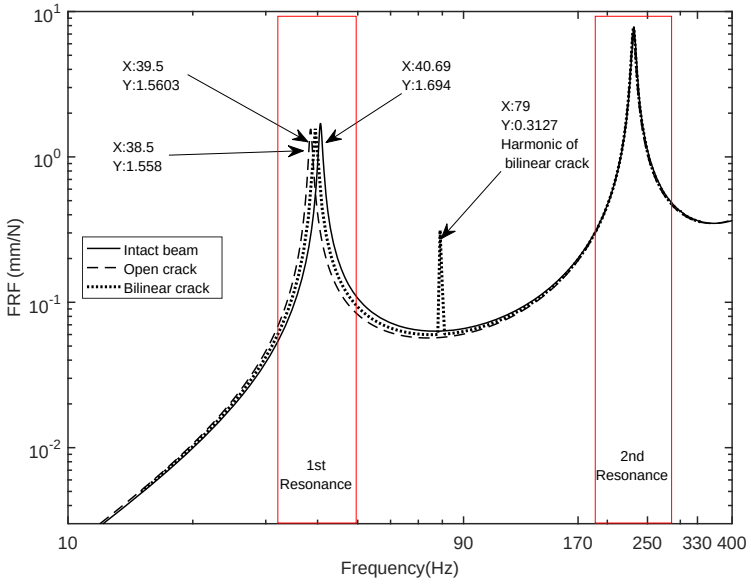

Figure 4.39: Comparison of the FRF for three types of rotating cantilever beam. The first curve for an intact beam, the second curve for a beam with an open crack and the third for a beam with a breathing crack. The bilinear crack FRF is obtained from the time domain simulation of the forced base vibration. All the three FRFs are determined for the rotating cantilever with a free end. The beam dimensions are 300mm, 15mm and 4mm for the length, width and thickness, respectively and the rotational speed is 1000 rpm. The crack is located at 0.25 of the beam length from the root and the depth is in 0.55 of the beam thickness.

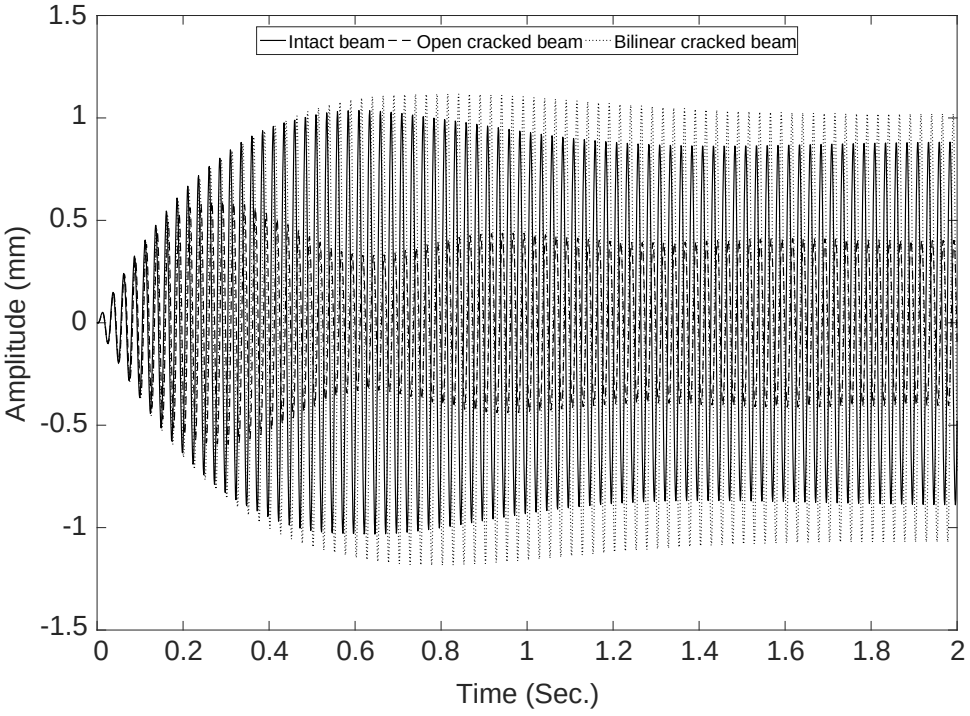

Figure 4.40: Time domain response comparison for an intact beam, beam with an open crack and a beam with a bilinear crack displacement at the free end of the rotating cantilever beam. Rotational speed=1000 rpm and the base excitation is at 40Hz. The crack located at 0.25 of the beam length from the root and the depth in 0.55 of the beam thickness.

4.6 Conclusions

The simulation of rotating beam with and without crack were presented and discussed in this chapter using both the finite element and Rayleigh-Ritz methods. The effect of various parameters on the natural frequencies are illustrated such as rotating speed, hub ratio and slenderness ratio. In addition, the critical points of the system are identified for example the critical speed, buckling speed and veering phenomena. Furthermore, the effect of cracks are investigated at various positions and depth. To sum up the following conclusions can be drawn from the present results:

Flapwise motion:

- The natural frequencies monotonically increase with increasing rotational speed.
- No critical angular speed arises, where the critical speed is reached when any natural frequency equals the rotational speed.
- An increase in the hub ratio increases the natural frequencies.

Chordwise motion:

- The natural frequencies do not increase monotonically due to the gyroscopic coupling.
- A critical rotational speed can occur i.e. the fundamental natural frequency of the rotating beam becomes equal to the rotational speed frequency.
- The existence of a buckling speed is evident, when the natural frequency of the beam reduces to zero with increasing the rotational speed.
- Slenderness and hub ratio have a significant effect on the critical rotational speed, since the thinner beam tends to bend more than stretch.

Cracked beam vibration:

- The crack location has a significant effect on the natural frequencies. The closer the crack is to the hub, the lower are the natural frequencies.
- There is an inverse relationship between the crack depth and the natural frequency.
- When a crack is located at one of the nodes of vibration of a particular mode then the frequency of that mode is unaffected.
- Treating a bilinear crack as an open crack could be lead to an underestimation of the depth of the crack. The bilinear crack reveals shallow depth if it considered as an open crack.

- The appearance of superharmonic and subharmonic in the frequency domain could be an indication of bilinear crack existence on the beam.
- The natural frequency of a bilinear cracked beam lies between the natural frequency of an open cracked beam, with the same dimension and depth, and the natural frequency of the identical but intact beam.

Finally, the results of the new simplified model for a rotating cracked beam was compared with both solid and the one dimensional FE model. The new approach was accurate and showed a good agreement, especially for the lowest three modes of the vibration, with FE numerical models using one-dimensional beam and solid elements. The maximum natural frequency error between the method proposed and FE was less than 0.5% for the flapwise and less than 0.77% for the chordwise. Furthermore, the predicted vibration mode shapes matched well with corresponding mode shapes evaluated using the FE model as shown with MAC plots. The bending vibration in the chordwise direction showed less sensitivity to the rotational speed than the bending vibration in the flapwise direction due to the gyroscopic coupling. Moreover, a veering phenomena clearly appeared in the higher natural frequencies for the chordwise vibration due to gyroscopic coupling at high rotational speeds.

The next chapter deals with the experimental vibration measurements for the rotating beam with and without crack using optical sensors and different digital image processing methods to verify the simulation results that were presented in this chapter.

Chapter 5

Experimental setup and results

After modelling of a rotating beam with and without crack in Chapter 3, illustrated by the simulation results in Chapter 4, the numerical results will now be validated experimentally. The results and comparison will then be discussed in detail. Measuring the natural frequencies and the mode shapes of a cracked rotational beam can have challenges, due to potentially the high rotational speed of the beam. Measuring the natural frequencies using wired sensors, such as accelerometers, is difficult to apply in this case. However, using wireless accelerometers can also affect the results due to mass loading. To overcome these problems, a non-intrusive optical method is applied using a high speed camera with the aid of digital image processing. This approach has many advantages; the most significant one is the remote non-contacting acquisition of the data.

In this chapter, first the experimental design will be described in detail. Then, the properties and dimensions of the specimen will be discussed. Next, three methods of digital image processing (DIP), which are namely digital image correlation (DIC), Marker detection and Colour blob detection, will be explained and contrasted to show the advantages and disadvantages of each approach and the suitable corresponding test method. Following this, four different configurations for the camera setup will be discussed. The choice of using speckles or markers also will be highlighted, to demonstrate suitable markers for various image processing techniques.

The experimental test setup for the non-rotating and rotating beam will be explained using the mathematical relationship between the different test parameters, such as optical sensor size, the area of the field of view and image magnification. Then, the experimental results will be processed for different test setups and image processing approaches. The results of the non-rotating beam will be presented first. Three different acquisition systems are validated for the image processing methods with comparison to accelerometer measurements. Subsequently, the results for the rotating beam with and without crack will be presented. Various tests were performed to measure the natural frequencies and mode shapes. In addition, the results will be compared with the model

that was developed in Chapter 3. Finally, the overall results will be briefly listed in the conclusions.

5.1 Experimental design

An experimental test rig was designed incorporating a controllable high rotational speed and vertical base excitation. The foundation of the design should be rigid enough to avoid frequency interference between the specimen and the foundation. To achieve these requirements, a test rig was designed as shown in Figure 5.1. This design comprises four main parts. A steel foundation, a high-speed air-cooled controllable motor, a rotating hub and a rotating beam.

The rotating hub assembly allows the introduction of a vertical excitation to the base of the rotational beam as shown in the Figure 5.2, where the four shafts can slide in the linear bearings. This vertical excitation was achieved using an electrodynamic shaker, which excites the beam in a flapwise direction at its base.

The rotating hub is connected to the high speed motor by a belt to reduce the transmission of vibration generated by the motor. Also, the motor is clamped to the foundation using a 3D printed plastic clamp for the same reason. The motor can provide a speed range between 0-24000 rpm using a variable frequency drive (VFD) to control the rotational speed as shown in Figure 5.3.

This design was optimised using FE vibration analysis in simulation software. The main component of the rig foundation is based on standard mild steel channel 150mm$\times$ 90mm$\times$24mm. These dimensions are fixed. The length of the Bridge, Side1, Side2 and the angle cut of the Side1 and Side2 as shown in Figure 5.1 were selected as variables in the optimisation process. The optimisation used is based on a single calculation of the modes over a matrix of the parameter values. The mechanical drawing and assembly of the Bridge, Side1 and Side2 can be found in Appendix A. The main design is built using SolidWorks, then the geometry file imported into ANSYS software. The mentioned variables lengths are selected as parameter sets (for more information see Chen and Liu (2014)) and the change step in the lengths set to 5 mm, then the lengths obtained from the maximum fundamental frequency. The estimated test beam natural frequencies, covering the fundamental, second and third modes are between 8-500Hz. The fundamental natural frequency of the test rig foundation after optimisation is about 850Hz, which is much higher than the specimens' frequencies. The fundamental mode of the test rig is shown in Figure 5.4.

Furthermore, the test rig was designed and manufactured with a changeable rotating hub mount for different test requirements. Figure 5.5 shows two different applications for the test rig. The camera off the system in Figure 5.5(a) using this test rig to be

used with the variable high-speed camera without considering the size of the camera. Furthermore, this configuration permits the use of an advanced application such as real-time measurement and control. However, using a reflecting mirror limits the array of the measurement points on the beam. This is due to the need for constantly processing rotating images with respect to the camera field of view.

The second configuration in Figure 5.5(b), shows the camera mount on the rotating hub. This configuration is suitable for performing tests with a smaller camera and is more accurate to directly capture the markers. Furthermore, more information can be extracted from the images such as flapwise, chordwise and torsional deflections. However, due to limited space for the camera, the acquisition images are recorded in the memory of the camera and are then post processed after performing the test.

The technical information and mechanical draw of the test rig design can be found in the appendix A.

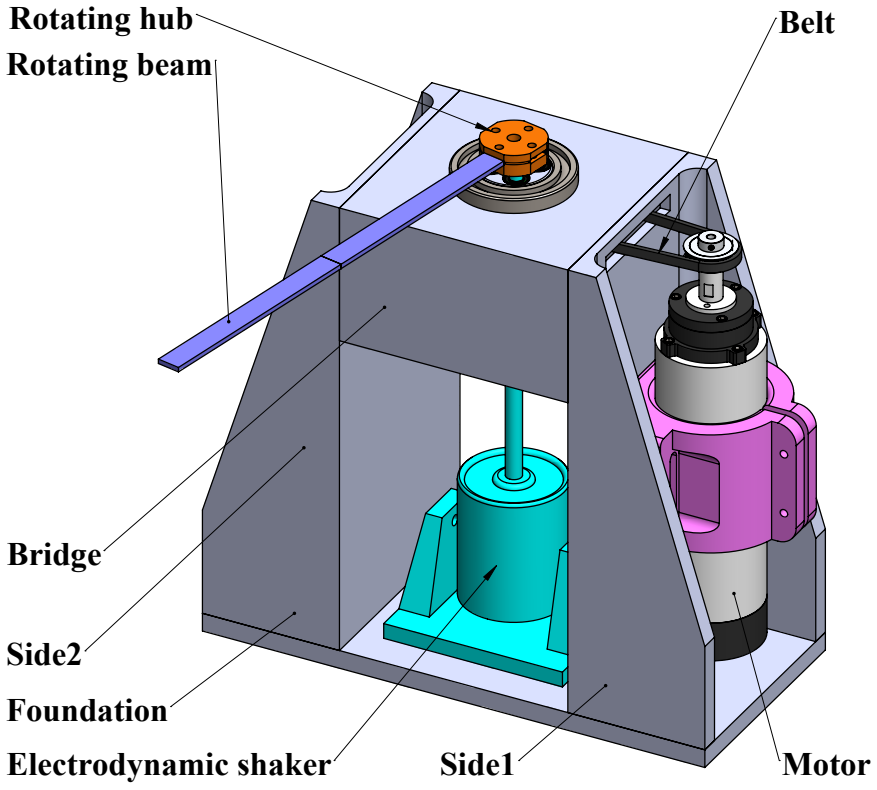

Figure 5.1: Experimental test rig

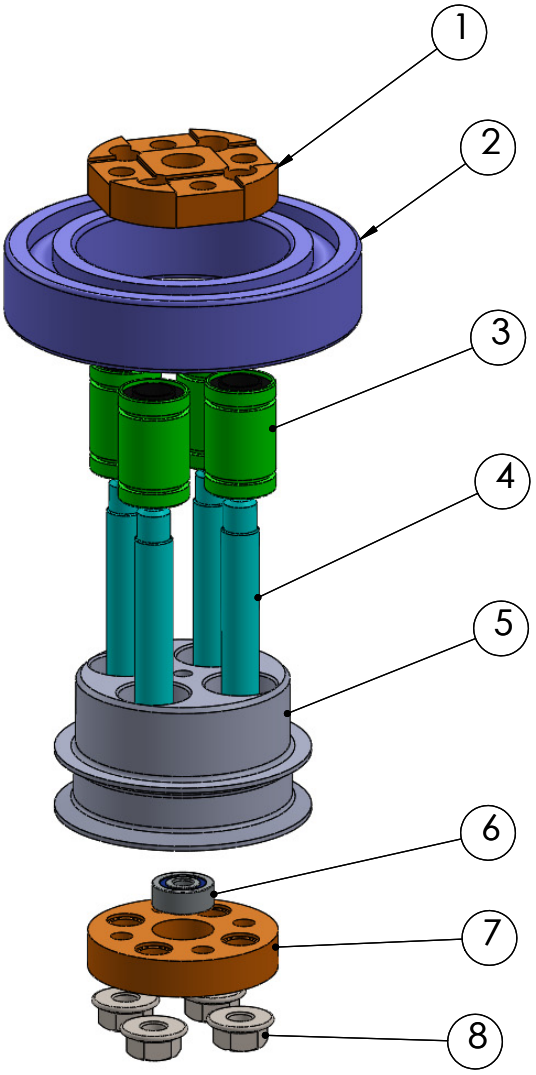

Figure 5.2: Rotating hub assembly

1. Main cover to clamp the beam,
2. Main rotational ball bearing "6009/C3" (high speed),
3. Linear bearings LM8UU,
4. Sliding shafts 8mm,
5. Linear bearing holder,
6. Small ball bearing (to connect with shaker),
7. bottom cover,
8. M6 nuts.

Figure 5.3: 0.8kw er11 air-cooled spindle motor and 1.5kw inverter drive "variable frequency drive (vfd)".

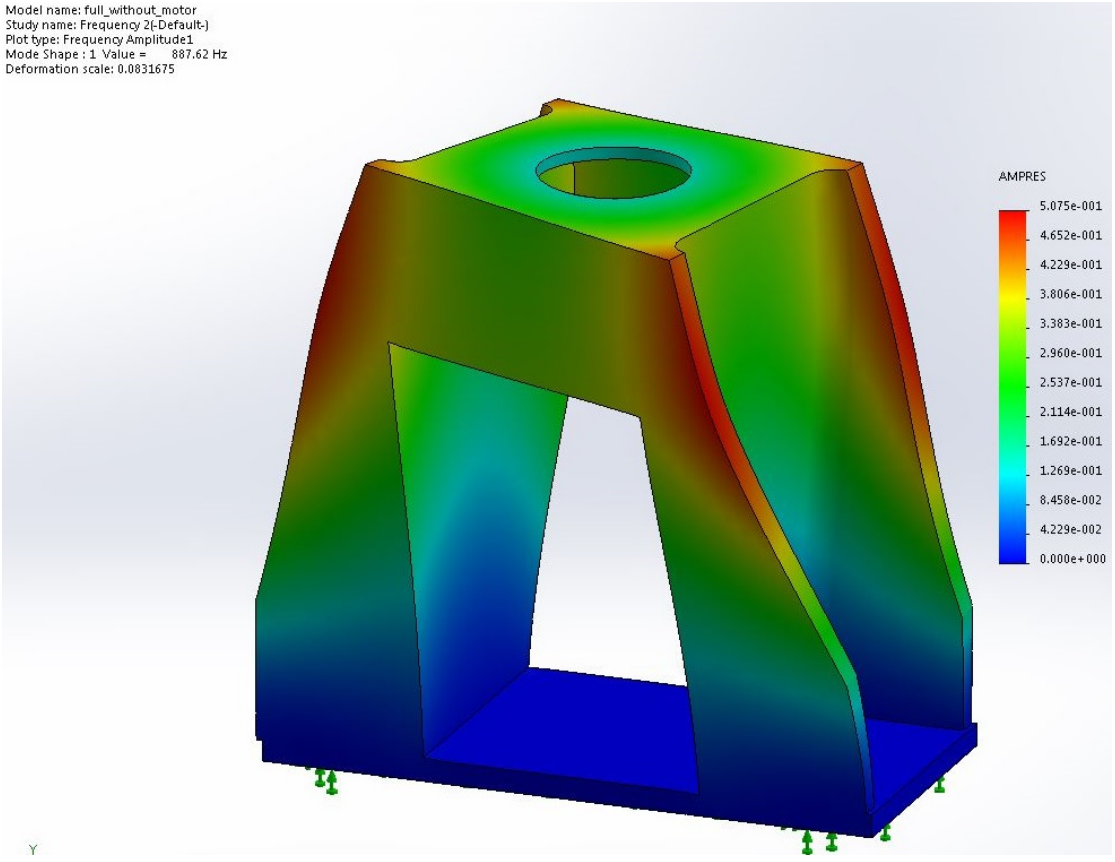

Figure 5.4: Fundamental natural frequency of the experimental test rig foundation.

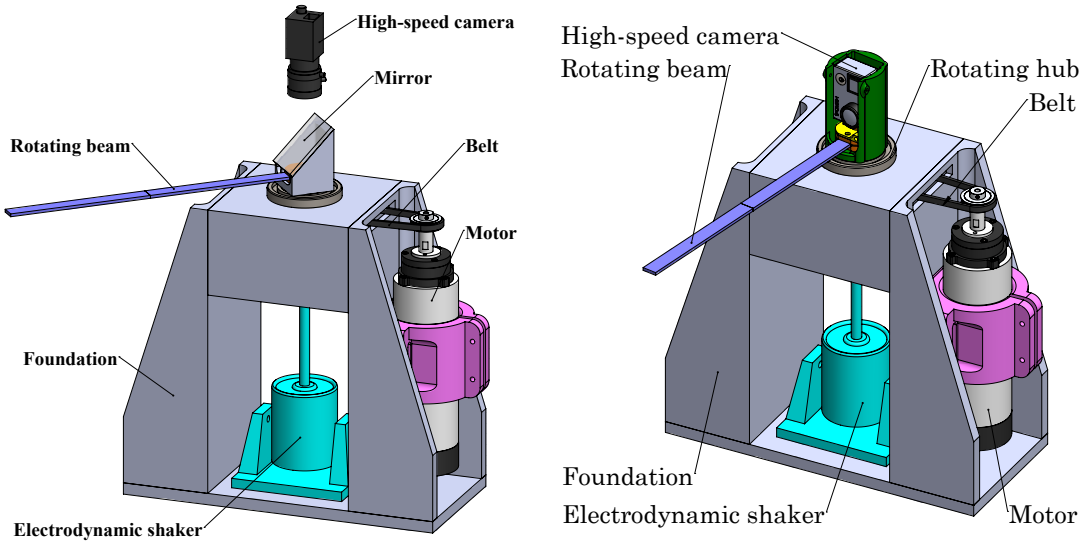

(a) (b)

Figure 5.5: The test rig with two different test configurations. (a) the test rig with a single camera and a reflecting mirror and (b) the test rig with an on hub camera

5.2 Specimen properties

Three specimens of different lengths were used in the tests. The specifications of these specimens are listed in Table 5.1, together with the three natural frequencies. These dimensions were selected to prevent interference between the vibration of the specimen and the rig. Moreover, the length of the beams was selected based on the size of the camera sensor.

Specimen	No.1	No.2	No.3	No.4	Units
Width	15	15	15		mm
Thickness	2	2	2		mm
Length	400	330	300		mm
Material	Aluminium	Aluminium	Aluminium		
1st freq	10.2		18.2		Hz
2nd freq	64.0		113.8		Hz
3rd freq	179.3		318.8		Hz

Table 5.1: Cantilever specimen dimensions and predicted natural frequencies.

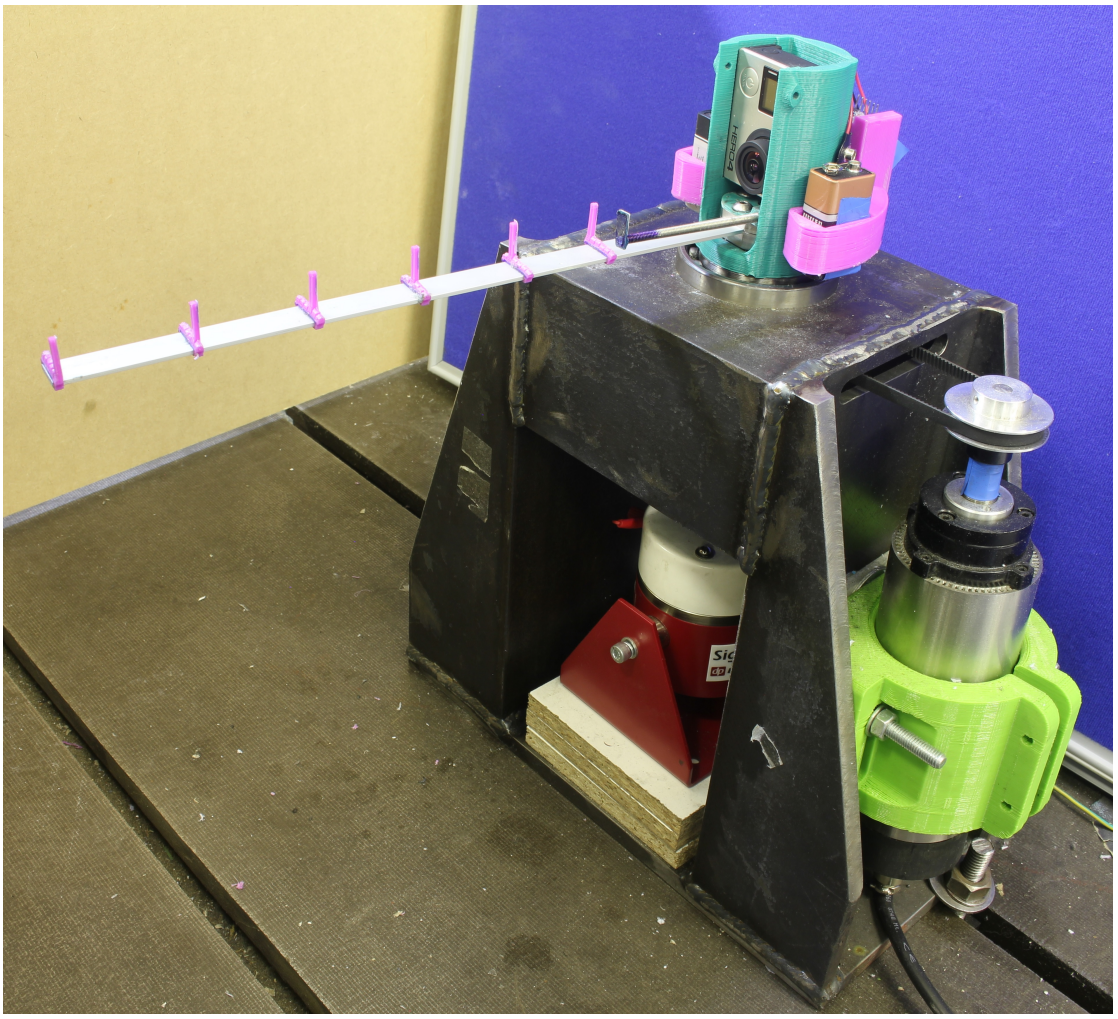

Figure 5.6: The manufactured test rig.

5.3 Digital image processing

There are numerous digital image processing methods to extract the information from the image. In this section, the three main types of image processing method will be described. These are digital image correlation, marker detection and blob area detection methods. The main reason for using three different methods is related to the advantages and the conveniences of each method with the specific applications. For example, the image correlation method (DIC) is more likely to be used in finding the strain of the surface of the object since the estimation of the rate of change of the surface displacement is more accurately measured. However, it is difficult to apply (DIC) for later control applications due to the processing delay.

5.3.1 Digital image correlation

Digital Image Correlation (DIC) is a pattern tracking method and it is designed to recognise and track a special density of grey levels Helfrick et al. (2011). To achieve this, specimens are typically painted with two contrasting colours such as black and white as shown in the Figure 5.11(a) (see section 5.5 for more information). This pattern should be random and the size of the black points should not be less than three pixels to avoid pixel aliasing. Three different markers were used instead of the speckles for the purpose of tracking the tags using a simple MATLAB image processing algorithm. This was in addition to using a commercial DIC software package for comparison of the results.

Figure 5.7 shows the digital image correlation steps, where Figure 5.7(a) shows the unprocessed image including the markers. Figure 5.7(b) illustrates the image of the second marker, which is selected for detection. Figure 5.7(c) shows the cross correlation result between the unprocessed image and the image of the marker. The white spot is the identified position for maximum correlation of the image.

Different approaches were used to extract the information from the image. The main procedure of DIC starts with applying a Gaussian filter to reduce pixel aliasing and noise. The latter is generated from the pixels' different sensitivity. Then, the main image was divided into the small subsets; each subset will correlate with the pattern image (target). The maximum correlation results refer to the best match between the location in the image and the target. However, the difference between the commercial software starts after the first matching point. The algorithm in MatchID tends to apply interpolation between higher correlated subsets to accurately locate the target in the image. These options are limited in the MATLAB image processing toolbox and required extra coding. The interpolation algorithms in MatchID used either a least-square based approach (Approximated NSSD, Normalized sum of the squared differences and zero-normalized sum of squared differences) or Cross-correlation based. Examples of the cross-correlation include normalized cross correlation and zero-normalized cross-correlation. For more information see MatchID (2016). Each of the algorithms have advantages and disadvantages according to the light condition, speckle size, optical sensor sensitivity and processing time.

5.3.2 Marker detection

The process of marker detection is based on detecting specific geometrical shapes such as a circle, square, pentagon or hexagon, etc. In this study, a single or a group of circles is selected as a marker and the algorithm of the Circular Hough Transform (CHT) Song et al. (2014) is applied as the detector. The purpose of the technique is to find circles for imperfect image inputs and return the positions of the centres of the circles.

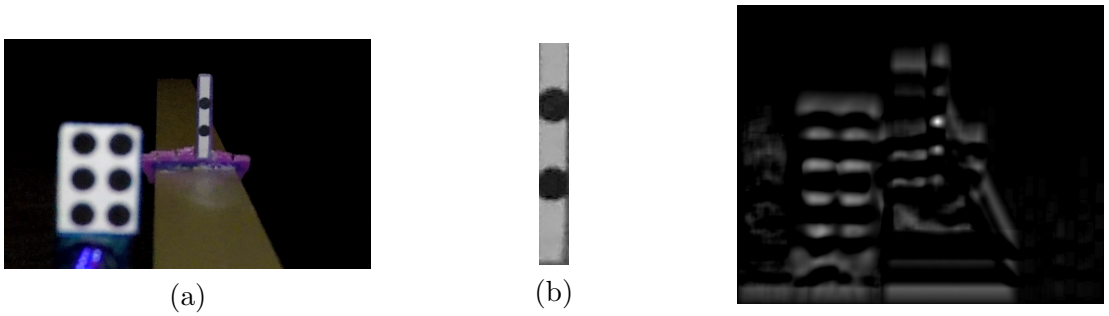

(a) (b) (c)

Figure 5.7: Digital image correlation process. (a) the original field of view, (b) the marker and (c) shows the result of two dimensional digital image correlation. The white circular area represents the point of best correlation between the original image and the marker.

In general, a circle can be defined by three parameters X_c, Y_c and R_c. The first two parameters specify the centre of the circle while the third one represents the radius of the circle. The designed markers are with known parameters as shown in Figure 5.8. However, the deflection of the beam will change the position of the circle centres within the field of view. As a result, the radius R_c of the circles is still constant during the position change of the marker. The fixed radius will reduce the unknown parameters to two, which are the parameters of the centres.

The procedure for detecting the centres of these circles can be explained in three steps Luo (1998)

- Converting the input image into a binary image using an edge detecting filter.
- Generate a circle from each edge with known radius.
- Using votes to the number of intersections of the generated circles and the higher intersected point, which represents the centre of the circle.

5.3.3 Colour blob detection

This approach is based on recognizing and detecting the area with different levels of the grey colour. This method is faster than the previous two approaches, especially if the tracking object has a significant different level of the grey colour from the surrounding. The procedure is firstly applied by a 2D Gaussian filter, to smoother and remove the pixel noise from the image. Then, a threshold is applied to the image to separate the high level of grey from the low level. The image produced becomes binary such as black and white. Then, the centre of the black colour is determined if selected as a tracking target by summation of the black pixels at x position and divided into the number of pixels. The same process is applied for the y detection. The resulting mean values for x and y represent the centre of the black marker area, as shown in Figure 5.9

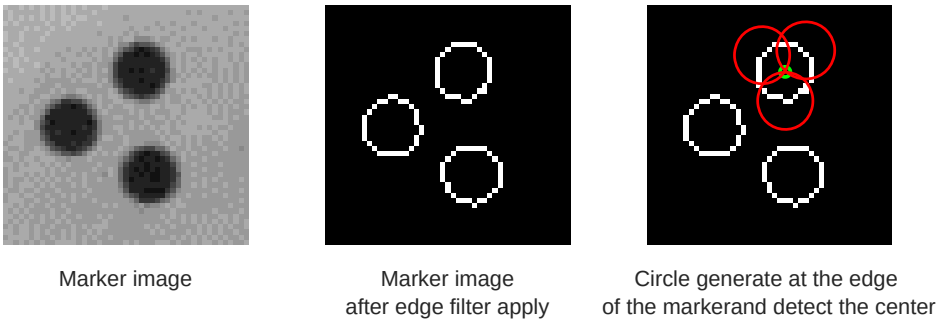

Figure 5.8: Circle detection procedure. After applying an edge filter a number of circles will be generated from the pixels of the edges with radius equal to the radius of the circles to be detected. The intersection of the circles generated becomes a centre candidate. The actual centres are selected according to the number of intersections. In this figure, the white circles represent the actual markers and the red circles are the generated circles used to detect the centre. Only the upper circles are illustrated in this figure for simplicity.

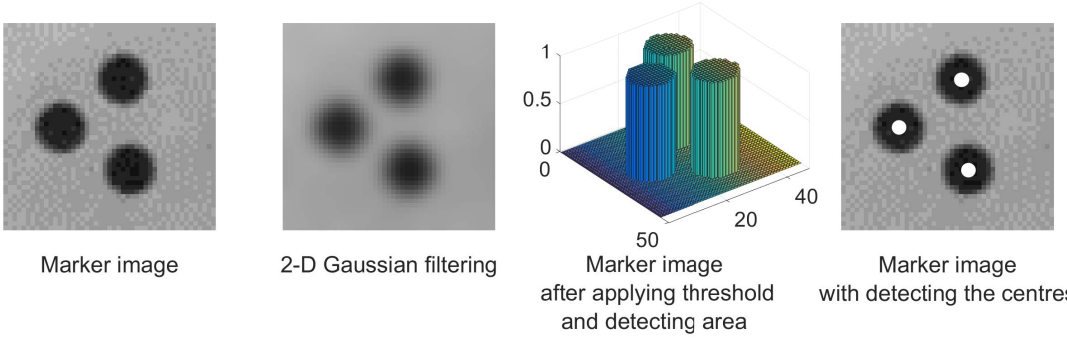

Figure 5.9: The colour blob detection procedure. The steps from left to the right are started by loading the image, then applying a 2D Gaussian filter to remove pixel noise. Then, one applies a threshold to separate the high and low grey level. Finally, obtain the centre of the markers, which are required by determining the mean value for the x and y.

5.4 Camera set up procedures

The test setup is based on, firstly, the measurement equipment capability which depends upon the frame rate and resolution of the camera sensor. Secondly, it is a function of the frequency range, which depends upon the rotational speed and measured frequencies and thirdly, the field test area.

For flapwise vibration of a non-rotating beam, the test configurations shown in Figure 5.10 are applicable. However, the most suitable arrangement is Figure 5.10(a), which

was used previously for non-rotating beams by Romaszko et al. (2015). A single high-speed camera is set perpendicular to the plane of motion. This arrangement allows the camera to capture the lateral vibration of the beam with minimum equipment.

For the rotating beam the first two setups are difficult to apply. In setup (a), the rotational speed is much lower than the frequencies of the beam. Therefore, more than one camera should be used to avoid frequency aliasing. For the second setup, Figure 5.10(b), the same sampling problem occurs, which requires a high-resolution camera to analyse the field of view and increasing the resolution can lead to a decrease in the image frame or sampling rate. In addition, using two cameras can increase the complexity of information and extracting information from the two images due to extra unnecessary data. The third and fourth setups, in Figure 5.10(c) and Figure 5.10(d), are considered for the rotating beam case, because of the continuous capture and minimum field of view area used. The images obtained from the latter also use a rotating frame of reference, which is the same speed as the rotating beam itself.

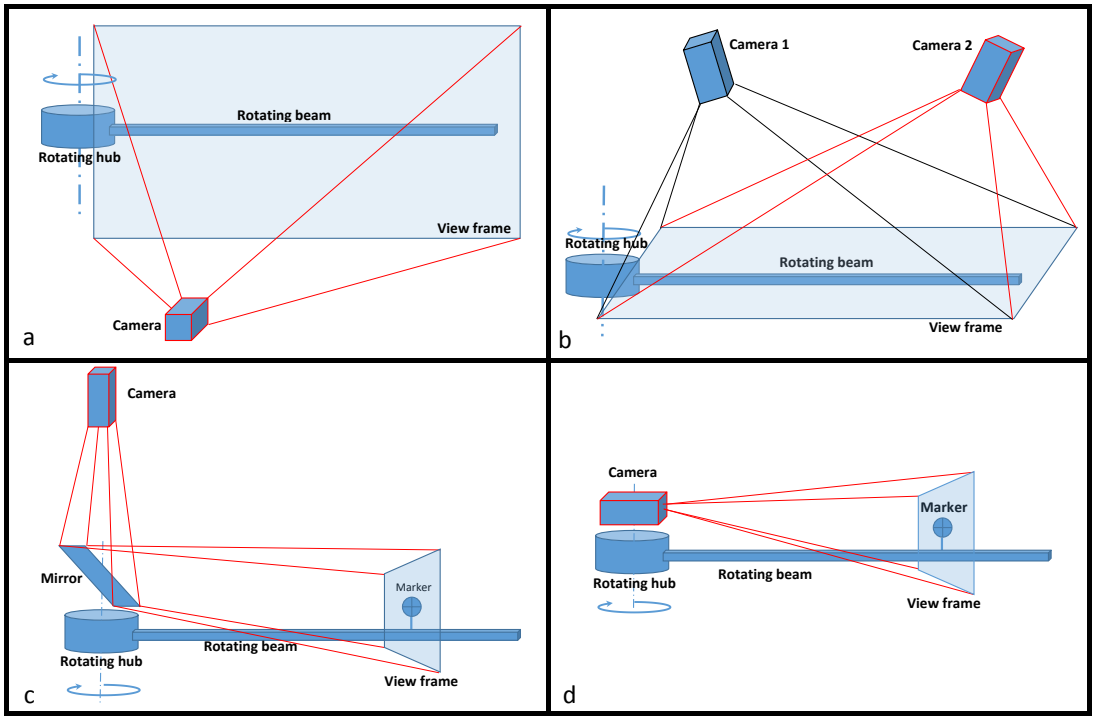

Figure 5.10: Types of camera setup: (a) single camera perpendicular to the plane of the lateral displacement, (b) stereo vision system for 3D imaging, two cameras with arbitrary setup angle, (c) single camera with a reflecting mirror that targets one or more markers along the beam and (d) a single camera fixed to the centre of rotation, targeting one or several markers along the beam.

5.5 Speckles or markers

Digital image processing, which is used in this research, is a pattern tracking method and it is designed to recognise and track a special density of grey levels. To achieve this, usually the specimen is painted with two contrasting colours such as black and white as shown in the Figure 5.11(a). This pattern should be random and the size of the black points should not be less than three pixels. Herein, three different markers were used instead of the speckles for the purpose of tracking the tags using digital image correlation and a simple MATLAB image processing algorithm. These three markers are 10mm in diameter black circles, three 2mm in diameter black points and a pattern of 2mm in diameter set of five black points as shown in Figure 5.11(b-d). The corresponding test configuration for the non rotating beam shown in Figure 5.12,Figure 5.13 and Figure 5.14, respectively.

In addition, to the speckles and markers, LED diodes can be use as traceable targets. An advantage of using LED is to create a significant grey level difference between the target and the background. Furthermore, the LED sources are usually made in standard geometrical shapes which can be recognised when using a circle detection method (see Section 5.3.2). These two advantages could be used to improve the processing speed, especially when used with a blob detection method (see Section 5.3.3). However, LEDs also have disadvantages such as adding extra mass and required a wired powering, which is not suitable for the direct application onto the rotating beam.

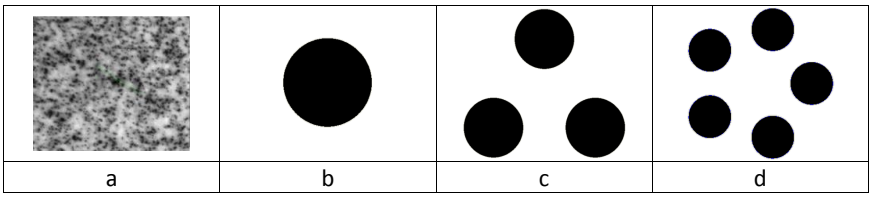

Figure 5.11: Speckle pattern (a), 10mm diameter black circle (b), three 2mm diameter black circles (d) and five 2mm diameter black circles (e).

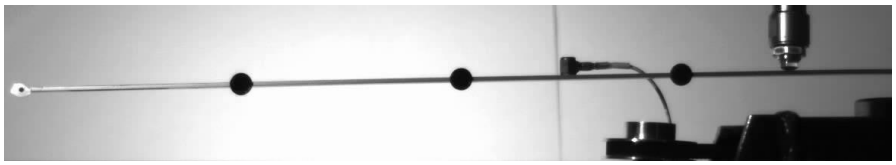

Figure 5.12: Marker 1 , 10mm diameter circle black single circle.

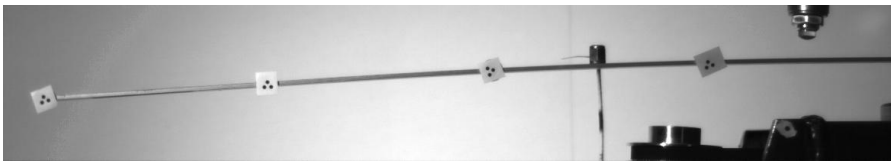

Figure 5.13: Marker 2 , 2mm diameter circle three black circles.

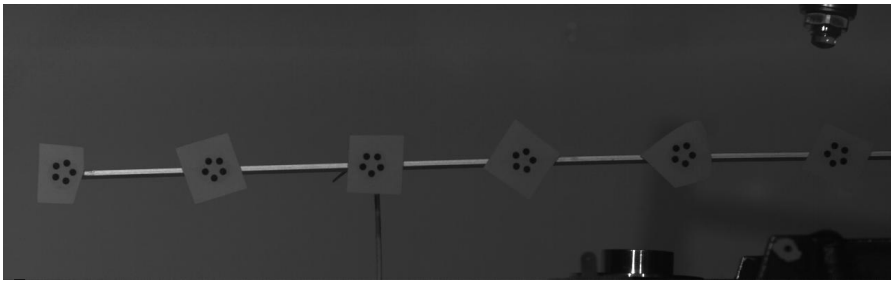

Figure 5.14: Marker 3 , 2mm diameter pattern of five black circles distributed along the beam.

5.6 Experimental test setup

5.6.1 Non-rotating beam

Experiments were first carried out for a non-rotating beam using DIC to compare the results with those obtained using accelerometers. For the DIC system setup, two LED lights were used with a Motion Pro X3 Plus high-speed camera. For the acquisition and recording of the data Motion Studio software (reference) was used. Simultaneously, on the other hand, the accelerometer and impact hammer were connected to the LMS test lab.

In this test, only flapwise or lateral displacement of the beam was measured. For this reason, only one camera is required. The camera is installed perpendicular to the plane containing the beam movement as explained in section 5.4 in Figure 5.10. The camera captured the motion in the XY plane when it was fixed at a perpendicular distance Z from this XY plane.

According to the DIC method, the minimum number of pixels per black speckle should be at least a 3x3 pixels array in the image. In addition, at least 3 speckles per subset are required to guarantee reasonable matching precision Pan et al. (2009). However, in this experiment the thickness of the beam is 2mm. The magnification is also the relationship between the object size on the beam and the image size on the sensor. The equivalent length to the number of the pixels is equal to 2.27 pixels/mm. For this reason, a large marker is used instead of a group of speckles as mentioned in Section 5.5. The sensor size, field of view (FOV), magnification and the distance from the object are obtained

from Equations 5.1 to 5.4.

$$Sensor\ size = pixels\ number \times size\ of\ each\ pixel \tag{5.1}$$

$$Sensor\ size = 1024\ pixels\ number \times 12\mu m\ size\ of\ each\ pixel = 12.288mm$$

$$FOV = \frac{Sensor\ size \times Distance\ to\ object}{focal\ length} \tag{5.2}$$

$$Magnification = \frac{Sensor\ size}{FOV} \tag{5.3}$$

$$Magnification = \frac{12.288mm\ Sensor\ size}{450mm\ FOV} = 0.0273$$

$$Distance\ from\ the\ object = \frac{FOV \times Lens\ focal\ length}{Sensor\ size} \tag{5.4}$$

The equivalent length to the number of the pixels is equal to 2.27 pixels/mm. For the test setup, the calculation steps are shown in Table 5.2

	Motion Pro X3 Plus	Photron SA3	units
Pixel equivalent in mm			
pixels	1024	1024	pixel
pixel size	12	17	μm
sensor size	12.288	17.408	mm
Magnification factor			
Field of view	450	450	mm
magnification	0.027306667	0.03868444	
Lens Focal length(mm)	Distance from the object		
Sigma f2.8 105mm	3845.215	2714.269	mm
AF NIKKOR 50mm	1831.055	1292.509	mm
Speckle size			
Pixel size on beam	0.439453125	0.439453125	mm
Minimum speckle size	1.318359375	1.318359375	mm

Table 5.2: DIC calculation for the sensor size, magnification, distance from the object and speckle size.

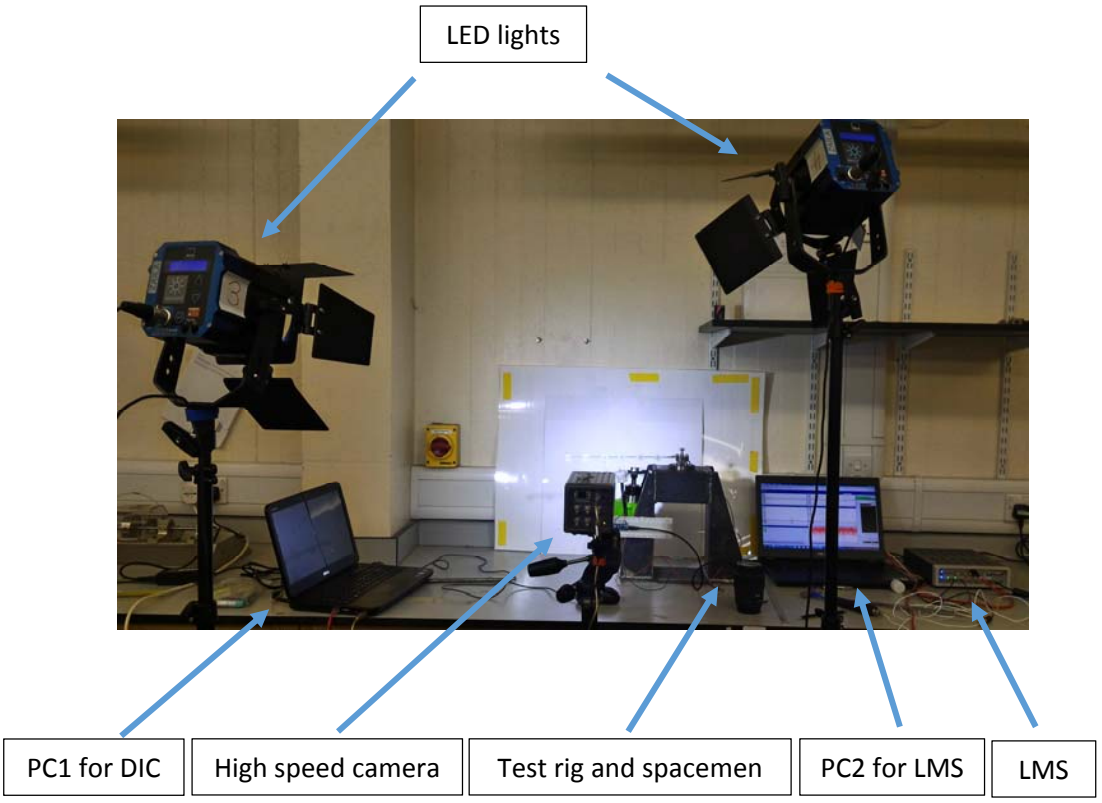

Figure 5.15: Experimental test rig set up showing the rig, camera and data acquisition system.

5.6.2 Rotating beam

Flapwise vibration is out of the rotational plane of motion of the beam. In addition, a rotating beam covers a circular area with a diameter equal to twice that of the rotating beam length and hub radius. This motion can be captured by setting up the high-speed camera perpendicular to the plane of vibration as shown in Figure 5.10(a). However, this method is limited to only being applicable when the maximum frequency of the vibration to be measured is less than twice the rotational speed of the beam in order to obey the Nyquist sampling rate. The second method uses a stereo vision system. Nevertheless, a larger area needs a larger number of pixels for accurate measurement. This problem becomes significant when a longer beam is used. Two high-speed cameras capturing the beam from two different angles, then matching these two images will reveal the deflection of the beam. Nevertheless, using a single high-speed camera with a reflecting mirror at the centre of rotation solves both aforementioned problems of the sampling rate and image resolution, as shown in Figures 5.10(c) and 5.10(d).

5.7 Experimental results

5.7.1 Results for the nonrotating beam

Vibration measurements performed for a non-rotating beam are used for comparison between the results from the image processing methods and the ones obtained using beam mounted accelerometers. The frequency response function of a non-rotating cantilever beam was measured using a simple impact hammer test using a hammer (PCB 5800B3 with sensitivity 207.287 mV/N). The frequency response function of the non-rotating beam was measured using an accelerometer (PCB 3035BG sensitivity=103.90 $\mathrm{mV/m/s^2}$) and the results were compared with simultaneous recordings using a high-speed camera (MotionPro X3 plus, 50mm lens at 800 frames per second). The camera was setup as shown in Figure 5.10(a).

MATLAB image processing toolbox was used to locate the displacement of a marker by using the circle detection method as shown in Figure 5.16, where specimen 1 was used. This program is limited to large displacements and therefore the data becomes very noisy for small displacements. However, there are several commercial software packages for DIC which are able to tackle this issue using the average grey level and sub-pixels for locating objects. MatchID was employed in this work to post-process the data. This software is based on pattern detecting using DIC, which selects the markers and the search area as shown in Figure 5.17. The program will track the pattern through the sequence of images. Then, the displacement result can be plotted as a function of time as shown in Figure 5.18. Figure 5.19 shows the comparison of the measured results for three different methods such as using an accelerometer (LMS), digital image processing using a circle detection method (MATLAB) and digital image correlation (MatchID).

The second test was performed using specimen 2, with five point marker patterns to check again the matching of the three methods, which are DIP circle detection, DIC and using an accelerometer. The results of digital image processing using marker detection method is shown in Figure 5.20. Similar to the first test, the DIC software shows the displacement as a function of time presented in Figure 5.21. Furthermore, the comparison between the results is shown in Figure 5.22.

Figure 5.19 and Figure 5.20 shows the comparison between the accelerometer measurement and the optical sensor results. The accelerometer data was converted to displacement amplitudes. Its curve tends to start from a higher amplitude due to this conversion from acceleration to displacement. The high value of the displacement at 0 Hz is due to the division by 0, according to Equation 5.5. At higher frequency, the accuracy of the optical sensors will reduce as the displacement amplitudes are low. Furthermore, in contrast the method DIC using MatchID shows a better performance in measuring the displacement than the DIP using the circle detection method.

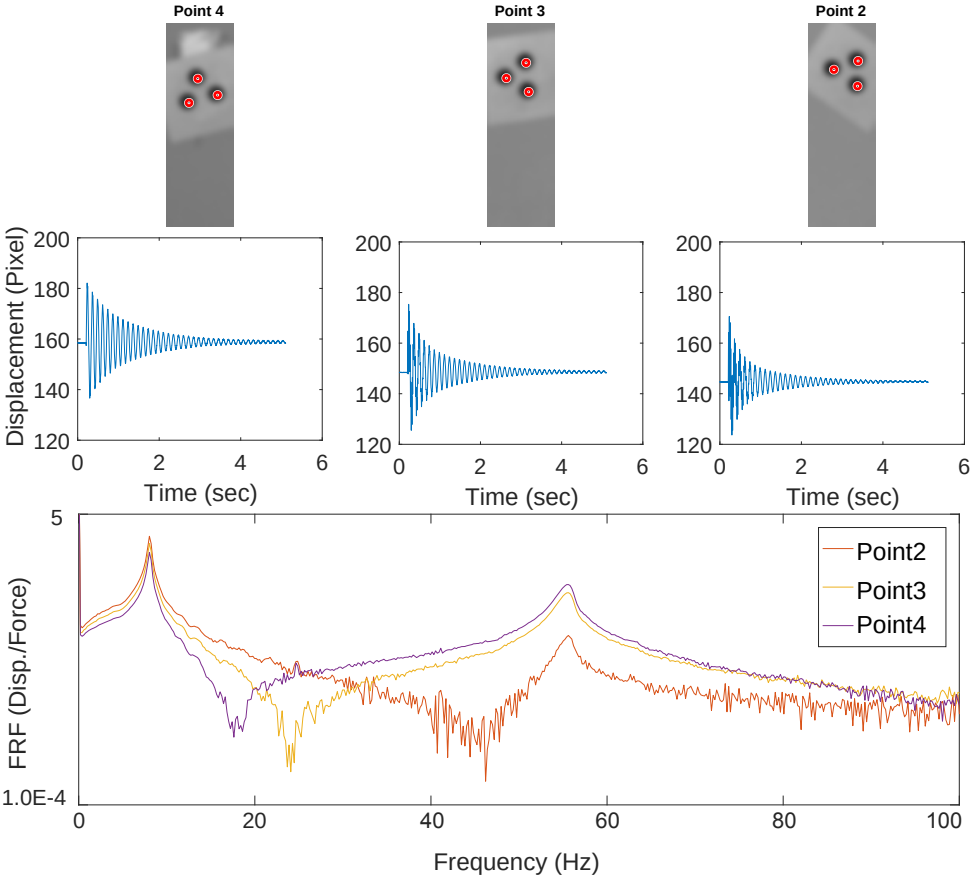

Figure 5.16: MATLAB results by an using image processing toolbox. In the first row the red circles refer to the marker detection points. The field of view is cropped to small search areas to speed up the image processing. The second row shows recorded time domain decay from a hammer input. The third row shows the transfer receptance measured for the three points.

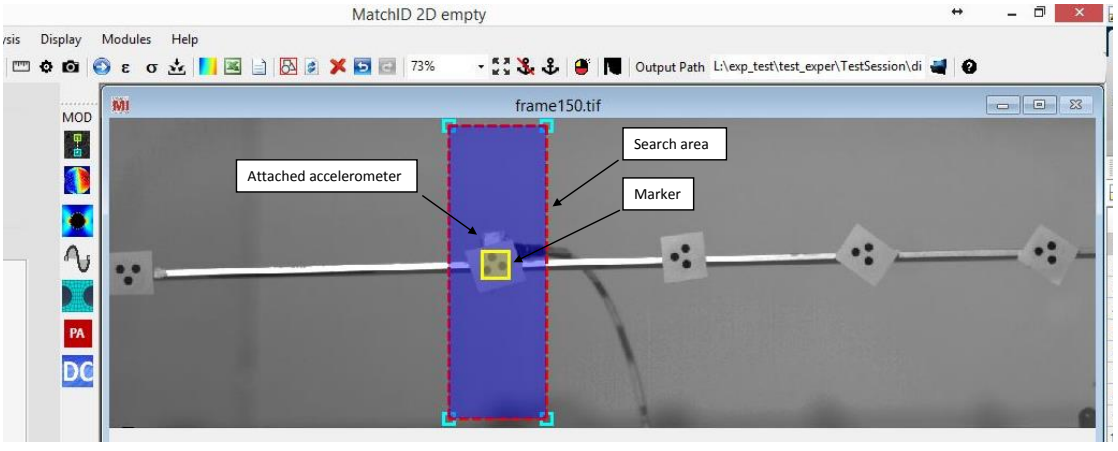

Figure 5.17: MatchID software showing the selected marker and the search area.

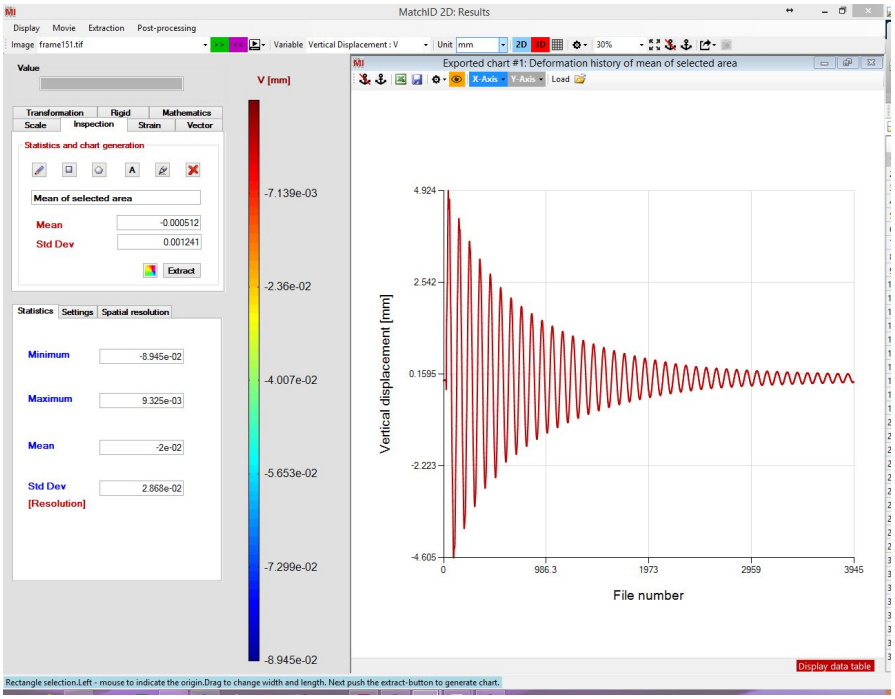

Figure 5.18: Displacement as a function of time obtained from the selected point using MatchID software

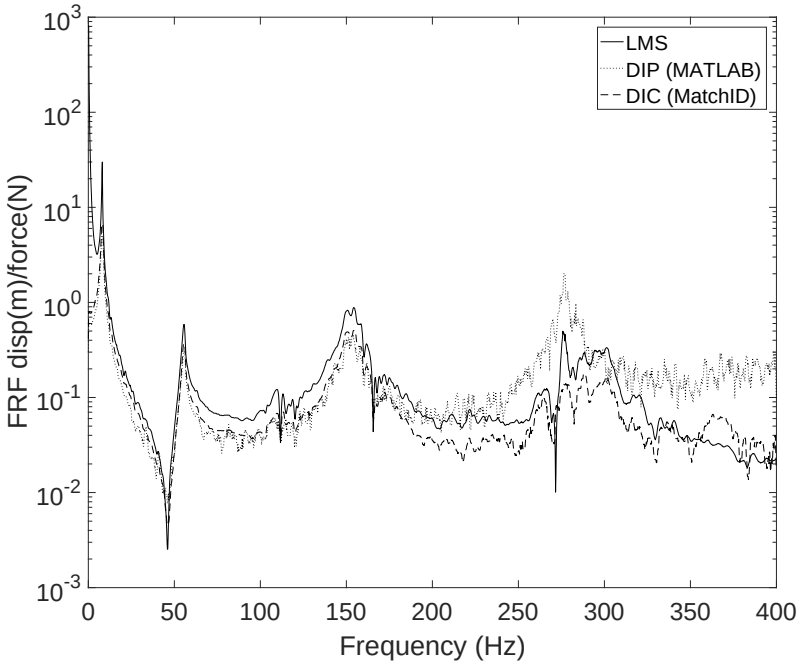

Figure 5.19: Comparison between the transfer receptance results using an accelerometer (LMS), the digital image processing DIP (MATLAB) and the digital image correlation DIC (MatchID) methods for specimen No.1. Beam length is 400mm, the hammer input at 100mm away from the fixed end and the output at 300mm from the fixed end. The fundamental natural frequency is 8.14 Hz, the second natural frequency is 55.54 Hz and the third natural frequency is 153 Hz.

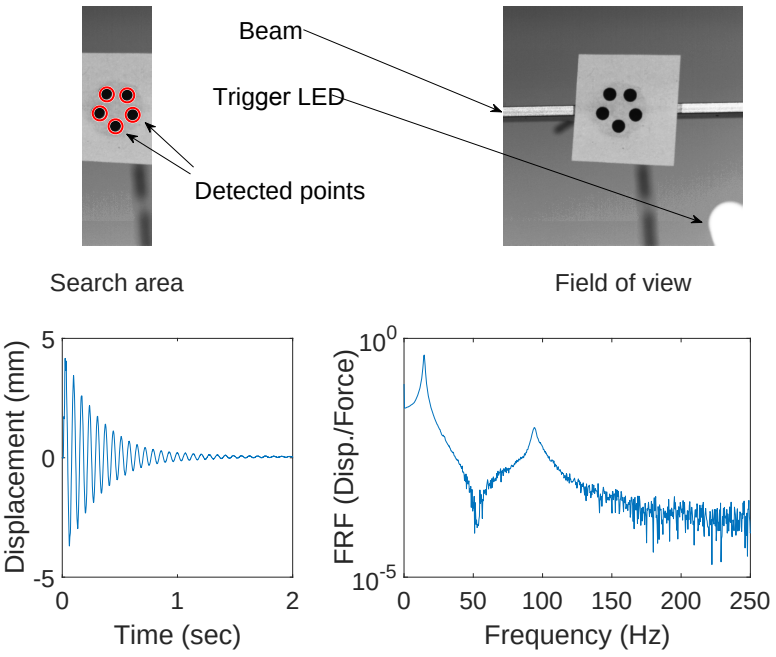

Figure 5.20: Specimen No.2 using MATLAB code for the displacement identification. Five point markers were used to increase the accuracy. In addition, an LED trigger was used to trigger the high-speed camera at the hammer impact. The dimensions of the beam are 200mm, 15mm and 2mm for the length, width and thickness, respectively.

.

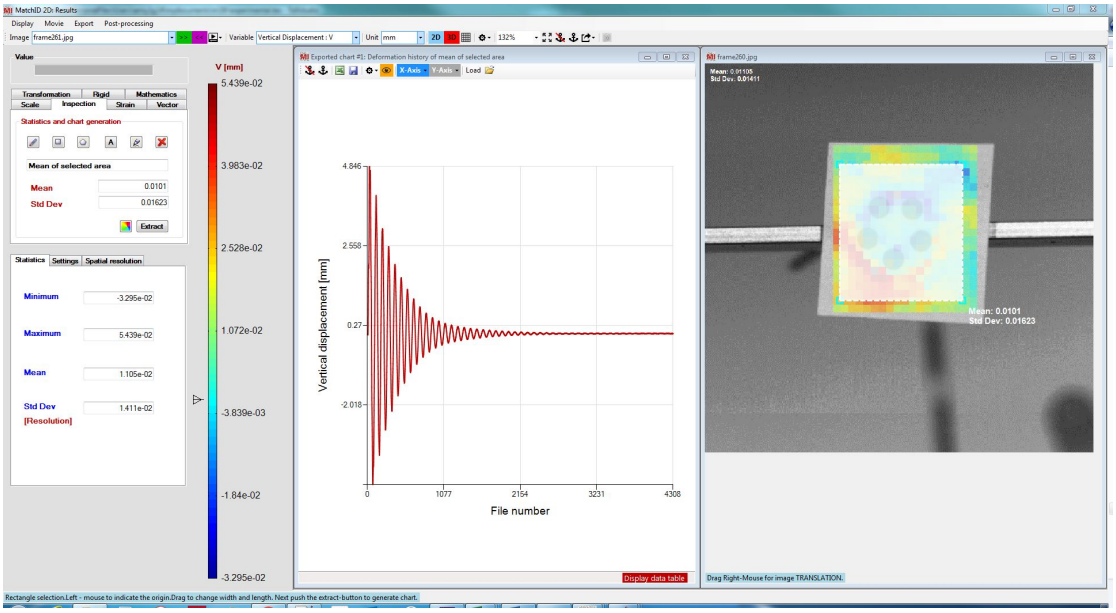

Figure 5.21: Specimen No.2 MatchID software processed results showing the vibration displacement impulse response versus time.

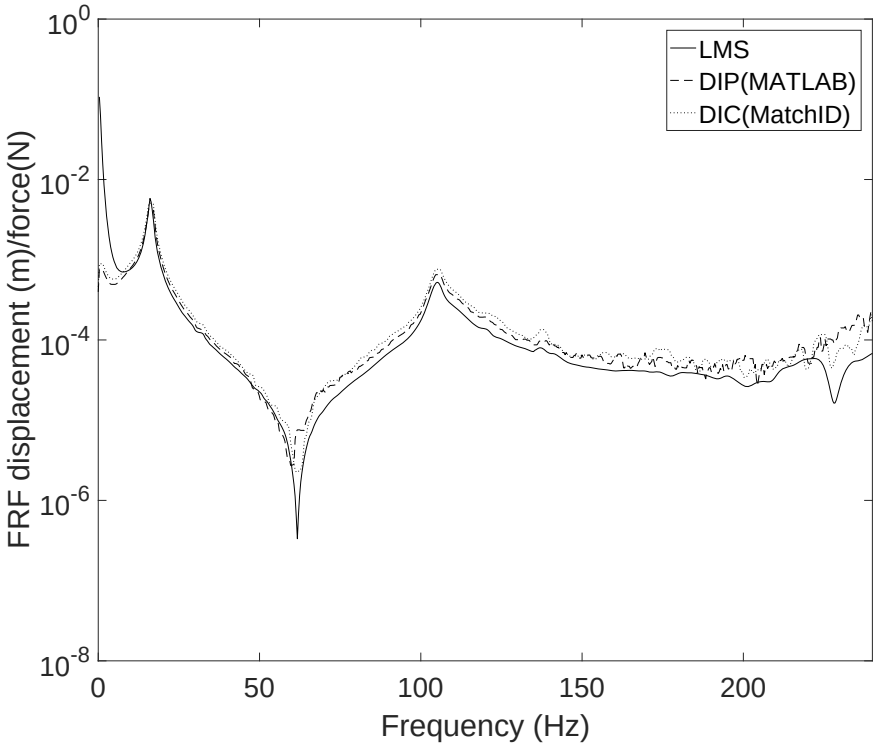

Figure 5.22: Comparison of the results using an accelerometer (LMS), DIP circle detection method (MATLAB) and DIC (MatchID) methods for specimen No.2. The beam length is 300mm, the hammer input is at 50mm from the fixed end and the output measured at 200mm away from the fixed end. The fundamental natural frequency is 16.04 Hz, and the second natural frequency is 105 Hz.

Since the accelerations are measured in g, the results are scaled and the sensitivity of the accelerometer are also included. LMS software calculates the accelerance, the transfer function between the acceleration and force ($\frac{acceleration}{force}$) where the DIC calculates the receptance, the transfer function between the displacement and force ($\frac{displacement}{force}$) as shown in Figure 5.23 . To convert accelerance of $G^a(jw)$ to the receptance $G^r(jw)$,

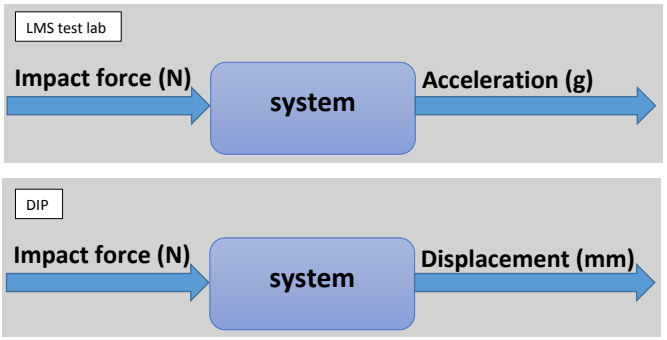

Figure 5.23: Measured output data is acceleration for LMS test lab and displacement for the DIP method.

$$G^r(jw) = G^a(jw) \times \frac{1}{-\omega^2} \tag{5.5}$$

$$\frac{x}{F} \quad (\frac{m}{N}) = \frac{\ddot{x}}{F} \quad (\frac{g}{N}) \times \frac{9.81 \quad \frac{m}{s^2}}{-\omega^2} \tag{5.6}$$

5.7.2 Results for the rotating beam

For the rotating beam, a single camera with a mirror, as shown in Figure 5.5(a) and Figure 5.10(c), was used to measure the vibration. The reflected image can reveal both the rotational speed and the beam deflection as a function of time in Figure 5.24. Converting the marker position from the Cartesian system to the Polar system and by taking the FFT of the time history, the fundamental and second resonance frequencies can be obtained as shown in Figure 5.25. The maximum percentage of the error between the theoretical predictions Yashar et al. (2016) and experimental results for the first and second resonances are less than 5% as illustrated in Figure 5.26. The differences between the analytical and the experimentally estimated natural frequencies are partly due to the uncertain boundary conditions in the experimental rig. Theoretically a fixed end was assumed, but here in the experimental test the beam constraint was dependent upon the clamped edges and applied bolt force. This factor led to a reduction in the estimated frequencies from the experimental results when compared to the theoretical results.

Utilizing two different systems is not efficient due to signal misalignment as well as due to having different sampling rates between the two systems, which requires subsequent data interpolation. This issue was resolved using the same camera to capture both the input signal as well the output signal. As shown in the block diagram in Figure 5.28,

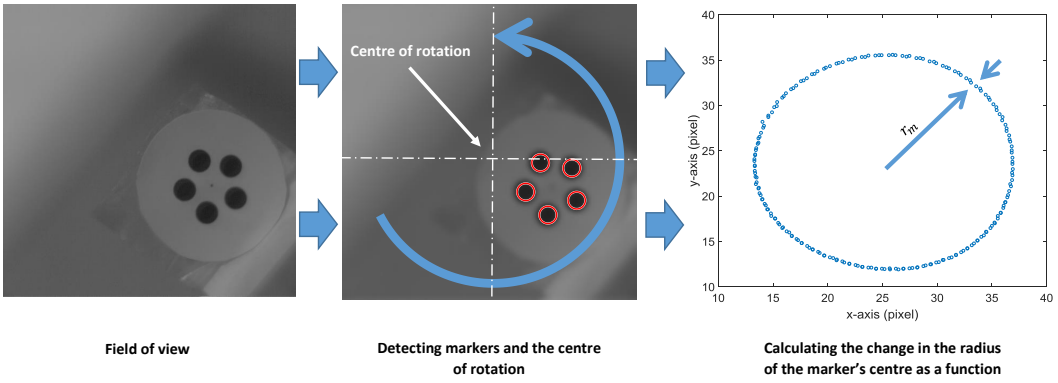

Figure 5.24: The camera off the hub test procedure. The marker is attached to the rotating beam and the camera is fixed on the tripod pointed to the mirror which reflecting the motion of the marker during the test. The rotational speed can be estimated from the motion of the marker around the centre of the rotation, while the change in the radius of the marker position reveals the response of the beam at the marker attached point.

another marker was placed at the centre of rotation. This method is used for random vibration tests to compare between the accelerometers and the response obtained from markers as shown in Figure 5.29.

The camera on hub method has a great advantage due to less complexity in extracting information for the images and have the capability to measure more than one measurement point along the rotating beam. The field of view of the camera is directly on the markers as shown in Figure 5.30(a). Furthermore, the chordwise and torsional vibration can be measured by using this method shown in Figure 5.30(b). As a result of measuring more than one point, using the camera on hub, the mode shapes of the beam can also be obtained. Figure 5.32 shows the fundamental and second mode shapes of the beam. These mode shapes were obtained from the experimental measurement in the frequency domain utilising the Nyquist circle fit to increase the accuracy.

The measured mode shapes are compared with the estimated ones corresponding to two different rotational speeds for the intact beam using the MAC method and the results are shown in Figure 5.33. For a rotating beam with a crack located at the length ratio equal to 0.103 and the depth ratio equal to 0.375, the results are shown in Figure 5.34. The MAC result shows over 99.5% of match between the theoretical and experimental mode shapes for the fundamental and second modes.

Similar to the theoretical study, the effect of the crack on the rotating beam shows a reduction in the natural frequency for the fundamental and second modes. Figure 6.7 shows the measured frequencies for different rotational speeds for the intact and cracked rotating beam with dimensions 330mm, 15mm and 2mm for the length, width and thickness respectively. The crack was located at 24.5mm from the root of the beam with a crack depth 1.1mm.

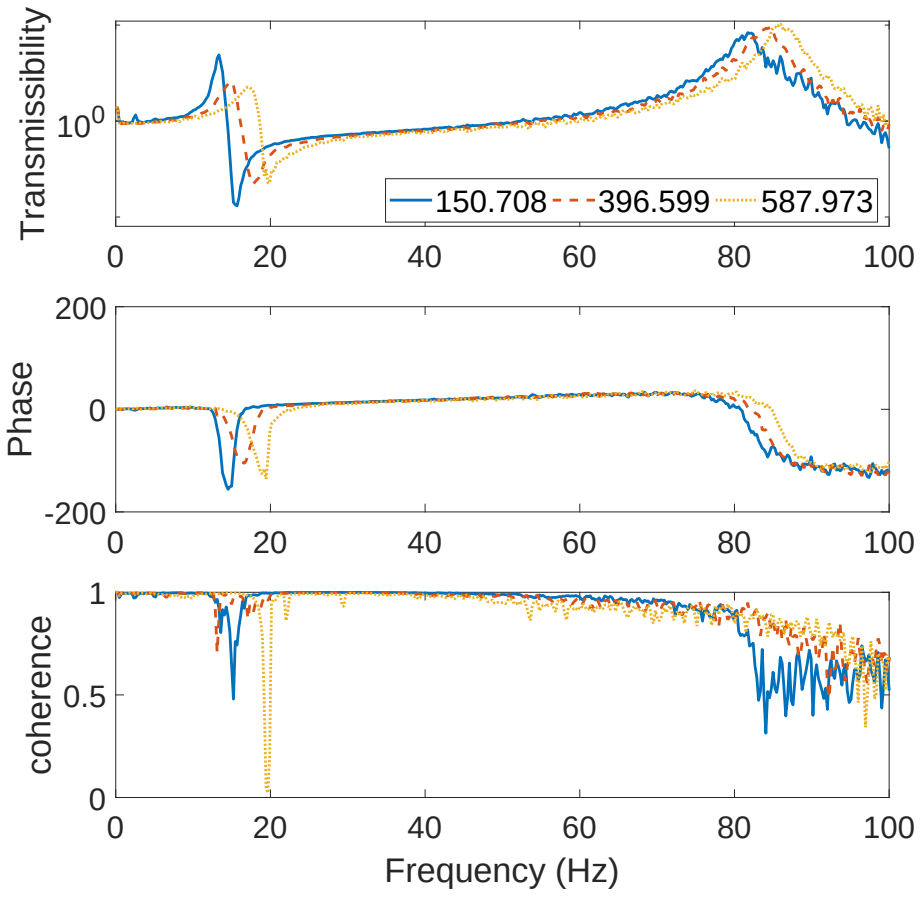

Figure 5.25: Frequency response function (transmissibility) of a cantilever aluminium beam with cross section (height=2mm, width=15mm and length=330mm), rotating at different speeds (150, 396 and 587).

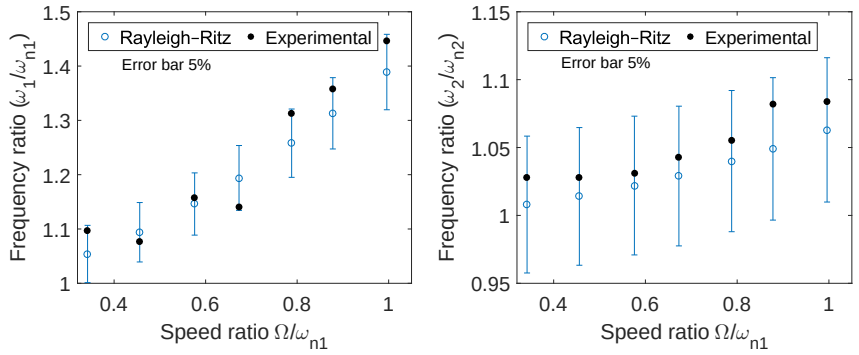

Figure 5.26: Comparison of the measured fundamental and second natural frequency of flapwise vibration versus a theoretical model using the Rayleigh-Ritz approach Yashar et al. (2016)

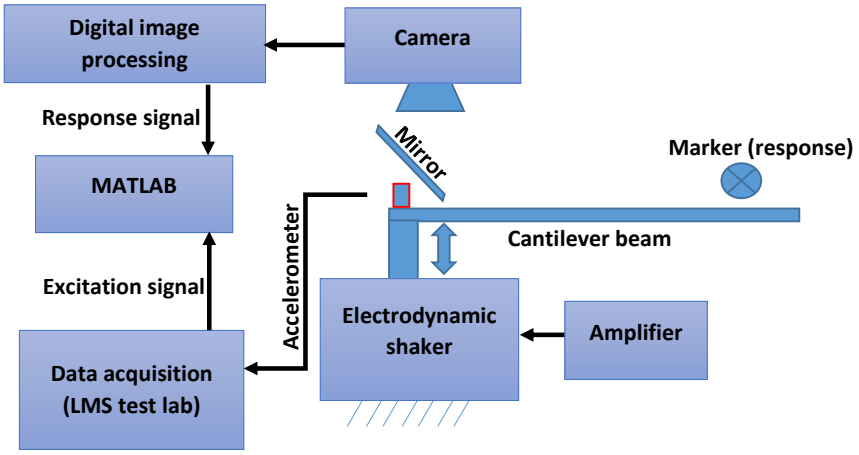

Figure 5.27: Experimental test set up for a single camera with a mirror on the hub. Two different systems were used for data acquisition; LMS lab test connected to an accelerometer to measure the excitation and digital high speed camera to measure the response of the beam.

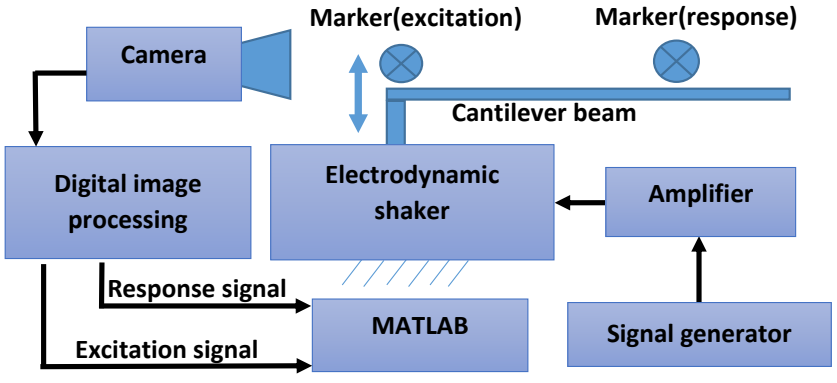

Figure 5.28: Experimental test set up with a single camera on the hub. Additional marker is placed on the centre of the rotation and a single camera is used to measure the excitation and response of the beam.

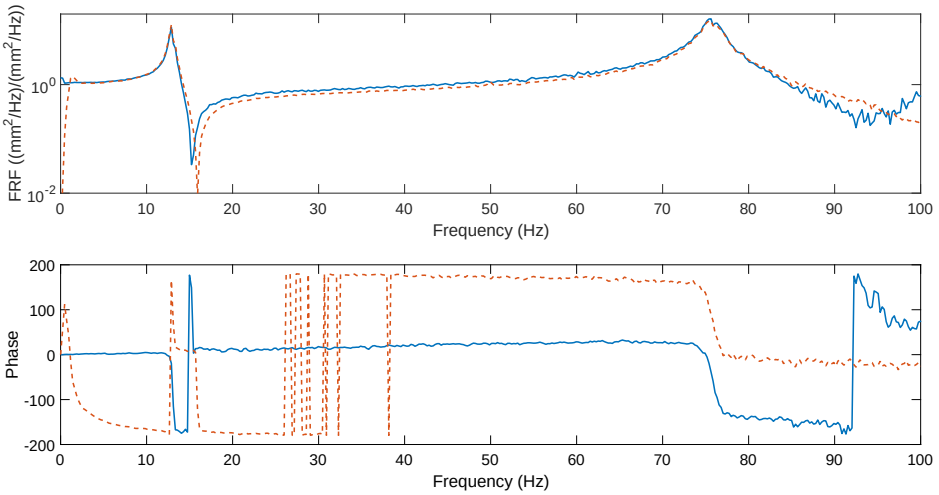

Figure 5.29: Single camera on hub is used to measure the FRF between the output marker and input marker (blue solid line) and output of the accelerometer and the input marker (red doted line) for the non rotating beam (length=330mm).

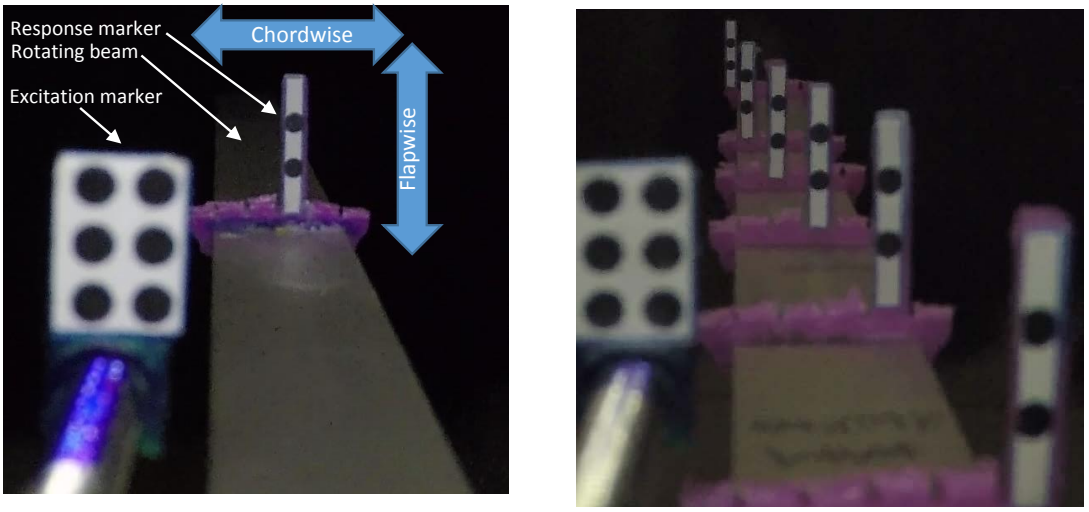

(a) Single excitation and response configuration for the marker. The deflection of the marker in the vertical direction represent the flapwise and in the horizontal direction represent chordwise.

(b) Single excitation multi response measurment points configuration.

Figure 5.30: The marker configuration on the rotating beam. These images are samples from the high-speed camera record.

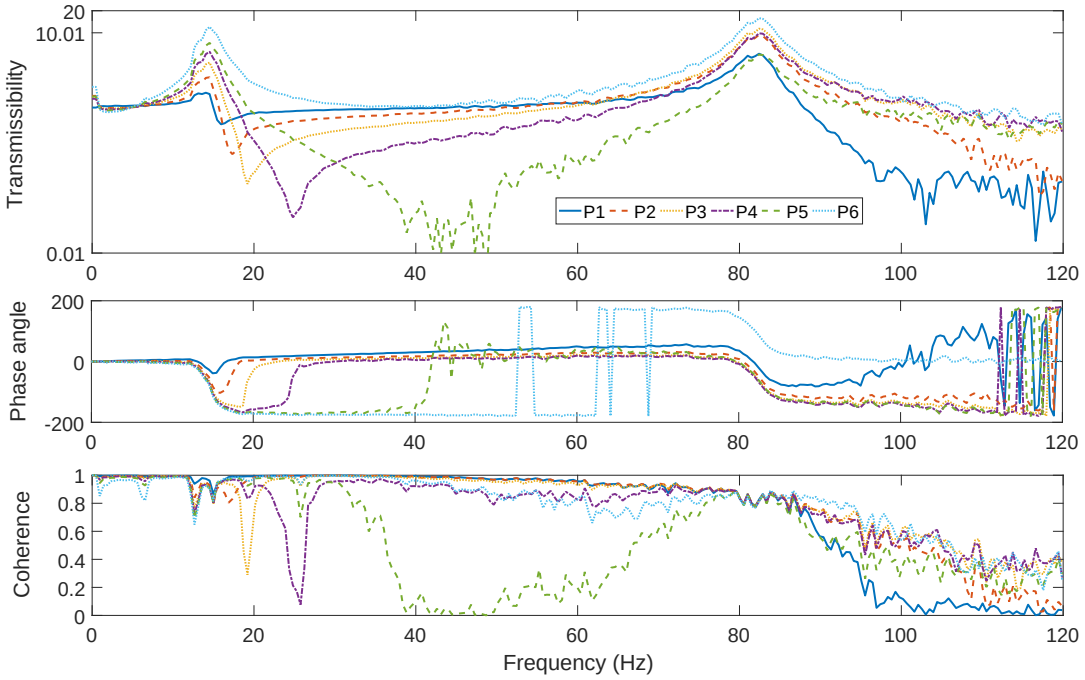

Figure 5.31: The transmissibility and coherence measurements for a rotating beam with six measurement points along the beam. The rotational speed is 373.11 rpm.

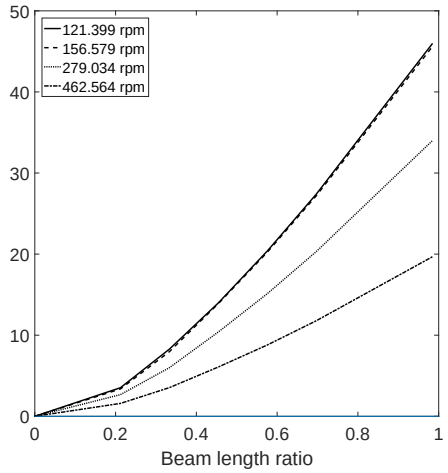

(a) First mode shape of the rotating beam.

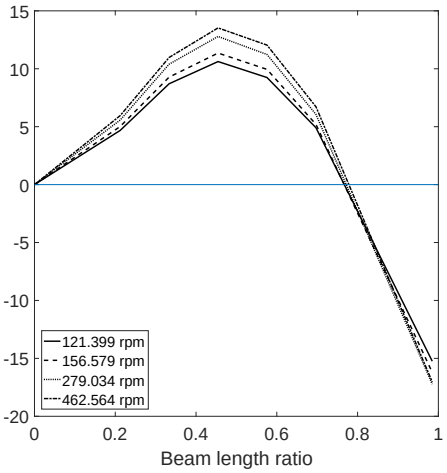

(b) Second mode shape of the rotating beam.

Figure 5.32: Experimental mode shapes of the rotating beam measured using digital image processing. The dimensions of the beam are 330mm, 15mm and 2mm for the length, width and thickness, respectively. The markers are attached at positions corresponding to the length ratios of 0.21, 0.33, 0.45, 0.57, 0.69 and 0.98 from the root of the rotating beam.

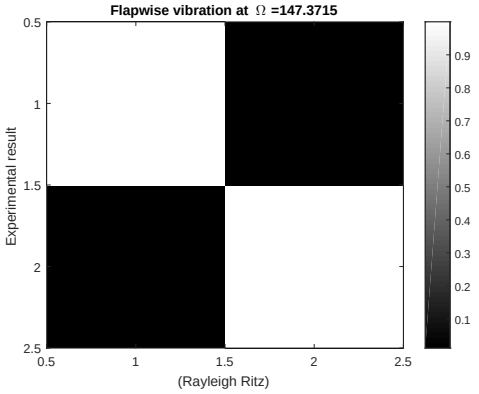

(a) MAC comparison between experiment and the RayleighRitz method for the fundemental and second mode shapes of the rotating beam at 147.37 rpm.

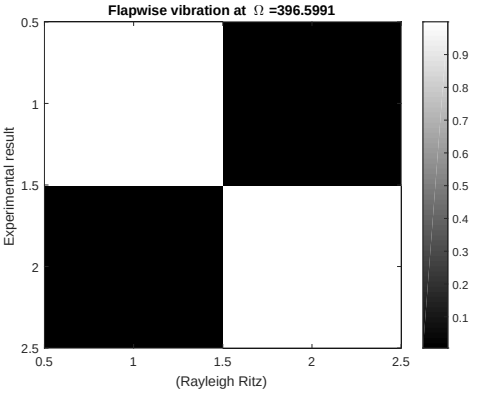

(b) MAC comparison between experiment and the RayleighRitz method for the fundemental and second mode shapes of the rotating beam at 396.59 rpm.

Figure 5.33: MAC comparison between experiment and the Rayleigh-Ritz prediction method. The dimensions of the beam are 330mm, 15mm and 2mm for the length, width and thickness respectively. The mode shape predictions are evaluated using the Rayleigh-Ritz method at the same point as the attached markers along the length, at ratios of 0.21, 0.33, 0.45, 0.57, 0.69 and 0.98 from the root of the rotating beam.

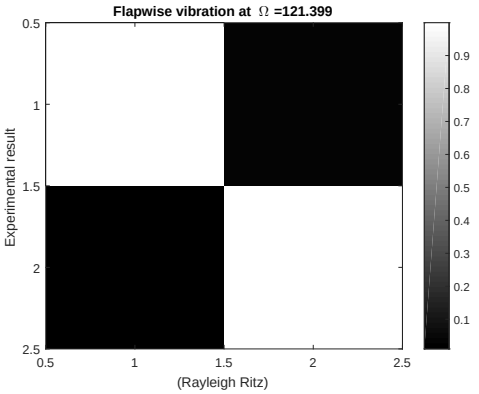

(a) MAC comparison between experiment and the RayleighRitz method for the fundemental and second mode shapes of the rotating beam at 147.37 rpm.

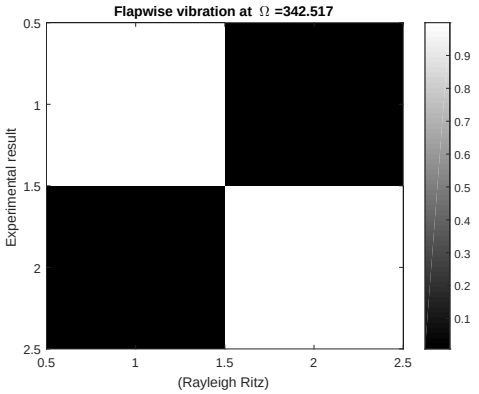

(b) MAC comparison between experiment and the RayleighRitz method for the fundemental and second mode shapes of the rotating beam at 396.59 rpm.

Figure 5.34: MAC comparison between experiment and the Rayleigh-Ritz method. The dimensions of the beam are 330mm, 15mm and 2mm for the length, width and thickness respectively. The estimated response at points which are the same as the attached marker points at the length ratios of 0.21, 0.33, 0.45, 0.57, 0.69 and 0.98 from the root of the rotating beam. The crack is located at 34 mm from the root of the beam and its depth is 0.75 mm.

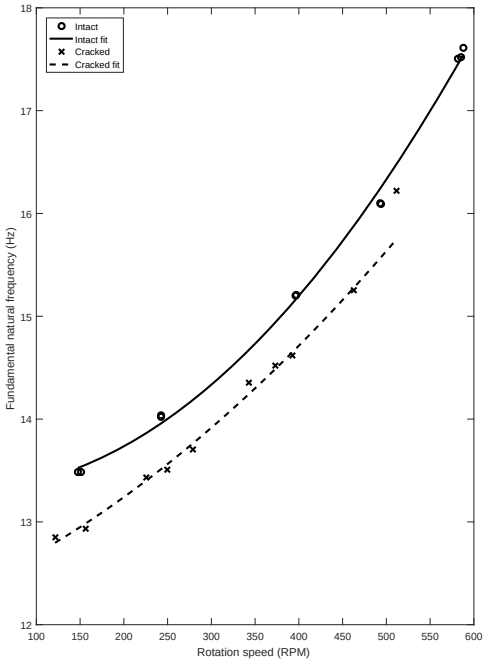

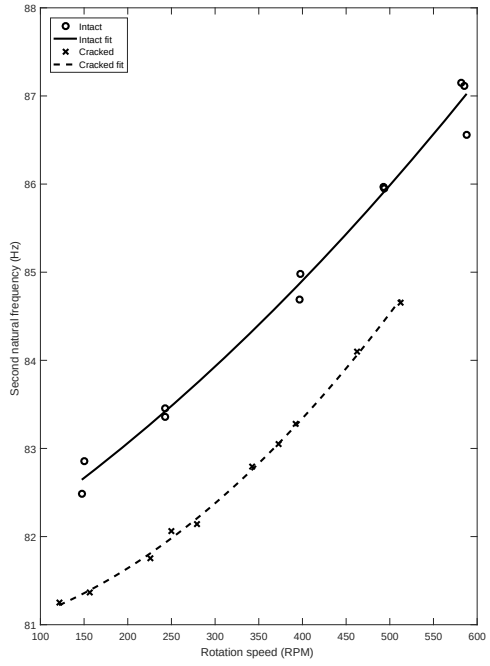

Figure 5.35: The fundamental and second flapwise natural frequencies measured using a high-speed camera for a rotating beam with and without crack. The length of the beam is 330mm and the cross section is 15mm wide and 2mm thick. The crack is located at 25.5mm from the root of the beam and the crack depth is 1.1mm.

5.8 Conclusions

The experimental measurement using possible alternative optical systems is presented in this chapter. The first sections of this chapter explained the test rig design and its capability in performing different types of configuration according to the required measurements. Then, the properties and dimensions of the used specimens are listed. The test rig and the specimens were designed and manufactured in dimensions and materials selected specially to avoid the interference between the resonance of the three lower modes of the rotating beam with the resonance of the test rig. Then, three different image processing approaches namely DIC, marker detection and colour blub detection are explained and illustrated in detail.

The first two image processing methods, which are the DIC and marker detection, are used in a post-processing procedure while the third method (colour blob detection) is more likely to be used in real-time applications. Moreover, the optical methods could be considered in four different camera setups. In this chapter, three different cameras setups used are shown in Figure 5.10(a) for a non-rotating beam test and in Figure 5.10(c),(d) for a rotating beam. Furthermore, the markers were used instead of speckles due to the simplicity and the ability to extract information from the image using marker detection as well as digital image correlation. The magnification, marker size and the distance of the lens from the beam are also illustrated and expressed for two different camera sensors and lenses. Before performing a test on the rotating beam, a non-rotating test was performed to verify the optical methods' accuracy using a simple impact hammer test with accelerometer measurement. The results of three different methods namely DIC, marker detection and accelerometer data analysed using the LMS test lab show good agreement, especially for the lower frequencies. The optical methods measure the displacement of the markers on the beam as a function of the time. The higher the amplitude, the better the measurement accuracy is from the optical measurements.

Regarding a rotating beam, a single camera with mirror is used first with a single marker to measure the response of the beam and an accelerometer attached at the centre of the rotation to measure the input excitation. This configuration can be used with different types of high-speed cameras regardless of the size of the cameras due to attaching the camera on the mount separate from the test rig. Although this method has the advantage of measuring high vibration frequencies, it has a signal alignment issue due to using more than one piece of equipment in the measuring set up. However, subsequently, a camera attached to the hub configuration was used. This method is limited by the size of the camera because of the camera is mounted on the rotating hub. In contrast to the first configuration, this method has the advantage of using multi-measurement points along the beam and the simple steps to extract the information from the images. Moreover, as a result of multi-point measurements, the mode shapes can be obtained from the

measurements. Furthermore, the excitation and the response markers are captured from the single camera, so there is no misalignment or delay in the signals obtained.

The increase in the rotational speed leads to the increase in the natural frequencies of the rotating beam as estimated from the simulation model in Chapter 4. In addition, the existence of the crack leads to a decrease in the natural frequencies of the rotating beam. Furthermore, the mode shapes of the experimental test and the prediction model are compared using MAC and the results show good agreement between the corresponding modes. The results for the natural frequencies from the experimental test are less than those estimated from the simulation model. The maximum percentage error between the simulation model and the experimental measurement is less than 5%. This error is most highly due to the uncertainty in the boundary conditions of the attached beam, such as strictly not fully clamped condition, and the damping in the system. Model updating will be discussed in the next chapter to obtain more accurate results from the simulation model.

Chapter 6

Crack detection

6.1 Introduction

The majority of existing vibration instrumentation used for vibration measurements on rotating objects is typically through an electrical connection using slip rings wired to an acquisition system. These connections have significant disadvantages, such as inherent low signal to noise ratio and the potentially unreliable electrical connections. An optical high-speed camera in conjunction with digital image processing is used herein to overcome these issues and monitor the health of a rotating system during operation.

Numerous studies Barad et al. (2013); Satpute et al. (2017); Mazanoglu and Sabuncu (2012) have investigated crack identification of non-rotating elements using various dynamic characteristic based techniques, such as natural frequency changes. Generally, these methods are based on detecting the crack location and depth from the lowest order natural frequencies, typically three frequencies for a cracked beam. Subsequently, the point of intersection for these three frequencies on a crack location and depth chart can identify the crack. Alternatively, Nguyen et al. Nguyen (2014) used the sudden change in the slope of the three-dimensional mode shapes as an indicator for the crack location and depth. In addition to changes in the natural frequencies, anti-resonance frequency shifting has also been used to identify multiple crack positions Douka et al. (2004). These reported studies are limited to non-rotating beams. In contrast, the analysis and identification for rotating cracked beams are relatively scarce in the literature Banerjee and Pohit (2014); Cheng et al. (2011). Masoud and Al-Said (2009) proposed an algorithm for crack detection in a rotating Timoshenko beam. The algorithm is based on firstly detecting the crack depth then locating the crack position along the beam. Further, the crack location was then confirmed by applying the same algorithm at different rotational speeds.

The objective of this chapter is to describe an experimental method to determine the crack location and depth using a contactless optical method, namely digital image correlation (DIC). Various on hub camera configurations are proposed in the previous chapter to measure the vibration of a rotating beam and tested on a non-rotating beam to verify the measured values. This was then followed by measurements on a rotating beam at different rotational speeds. Subsequently, model updating is applied to the intact rotating beam results in order to characterise and capture the boundary conditions at the attached end more accurately. Later, an updated model is then used with the measured fundamental and second natural frequencies of the cracked rotating beam to identify a crack, which has been deliberately introduced. The crack detection method is then tested by comparing the two lowest natural frequencies from the updated simulation model and the actual cracked beam. The natural frequency-speed curve generated from the actual model is then optimised to find the best combination of crack depth, location and rotational speed curve.

6.2 Rotating beam measurements

For the rotating beam, the captured footage can reveal both the rotational speed and the beam deflection as a function of time. The rotational speed is obtained from tracking the background of the images and the beam deflection from the markers' position according to the field of view image frame, which is fixed in the process. The measured displacement is converted from the image pixels to actual displacement in mm.

The fundamental and second resonance frequencies can be estimated from the power spectral density (PSD) of the time history, as shown in Figure 6.1.

The values of the measured natural frequencies marked with circles in Figure 6.4 are lower than the predicted numerical results Yashar et al. (2018) marked with a dotted line for a cantilever beam. This difference in the natural frequencies is due to the flexibility at the end of the beam attached to the rotational hub and the approximate clamped edge boundary conditions.

In order to subsequently use the numerical model for assisting with the crack detection, it is necessary to update the simulation boundary conditions at the hub in order to improve the accuracy of the numerical model.

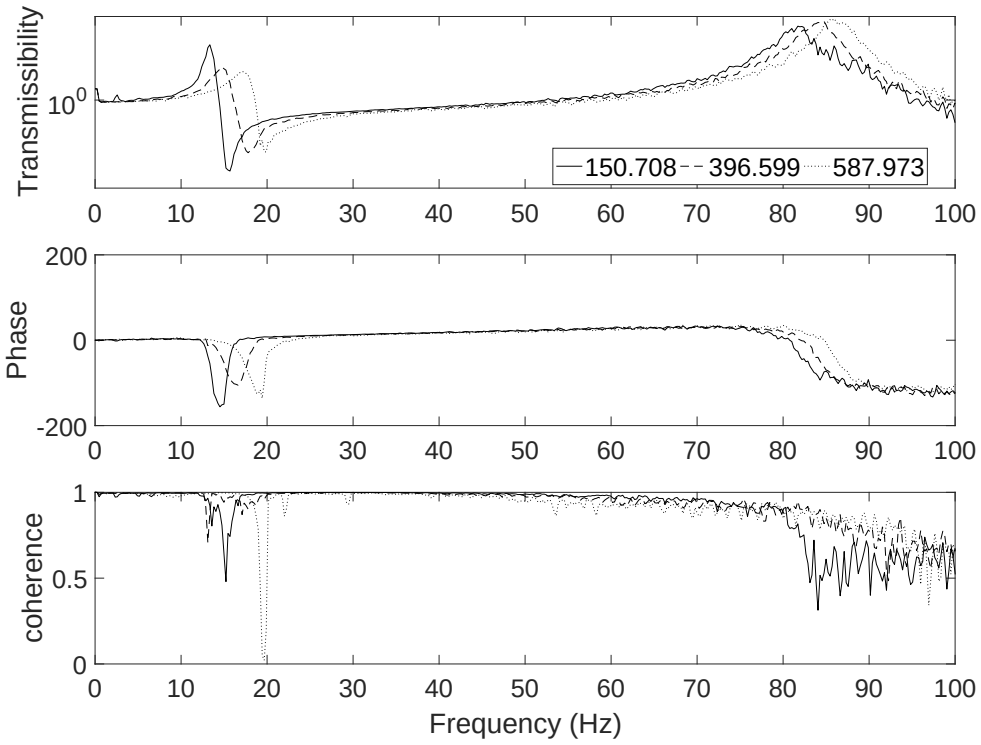

Figure 6.1: Frequency response function (transmissibility) of a non-cracked cantilever aluminium beam with rectangular cross section (height=2mm, width=15mm and length=330mm), rotating at three different speeds (150, 396 and 587rpm). Random excitation is applied at the centre of rotation of the cantilever beam and the response is measured at 70mm from the root of the beam. A Go Pro hero 4 black camera is used with images acquired at 240 frames per second, a shutter speed of 1/960s and an equivalent ISO of 100.

6.2.1 Model updating

The first and second natural frequencies of the intact rotating beam were measured for different rotational speeds and were used to update the boundary conditions in the simulation model. Typically, in structural dynamics, the experimentally measured frequencies are lower than predicted ones due to the additional flexibility in the physical boundary conditions. To update the model, a linear and torsional spring were added to represent the constrained end of the cantilever, representing the additional flexibility due to the complex mechanism of the rotating hub and linear bearings and replacing the fully built in conditions.

The theoretical admissible function $Y(x)$ of the rotating cracked beam, which is based on static deformation of cantilever beam under a concentrated load applied at the free end, can be expressed as Yashar et al. (2018);

$$Y_{wn}(x) = \left(\frac{x}{L}\right)^{n-1} \frac{1}{EI}\left(\frac{-Lx^2}{2} + \frac{x^3}{6}\right) \tag{6.1}$$

where L, x, n, E and I represent the beam length, distance from the root of beam to the location of the lateral deflection, order of the shape function, Young's modulus of elasticity and the second moment of area, respectively.

In the updated model the end attached to the rotating hub, which is considered to be at a point, is constrained by a linear and a rotational spring and the second end is free, as illustrated in Figure 6.2.

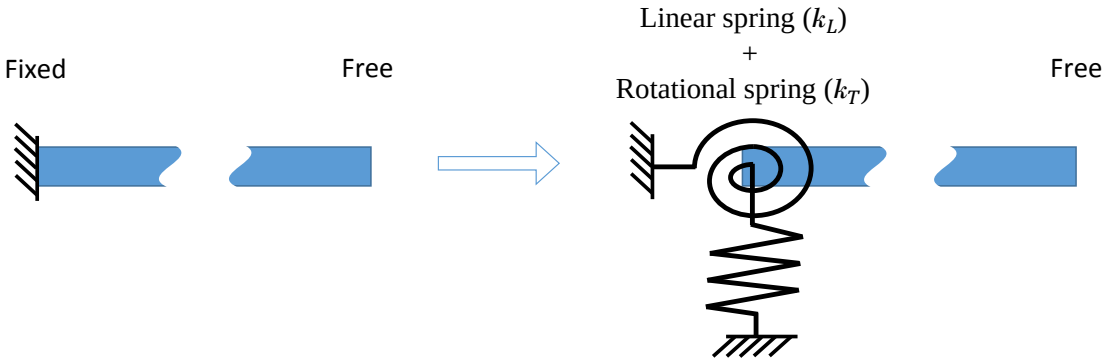

Figure 6.2: The boundary conditions of the beam, initial theoretical model and updated model to fit to the experimental test beam.

The corresponding updated admissible function for predictions of the rotating cracked beam can be expressed from the resulting tip load static flexibility shape function Wang and Yang (2011);

$$Y_{wn}(x) = \left(\frac{x}{L}\right)^{n-1}\left(\frac{1}{EI}\left[\frac{-Lx^2}{2}+\frac{x^3}{6}\right]-\frac{xL}{k_T}+\frac{1}{k_L}\right); \tag{6.2}$$

where k_L and k_T represent the linear and torsional spring stiffnesses respectively at the attached end of the rotating beam.

A genetic algorithm was used to obtain the two stiffness parameters that minimise the error between the experimental intact beam frequency-speed curve and the curve obtained from simulation model as expressed by the error function.

$$error_{stiffness} = \sum_{\Omega=\Omega_1}^{\Omega_n} \frac{|f_{1s}(k_L,k_T)-f_{1e}|}{f_{1e}} + \frac{|f_{2s}(k_L,k_T)-f_{2e}|}{f_{2e}} \tag{6.3}$$

Here f_1 and f_2 are the first and second natural frequencies of the rotating intact beam, $\Omega_{1,2,3,\ldots,n}$ represent the speeds at which the natural frequencies are estimated and the subscripts s and e refer to the simulation and the experimental values, respectively. Here a genetic algorithm was used due to its capability in finding the global minimum for the error in terms of the two unknown stiffnesses.

6.3 Crack detection using a frequency-speed curve

Crack detection herein is based on a frequency change using the experimental measurements and numerical model predictions. The crack detection process is divided into two main steps. Firstly, the simulation model boundary conditions were updated using the experimentally measured first two natural frequencies of the uncracked rotating beam as mentioned in Section 6.2.1. Secondly, the comparison was made between the measured frequencies of the rotating cracked beam and the updated simulation model results for a cracked rotating beam.

The frequencies of a cracked rotating beam were measured for various rotational speeds and the experimental natural frequencies versus rotational speed curves were generated. From the updated simulation model, a two-dimensional parametric study was performed to generate the frequency change due to different crack location and crack depth. Then, a comparison was made between the experimental curves and corresponding theoretical curves. This comparison was obtained using the MATLAB Optimization Toolbox.

A genetic algorithm was used to find the global minimum error. In general, this algorithm was inspired from the Darwinian evolution theory which is based on the mutation in the new generation and natural selection as a filter Vakil-Baghmisheh et al. (2008); Mehrjoo et al. (2013). Figure 6.3 illustrates the procedure to obtain the crack location and depth. The search area was limited to the actual beam length and the crack depth between 0 to a maximum crack depth ratio of 0.60 of the beam thickness in order to find the best fit crack location and depth.

The procedure starts by generating a population of about 70 elements. Each element contains one chromosome which is a pair comprising the crack location and depth. The search minimises the error between the experimental and updated simulation model curves for the natural frequencies versus rotational speed. The two parametric chromosomes namely the crack location and depth, are given in Equation 6.4. The elements that produce minimum error will survive to the next iteration and will produce a new generation. The crossover fraction set to 0.8 and the uniform mutation with rate 0.01 are setted as a default of the Matlab optimisation toolbox. The chromosomes of the fitted elements are retained, whilst the rest of the elements will be discarded. The iteration loop will stop when the maximum stall generation reaches 20 and the function tolerance selected is equal to 1×10^{-5}.

$$error_{crack} = \sum_{\Omega=\Omega_1}^{\Omega_n} \frac{|f_{1s}(C_L, C_D) - f_{1e}|}{f_{1e}} + \frac{|f_{2s}(C_L, C_D) - f_{2e}|}{f_{2e}} \tag{6.4}$$

Here C_L and C_D represent the crack location ratio $\frac{x_c}{l}$ and the crack depth ratio; the latter is equal to the crack depth divided by the beam thickness.

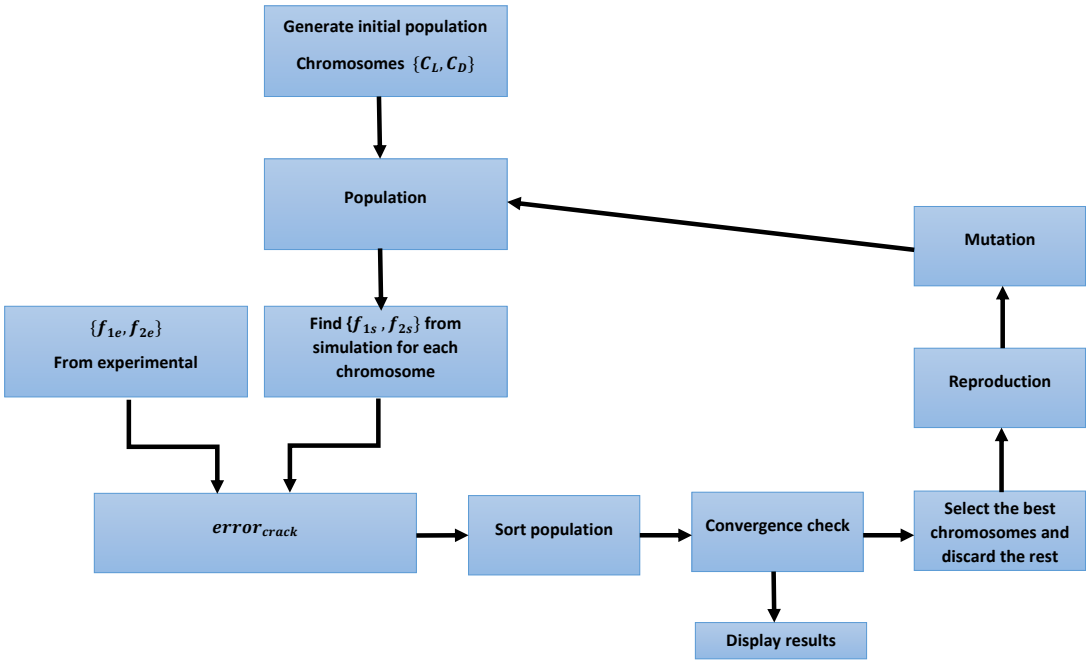

Figure 6.3: The procedure for obtaining the crack location and depth based on a genetic algorithm.

6.4 Crack detection experimental validation

The experimental tests were performed to validate the proposed crack detection method with two aluminium beams. The material properties were the density of 2633 kg.m^{-3} and modulus of elasticity 71 GPa. The geometric dimensions of both beams were 330 mm length, 15 mm width and 2 mm thickness. A crack with 0.75 mm depth was introduced to the first beam at a distance 34 mm away from the end constrained by the rotating hub. For the second beam a deeper crack with 1.1 mm depth was introduced at a distance 24.5 mm away from the end constrained by the rotating hub The test procedure, results and discussion will be presented in the next three sections.

6.4.1 Case 1

The intact natural frequencies of the first beam was measured first to update the model by adding equivalent linear and torsional springs to the boundary conditions at the cantilever attached end. The stiffness of the springs determined by minimising the error using Equation 6.3.

The numerical values for the linear and torsional spring stiffnesses were investigated. The estimated and best fit linear spring k_L is almost constant with rotational speed and is equal to 166.4 kN.m^{-1}. However, the best fit torsional stiffness k_T is not constant, being a function of the rotational speed and varying linearly from 45 Nm at a rotational

speed of 150 rpm, increasing up to 50.7 N m at a speed of 510 rpm, ie about 10% variation.

Substituting k_L and k_T for the intact beam in Equation 6.2 produces a closer numerical intact beam model to the experimental measurements, as illustrated in Figure 6.4 for the rotating intact beam.

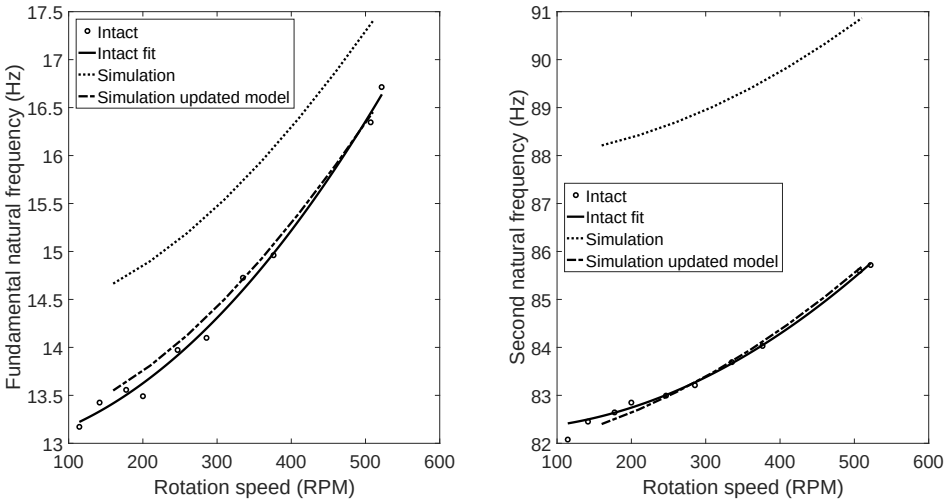

Figure 6.4: Comparison of the fundamental and second natural frequencies of the flapwise vibration between the experimental results and theoretical results using a Rayleigh-Ritz approach Yashar et al. (2018). The length of the beam is 330mm and the cross section is 15mm wide and 2mm thick. The solid curve refers to an experimental data fit. The dotted curve is for the numerical simulation assuming a fully fixed base for the beam. The dash-dotted curve represents the updated simulation results.

After introducing the crack to the first beam, the effect of the crack can be observed in Figure 6.5. The measured results for the intact beam marked with "o" and cracked beam marked with "x". For example, at the rotational speed of 202 rpm the first and second natural frequencies of the intact beam are 13.64Hz and 82.76Hz, while the corresponding natural frequencies of the cracked beam are 13.56 Hz and 82.53, Hz respectively. This reduction was predicted previously Yashar et al. (2018) due to the additional local flexibility from the edges of the crack.

Finally, using a genetic algorithm with two chromosome parameters namely the crack location and crack depth a global minimum for Equation 6.4 was determined. The minimum error indicates a closer match for the predicted fundamental and second natural frequencies versus speed curves to the experimental results. In this validation test, the lowest value of the error function was 0.0312 and the value of the crack location and depth were accurately estimated and found to be 34.32 mm and 0.762 mm, respectively. The actual crack location and crack depth were 34 mm and 0.75 mm, respectively.

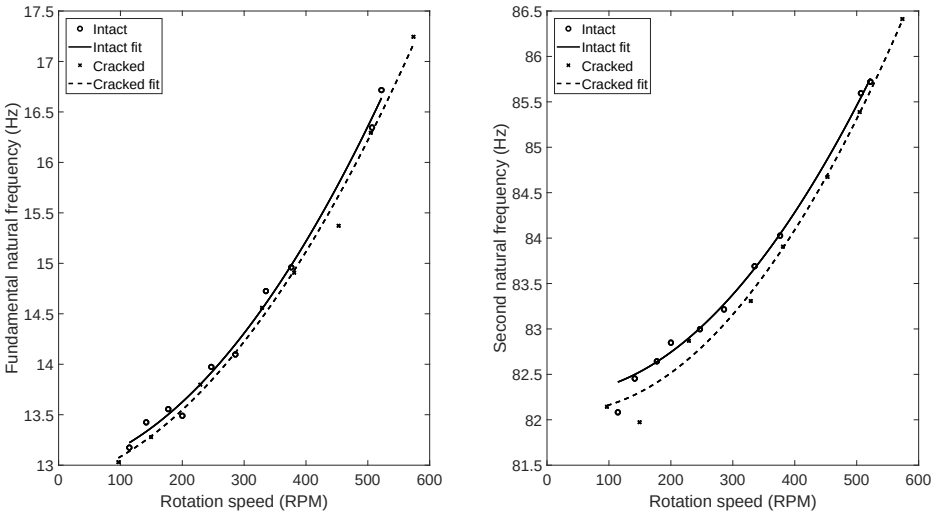

Figure 6.5: The fundamental and second lowest natural frequencies are measured using a high-speed camera for a rotating beam with and without crack. The beam length is 330 mm and the cross section is 15 mm wide and 2 mm thickness. The crack is located at 34 mm from the root of the beam and the crack depth was 0.75 mm.

6.4.2 Case 2

A test was then repeated and assessed the applicability of the procedure on a second beam having the same geometrical dimensions and physical properties. The estimated and best fit linear spring k_L is almost constant with rotational speed and identical to case 1 being equal to 166.4 kN.m^{-1}. The best fit for the torsional stiffness k_T is not constant, being a function of the rotational speed and varying from 65.41 Nm at a rotational speed of 150 rpm decreasing down to 56.54 Nm at a speed of 510 rpm. However, the deeper crack introduced to this beam was at 24.50 mm thus closer to the root of the beam with a depth equal to 1.1 mm. The equivalent linear and torsional springs were determined from the difference between the simulation and experimental results for the intact beam as shown in Figure 6.6. The natural frequencies measured for the cracked beam and the reduction was significant, as shown in Figure 6.7, due to the size and location of the crack. The estimated crack location from the frequency-speed curve fitting was at 24.62 mm with a depth equal to 1.07 mm. The difference between the actual and estimated crack location is 0.12 mm and the difference for the crack depth is 0.03 mm.

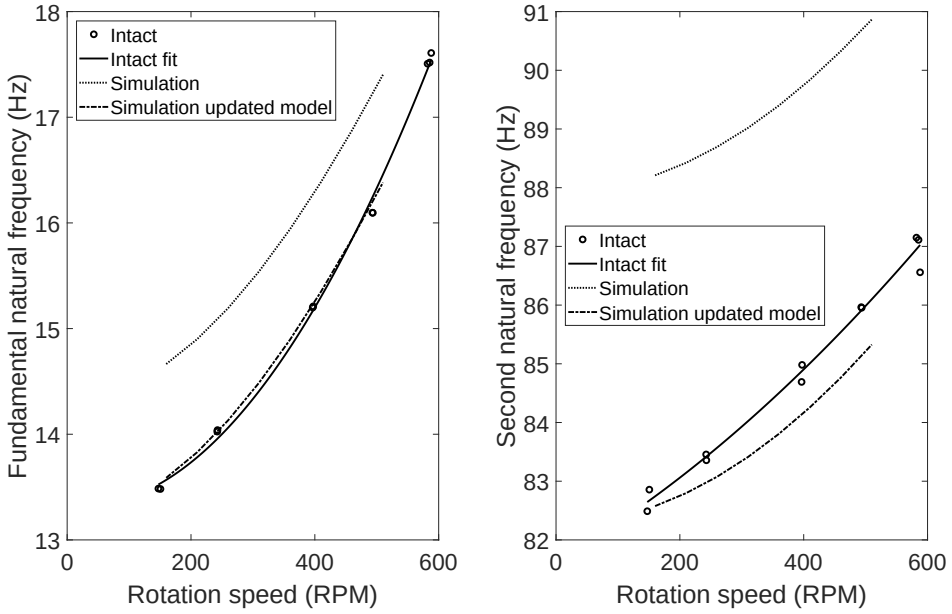

Figure 6.6: Comparison of the experimental results with numerical simulation using an updated uncracked beam model with translation and rotational springs at the root of the beam.

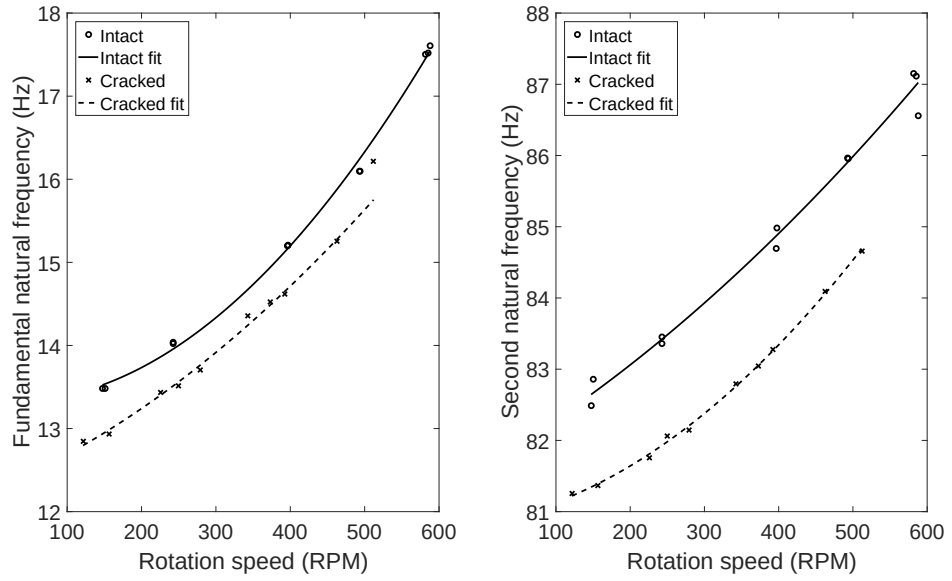

Figure 6.7: The fundamental and second lowest natural frequencies measured using a high-speed camera for a rotating beam with and without crack. The length of the beam is 330 mm and the cross section is 15 mm wide and 2 mm thick. The crack is located at 25.5 mm from the root of the beam and the crack depth is 1.1 mm.

6.4.3 Discussion

Theoretically, the closer the crack is to the root and the deeper that the crack is, the more accurate the detection results should be, due to the greater effect of the crack on the natural frequencies. However, the experimental results show a slightly increased error in the estimated crack depth for the closer and deeper crack. The error between the actual and estimated crack depth is 0.018 mm. This error could be related to the experimental error in measuring the natural frequency or due to the multi post processing of the data including digital image correlation, Nyquist circle fitting, model updating and the optimization process in determining the boundary conditions.

In this study, the model updating is based on comparing the experimental and estimated uncracked beam frequencies. However, for the sake of evaluating the accuracy of the updated method, a new simulation was performed applied to the cracked beam based on the comparing the measured cracked with the actual crack location and depth substituted into the model. The results obtained for first beam are shown in Figure 6.8 and the maximum error is less than (0.52%) between the two estimations, i.e the update based on intact measured and cracked measured. Figure 6.8 shows the results for the second beam and the maximum error is about (1.34%) between the two estimations. The results of this test show a higher error in the updated second beam, and this reveals the slightly higher error in identification of the crack in the second case due to the crack depth, which is close to the limitation of the crack modelling assumption. The maximum numerically valid allowed crack depth ratio is 0.6 for the derived expressions and in this experiment it is 0.55. Also another factor which might affect the test such as the change in the boundary conditions of the clamped end of the beam in addition to the aforementioned factors. One would expect that the clamping force in the attachment of the beams tested would produce some variability. In practice, this might well be the cause of the slight of difference in the estimated rotational spring stiffness at the root of the beam.

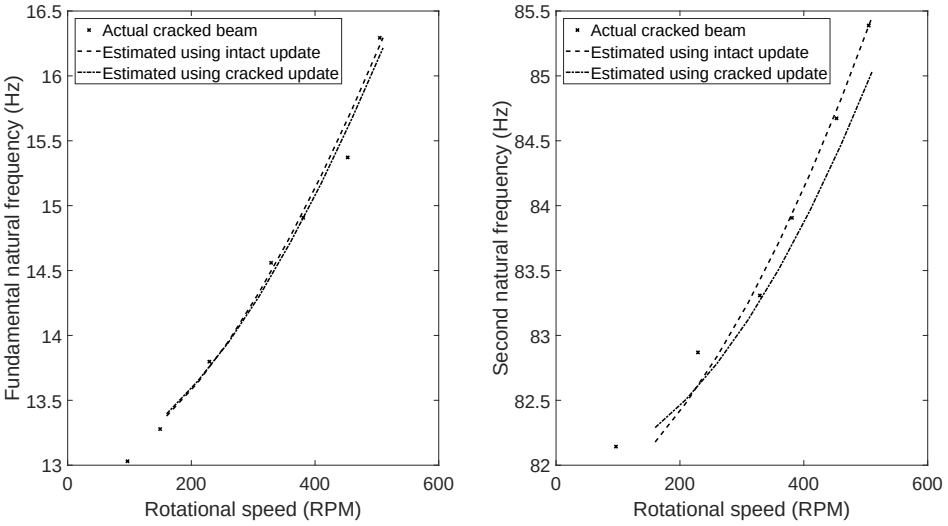

Figure 6.8: The comparison between the actual and two different estimated results using updated intact and cracked beams for the fundamental and second lowest natural frequencies of a rotating cracked beam. The length of the beam was 330 mm and the cross section was 15 mm wide and 2 mm thick. The crack located at 34 mm from the root of the beam and the crack depth was 0.75 mm.

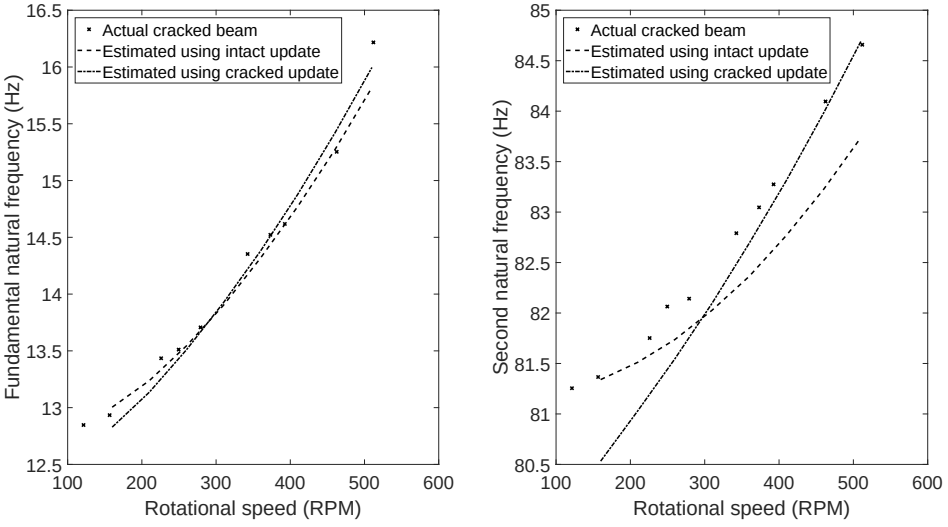

Figure 6.9: The comparison between the actual and two different estimated results using updated intact and cracked beams for the fundamental and second natural frequencies of a rotating cracked beam. The length of the beam is 330 mm and the cross section is 15 mm wide and 2 mm thick. The crack was located at 25.5 mm from the root of the beam and the crack depth is 1.1 mm.

6.5 Robustness of the detection method

The reliability of the proposed crack identification method was investigated using a Monte-Carlo simulation(MCS). This simulation was used to determine the sensitivity

of the crack location and depth identification on a rotating beam. The simulation was performed for different combinations of normalised random crack location and depth in the updated rotating cracked beam model. The same dimensions, boundary conditions and material properties were used for each case.

The simulation was repeated for 100 samples for each of four specified crack locations along the beam and these locations were selected at fixed positions corresponding to points where the ratios of the positions to the length of the beam are 0.1, 0.3, 0.6 and 0.9 from the supported end of the beam.

Figure 6.10 shows the simulated and estimated crack locations and depth for all four locations. The closer that the introduced crack is to the fixed end, the more accurate were the estimated results due to the greater effect of the crack on the reduction of the natural frequencies. In contrast, the crack identification becomes difficult when a crack is located closer to the free end due to the smaller reduction in the natural frequencies. For example, a crack at a location ratio of 0.9 shows in Figure 6.10 an increased error in the crack identification. The optimisation algorithm had difficulty in determining both simultaneously the exact location and depth due to the flat area in the global minimum of the optimisation surface.

Figure 6.11 show an increase in the standard deviation of the error in the crack depth ratio and location ratio respectively for cracks located closer to the free end of the rotating beam.

Regarding the effect of the crack depth, a deeper crack is more accurately estimated due to the greater reduction in the natural frequencies. Figure 6.12 shows the comparison of the standard deviation for the two sets of the crack depth. In both figures, for the crack depth ranging between 0.36-0.39 of the beam thickness, the identification procedure produces smaller error for the standard deviation compared to the case for larger cracks in the depth range of 0.4-0.46.

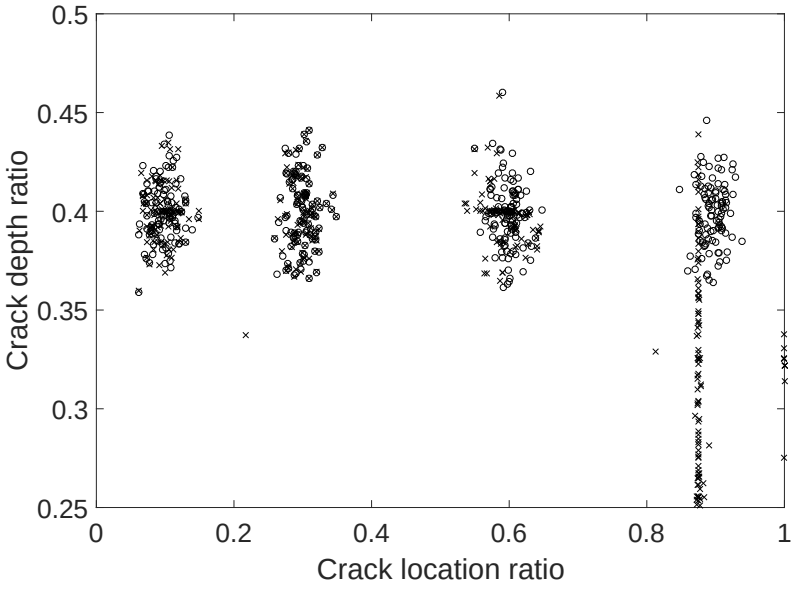

Figure 6.10: The simulated crack "$\circ$" and estimated crack "$\times$" for four different crack locations at position equal to 0.1, 0.3, 0.6 and 0.9 of the beam length. These results obtained from simulated frequency-speed curves for the two natural frequencies for the rotational speed range between 160 rpm to 510 rpm.

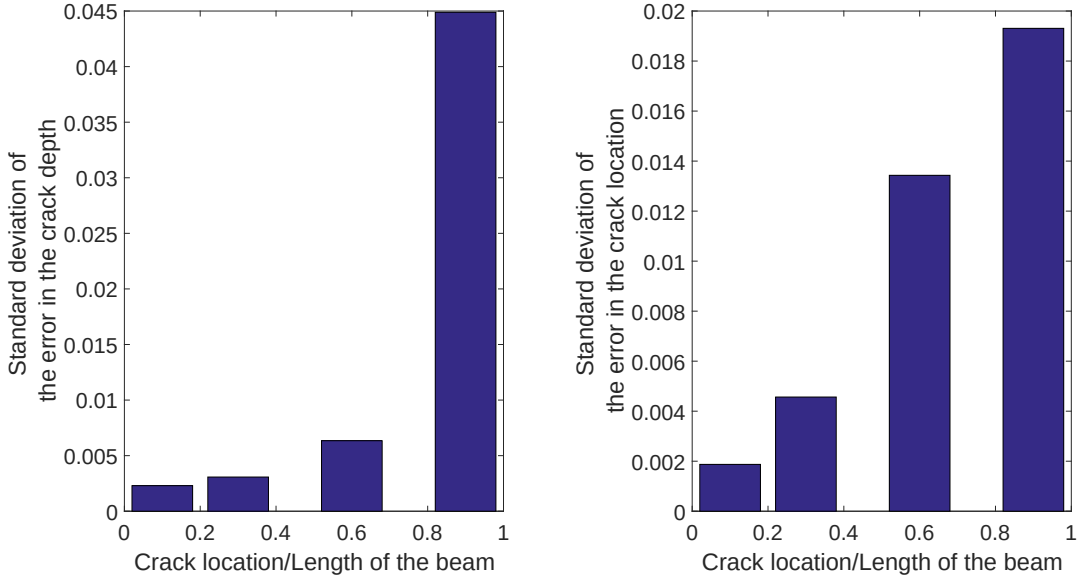

(a) (b)

Figure 6.11: The standard deviation of the normalised difference between the actual and estimated crack depth (a) and crack location (b), where the value of the standard deviation increases when the crack is located close to the free end of the rotating cantilever beam.

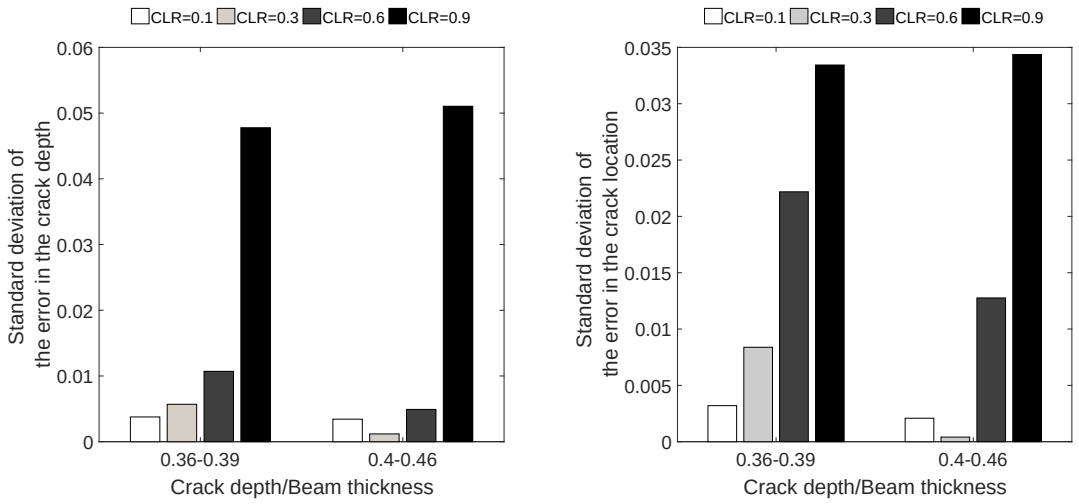

Figure 6.12: The standard deviation of the normalised difference between the actual and estimated crack depth (a) and crack location (b), where the value of the standard deviation decreases when the introduced crack is deeper. CLR = crack location divided by beam length.

6.6 Conclusions

Using the previous developed optical methods in Chapter 5, the measurement technique was applied to rotating intact and cracked beams in order to produce a crack detection identification. This method estimate a crack location and depth in a rotating cracked beam using the predicted natural frequency-speed curves. The frequency-speed curves of the intact beam were initially used to update a numerical model for the boundary conditions at the root of the beam. Then, the numerical frequency-speed curves of the cracked beam were used to identify the crack. The experimentally detected crack location and depth are found to be in good agreement with the actual crack location and depth. This method shows a sensitivity to the boundary conditions changed at the clamped end of the rotating cantilever beam due to the model updating step.

Finally, Monte-Carlo simulations were performed to check the robustness of the frequency-speed crack detection method and identify how accurately the crack location and depth can be determined. The method was subsequently shown to be more accurate in detecting the location and depth of the crack when a crack is deeper or located close to the supported end of the rotating cantilever beam. The next chapter will be deal with active vibration control of the rotating beam using the optical measurement procedure. This has the potential to reduce the vibration response, increasing the fatigue life or reducing the accrue of failure.

Chapter 7

Active vibration control of a rotating beam using the developed model and optical measurement

7.1 Introduction

Vibration control of rotating beams plays an essential role in aviation and space applications for better performance and increased stability. Numerous investigations deal with vibration control of beams using passive modification, such as using tuned mass dampers and eddy current dampers Sodano et al. (2005); Younesian et al. (2006, 2008); Cheng and Oh (2009); Yan et al. (2012). In addition to passive control, active vibration control has been widely used for control, where actuators and sensors are employed typically to generate velocity feedback using inertial actuators by Rohlfing et al. (2016); Camperi et al. (2016) and piezoelectric actuators by Xue and Tang (2008).

In passive control, the change in the response of the structure can be obtained by modifying the system properties such as damping and stiffness. In active control, the structural response is controlled by adding control forces to the structure using sensors and actuators. Although the extra added equipment may increase the cost of the system, the system's performance however in vibration suppression is significantly improved when compared with passive control.

This chapter presents an application of the developed rotating beam model from Chapter 3 in conjunction with the optical vibration measurement technique in Chapter 5 to active vibration control of a rotating beam. A simple velocity feedback system is developed. It comprises a collocated electromagnetic force actuator and a hi-speed camera.

The latter is used as a velocity sensor and implemented to suppress the response of the rotating beam by means of actuator applied active damping. The colour blob detection method (see Section 5.3.3) is used to extract the displacement from the images as a function of time. This information is subsequently differentiated in real time to obtain the velocity of the beam. The simulation model for the active control system, based on velocity feedback, and the model of the rotating beam, developed in (see Chapter 3.2), is used for the simulations. In an ideal velocity feedback loop, the collocated sensor-actuator guarantees unconditional stability Rohlfing et al. (2016) if the dynamics of the actuator is not included. In the experimental test, different factors affect the stability, especially the sampling frequency and feedback gain.

7.2 Active control simulation

The simulation model of the rotating beam with vibration control is based on velocity feedback as shown in Figure 7.1 The system based on the developed FE model in Chapter 3, where **M**, **C**, **K** and **S** represent the mass, damping, stiffness and rotational stiffness matrices for a rotating beam that has been divided into five beam elements. Each element has two nodes and each node has two degrees of freedom, which are the vertical displacement and slope as shown in Figure 7.2. $F_p(t)$ and $F_m(t)$ represent the excitation forces at the base of the beam and the controller feedback force. The measurement point and the actuator collocated at the third node, where the sensor measures the vertical velocity of the node and the actuator applies a vertical force. The dynamic equation of the system with the control is

$$\mathbf{M}\ddot{w}(t) + \mathbf{K}w(t) + \mathbf{C}\dot{w}(t) = F_m(t) + F_p(t) \tag{7.1}$$

The velocity feedback is activated by the manual switch. The signal of the feedback depends on the gain and actuator transfer function. The actuator is made of a permanent neodymium magnet and electromagnetic coil. The generated force by the actuator, which is shown in Figure 7.3, can be expressed using Lorentz law. The current i flows in a conductor L_m in a magnetic flux density of B_m, which produces a control force F_m given by Equation 7.2

$$F_m = B_m L_m i \tag{7.2}$$

The applied current is chosen to be proportional to the velocity therefore the current can be expressed as,

$$i = -h_m \dot{w} \tag{7.3}$$

where h_m is the velocity to current conversion constant. The relation between the force and the velocity can be written as,

$$F_m = B_m L_m h_m \dot{w} \tag{7.4}$$

The characteristic of the actuator is measured by applying a 300 mA current to the coil and measuring the force generated between the magnet and the coil, which was equal to 0.39 N when the distance between the coil and magnet is 4 mm. Substituting these values in Equation 7.2 produces results for the value of $B_m L_m$ which is equal to 1.3 T.H^{-1}.

By substituting Equation 7.4 into Equation 7.1 the dynamic equation of the system becomes,

$$\mathbf{M}\ddot{w}(t) + \mathbf{K}w(t) + (\mathbf{C} + B_m L_m h_m)\dot{w}(t) = F_p(t) \tag{7.5}$$

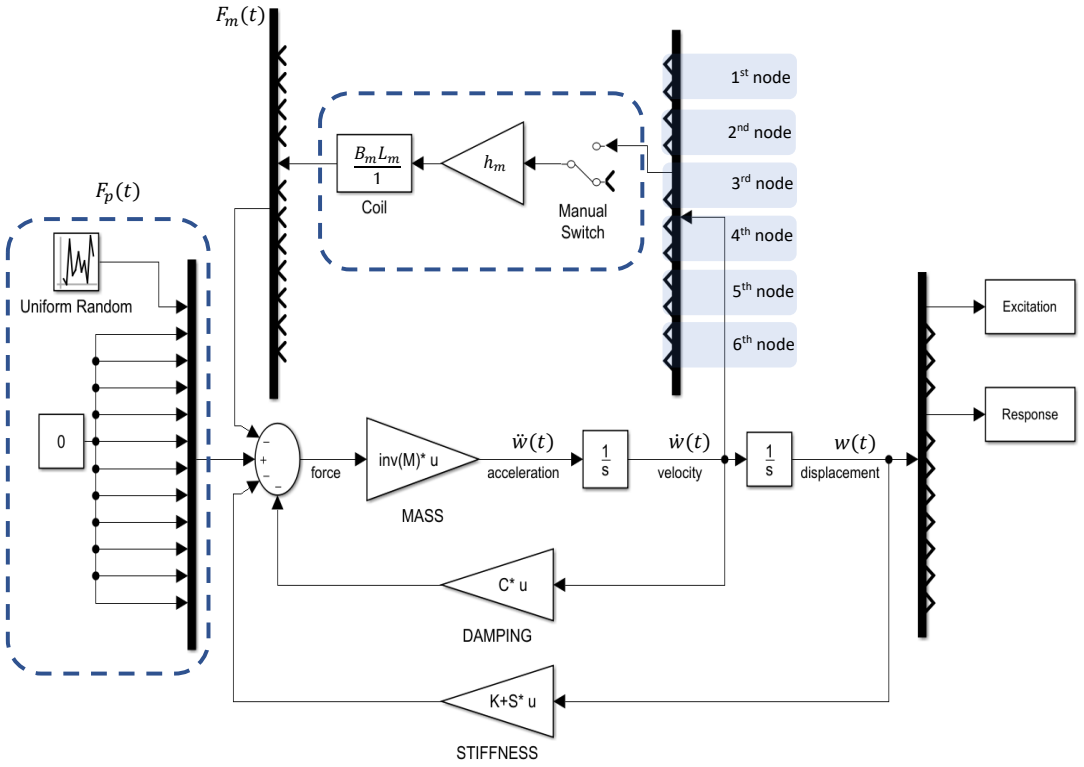

Figure 7.1: The Simulink diagram of the system with velocity feedback. The manual switch is placed to select between open-loop and closed-loop systems. The Mux is used to select the specific degree of freedom to apply the force or to measure the velocity/displacement.

The amplitude of transmisibility and phase obtained from simulation of the open-loop and closed-loop response of the system are shown in Figures 7.4,7.5 and 7.6 for a non-rotating beam and for two rotational speeds of 250 rpm and 500 rpm, respectively. Active control shows a significant reduction in the transmisibility amplitude. Here, open-loop is the system under base excitation with no active control and closed-loop is the system under base excitation with active control.

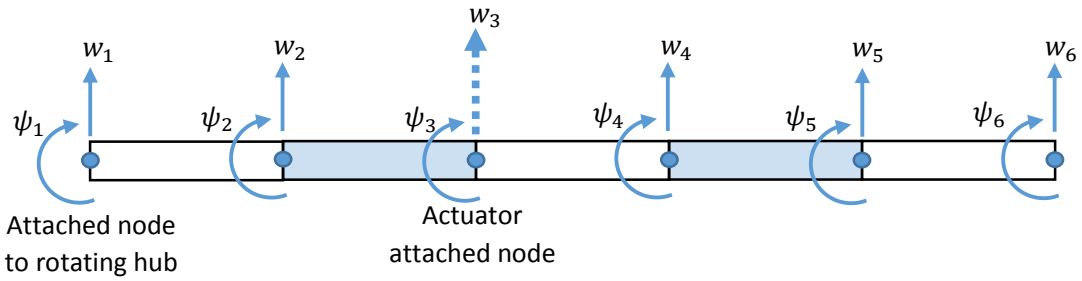

Figure 7.2: The finite element model representation of a rotating beam. The first node is attached to the rotating hub. The vertical displacement in the third node is attached to the actuator.

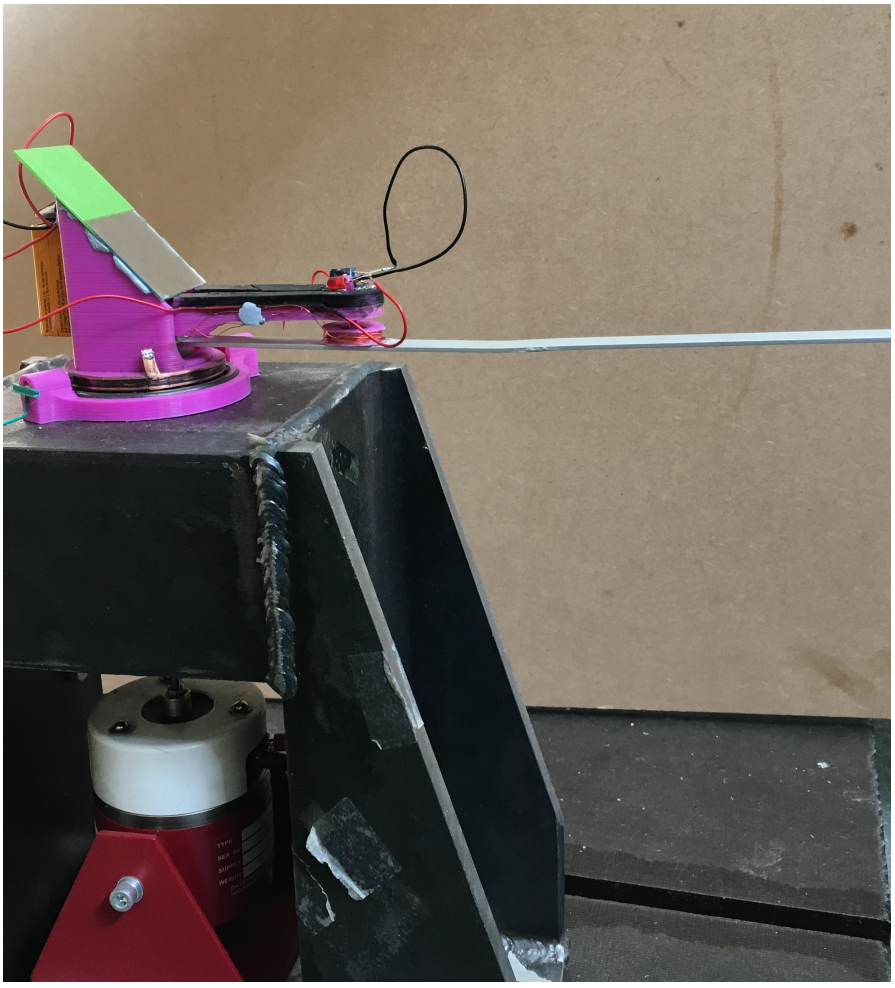

(a)

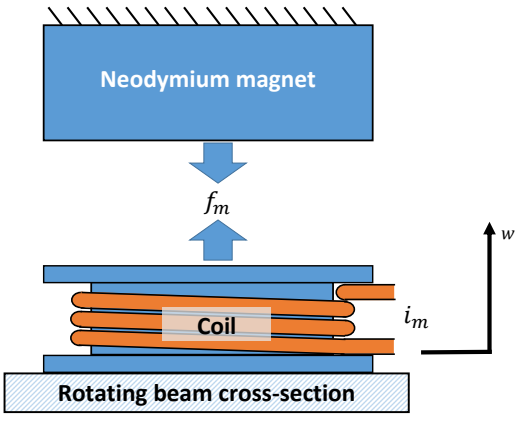

(b)

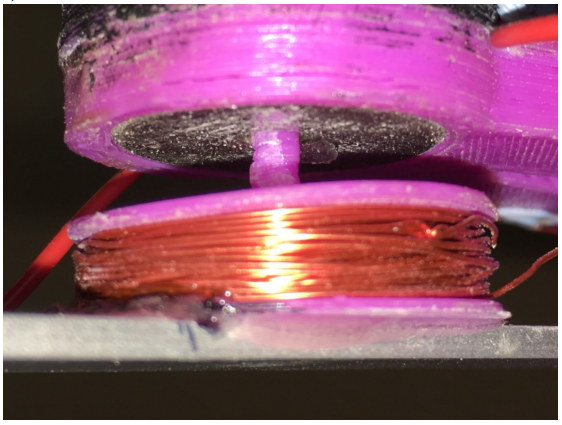

(c)

Figure 7.3: The actuator used for the vibration control. (a) The test rig with attached mirror and actuator, (b) The configuration of the actuator components and (c) the actuator with magnet and coil attached to the rotating beam.

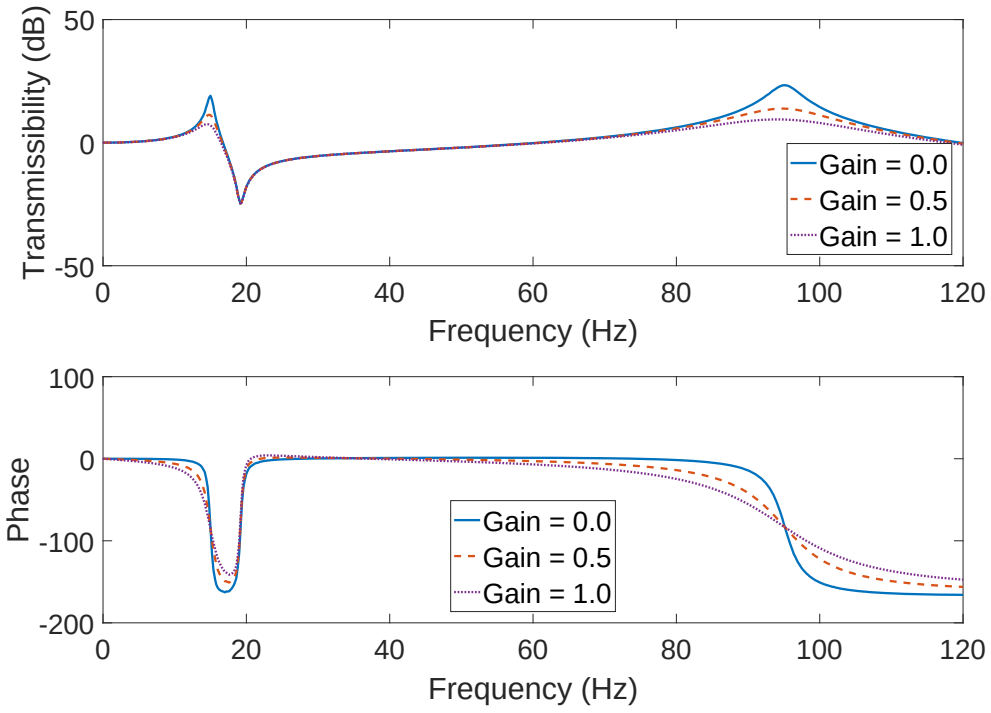

Figure 7.4: The simulated transmisibility of the non-rotating beam. The first (15 Hz) and second (95 Hz) resonance of the beam without control represented by the solid line. The dashed and dotted lines represent the close-loop system with the velocity feedback gains equal to 0.5 and 1, respectively.

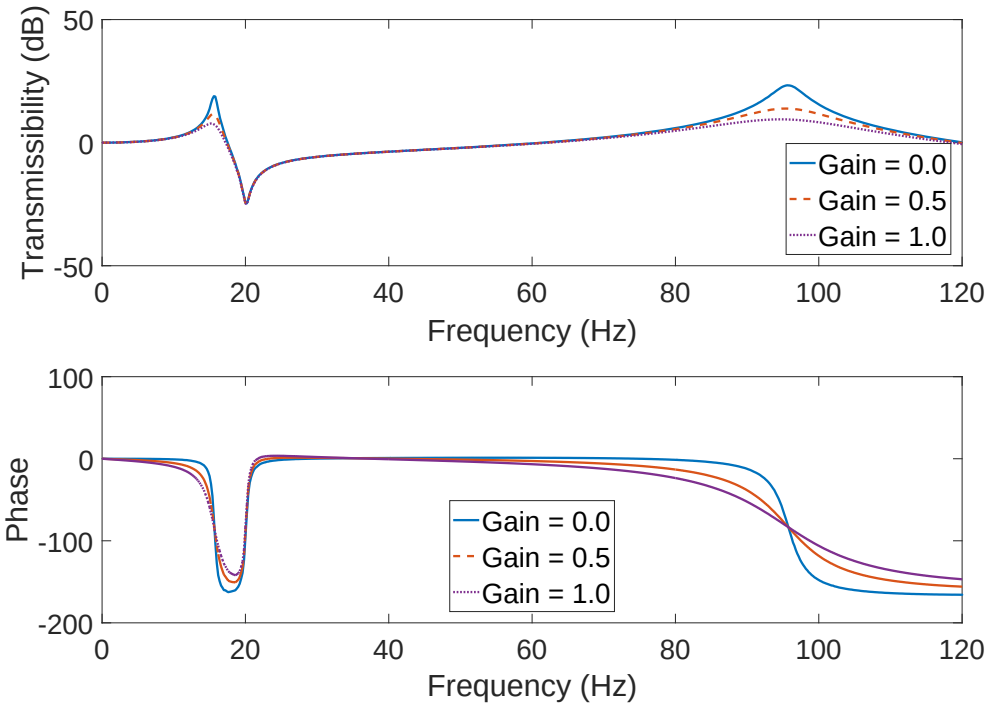

Figure 7.5: The simulated transmisibility of a beam rotating at 250 rpm. The first (15.6 Hz) and second (95.8 Hz) resonance of the beam without control represented by the solid line. The dashed and dotted lines represent the close-loop system with the velocity feedback gains equal to 0.5 and 1, respectively.

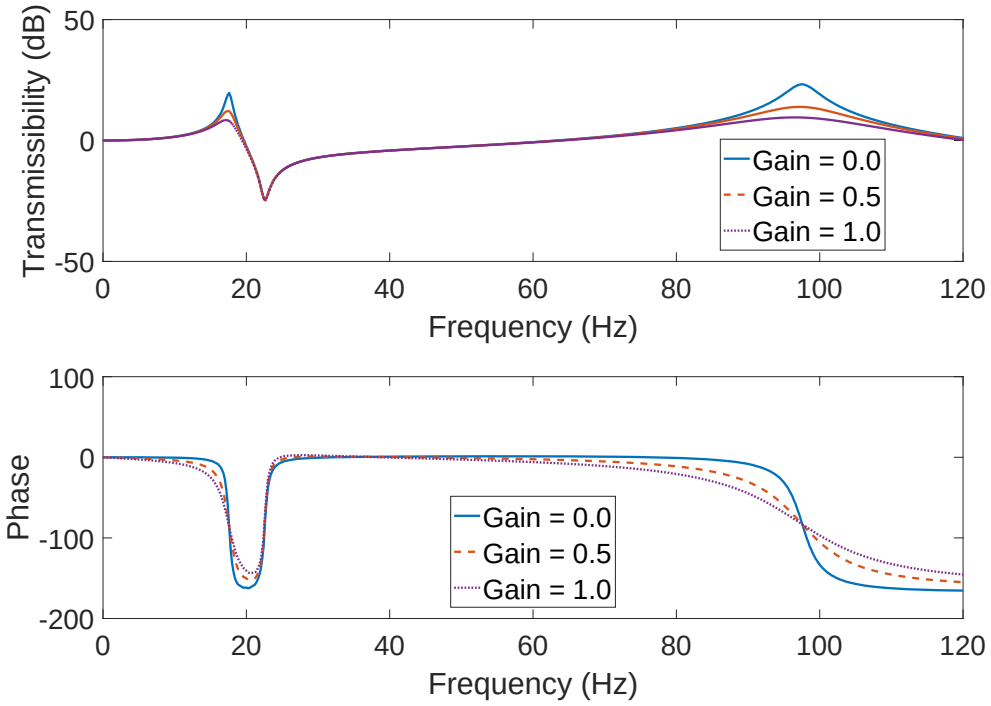

Figure 7.6: The simulated transmisibility of a beam rotating at 500 rpm. The first (17.6 Hz) and second (97.6 Hz) resonance of the beam without control represented by the solid line. The dashed and dotted lines represent the close-loop system with the velocity feedback gains equal to 0.5 and 1, respectively.

7.3 Experimental validation

The test rig was updated for the active control test. The new modification was designed and simulated using SolidWorks software and manufactured using a 3D printer. Basically, the new mount consists of an electromagnetic actuator and a marker holder in addition to the reflection mirror.

The electromagnetic actuator comprises of two parts; a neodymium magnet ring and an electromagnetic coil. The direction and amount of current that passes through the coil defines the force direction and quantity between the coil and the magnet.

The distance between the coil and the magnet is about 4mm. The relationship between the current and the force of the magnet is about $L_m B_m = 1.3$ T.H^{-1} as described in Section 7.2 . The dimensions of the magnet are 20mm, 10mm and 5.2mm for the outer diameter, height and inner diameter, respectively. The pulling force of the magnet is approximately 100 N.

Furthermore, two LED lights were attached on the actuator as markers. One of the LEDs is connected to the coil, which is attached to the beam and the second one is directly attached to the magnet to represent the base excitation motion. The LEDs are selected with two different colours to separate the displacements by using digital image processing.

A copper ring with a carbon brush is used as a slip ring to connect the coil of the actuator, which is on the rotating part, to the amplifier which is on the non moving part.

The test setup in this chapter is similar to the single camera with the mirror in Figure 5.10(c) that was described in Chapter 5. However, the previous test was used to measure the vibration of the beam. In this test, the measured signal is used as a velocity feedback to excite the actuator in order to apply a control force to the beam. The controller can reduce the amplitude of the vibration by damping the amplitude of the fundamental or higher frequency resonance of the beam.

In order to control the beam in real time, the camera should be connected to the data image processing unit directly and the images should be processed fast enough to reduce the effect of any delay in the feedback system. A high speed camera was used in this test, with a modified lens to reduce the image distortion and to cover the required field of view.

The lens of the camera should be in alignment with the centre of the rotation to reduce the distortion. A LabVIEW block diagram was assembled to assist with aligning the camera with the centre of rotation. This program uses the rotating markers by collecting 62 points each second and from the collected point clouds a circle which is fitted to

determine the centre and the radius of the circle. Then, the radius is changed by varying the location and angle of the camera and the minimum radius represents the best alignment between the camera and the centre of the rotating beam. After locating and fixing the camera, another LabVIEW block diagram was implemented and used to measure and control the vibration of the beam.

The test setup is shown in the Figure 7.9, where the camera is fixed on a tripod and it is about 2m away from the test rig.

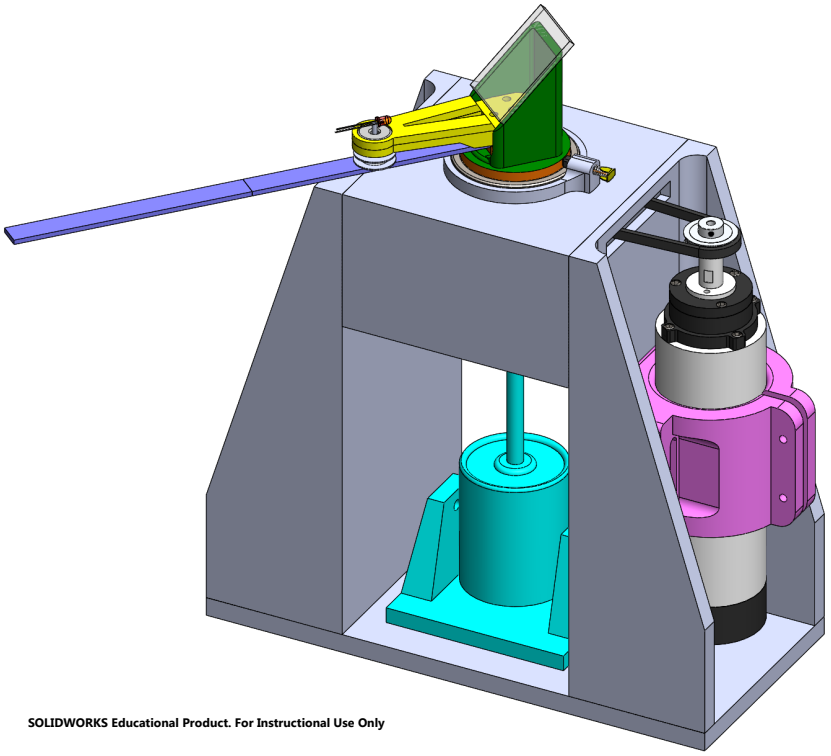

Figure 7.7: Modified hub for vibration control test.

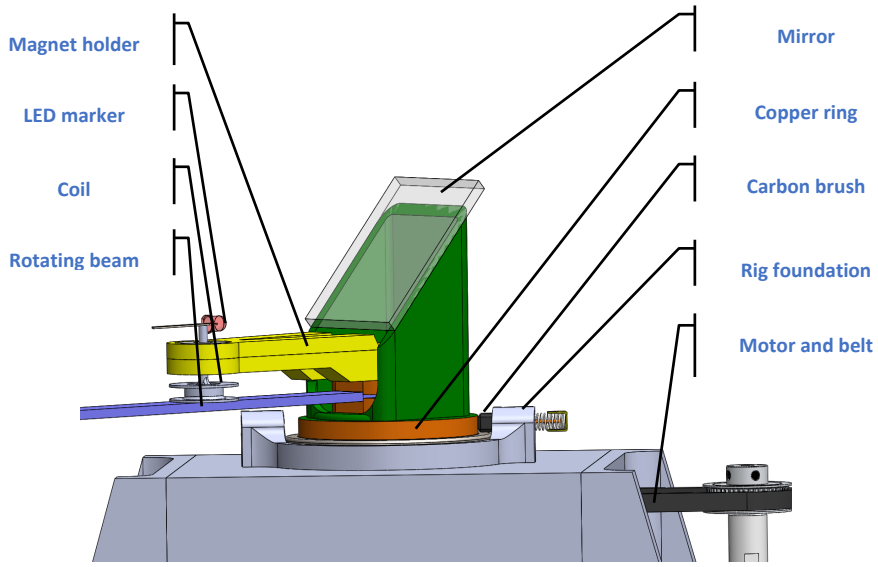

Figure 7.8: Modification on the rotating hub mount. The rotating hub comprise an electromagnetic actuator, mirror, two LEDs as markers and a slip ring to connect the actuator to the amplifier.

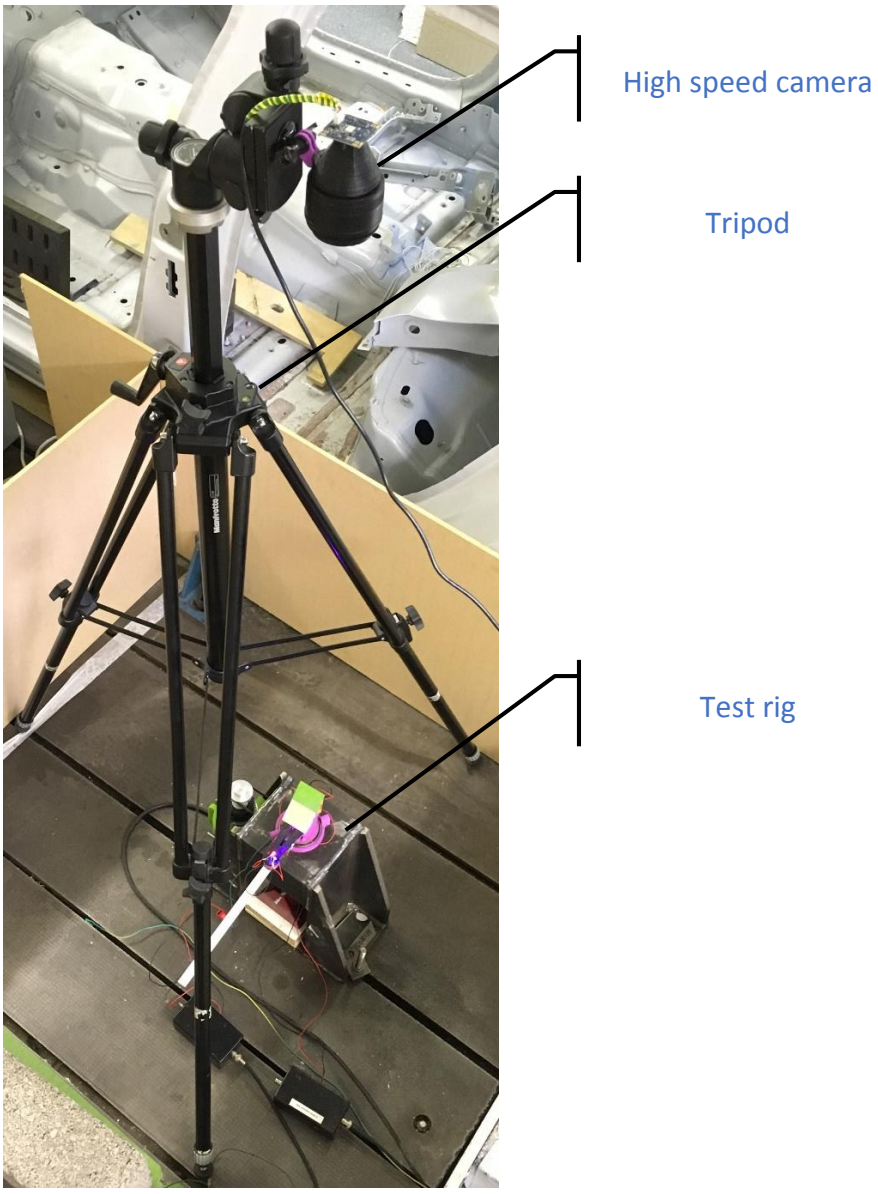

Figure 7.9: Test setup for the rotating beam control using an optical system and velocity feedback.

7.3.1 Vibration control of a non-rotating beam

A pre-test was performed first for a non-rotating beam in order to verify the optical measurement. An accelerometer was attached to the base of the beam to measure the excitation and another accelerometer attached to the marker to measure the response of the beam at the same point of the marker. Figure 7.10 shows the agreement between the results from the accelerometer and the optical system for a beam of 300 mm length, 15 mm wide and 2 mm thick. The accelerometer and the marker are at 70 mm from the root of the beam. The camera was set to 640 × 480 pixels, 100 fps, ISO 100 and a shutter speed of 1/8000 s. The transmisibility using the optical measurements is marked with a solid line and the one obtained from accelerometer measurement is marked with a dashed line.

After verifying the optical system measurement, a closed-loop control with velocity feedback was applied to the beam. Figure 7.11 shows the result of the amplitude of the transmissibility for a non-rotating cantilever beam for the open-loop (marked solid line) and the closed-loop system (marked with dotted line). The active vibration control shows about 17dB reduction in the first resonance amplitude. The next step was to apply the active vibration control on the rotating beam.

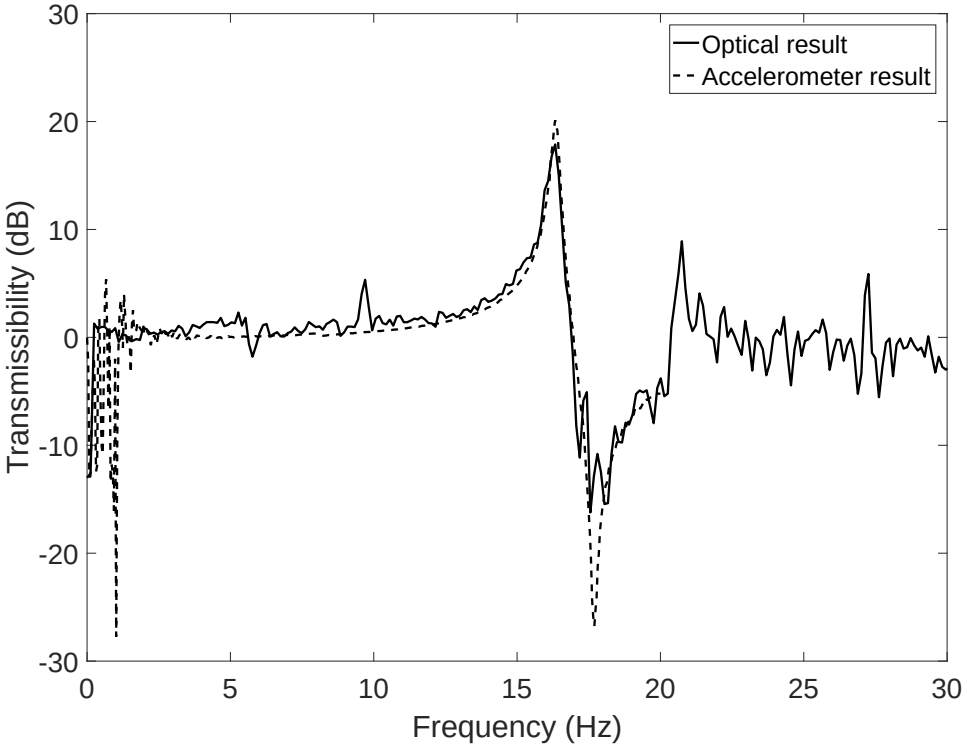

Figure 7.10: Comparison of the transmissibility between optical measurements and accelerometer result. The dimensions of the beam are 300mm, 15mm and 2mm for the length, width and thickness respectively.

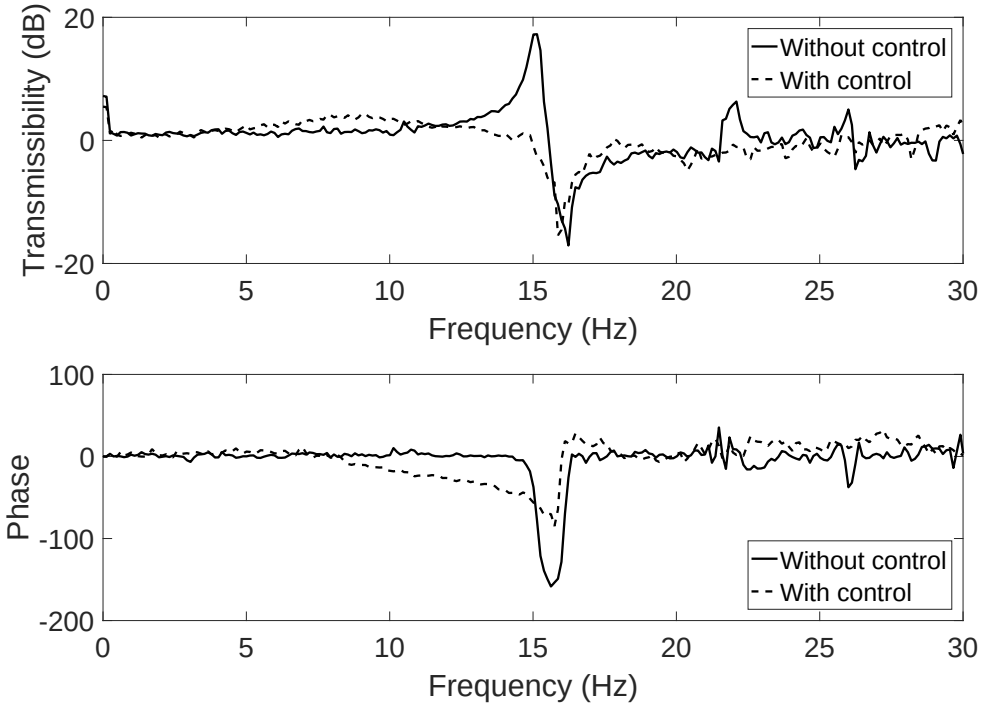

Figure 7.11: The non-rotating beam vibration with and without control.The dimensions of the beam is 320mm, 15mm and 2mm for the length, width and thickness respectively.

7.3.2 Vibration control of the rotating beam at different rotational speeds

An experimental vibration control test was performed on a rotating beam for a number of different rotational speeds. The optical measurements for the rotating beam without control, i.e. open-loop, using electromagnetic shaker excitation at the root of the beam and the response at 70 mm from the root of the beam were obtained. As explained previously in Chapter 4, an increase in the rotational speed leads to an increase of the natural frequencies as shown in Figure 7.12.

Figure 7.13 shows the transmissibility of the rotating beam at different rotational speeds under active velocity feedback control. The results show a significant reduction in dB for the peak response in the first resonance of the rotating beam, especially when compared to the non-rotating beam without control. The velocity feedback gain was kept fixed.

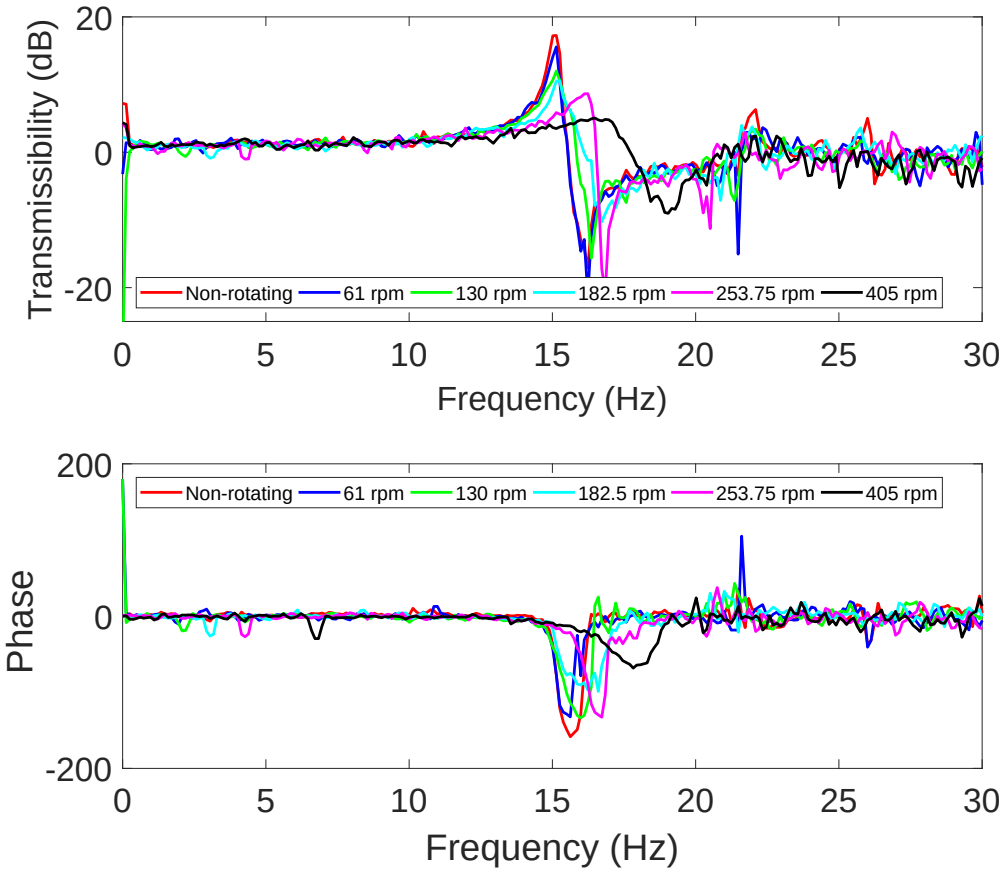

Figure 7.12: The transmissibility and phase angle for the rotating beam vibration without control. Open-loop diagram between the base excitation and the beam response at 70mm from the root of the beam.

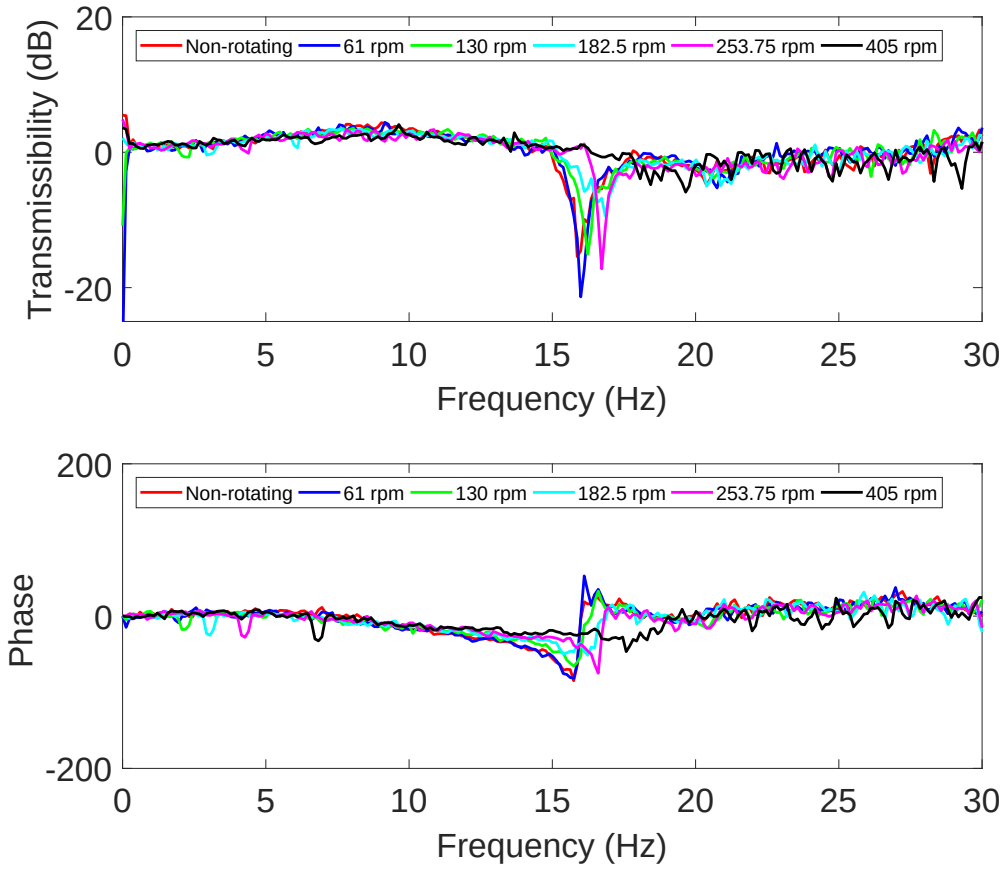

Figure 7.13: The transmissibility and phase angle for the rotating beam vibration with active velocity feedback control. The closed-loop diagram between the base excitation and the beam response at 70mm from the root of the beam.

7.3.3 Signal to noise ratio (SNR)

The measurement for the rotating beam becomes more difficult due to the camera alignment, light setting, background noise interference and additional noise from the rotational and moving parts such as the ball and linear bearings. However, to improve the quality of the signal, fine tuning was applied by using the alignment aid shown in the LabVIEW block diagram, which was developed according to the least squares circle fit algorithm and by increasing the camera shutter speed to reduce the background noise. Figure 7.14 shows the noise level in the measured signal. The signal to noise ratio measured between the test signal and the camera noise was obtained for the non rotating beam and then for the rotating beam. After applying Equation 7.6 the results were 23.96 dB and 22.23 dB respectively.

$$SNR = \frac{\sqrt{\frac{1}{N}\sum_{n=1}^{N}|signal_n|^2}}{\sqrt{\frac{1}{N}\sum_{n=1}^{N}|noise_n|^2}} \tag{7.6}$$

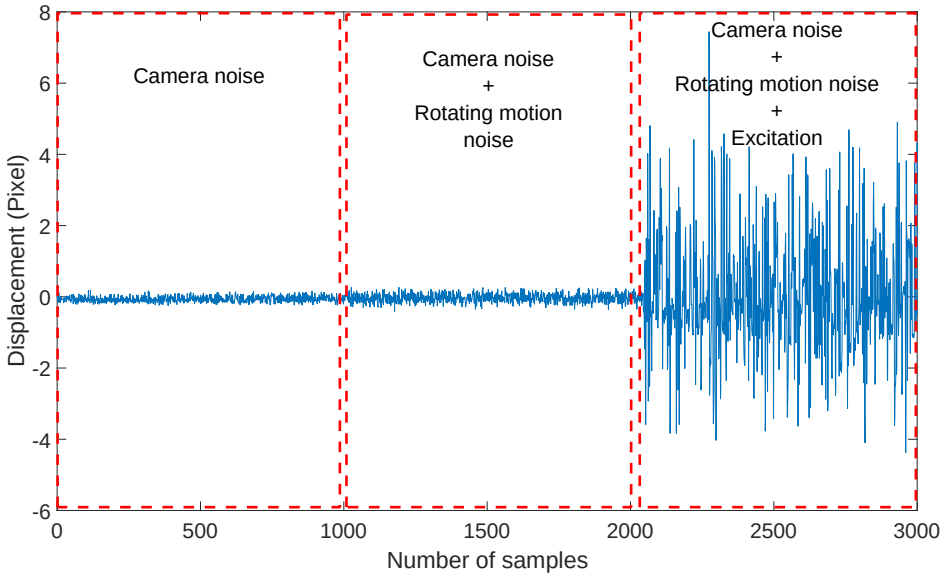

Figure 7.14: The time domain result of optical displacement measurement for a beam in nonrotating, rotating and rotating with base excitation. This test is performed to measure signal to noise ratio (SNR).

7.3.4 Stability analysis for different rotational speeds

For stability, the system shown in Figure 7.15 is considered where $G(s)$ and $H(s)$ represent the rotating beam system and the controller transfer function respectively. The

closed-loop system response can be expressed as Equation 7.7. The value of the denominator becomes zero when the value of $G(s)H(s)$ is equal to -1 and the system becomes unstable when $G(s)H(s)$ encircles point (-1,0) is encircled. Herein, the gain margin and phase margin are important indicators to measure the robust stability of the closed-loop system.

The gain margin represents the maximum gain value in which the system can have before reaching instability. An open-loop transfer function between the controller actuator input and the beam velocity was measured. The results are shown in the Figure 7.16 where by increasing the rotational speed the gain margin increases due to the reduction in the response peak amplitude with increased the rotational speed. The actual gain margins are measured from the circular curve fit to the Nyquist plot of $G(s)H(s)$ as shown in Figure 7.16. These results can be presented as a function of the rotational speed as shown in Figure 7.17. Regarding the phase margin, the values are infinity except for the non-rotating beam case where the phase margin is 100.65 degrees.

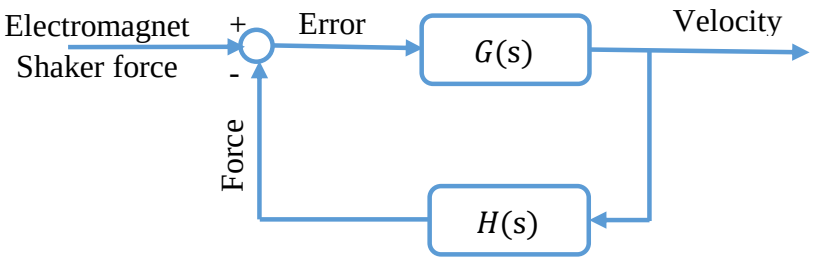

Figure 7.15: The system block diagram for the rotating beam and controller closed-loop. where $G(s)$ and $H(s)$ represent the transfer function of the plant and controller respectively.

$$Closed-loop \quad TF = \frac{G(s)}{1+G(s)H(s)} \tag{7.7}$$

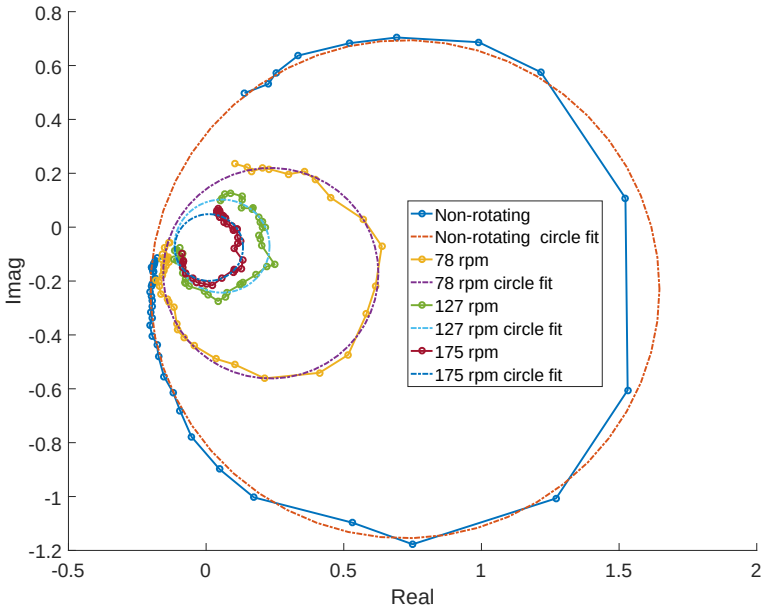

Figure 7.16: The circular curve fit for the Nyquist plot of the different rotational speed of the open-loop between the actuator excitation and beam response at 70mm from the root of the beam.

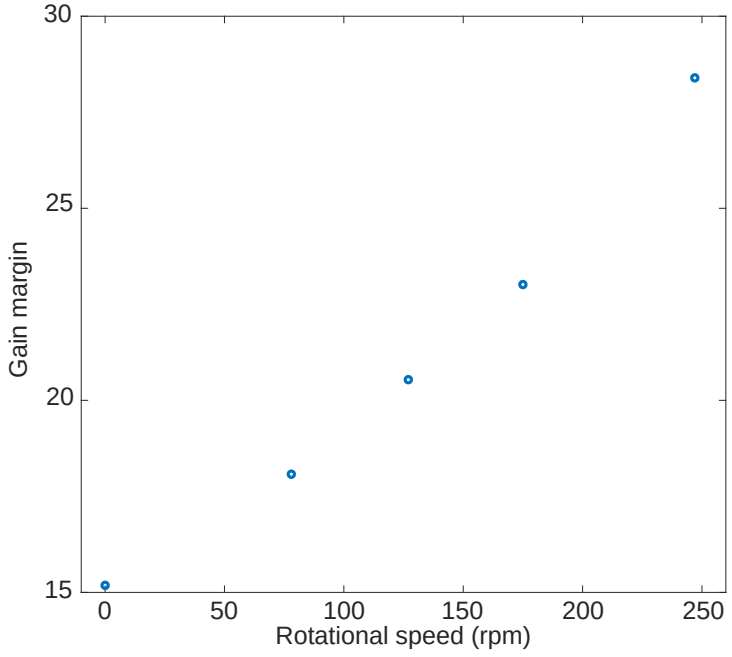

Figure 7.17: The gain margin for the active velocity feedback control of the rotating beam as a function of the rotational speed. These results are extracted from the circular curve fit to the Nyquist plot of the open-loop between the actuator excitation and beam response at the same position 70mm from the root of the beam. The increasing rotational speed of the beam leads to an increase in the gain margin of the controller.

7.4 Conclusions

In this chapter, an active control using velocity feedback was presented for the non-rotating and then the rotating beam, the latter at different rotational speeds. A simulation study was first established for the system using MATLAB Simulink. The estimated transmissibility shows a significant reduction in the fundamental and second resonance of the system after application of the feedback control. Furthermore, the estimated natural frequencies show the same pattern as discussed in the previous chapters where the resonance frequencies increase when the rotational speed increases. In addition to the simulation, experiments were performed using a high speed camera with a reflecting mirror of the image of the beam and its markers as a response sensor. The sampling frequency of the sensor was set to 100 fps. However, since the processing speed is limited to about 60 fps the active control targeted the fundamental resonance only . A new method of real time active control using a high speed camera shows a significant reduction in the resonance peak level of the transmissibility function. The use of optical measurements in real time control using camera is novel and is the main contribution of this chapter.

Chapter 8

Overall conclusions and suggestions for future work

In this chapter, a summary of the thesis is presented, which includes the main findings and contributions of research work done. In addition, the limitations of the current work are described. Finally, some possible points for future work and research in this area are provided.

8.1 Summary of the thesis

In this thesis, the main aim was to study the dynamic behaviour of a rotating beam. For this reason, the modelling of a rotating beam with and without crack is presented using force equilibrium and Hamilton's principle. Then, two approximate numerical methods were used to solve the equations of motion. The methods being namely the finite element and the Rayleigh-Ritz methods. The models were simulated to study the effect and variation of many factors on the natural frequencies. The factors considered included the rotational speed, beam slenderness and hub ratio. Furthermore, the important features in the results such as the critical speed, buckling speed and veering phenomena were identified. The simulation results were divided into two categories for the flapwise and the chordwise vibration, where they refer to the out of the plane and in-plane vibration (rotating plane).

The behaviour of the beam simulated under different rotational speeds revealed the general increase in the natural frequencies with the increased rotational speed. The slenderness ratio did not affect the dimensionless natural frequencies for flapwise vibration. In contrast, the dimensionless natural frequencies for chordwise vibration increase when the slenderness ratio increases. Furthermore, the diameter of the hub significantly

affects the natural frequencies. The larger the hub radius, the greater the increase in the natural frequencies for both the flapwise and chordwise vibration.

Regarding critical feature behaviour, the simulation shows the interference between the natural frequency and the rotational speeds for chordwise vibration where this is not the case in the flapwise vibrations. Moreover, a buckling speed appears in the chordwise vibration due to the decrease in the fundamental natural frequency of the beam at high rotational speeds. Finally, a veering phenomenon was observed wherein the chordwise vibration of the rotating beam at high rotational speeds leads to veering in the natural frequencies and the modes changing order from being previously bending to axial deformation. This behaviour is a result of a coupling effect between the chordwise bending and longitudinal vibration.

The simulation results showed a good match between the two numerical methods regarding the natural frequencies and mode shapes. The results were in good agreement with a 3D FE model assembled using solid elements and solved in commercial software such as SolidWorks and ANSYS.

In the experimental work, a test rig was designed and manufactured to test a rotating beam and its measured response using optical measurements. Three different image processing methods, namely digital image correlation, marker detect and blob detect, were utilised to extract the dynamic deflection data from the sequence of images. The new approach showed the capability of estimating the natural frequencies and mode shapes for the flapwise vibration of the rotating beam. The optical method applied is non-invasive with remote sensing of the vibration for a wide range of rotational speed representing one of the main goals of this research. Moreover, a new crack detection method was developed and validated based on a natural frequency-speed curve. The robustness of the method was assessed using Monte Carlo simulation (MCS). Finally, real-time active vibration control of the rotating beam was undertaken and completed using velocity feedback. This involved the measurements using a high-speed camera and image processing. The control results produced a significant reduction in the flapwise vibration over a wide range of rotational speeds. The crack detection and rotating beam control can be considered as applications of the developed numerical model and optical measurement capabilities.

8.2 Limitations of the current work

The limitation of the study can be divided into three main areas namely modelling, simulation and experimental implementation. Regarding modelling, the three main types of vibration which are flapwise bending, chordwise bending and longitudinal stretch are covered in Chapter 3. However, for modelling more realistic rotating beams, the model should include torsional deformation and vibration. In addition, the crack modelling

covers the two modes, which are opening and sliding. For torsional vibration it will be necessary to include the tearing mode of the crack, which might be associated with torsional vibration. The breathing or bilinear crack is briefly covered in this thesis and can be developed for future analysis. In addition, the breathing type of crack has not been applied yet in the Rayleigh-Ritz modelling approach.

Although the chapter containing experimental validation covers the optical measurement of the flapwise vibration of the rotating beam, the tests were limited to the measurement of the response in the first two resonances of the rotating beam. This was due to a limitation in the frame rate of the camera. Furthermore, the chordwise test did not contribute as it would require an additional upgrade to the test rig's design, which was limited in the time available for this study.

The optical measurement was partially limited to the finite number of markers along the beam. While using a speckle pattern with digital image correlation, it would be possible to obtain a full-field measurement of the rotating beam. In this research, the markers were used to reduce the complexity of the system and to use different image processing methods for which the speckle pattern approach is not suitable. Also, for full-field measurements, at least two compatible and preferably identical high-speed cameras are required to obtain the out of plane vibration.

The closed-loop response used for active vibration control shows a significant reduction in the first resonance of the rotating beam. Nevertheless, the sampling rate for the camera is insufficient to cover the first two beam resonances. The image processing added a delay to the feedback and limited the level of the active damping to the frequency range up to the first resonance only. The crack detection method was also limited to using the lowest two natural frequencies due to the limitation in the experimental measurements.

8.3 Future work

The work that has been presented in this thesis covers the theoretical formulation and experimental validation method for modelling a rotating beam with and without a crack. In addition, two applications based on the developed model has been illustrated, which are the crack identification and active control of rotating beam. Further improvements to the method and the experimental investigation may result from research work regarding the following issues:

The proposed model can be improved by including the torsional vibration, especially if the model extended to cover plate or wide beams, which is more like to represent blades. Likewise, tapered beams which functionally change in cross-section along the beam as in Mazanoglu and Guler (2017). In addition, crack modelling in the Rayleigh-Ritz model can be extended to the breathing or bilinear cracks. Furthermore, the third mode of the

crack, which is tearing mode should be added when the torsional vibration is observed for representation of the crack.

Concerning experimental work, the speckles can be used with the dual camera to perform full-field vibration analysis. In addition, it is necessary to use more than one camera to measure the 3D displacement of the beam or at least the out of plane vibration of the beam. Moreover, to improve the sensitivity of the optical measurement, a combination of DIC with motion magnification algorithm can be applied in a nonrotating beam by Molina-Viedma et al. (2018). Furthermore, a new design is required for the test rig to include the chordwise vibration test. Additionally, an extra actuator is essential to perform torsional vibration.

The crack identification method based on mode shape changes can be applied to the present measurement method, since multi-measurement points are obtained. In addition, a real-time crack detection method can be developed based on the optical blob detection method, which is fast in terms of image processing speed.

Different passive and active vibration control strategies can be applied to reduce the vibration, for example, eddy current damper method Yan et al. (2012) or tuned mass damper Sodano et al. (2005) for passive control. For active control, different actuators can be used such as piezoelectric actuators Xue and Tang (2008) and inertial actuators Rohlfing et al. (2016). Active control can also be used to reduce the effect of the presence of any crack especially if the vibration is excessive and potentially damaging.

Appendix A

Design

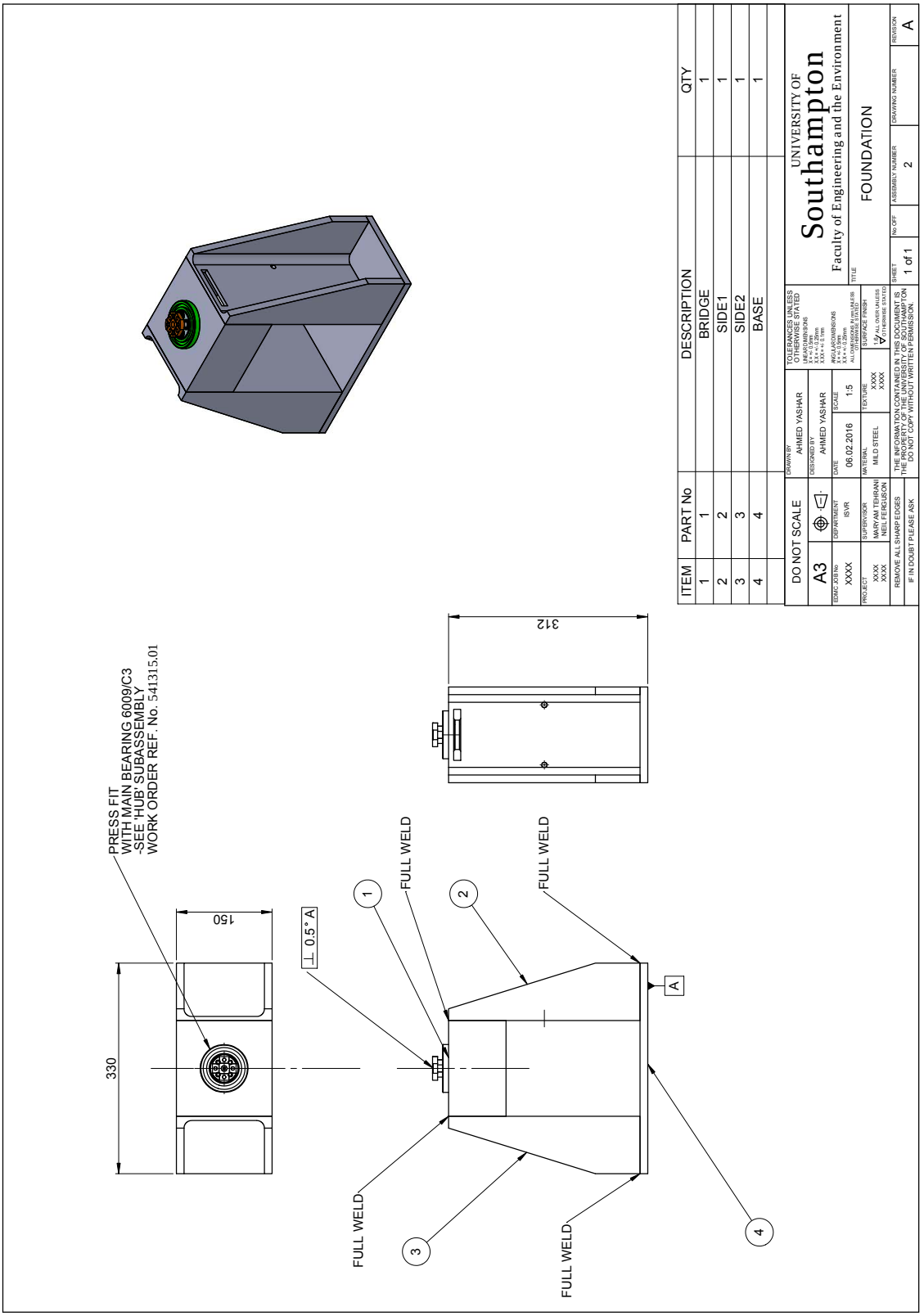

Figure A.1: Test rig: Foundation.

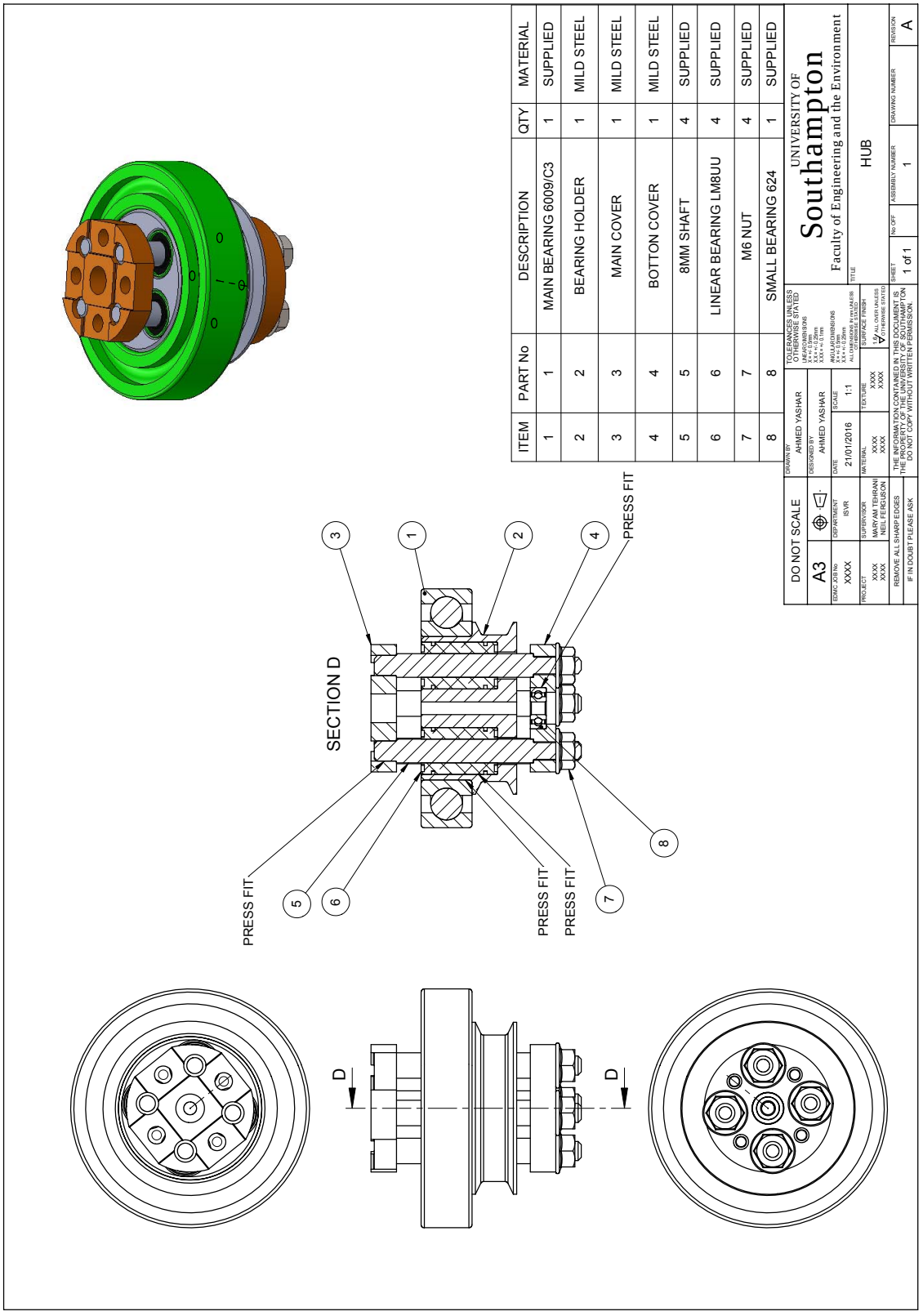

Figure A.2: Test rig: Rotating hub.

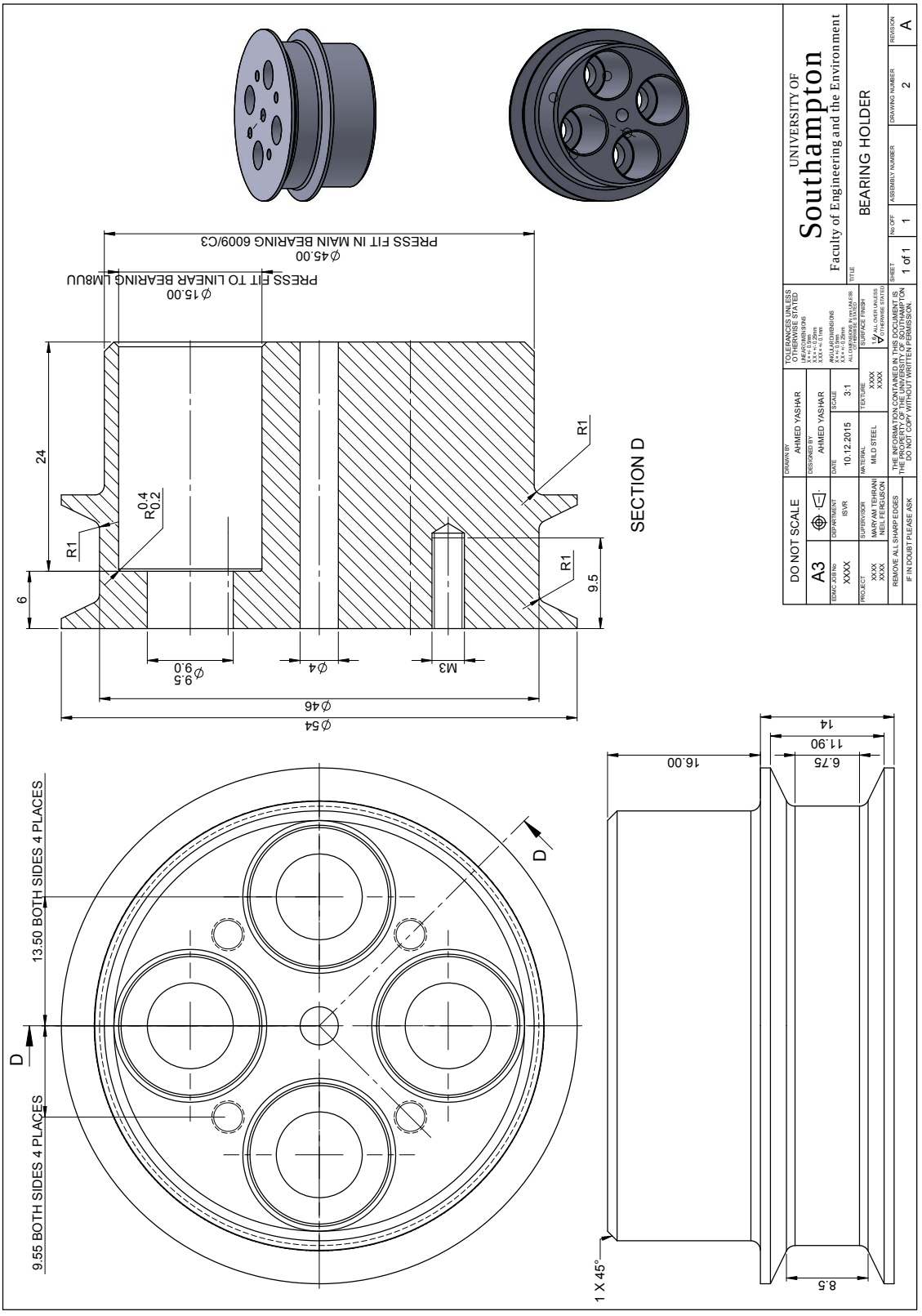

Figure A.3: Test rig: Bearing holder

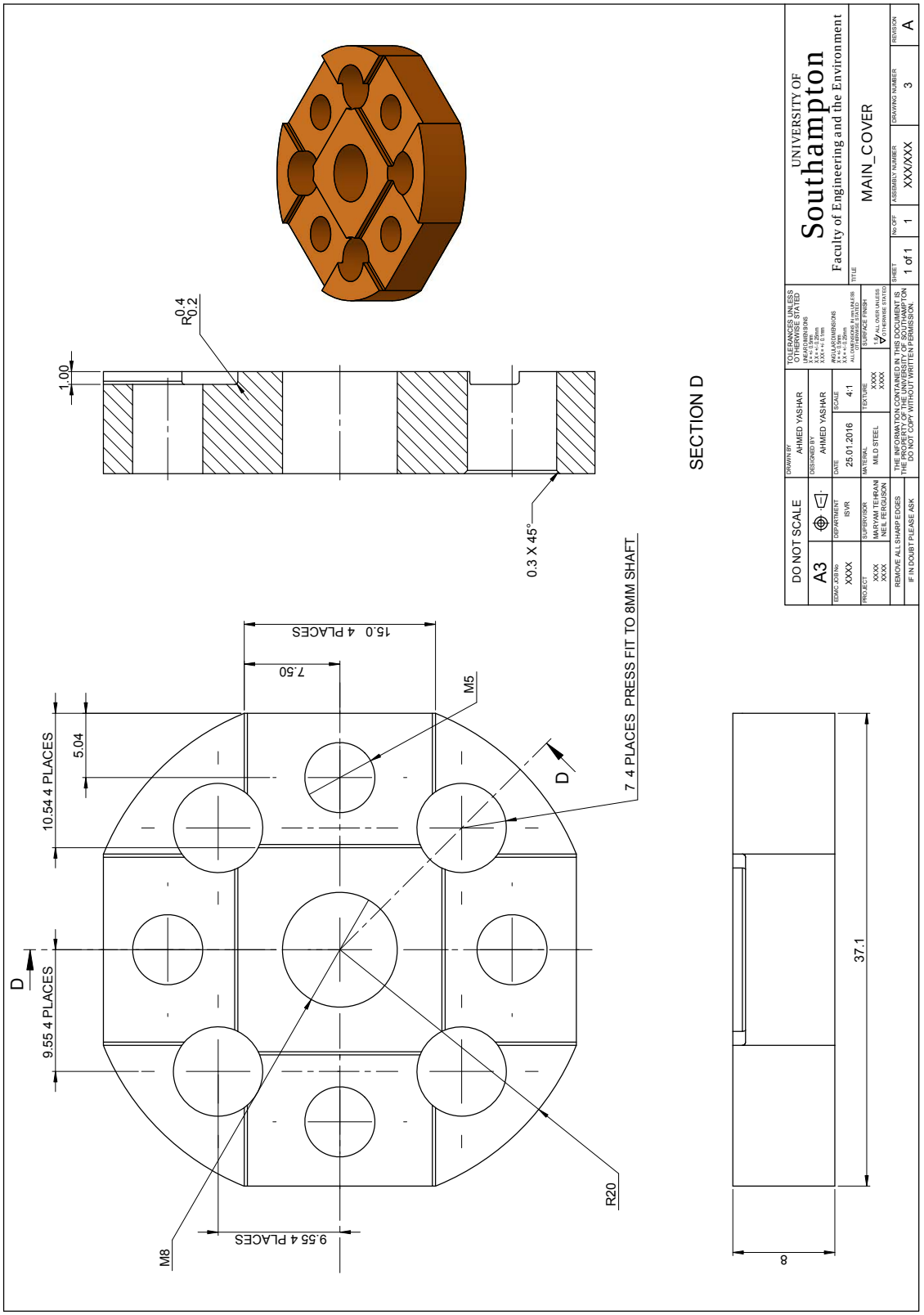

Figure A.4: Test rig: Main cover

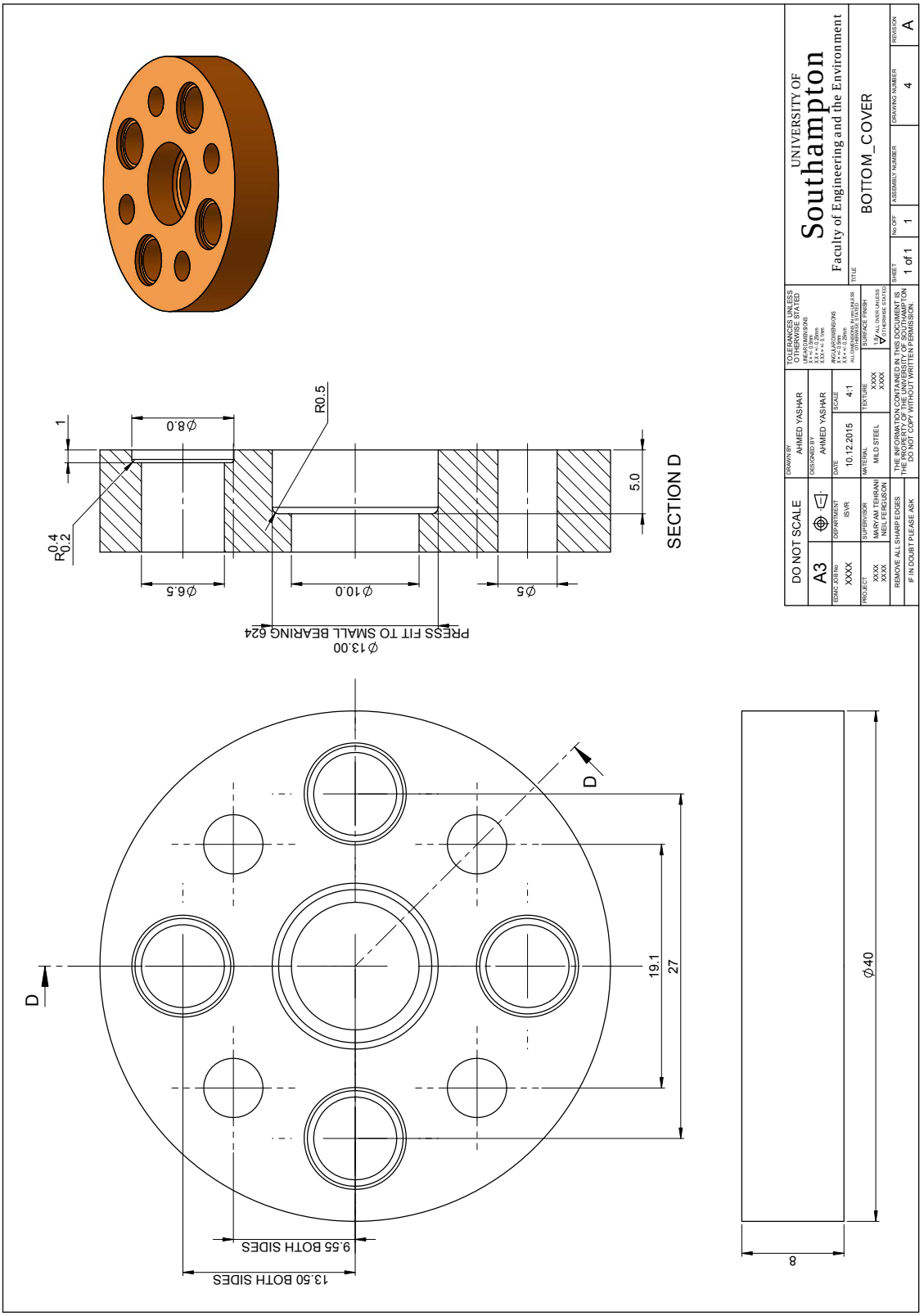

Figure A.5: Test rig: Bottom cover

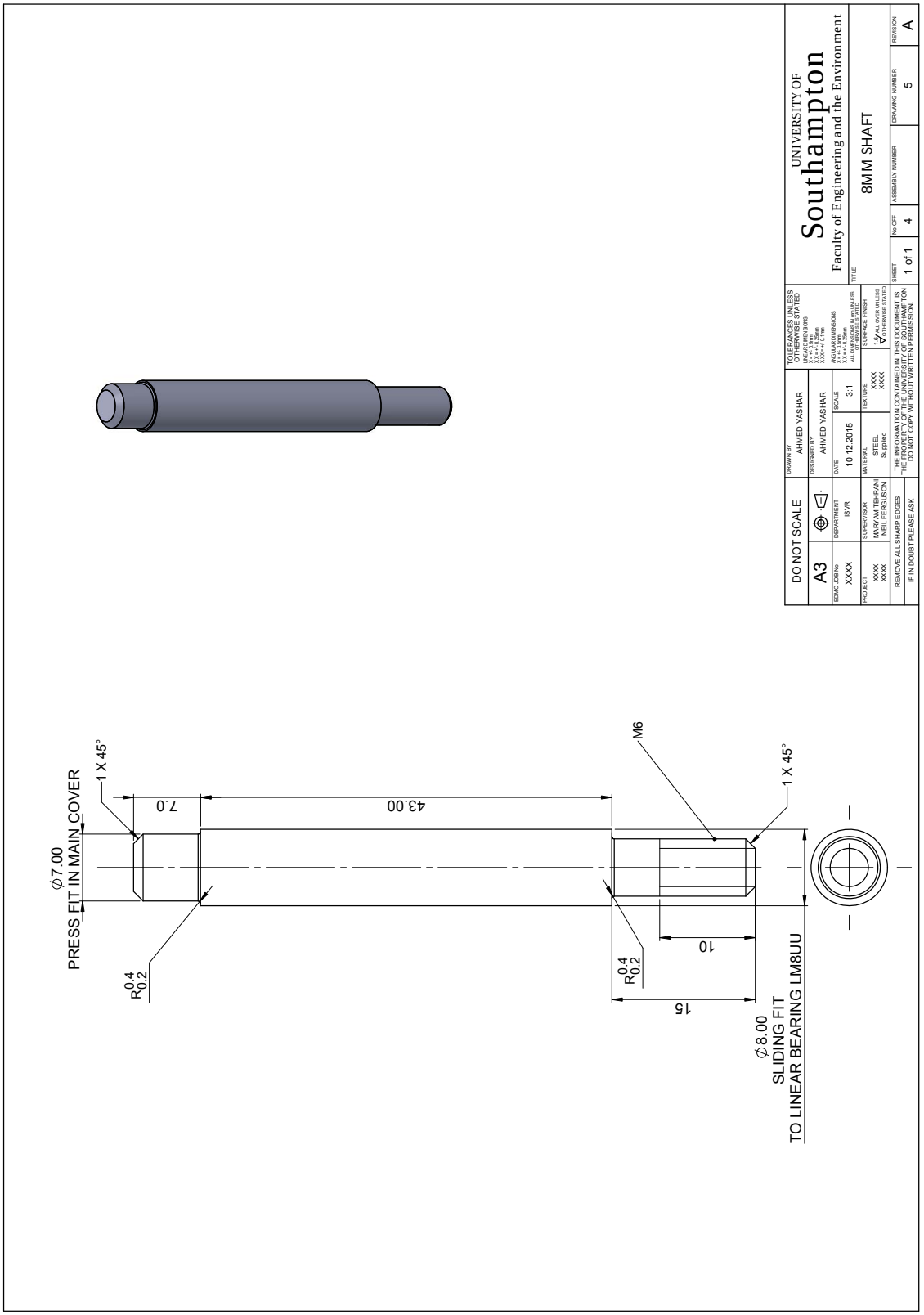

Figure A.6: Test rig: 8mm shaft

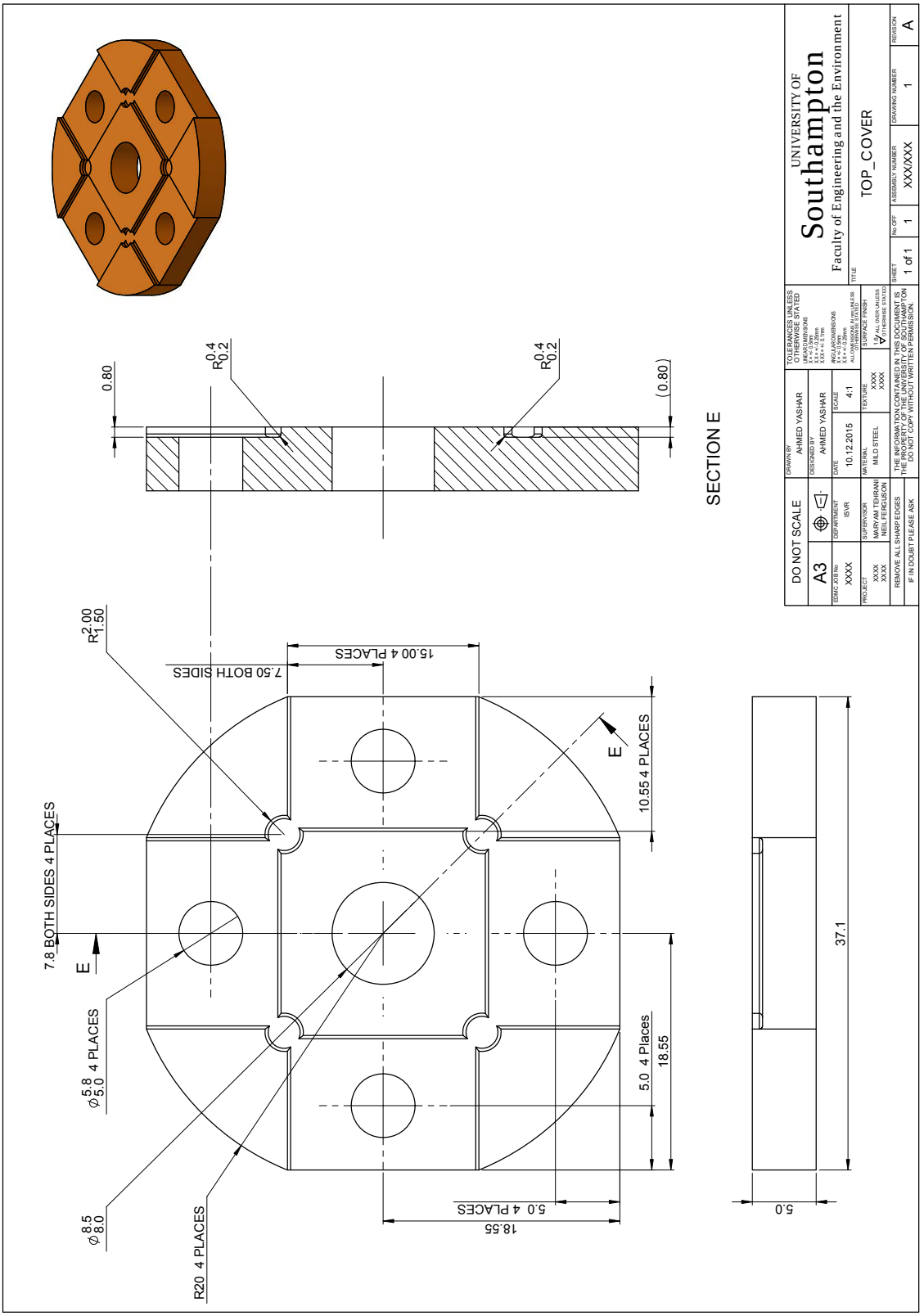

Figure A.7: Test rig: Top cover

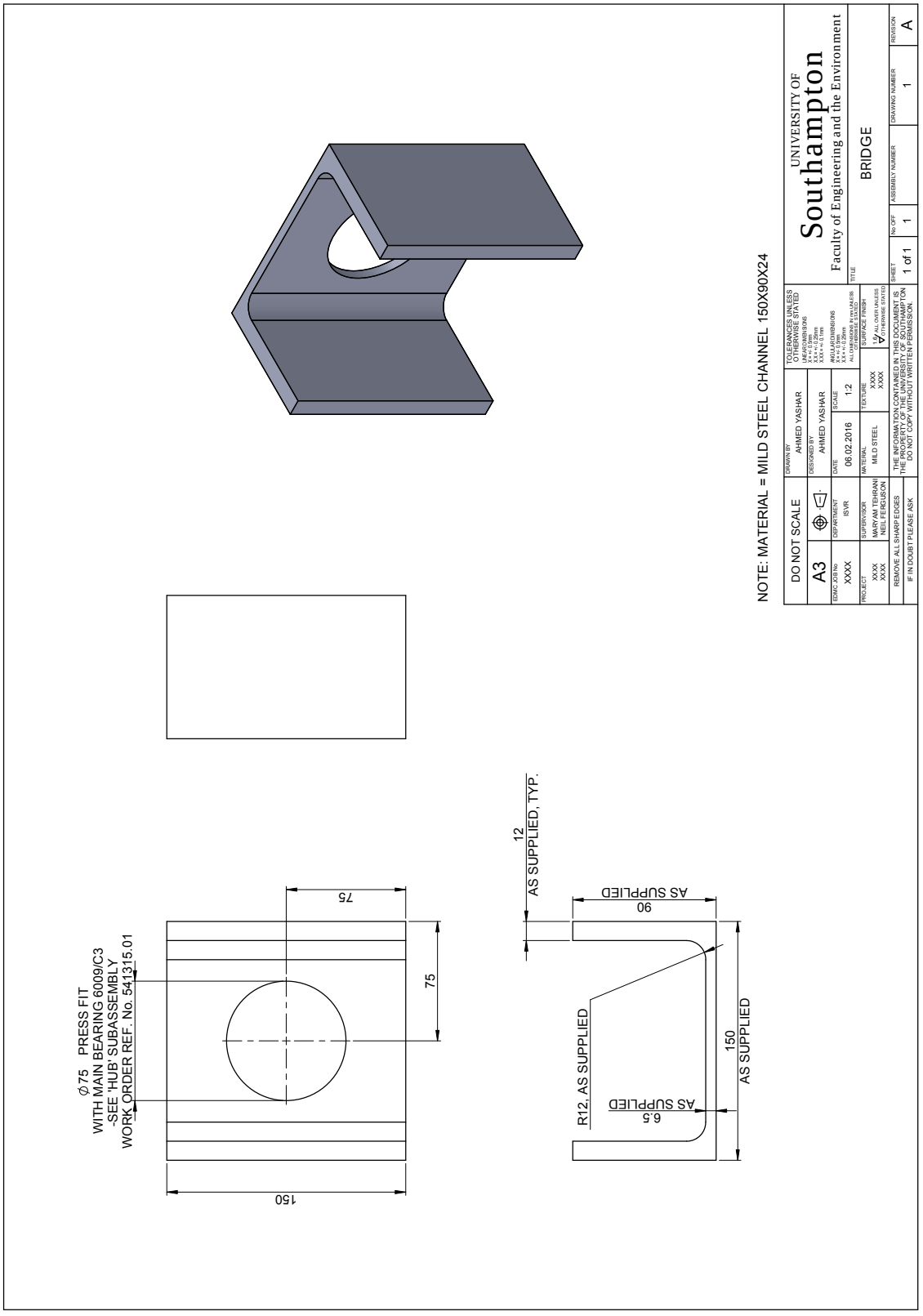

Figure A.8: Test rig: Bridge

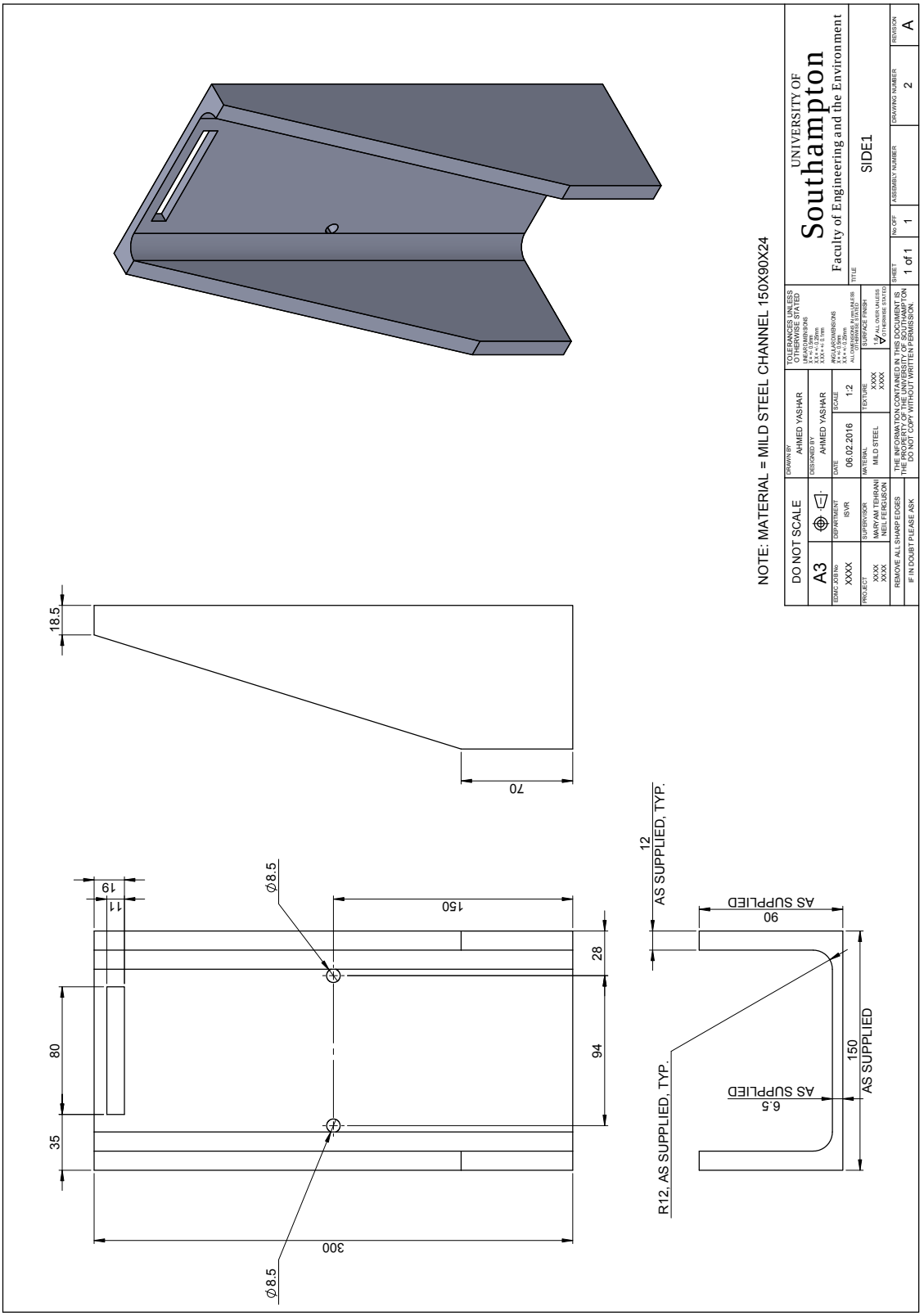

Figure A.9: Test rig: Side1

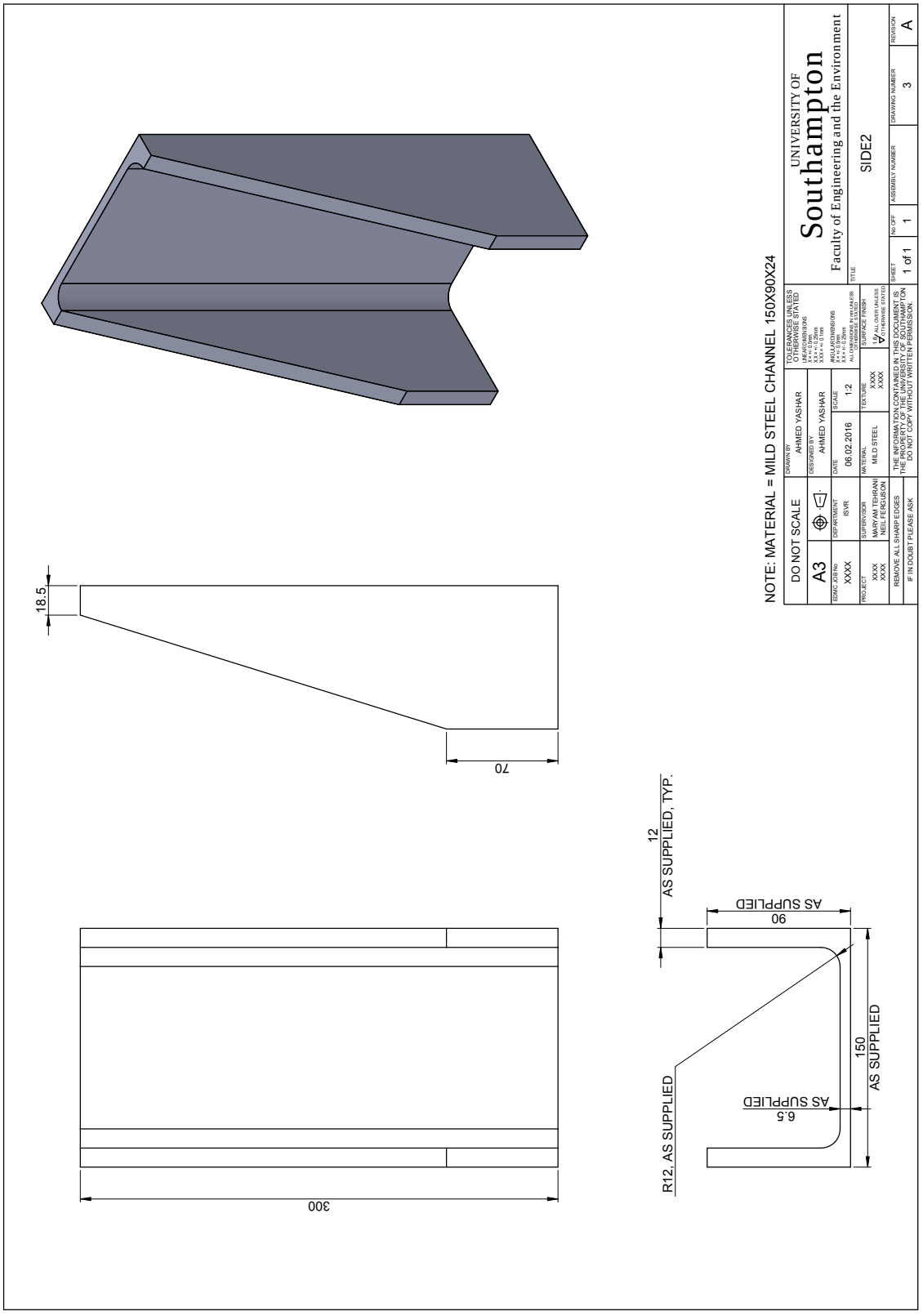

Figure A.10: Test rig: Side2

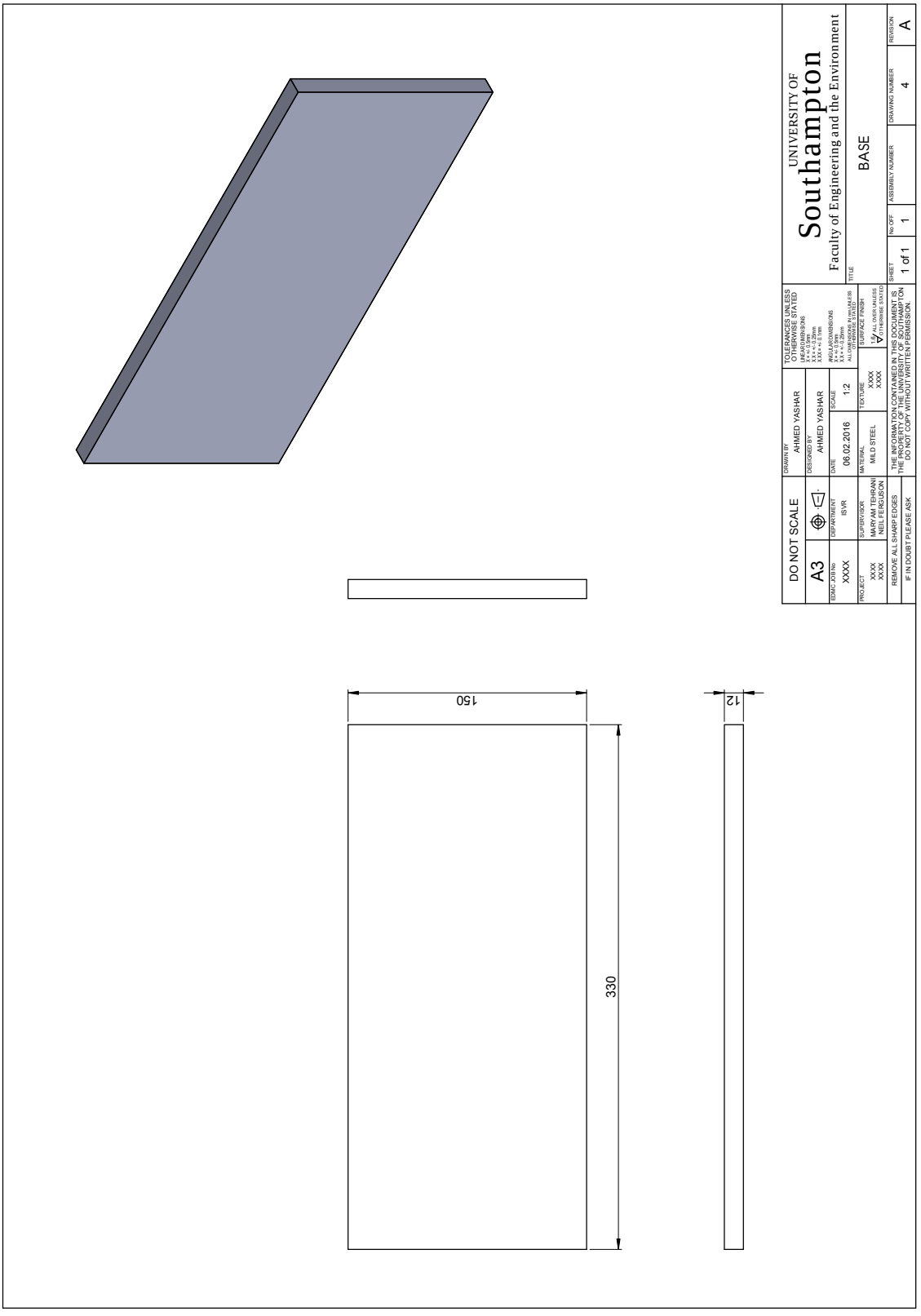

Figure A.11: Test rig: Base

Appendix B

Measurement equipment

ZAILA

TECHNICAL DATA

input voltage: 100-240V AC, 10-18V DC
power draw: 40 watts (power factor corrected)
dim range: 0-100% (onboard dimmer)
control: wireless or wired DMX
focus range: 10°- 80°
focusing method: holographic film lenses
UV: none
warm-up time: none (instant on)
lamp life: 60,000 hours
color spectrum: continuous
compatible shutter speeds: all (flicker-free*)

*flicker-free up to 5000 FPS for full dim range & at any speed at 100%

DIMENSIONS

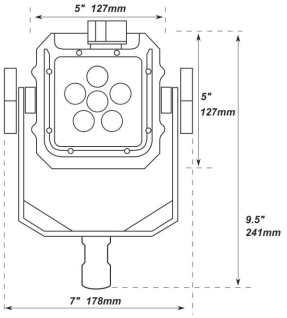

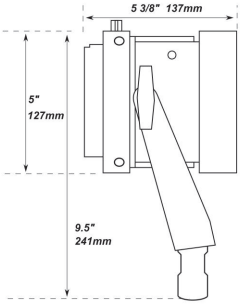

weight: 5 lbs. (2.3 kg)
construction: machined aluminum
finish: anodized
mount: yoke (w/baby pin or bolt)
operating position: any
tilt control (with yoke): friction
cooling: passive (no fans)
power cable: 10'
power connector: NEMA 5-15P
compliance: ETL & CE
warranty: two years
country of origin: USA

PHOTOMETRICS

Lens	3 Ft (FC)	10 Ft (FC)	20 Ft (FC)	1m (lux)	3m (lux)	6m (lux)
Raw	2500	200	52	26910	2150	560
10	1400	120	30	15070	1290	320
20	800	64	16	8610	690	170
40	500	42	11	5380	450	115
60	190	17	5	2045	180	55
80	110	11	3	1180	115	30
60x10	500	42	11	5380	450	115

BEAM SPREADS

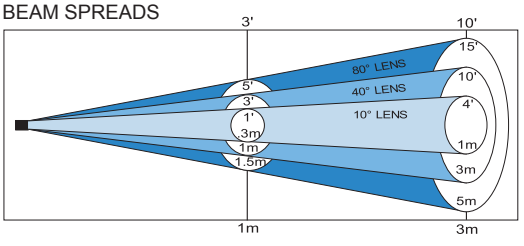

Nila, Inc. 723 West Woodbury Rd. Altadena, CA 91001 818-392-8370 Nila.com

Resolve the Moment...

REDLAKE

MotionPro X3 and X3*PLUS*

Redlake's MotionPro® X3 high-speed motion camera combines excellent resolution to frame rate performance, along with the advanced features you require for accurate high-speed motion analysis on your PC or Mac laptop or desktop computer. The enhanced sensitivity of the MotionPro® X3 combined with 1000 fps at 1280 x 1024 is perfect for research and development laboratory environments. The NEW *PLUS* option (available on monochrome cameras only) uses *SmartCapture* technology to effectively double the frame rate to 2000 fps at full resolution while preserving the total length of record time.

The X3 and X3*PLUS* cameras feature uses the latest Gigabit ethernet along with USB2.0 for easy interface. They also feature live video for continuous monitoring.

With the MotionPro®, camera integration could not be simpler. Just install the software, connect one or more X series cameras to USB 2.0 or ethernet ports (or both), and you are ready to capture high-speed digital imagery. Control the camera with the feature-rich MotionPro® X software or use the LabVIEW™ or MATLAB® plug-in to integrate it into a larger experiment setup. To create your own control software, an SDK is included.

The extensive image processing algorithms include binning (2x2, 3x3, and 4x4), filtering, advanced color control, and programmable LUT enable you to maximize the image quality under various lighting conditions.

Flexible recording options allow the user to capture pre-selected number of frames before and/or after receiving a trigger. Double-exposure mode, with a 100 nanoseconds inter-frame time, is perfect for motion analysis on objects moving at very high speeds. Memory may be divided into multiple sessions with or without automatic download to assure no event is missed.

Applications: Microscopy, Ballistics and Munitions esting, Biomechanical research, Fluid dynamics research (PIV), Off-board vehicle impact testing

Features	Benefits
Up to 1280 x 1024 resolution color or mono	High resolution allows fine detail to be captured even at high frame rates
Fast frame rates from 1000 fps at full resolution to over 64,000 fps at reduced resolution	Perfect for capturing movies of fast dynamics of a process or event
NEW *PLUS* option to effectively double the frame rate and memory size (Mono only)	Allows twice the time resolution while preserving the total length of record time
Gigabit Ethernet and USB2.0	Operate camera from remote locations via Gigabit Ethernet while using USB 2.0 for local monitoring
100 nanosecond inter-frame time in double exposure mode	perform particle imaging velocimetry (PIV) measurements to study fast moving fluids
iPod and PDA compatibility	Store movies on to iPod (video) for quick review. Control the camera operation remotely and wirelessly via PDA interface

Sample Frame Rates (@ Max. Horizontal resolution of 1280)

Vertical Resolution	X3 (fps)	X3*PLUS* frame rate* (fps)
1024	1000	2000
768	>1300	>2600
512	2000	4000
256	4000	8000
128	8000	16,000
64	16,000	32,000
32	32,000	64,000
16	64,000	128,000

Note: Horizontal resolution does not affect frame rate performance. **PLUS* option is available for monochrome versions only. Effective frame rate is shown for X3*PLUS*.

Accessories

X Timing Hub	8 independently adjustable CMOS level outputs, 2 inputs; USB interface
X Data Acquisition System	16 analog inputs and 4 analog outputs, USB interface
USB Repeater	For use up to 15m

Spectral Range

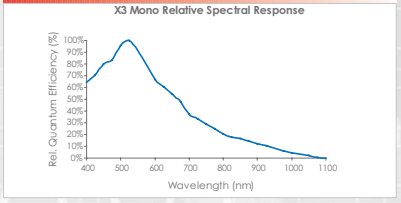

Resolve the Moment...

MotionPro X3 and X3*PLUS* Performance Specifications

CMOS Imager	
Sensor Array	Area Array with 12µm x 12µm pixels, color or monochrome
Image Resolution	Up to 1280 x 1024
Dynamic Range	59 dB at sensor
Memory and Record Rates	
On-board Storage	4 GB; with *PLUS* option, the memory is effectively doubled
Recording Rates	X3: Selectable, up to 64,000 fps X3*PLUS* (optional): Selectable, up to 128,000 fps
Playback Rates	User selectable
Camera Control	
Shutter	Global Electronic Shutter variable from 1µs, optional 100 nanosecond exposure*
Exposure modes	Single, Double, XDR (eXtended Dynamic Range)
Trigger Frame	Variable position from start to the maximum available frame capacity
Trigger Mode	CMOS level (3.3v) via BNC connectors
Time Stamp	Each frame
Software	
Control Software	MotionPro X; Windows 2000/XP, Mac OS X** (10.3 or later)
Image Processing Algorithms	Binning, filtering, advance color control, and programmable LUT
Plug-ins	LabVIEW™ for PC; MATLAB® for PC and Mac; Twain Driver for PC and Mac
File Formats	TIFF, BMP, PNG, MRF, MCF, AVI, BLD, MPEG, and MOV (Mac only)
Mechanical Description	
Camera Dimensions	3.7 in (95 mm) H x 3.7 in (95 mm) W x 6.4 in (162 mm) L
Camera Weight	4.2 lbs (1.9 kg)
Camera to PC Interface	USB 2.0; Dual USB 2.0&Gigabit Ethernet (optional)
Camera Cable Lengths	5m (USB2.0); Longer cable lengths (not supplied) may be used with GigE
Lens Compatibility	1" C-mount
Lens Mount	C-mount, F-mount adapter (optional)
Synchronization	
Synchronization (USB Hub Optional)	All cameras are synchronized with each other using an external sync pulse on 3.3v CMOS BNC connector
Environmental	
Camera Power	+24 vdc (100-240 VAC, 50-60 Hz ac/dc convertor)
Operating Temperature	+5°C to +40°C Ambient (0°F to 122°F)
Emission/Safety	CE approved, FCC Class B compliant, UL listed
Input/Output	
Trig In (BNC) **Sync In (BNC)** **Sync Out (BNC)** **USB 2.0 (LEMO)** **Gigabit Ethernet** **Live Out (BNC) RS170 (NTSC/PAL)** **DC Power (LEMO)**	

*Enquire with factory
**GigE interface is not supported under Mac.
Specifications are subject to change.

REDLAKE

Distributed by DEL Imaging Systems
1781 Highland Avenue, Cheshire, CT 06410
Phone: (203) 250-1545 www.delimaging.com

TSRL: CAMERAS, LENSES and LIGHTING

AF NIKKOR 50mm

Specifications

Focal length: 50mm

Maximum aperture: f/1.8

Type of lens: D-type AF Nikkor lens having built-in CPU and Nikon bayonet mount

Lens construction: 6 elements in 5 groups

Picture angle: 46° (38° with IX240 system cameras, 31°30′ with Nikon Digital Camera D1)

Distance information: Output to camera body

Focusing: Autofocus with Nikon autofocus cameras (except F3AF); manually via separate focus ring

Shooting distance scale: Graduated in meters and feet from 0.45m (1.75 ft) to infinity (∞)

Closest focus distance: 0.45m (1.5 ft.)

Aperture scale: f/1.8 to f/22 on both standard and aperture-direct-readout scales

Diaphragm: Fully automatic

Exposure measurement: Via full-aperture method with cameras having CPU interface system; via stop-down method for other cameras

Attachment size: 52mm (P = 0.75mm)

Dimensions: Approx. 63.5mm dia. x 39mm extension from the camera's lens mounting flange

Weight: Approx. 155g (5.5 oz)

October 2014

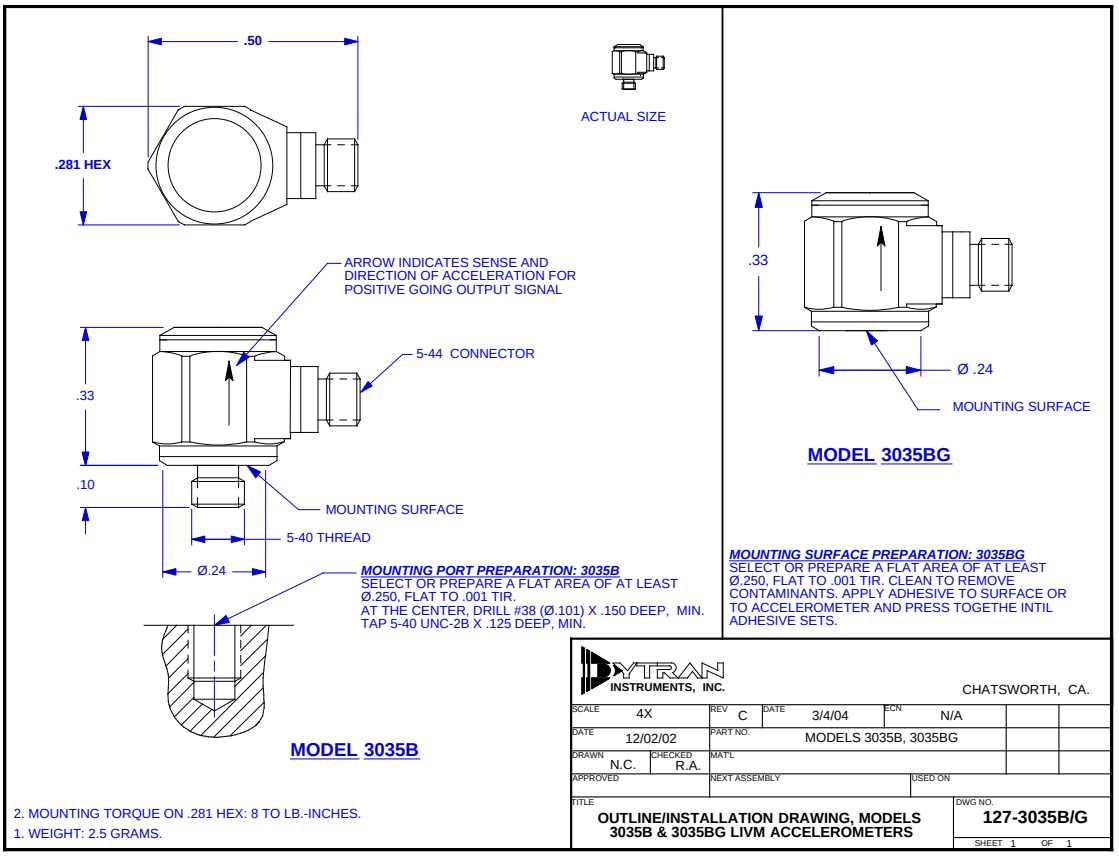
.50
.281 HEX
ACTUAL SIZE
ARROW INDICATES SENSE AND DIRECTION OF ACCELERATION FOR POSITIVE GOING OUTPUT SIGNAL
5-44 CONNECTOR
.33
.10
MOUNTING SURFACE
5-40 THREAD
Ø.24
MOUNTING PORT PREPARATION: 3035B
SELECT OR PREPARE A FLAT AREA OF AT LEAST Ø.250, FLAT TO .001 TIR.
AT THE CENTER, DRILL #38 (Ø.101) X .150 DEEP, MIN.
TAP 5-40 UNC-2B X .125 DEEP, MIN.
MODEL 3035B
.33
Ø .24
MOUNTING SURFACE
MODEL 3035BG
MOUNTING SURFACE PREPARATION: 3035BG
SELECT OR PREPARE A FLAT AREA OF AT LEAST Ø.250, FLAT TO .001 TIR. CLEAN TO REMOVE CONTAMINANTS. APPLY ADHESIVE TO SURFACE OR TO ACCELEROMETER AND PRESS TOGETHE INTIL ADHESIVE SETS.
2. MOUNTING TORQUE ON .281 HEX: 8 TO LB.-INCHES.
1. WEIGHT: 2.5 GRAMS.
DYTRAN INSTRUMENTS, INC.
CHATSWORTH, CA.
SCALE 4X
REV C
DATE 3/4/04
ECN N/A
DATE 12/02/02
PART NO. MODELS 3035B, 3035BG
DRAWN N.C.
CHECKED R.A.
MAT'L
APPROVED
NEXT ASSEMBLY
USED ON
TITLE
OUTLINE/INSTALLATION DRAWING, MODELS 3035B & 3035BG LIVM ACCELEROMETERS
DWG NO. 127-3035B/G
SHEET 1 OF 1

SPECIFICATIONS
MODEL 3035B & 3035BG LIVM ACCELEROMETERs

SPECIFICATION	VALUE	UNITS
PHYSICAL		
WEIGHT	2.5	grams
SIZE, HEX x HEIGHT	.281 x .33	inches
MOUNTING PROVISION, 3035B	5-40 integral stud	
MOUNTING PROVISION, 3035BG	flat surface for adhesive mount	
CONNECTOR, RADIALLY MOUNTED	5-44 coaxial	
MATERIAL, HOUSING AND CONNECTOR	300 series stainless steel	
PERFORMANCE		
SENSITIVITY, ± 10% [1]	100	mV/g
RANGE F.S. FOR ± 5 VOLTS OUTPUT	± 50	g
FREQUENCY RANGE, ± 5%	0.5 to 10k	Hz
RESONANT FREQUENCY, NOM.	45	kHz
EQUIVALENT ELECTRICAL NOISE FLOOR	.007	g rms
LINEARITY [2]	± 1%	% F.S.
TRANSVERSE SENSITIVITY, MAX.	5	%
STRAIN SENSITIVITY	.002	g/με @ 250με
ENVIRONMENTAL		
MAXIMUM VIBRATION/SHOCK	600/3000	± g pk
TEMPERATURE RANGE	-60 to +300	°F
SEAL, HERMETIC	Glass-to-metal and welds	
COEFFIEICNT OF THERMAL SENSITIVITY	.04	%/°F
ELECTRICAL		
SUPPLY CURRENT [3]	2 to 20	mA
SUPPLY COMPLIANCE VOLTAGE RANGE	+18 to +30	volts
OUTPUT IMPEDANCE, TYP.	100	ohms
BIAS VOLTAGE, +10.5 VOLTS NOM.	+9 to +12	Vdc
DISCHARGE TIME CONSTANT, NOM.	0.5	seconds
OUTPUT SIGNAL POLARITY		
FOR ACCELERATION TOWARD TOP	positive	
CASE GROUNDING	case is grounded to electrical power ground	

[1] Measured at 100 Hz, 1g rms per ISA RP 37.2.
[2] Measured using zero-based best straight-line method, % of full scale (F.S.) or any lesser range.
[3] Do not apply power to this device without current limiting, 20 mA MAX. To do so will destroy the integral IC amplifier.

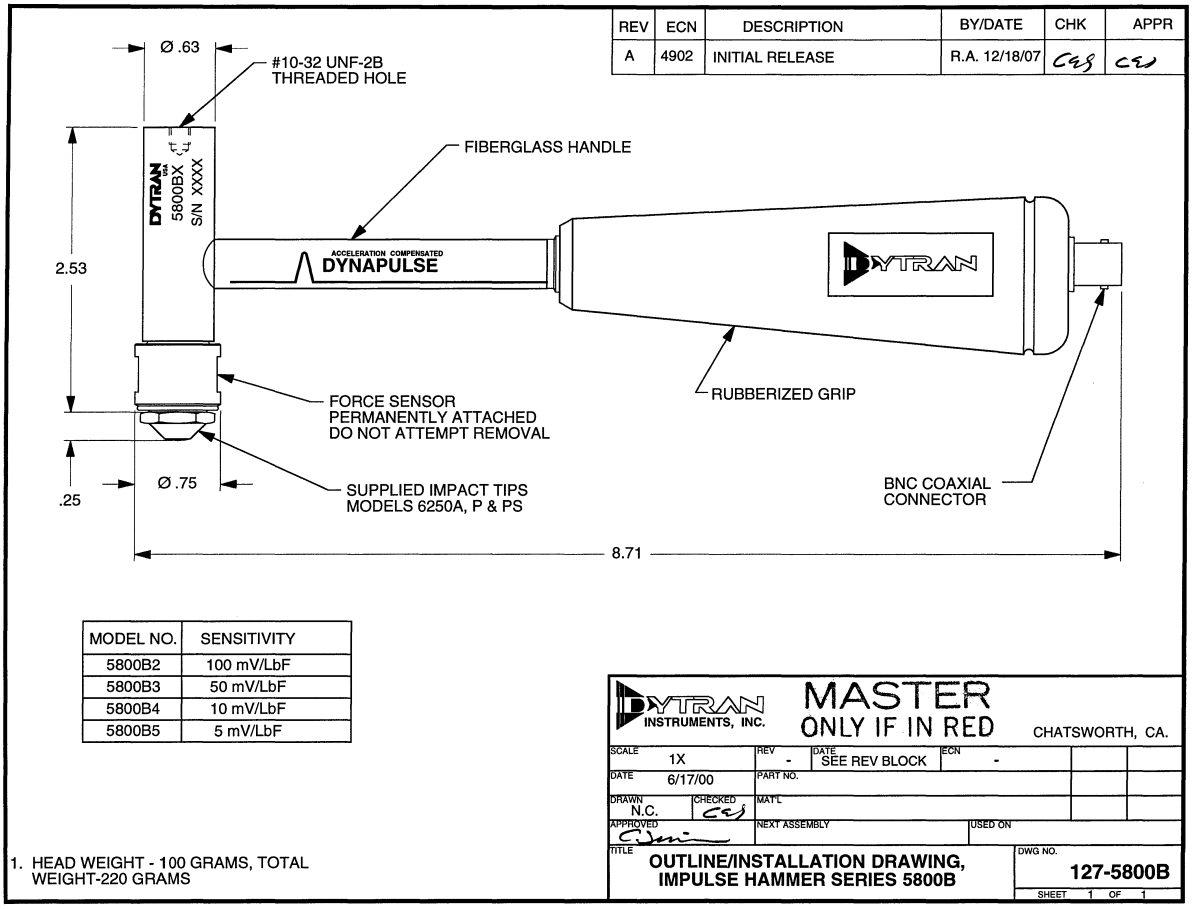
REV | ECN | DESCRIPTION | BY/DATE | CHK | APPR
A | 4902 | INITIAL RELEASE | R.A. 12/18/07
Ø .63
#10-32 UNF-2B
THREADED HOLE
FIBERGLASS HANDLE
DYTRAN
5800BX
S/N XXXX
ACCELERATION COMPENSATED
DYNAPULSE
2.53
FORCE SENSOR
PERMANENTLY ATTACHED
DO NOT ATTEMPT REMOVAL
RUBBERIZED GRIP
Ø .75
.25
SUPPLIED IMPACT TIPS
MODELS 6250A, P & PS
BNC COAXIAL
CONNECTOR
8.71
MODEL NO. | SENSITIVITY
5800B2 | 100 mV/LbF
5800B3 | 50 mV/LbF
5800B4 | 10 mV/LbF
5800B5 | 5 mV/LbF
DYTRAN INSTRUMENTS, INC.
MASTER
ONLY IF IN RED
CHATSWORTH, CA.
SCALE 1X
REV -
DATE SEE REV BLOCK
ECN -
DATE 6/17/00
PART NO.
DRAWN N.C.
CHECKED
MAT'L
APPROVED
NEXT ASSEMBLY
USED ON
TITLE
OUTLINE/INSTALLATION DRAWING,
IMPULSE HAMMER SERIES 5800B
DWG NO.
127-5800B
SHEET 1 OF 1
1. HEAD WEIGHT - 100 GRAMS, TOTAL
WEIGHT-220 GRAMS

Model Number 5800B5	PERFORMANCE SPECIFICATION	DOC NO PS5800B5
	IMPULSE HAMMER	REV A, ECN 11034, 06/25/14

- **ACCELERATION COMPENSATED**
- **EXCELLENT LINEARITY**
- **INTERCHANGABLE IMPACT TIPS**

		ENGLISH		SI	
PHYSICAL					
Weight, Head		3.5	oz	100	grams
Connector		BNC		BNC	
Head	Material	Stainless Steel		Stainless Steel	
Handle	Material	Fiberglass		Fiberglass	
Impact Tips	Material	Aluminum / Plastic		Aluminum / Plastic	
Sensing Element	Material	Quartz		Quartz	
	Mode	Compression		Compression	
PERFORMANCE					
Sensitivity, ± 10 %		5	mV/LbF	1.1	mV/N
Range		1,000	Lbs. Force	4448	N
Maximum Force		2,000	Lbs. Force	8896	N
Linearity [1]		±1	% Full Scale	±1	% Full Scale
Resonant Frequency		75	kHz	75	kHz
Stiffness, Force Sensor		11.4	Lb/µin	2.0	kN/µm
ELECTRICAL					
Output Voltage F.S		±5	V	±5	V
Output Impedance, Max		100	Ω	100	Ω
Bias Voltage		7 to 12	VDC	7 to 12	VDC
Compliance Voltage Range		18 to 30	VDC	18 to 30	VDC
Supply Current Range		2 to 20	mA	2 to 20	mA
Discharge Time Constant, Nom		300	Sec	300	Sec

This family also includes:

Model	Sensitivity (mV/Lb)	Range (Lb. Force)	Max.Force (Lb. Force)	Discharge T.C. (sec)
5800B1	500	10	200	5
5800B2	100	50	1000	20
5800B3	50	100	1000	50
5800B4	10	500	1000	170
5801B4	10	500	6000	170
5801B5	5	1,000	8000	300
5801B6	1	5,000	8000	1700

Refer to the performance specifications of the products in this family for detailed description.

Supplied Accessories:

1) Accredited calibration certificate (ISO 17025)
2) Impact tips: 1X Model 6250A (aluminum), 1X Model 6250P (plastic), 1X model 6250PS (soft plastic)

Notes:

[1] Percent of full scale or any lesser range, Zero based best-fit straight line method.
[2] In the interest of constant product improvement, we reserve the right to change specifications without notice.

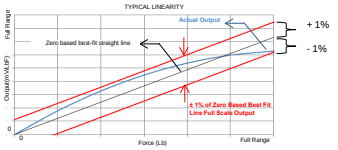

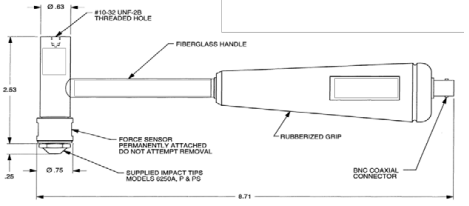

Units on the line drawing are in inches, units in brackets are in millimeters. Refer to 127-5800B for more information.

DYTRAN INSTRUMENTS, INC.
21592 Marilla Street, Chatsworth, California 91311 Phone: 818.700.7818 Fax:818.700.7880 www.dytran.com

Bibliography

Acharya, S. (2008). Gas turbine photo. https://upload.wikimedia.org/wikipedia/commons/5/56/J85_ge_17a_turbojet_engine.jpg. (accessed April 25, 2018).

Afshari, M. and Inman, D. J. (2012). Continuous crack modeling in piezoelectrically driven vibrations of an Euler-Bernoulli beam. *Journal of Vibration and Control*, 19(3):341–355.

Anderson, T. L. (2005). *Fracture Mechanics: Fundamentals and Applications, Third Edition*. Taylor and Francis, third edit edition.

Andreaus, U., Casini, P., and Vestroni, F. (2007). Non-linear dynamics of a cracked cantilever beam under harmonic excitation. *International Journal of Non-Linear Mechanics*, 42(3):566–575.

Anifantis, N. and Dimarogonas, A. (1984). Post buckling behavior of transverse cracked columns. *Computers and Structures*, 18(2):351–356.

Bachschmid, N., Tanzi, E., and Pennacchi, P. (2010). *Cracked rotors: A survey on static and dynamic behaviour including modelling and diagnosis*. Springer-Verlag.

Banerjee, A. and Pohit, G. (2014). Crack investigation of rotating cantilever beam by fractal dimension analysis. *Procedia Technology*, 14:188–195.

Banerjee, J. R., Su, H., and Jackson, D. R. (2006). Free vibration of rotating tapered beams using the dynamic stiffness method. *Journal of Sound and Vibration*, 298(4-5):1034–1054.

Barad, K. H., Sharma, D. S., and Vyas, V. (2013). Crack Detection in Cantilever Beam by Frequency based Method. *Procedia Engineering*, 51:770–775.

Baxter, M. G., Pullin, R., Holford, K. M., and Evans, S. L. (2007). Delta T source location for acoustic emission. *Mechanical Systems and Signal Processing*, 21(3):1512–1520.

Bhat, R. B. (1986). Transverse vibrations of a rotating uniform cantilever beam with tip mass as predicted by using beam characteristic orthogonal polynomials in the Rayleigh-Ritz method. *Journal of Sound and Vibration*, 105(2):199–210.

Bovsunovsky, A. and Surace, C. (2015). Non-linearities in the vibrations of elastic structures with a closing crack: A state of the art review. *Mechanical Systems and Signal Processing*, 62:129–148.

Cai, G.-P., Hong, J.-Z., and Yang, S. X. (2004). Model study and active control of a rotating flexible cantilever beam. *International Journal of Mechanical Sciences*, 46(6):871–889.

Camperi, S., Ghanchi-Tehrani, M., Zilletti, M., and Elliott, S. J. (2016). Active vibration control of an inertial actuator subject to broadband excitation. *Journal of Physics: Conference Series*, 744(1).

Castorrini, A., Corsini, A., Rispoli, F., Venturini, P., Takizawa, K., and Tezduyar, T. E. (2016). Computational analysis of wind-turbine blade rain erosion. *Computers and Fluids*, 141:175–183.

Centro de Publicaciones (2006). Report A-037/2006 accident involving a SIKORSKY S-61N, registration EC-FJJ, on 8 July 2006, in Roque Bermejo (Tenerife-Canary Islands-Spain). Technical Report July, Secretaria General Tecnica, Ministerio de Fomento., Madrid.

Chai, G. B. (1994). Free vibration of generally laminated composite plates with various edge support conditions. *Composite Structures*, 29(3):249–258.

Chati, M., Rand, R., and Mukherjee, S. (1997). Modal Analysis of a Cracked Beam. *Journal of Sound and Vibration*, 207(2):249–270.

Chatterjee, A. (2010). Structural damage assessment in a cantilever beam with a breathing crack using higher order frequency response functions. *Journal of Sound and Vibration*, 329(16):3325–3334.

Chen, L.-W. and Shen, G. S. (1997). Dynamic stability of cracked rotating beams of general orthotropy. *Composite Structures*, 37(2):165–172.

Chen, P. (2012). Sikorsky S-61N. https://www.flickr.com/photos/milchcow_peng/7145801099/. (accessed April 25, 2018).

Chen, X. and Liu, Y. (2014). *Finite element modeling and simulation ansys workbench*. Taylor & Francis Group, Boca Raton, FL.

Chen, Z., Yang, Y., Xie, Y., Guo, B., and Hu, Z. (2013). Non-contact crack detection of high-speed blades based on principal component analysis and Euclidian angles using optical-fiber sensors. *Sensors and Actuators, A: Physical*, 201:66–72.

Cheng, T. H. and Oh, I. K. (2009). Coil-based electromagnetic damper and actuator for vibration suppression of cantilever beams. *Journal of Intelligent Material Systems and Structures*, 20(18):2237–2247.

Cheng, Y., Yu, Z., Wu, X., and Yuan, Y. (2011). Vibration analysis of a cracked rotating tapered beam using the p-version finite element method. *Finite Elements in Analysis and Design*, 47(7):825–834.

Chondros, T., Dimarogonas, A., and Yao, J. (1998). A continuous cracked beam vibration theory. *Journal of Sound and Vibration*, 215(1):17–34.

Chondros, T., Dimarogonas, A., and Yao, J. (2001). Vibration of a beam with a breathing crack. *Journal of Sound and Vibration*, 239(1):57–67.

Chondros, T. G. and Dimarogonas, A. D. (1998). Vibration of a cracked cantilever beam. *Journal of vibration and acoustics*, 120(3):742–746.

Chung, J. and Yoo, H. (2002). Dynamic Analysis of a Rotating Cantilever Beam By Using the Finite Element Method. *Journal of Sound and Vibration*, 249(1):147–164.

Davis, J. (2000). *Corrosion: understanding the basics*.

Dervilis, N., Choi, M., Taylor, S. G., Barthorpe, R. J., Park, G., Farrar, C. R., and Worden, K. (2014). On damage diagnosis for a wind turbine blade using pattern recognition. *Journal of Sound and Vibration*, 333(6):1833–1850.

Dimarogonas, A. D. (1996). Vibration of cracked structures: A state of the art review. *Engineering Fracture Mechanics*, 55(5):831–857.

Douka, E., Bamnios, G., and Trochidis, A. (2004). A method for determining the location and depth of cracks in double-cracked beams. *Applied Acoustics*, 65(10):997–1008.

Douka, E. and Hadjileontiadis, L. J. (2005). Timefrequency analysis of the free vibration response of a beam with a breathing crack. *NDT & E International*, 38(1):3–10.

Eroglu, U. and Tufekci, E. (2016). Exact solution based finite element formulation of cracked beams for crack detection. *International Journal of Solids and Structures*, 96:240–253.

Fernández-Sáez, J., Rubio, L., and Navarro, C. (1999). Approximate calculation of the fundamental frequency for bending vibrations of cracked beams. *Journal of Sound and Vibration*, 225(2):345–352.

Field, M. (2006). Helicopter. https://commons.wikimedia.org/wiki/File:LAPD_Bell_206_Jetranger.jpg. (accessed April 25, 2018).

Friswell, M. I. and Penny, J. E. T. (1992). a Simple Nonlinear Model of a Cracked Beam.

G. P. Engels and Thomas, M. C. (1993). Helicopter blade crack detection system.

Gounaris, G. and Dimarogonas, A. (1988). A finite element of a cracked prismatic beam for structural analysis. *Computers and Structures*, 28(3):309–313.

Hagara, M., Huady, R., Lengvarský, P., and Pavelka, P. (2015). Analysis of Reliability of Modal Parameters Estimation Using High-speed Digital Image Correlation Method. 3(6):190–194.

Han, W., Kim, J., and Kim, B. (2018). Effects of contamination and erosion at the leading edge of blade tip airfoils on the annual energy production of wind turbines. *Renewable Energy*, 115:817–823.

Helfrick, M. N., Niezrecki, C., Avitabile, P., and Schmidt, T. (2011). 3D digital image correlation methods for full-field vibration measurement. *Mechanical Systems and Signal Processing*, 25(3):917–927.

Hh, Y. (1995). Dynamics of flexible beams undergoing overall motions. *Journal of Sound and Vibration*, 181(2):261–278.

Hillewaert, H. (2008). Wind turbine.

Ibrahim, A. M., Ozturk, H., and Sabuncu, M. (2013). Vibration analysis of cracked frame structures. *Structural Engineering and Mechanics*, 45(1):33–52.

Inman, D. J. and Tech, V. (2006). *Vibration with Control*. Wiley, Chichester.

Jochems, C. E. A., Van der Valk, J. B. F., Stafleu, F. R., and Baumans, V. (2002). The use of fetal bovine serum: Ethical or scientific problem?

Karaagac, C., Öztürk, H., and Sabuncu, M. (2009). Free vibration and lateral buckling of a cantilever slender beam with an edge crack: Experimental and numerical studies. *Journal of Sound and Vibration*, 326(1-2):235–250.

Kim, H., Hee Yoo, H., and Chung, J. (2013). Dynamic model for free vibration and response analysis of rotating beams. *Journal of Sound and Vibration*, 332(22):5917–5928.

Kim, S. S. and Kim, J. H. (2003). Rotating composite beam with a breathing crack. *Composite Structures*, 60(1):83–90.

Krawczuk, M., Zak, A., and Ostachowicz, W. (2000). Elastic beam finite element with a transverse elasto-plastic crack. *Finite elements in analysis and design*, 34(1):61–73.

Lien-Wen, C. and Chiung-Lu, C. (1988). Vibration and stability of cracked thick rotating blades. *Computers and Structures*, 28(1):67–74.

Lima, M. A. C. F. (2012). *Rotating Cantilever Beams : Finite Element Modeling and Vibration Analysis*. PhD thesis, Faculdade de Engenharia da Universidade do Porto.

Liu, C. and Jiang, D. (2014). Crack modeling of rotating blades with cracked hexahedral finite element method. *Mechanical Systems and Signal Processing*, 46(2):406–423.

Luo, D. (1998). *Pattern Recognition and Image Processing*. Woodhead Publishing Series in Electronic and Optical Materials. Elsevier Science, second edi edition.

Marks, R., Gillam, C., Clarke, A., Armstrong, J., and Pullin, R. (2017). Damage detection in a composite wind turbine blade using 3D scanning laser vibrometry. *Proceedings of the Institution of Mechanical Engineers, Part C: Journal of Mechanical Engineering Science*, 231(16):3024–3041.

Masoud, A. A. and Al-Said, S. (2009). A new algorithm for crack localization in a rotating Timoshenko beam. *Journal of Vibration and Control*, 15(10):1541–1561.

MatchID (2016). *MatchID 2D, Metrology beyond colors v2016.2.2*. Http://matchidmbc.be, Belgium.

Mazanoglu, K. and Guler, S. (2017). Flap-wise and chord-wise vibrations of axially functionally graded tapered beams rotating around a hub. *Mechanical Systems and Signal Processing*, 89:97–107.

Mazanoglu, K. and Sabuncu, M. (2012). A frequency based algorithm for identification of single and double cracked beams via a statistical approach used in experiment. *Mechanical Systems and Signal Processing*, 30:168–185.

Mehrjoo, M., Khaji, N., and Ghafory-Ashtiany, M. (2013). Application of genetic algorithm in crack detection of beam-like structures using a new cracked Euler-Bernoulli beam element. *Applied Soft Computing Journal*, 13(2):867–880.

Molina-Viedma, A. J., Felipe-Sesé, L., López-Alba, E., and Díaz, F. (2018). High frequency mode shapes characterisation using Digital Image Correlation and phase-based motion magnification. *Mechanical Systems and Signal Processing*, 102:245–261.

Nahvi, H. and Jabbari, M. (2005). Crack detection in beams using experimental modal data and finite element model. *International Journal of Mechanical Sciences*, 47(10):1477–1497.

Nguyen, K. V. (2014). Mode shapes analysis of a cracked beam and its application for crack detection. *Journal of Sound and Vibration*, 333(3):848–872.

Oliveri, V. and Milazzo, A. (2018). A Rayleigh-Ritz approach for postbuckling analysis of variable angle tow composite stiffened panels. *Computers and Structures*, 196:263–276.

Ozdemir, O. and Kaya, M. O. (2006). Flapwise bending vibration analysis of a rotating tapered cantilever Bernoulli-Euler beam by differential transform method. *Journal of Sound and Vibration*, 289(1-2):413–420.

Ozturk, H., Yashar, A., and Sabuncu, M. (2016). Dynamic stability of cracked multi-bay frame structures. *Mechanics of Advanced Materials and Structures*, 23(6):715–726.

Pan, B., Qian, K., Xie, H., and Asundi, A. (2009). Two-dimensional digital image correlation for in-plane displacement and strain measurement : a review. *Meas. Sci. Technol.*, 20:1–17.

Panigrahi, I. and Parhi, D. R. (2009). Dynamic analysis of Cantilever beam with transverse crack. In *Mechanical Engineering*, pages 310–315.

Papadopoulos, C. A. and Dimarogonas, A. D. (1987). Coupled longitudinal and bending vibrations of a rotating shaft with an open crack. *Journal of Sound and Vibration*, 117(1):81–93.

Pastor, M., Binda, M., and Harčarik, T. (2012). Modal assurance criterion. *Procedia Engineering*, 48:543–548.

Pawar, P. M. and Ganguli, R. (2007). Helicopter rotor health monitoring - A review. *Proceedings of the Institution of Mechanical Engineers, Part G: Journal of Aerospace Engineering*, 221(5):631–647.

Qian, G. L., Gu, S. N., and Jiang, J. S. (1990). The dynamic behaviour and crack detection of a beam with a crack. *Journal of Sound and Vibration*, 138(2):233–243.

Rao, S. and Gupta, R. (2001). Finite element vibration analysis of rotating timoshenko beams. *Journal of Sound and Vibration*, 242(1):103–124.

Rao, S. S. (2005). *The Finite Element Method in Engineering*. Elsevier.

Rohlfing, J., May, T., Walter, L., and Millitzer, J. (2016). Self-tuning velocity feedback control for a time varying structure using a voltage driven electrodynamic inertial mass actuator. *Proceedings of ISMA 2016 - International Conference on Noise and Vibration Engineering and USD2016 - International Conference on Uncertainty in Structural Dynamics*, pages 259–274.

Romaszko, M., Sapiński, B., and Sioma, A. (2015). Forced vibrations analysis of a cantilever beam using the vision method. *Journal of Theoretical and Applied Mechanics*, page 243.

Rubinstein, N. and Stadter, J. T. (1972). Bounds to bending frequencies of a rotating beam. *Journal of the Franklin Institute*, 294(4):217–229.

Ruotolo, R., Surace, C., Crespo, P., and Storer, D. (1996). Harmonic analysis of the vibrations of a cantilevered beam with a closing crack. *Computers and Structures*, 61(6):1057–1074.

Satpute, D., Baviskar, P., Gandhi, P., Chavanke, M., and Aher, T. (2017). Crack detection in cantilever shaft beam using natural frequency. *Materials Today: Proceedings*, 4(2):1366–1374.

Schijve, J. (2004). *Fatigue of Structures and Materials*. Springer Science & Business Media, 2008, Netherlands.

Sekhar, A. and Prabhu, B. (1998). Condition monitoring of cracked rotors through transient response. *Mechanism and Machine Theory*, 33(8):1167–1175.

Silani, M., Ziaei-Rad, S., and Talebi, H. (2013). Vibration analysis of rotating systems with open and breathing cracks. *Applied Mathematical Modelling*, 37(24):9907–9921.

Sodano, H. A., Bae, J. S., Inman, D. J., and Keith Belvin, W. (2005). Concept and model of eddy current damper for vibration suppression of a beam. *Journal of Sound and Vibration*, 288(4-5):1177–1196.

Song, Y. Z., Bowen, C. R., Kim, H. A., Nassehi, A., Padget, J., Gathercole, N., and Dent, A. (2014). Non-invasive damage detection in beams using marker extraction and wavelets. *Mechanical Systems and Signal Processing*, 49(1-2):13–23.

Tada, H., Paris, P. C., and Irwin, G. R. (2000a). *The stress analysis of cracks handbook*. ASME Press.

Tada, H., Paris, P. C., and Irwin, G. R. (2000b). *The Stress Analysis of Cracks Handbook, Third Edition*. ASME Press, New York.

Thomsen, J. J. (2003). *Vibrations and Stability: Advanced Theory, Analysis, and Tools*. Springer complexity. Springer, Verlag Berlin Heidelberg, 2 edition.

Vakil-Baghmisheh, M. T., Peimani, M., Sadeghi, M. H., and Ettefagh, M. M. (2008). Crack detection in beam-like structures using genetic algorithms. *Applied Soft Computing Journal*, 8(2):1150–1160.

Vakil Baghmisheh, M. T., Peimani, M., Sadeghi, M. H., Ettefagh, M. M., and Tabrizi, A. F. (2012). A hybrid particle swarm-Nelder-Mead optimization method for crack detection in cantilever beams. *Applied Soft Computing Journal*, 12(8):2217–2226.

Vigneshwaran, K. and Behera, R. K. (2014). Vibration analysis of a simply supported beam with multiple breathing cracks. *Procedia Engineering*, 86(1990):835–842.

Wang, L. and Yang, Z. (2011). Identification of boundary conditions of tapered beam-like structures using static flexibility measurements. *Mechanical Systems and Signal Processing*, 25(7):2484–2500.

Xue, X. and Tang, J. (2008). Vibration control of nonlinear rotating beam using piezoelectric actuator and sliding mode approach. *JVC/Journal of Vibration and Control*, 14(6):885–908.

Yan, B., Zhang, X., and Niu, H. (2012). Vibration isolation of a beam via negative resistance electromagnetic shunt dampers. *Journal of Intelligent Material Systems and Structures*, 23(6):665–673.

Yan, G., De Stefano, A., Matta, E., and Feng, R. (2013). A novel approach to detecting breathing-fatigue cracks based on dynamic characteristics. *Journal of Sound and Vibration*, 332(2):407–422.

Yang, J. B., Jiang, L. J., and Chen, D. C. (2004). Dynamic modelling and control of a rotating Euler-Bernoulli beam. *Journal of Sound and Vibration*, 274(3-5):863–875.

Yang, Y., Dorn, C., Mancini, T., Talken, Z., Kenyon, G., Farrar, C., and Mascareñas, D. (2017). Blind identification of full-field vibration modes from video measurements with phase-based video motion magnification. *Mechanical Systems and Signal Processing*, 85:567–590.

Yashar, A., Ferguson, N., and Ghandchi-Tehrani, M. (2018). Simplified modelling and analysis of a rotating Euler-Bernoulli beam with a single cracked edge. *Journal of Sound and Vibration*, 420:346–356.

Yashar, A., Ghandchi-Tehrani, M., and S. Ferguson, N. (2016). Dynamic behaviour of a rotating cracked beam. *Journal of Physics: Conference Series*, 744(1):012057.

Yoo, H. H., Cho, J. E., and Chung, J. (2006). Modal analysis and shape optimization of rotating cantilever beams. *Journal of Sound and Vibration*, 290(1-2):223–241.

Yoo, H. H. and Shin, S. H. (1998). Vibration analysis of rotating cantilever beams. *Journal of Sound and Vibration*, 212(5):807–828.

Younesian, D., Esmailzadeh, E., and Sedaghati, R. (2006). Passive vibration control of beams subjected to random excitations with peaked PSD. *JVC/Journal of Vibration and Control*, 12(9):941–953.

Younesian, D., Kargarnovin, M. H., and Esmailzadeh, E. (2008). Optimal passive vibration control of Timoshenko beams with arbitrary boundary conditions traversed by moving loads. *Proceedings of the Institution of Mechanical Engineers, Part K: Journal of Multi-body Dynamics*, 222(2):179–188.

Zhao, G. and Wu, Z. (2017). Coupling vibration analysis of rotating three-dimensional cantilever beam. *Computers and Structures*, 179:64–74.

Zheng, D. Y. and Kessissoglou, N. J. (2004). Free vibration analysis of a cracked beam by finite element method. *Journal of Sound and Vibration*, 273(3):457–475.